PULSED MAGNETOHYDRODYNAMIC PROGRAM

HERCULES, INCORPORATED

PREPARED FOR

AIR FORCE AERO PROPULSION LABORATORY

16 JULY 1976

UNCLASSIFIED

SECURITY CLASSIFICATION OF THIS PAGE *(When Data Entered)*

REPORT DOCUMENTATION PAGE		READ INSTRUCTIONS BEFORE COMPLETING FORM
1. REPORT NUMBER AFAPL-TR-76-34	2. GOVT ACCESSION NO.	3. RECIPIENT'S CATALOG NUMBER
4. TITLE *(and Subtitle)* Pulsed Magnetohydrodynamic Program		5. TYPE OF REPORT & PERIOD COVERED Final 2 Jan. 72-31 March 76 6. PERFORMING ORG. REPORT NUMBER
7. AUTHOR(s) C. D. Bangerter & B. D. Hopkins, Hercules Inc. T. R. Brogan, MEPPSCO, Inc.		8. CONTRACT OR GRANT NUMBER(s) F33615-72-C-1394
9. PERFORMING ORGANIZATION NAME AND ADDRESS Hercules Incorporated Systems Group Bacchus Works, Magna, Utah 84044		10. PROGRAM ELEMENT, PROJECT, TASK AREA & WORK UNIT NUMBERS 31452624
11. CONTROLLING OFFICE NAME AND ADDRESS Air Force Aero Propulsion Laboratory, AFAPL/POD Air Force Systems Command Wright-Patterson AFB, Ohio 45433		12. REPORT DATE 16 July 1976 13. NUMBER OF PAGES 254
14. MONITORING AGENCY NAME & ADDRESS*(if different from Controlling Office)*		15. SECURITY CLASS. *(of this report)* Unclassified 15a. DECLASSIFICATION/DOWNGRADING SCHEDULE

16. DISTRIBUTION STATEMENT *(of this Report)*

Approved for public release;
distribution unlimited

17. DISTRIBUTION STATEMENT *(of the abstract entered in Block 20, if different from Report)*

18. SUPPLEMENTARY NOTES

19. KEY WORDS *(Continue on reverse side if necessary and identify by block number)*

Magnetohydrodynamics, deflagrating solid explosive MHD, solid propellant MHD, detonating solid explosive MHD, explosive MHD

20. ABSTRACT *(Continue on reverse side if necessary and identify by block number)*

This report is the final report for Contract F33615-72-C-1394. It supplements interim report AFAPL-TR-73-16 published in May 1973. Part I of this report covers the design, fabrication and testing of an MHD generator using a deflagrating solid explosive as the energy source. A power output of 2.4 MW was obtained at a mass flow rate of 3.2 kg/s from this generator. Part II covers the fabrication, testing and analysis of an MHD generator using a detonating solid as the energy source. An energy output of 11.8 kJ was obtained from 0.05 kg of Composition C-4 explosive for an efficiency of 5.7% from this generator

DD FORM 1 JAN 73 1473 EDITION OF 1 NOV 65 IS OBSOLETE

UNCLASSIFIED

SECURITY CLASSIFICATION OF THIS PAGE *(When Data Entered)*

NOTICE

When Government drawings, specifications, or other data are used for any purpose other than in connection with a definitely related Government procurement operation, the United States Government thereby incurs no responsibility nor any obligation whatsoever; and the fact that the government may have formulated, furnished, or in any way supplied the said drawings, specifications, or other data, is not to be regarded by implication or otherwise as in any manner licensing the holder or any other person or corporation, or conveying any rights or permission to manufacture, use, or sell any patented invention that may in any way be related thereto.

This final report was submitted by Hercules Incorporated under Contract F33615-72-C-1394. The effort was sponsored by the Advanced Research Projects Agency under ARPA Order No. 2357 and the Air Force Aero Propulsion Laboratory, Air Force Systems Command, Wright-Patterson AFB, Ohio under Work Unit 31452624 with R. F. Cooper, AFAPL/POD, as Program Manager. C. D. Dangerter and B. D. Hopkins of Hercules Incorporated were technically responsible for the work.

This report has been reviewed by the Information Office, (ASD/OIP) and is releasable to the National Technical Information Service (NTIS). At NTIS, it will be available to the general public, including foreign nations.

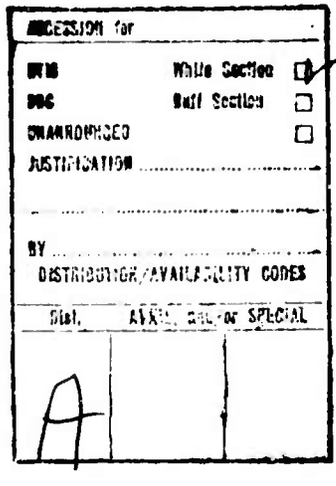

Copies of this report should not be returned unless return is required by security considerations, contractual obligations, or notice on a specific document.

TABLE OF CONTENTS

SECTION I

SUMMARY

This is the final report on work completed under Contract F33615-72-C-1394. The goals of the program were twofold: (1) To develop the technical base to allow for the design and construction of lightweight, multimegawatt deflagrating solid explosive driven MHD (C-MHD) and, (2) to evaluate the feasibility of multikilowatt, high-repetition-rate detonating solid explosive MHD (X-MHD) generators. This work was to include demonstration of 4 MW power output from a deflagrating explosive generator with a mass flow rate of 4 kg/s and 25 kJ energy from a detonating explosive generator at an efficiency of 5%.

The report is divided into two sections which are organized in a roughly parallel format. Part I covers the work on deflagrating explosive MHD while Part II covers detonating explosive MHD. Each part has an introduction, a description of the experimental apparatus, the test results, conclusions and recommendations for future development. In addition, Part I has a section covering the selection of a solid propellant while Part II has a separate section with some additional discussion of the X-MHD channel performance.

The early part of the program dealt almost exclusively with the theory and design of X-MHD systems involving explosives, generator geometry, and magnet. That portion of the program has already been reported in an interim report,[1] AFAPL TR-73-16 (DDC-AD 762934) dated May 1973 and is not included in the present discussion. The fabrication of the experimental apparatus was not covered in the earlier report and is, therefore, discussed in the present report. Additional detail is also given on the design of the C-MHD channel and fuel since they were not covered in the earlier report.

Although it cannot be claimed that the very ambitious goals of the program were fully achieved, some significant positive steps toward fulfillment were taken. A maximum power output of 2.4 MW was achieved in the C-MHD channel at a mass flow rate of 3.2 kg/s. This corresponds to a power extraction of 0.74 MW/(kg/s). The X-MHD device produced a maximum energy output of 11.8 kJ from 1/2 of the dual linear channel using 0.05 kg of Composition C-4 explosive. This corresponds to an efficiency of 5.7% based on the heat of explosion of the charge material. As is shown in the following sections of the report, the reasons for reduced performance have been identified and a future course of action has been suggested to obtain the desired performance from both types of generator.

REFERENCES

1. C. D. Bangerter, L. R. West, T. R. Brogan, D. B. Sheldon, Z. J. J. Stekley and J. Farrh, Explosive Magnetohydrodynamic Program, Interim Technical Report No. AFAPL-TR-73-16, May 1973.

PART I

DEFLAGRATING EXPLOSIVE MHD STUDIES

SECTION II

INTRODUCTION

Deflagrating solid explosives have found extensive application in tactical and strategic rockets because of small size and high energy content. The propellant contains both the fuel and oxidizer which eliminates any requirement for separate storage of these components or need to provide a way of mixing prior to ignition. This is particularly important when long-term storage or portability is required. The lack of valves or cryogenics for the combustor also increases reliability of the system.

The advantages of a solid propellant in an MHD application are expected to be as follows:

(a) High conductivity of combustion products

(b) Relatively constant conductivity with expansion

(c) Efficient conversion of gas dynamic energy to electrical energy

(d) Compact, high density source of high temperature gas

(e) No valves or cryogenics for combustor

(f) Long-term storage capability

(g) Fast startup even after long, inactive period

(h) High reliability

Figure 2-1 shows the calculated conductivity of a cesium-seeded propellant as a function of channel entrance pressure starting from a 20.4 atm chamber pressure. This figure demonstrates that the expected conductivity is several times higher than normally associated with seeded combustion products of liquid hydrocarbon fuels and oxygen.

Both the high conductivity and its relative constancy are due to the extremely high flame temperature, the relatively slow temperature

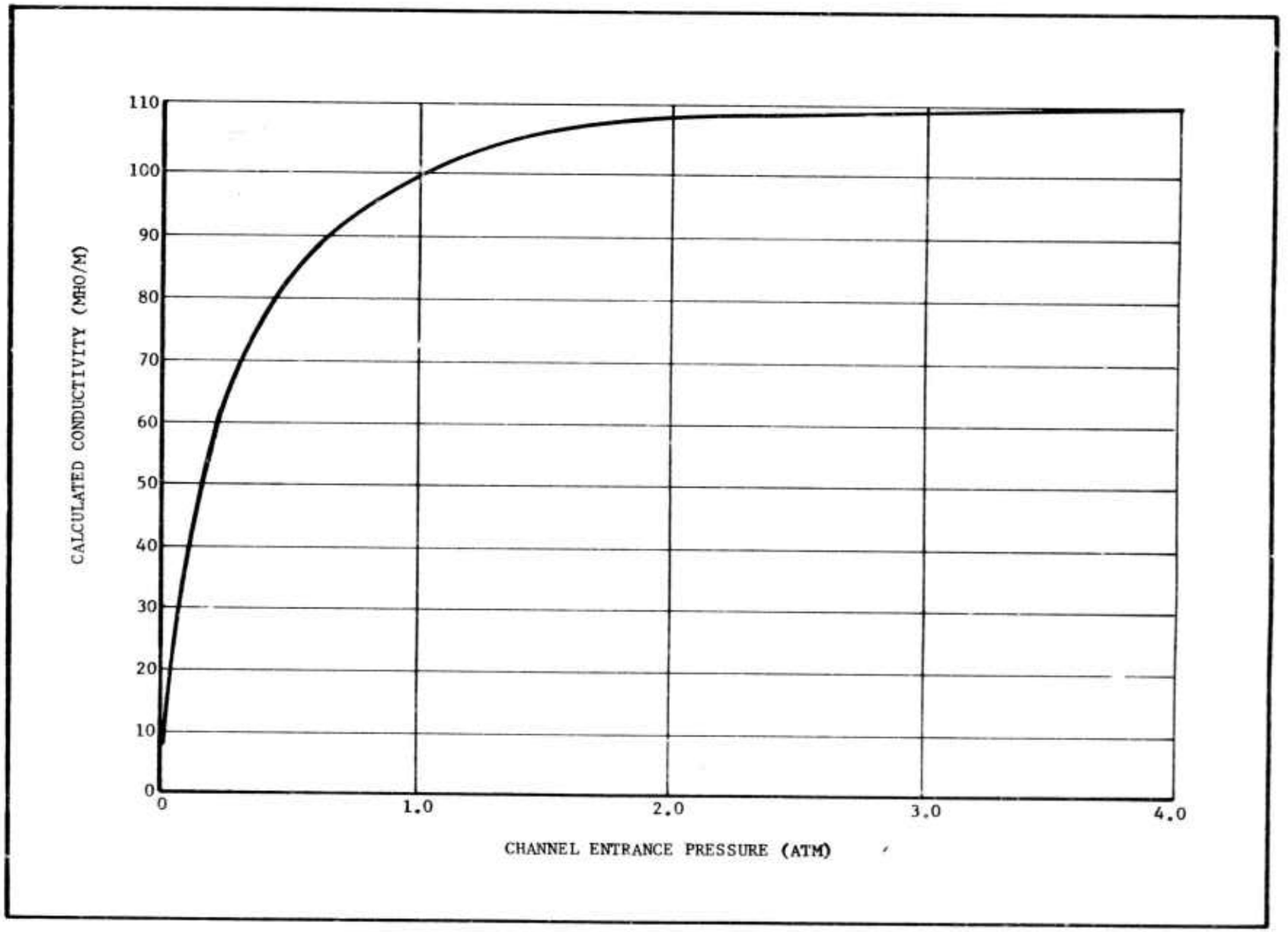

Figure 2-1. Calculated Conductivity of $CsNO_3$ Seeded Fuel Versus Channel Entrance Pressure (Chamber Pressure - 20.4 atm)

drop with pressure along the isentrope, the high seed concentration, and the relatively greater importance of electron-ion collisions which tend to make the conductivity insensitive to temperature.

High power density and a small length-to-diameter ratio with reduced friction and heat transfer losses and low weight are direct results of high conductivity. Additional benefits include reduced field requirements, reduced breakdown probability for fixed power density, and greater factor of safety. The benefits of the relative constancy of the conductivity are more subtle and can be described as ease of diagonalization over wide static pressure ratio and much greater design flexibility.

The first experiments with a deflagrating solid explosive as an energy source for MHD power were performed in 1963 at Hercules Incorporated. This work was continued through 1967 under both IR&D and contract funding and it included demonstration of 1.5 MW at an efficiency of 5.3 percent.[1]

A well documented example of the use of solid propellants for an MHD application is given in Reference 2. This example shows clearly that excellent performance can be obtained from solids even though the channel used for the testing was not designed for use with this propellant. This work began in mid-1967 when Hercules obtained a contract to furnish 20 10-pound solid propellant grains, motor hardware, and a mating transition section to the University of Tennessee Space Institute (UTSI). These grains were fired in the UTSI diagonal conducting wall generator and also in a UTSI Hall channel. The basic conclusions that can be drawn from the UTSI work are as follows:

(a) Solid propellants offer an increase of at least a factor of 4 to 5 in the specific energy over that provided by RP-1

and gaseous oxygen.

(b) The solid propellant gave a specific power of 0.23 MJ/kg with an average efficiency of 3.5 percent and a one-test efficiency of 5 percent.

(c) Condensation of aluminum oxide on electrodes and channel walls is not detrimental to the generator performance.

The solid propellant was of a type similar to the double-base metallized propellants used for rocket applications, except for the high potassium nitrate loading (12.7 wt percent). The solid combustor used a cylindrical core solid rocket motor operating at 23.8 atm through a heat sink graphite nozzle and a transition section connected to the generator channel. The nozzle throat area was a 3.2 cm^2 with a channel inlet ratio of 16:1. Computations indicate the following channel entrance conditions: Mass flow rate, 0.52 kg/sec; pressure, 0.211 atm; gas temperature, 2630°K; mixture velocity, 2250 m/sec; electrical conductivity, 73 mhos/m; and $\omega\tau/B$, 2.1 m^2/volt-sec (where ω is the cyclotron frequency, τ is the mean time between collisions for an electron, and B is the applied magnetic field). The calculation did not consider heat transfer or particle lag so the correct temperature would be below 2630°K.

UTSI fired the Hercules propellant in two different types of channels. The first type was a Hall channel while the second set of tests were performed in a 45° diagonal conducting wall (DCW) device. Both conductivity and power output were measured in the DCW channel. The results of these tests[2] were as follows:

	Hall	DCW
Conductivity (σ)	40-55 mho/m	--
Hall Parameter ($\omega\tau$)	--	0.47 - 0.73
Peak Power*	18 KW	117 KW
Peak Specific Output Energy*	0.021 MJ/kg	0.23 MJ/kg

The average power produced during the first test run in the DCW channel was 162 KW at a load resistance of 7 ohms. The maximum power produced was 208 KW during part of one test.

The most significant aspect of these tests was the fact that the 45° DCW channel with a solid propellant produced a generator output of three to four times that produced by a 20 percent higher mass flow rate of RP-1 and gaseous oxygen. For an airborne system this would be a substantial advantage in addition to the greatly superior handling convenience of a solid propellant over liquid or gaseous reactants.

The efficiency of converting the total mixture enthalpy into electrical energy can be calculated from

$$\text{Eff} = \frac{\text{Electrical Power Out.} \times 100\%}{\text{Total Mixture Enthalpy per Unit Time}}$$

The available total enthalpy for the UTSI experiments was 6.6 MJ/kg which, at a mass flow rate of 0.52 kg/sec, gives an energy per unit time of 3.4 MW. This input power gives an efficiency of 3.5 percent. It should be noted that the channel used in these tests was not designed for use with solid propellants.

This part of the report covers all work which was performed on deflagrating explosive MHD (C-MHD) under Contract No. F33615-72-C-1394. The work was mainly experimental, although a significant amount of analysis was

---

*Based on best fit, voltage-current characteristic curve.

done as a part of the channel design task. The following sections discuss the solid propellants used, give a description of the experimental apparatus, including the subscale test hardware, present the test data obtained with two different propellants, and give a description of problem areas. The final section of this part contains suggestions for future development of C-MHD.

REFERENCES

1. C. D. Bangerter, A. H. Peterson and E. E. Covert, "Operation of Solid Fuel MHD Generators," Proceedings of the Eighth Symposium on Engineering Aspects of MHD, Stanford, 1967.

2. D. L. Denzel, L. J. Davis, J. Muehlhauser, Y. C. L. Wu, R. E. Raylor, R. H. Oliver and J. B. Dicks, "Performance of Solid Propellants in Diagonal Wall Generators," in proceedings of the 9th Symposium on Eng. Aspects of MHD, Tullahoma, Tenn., Apr. 1968. Also see "Experimental Study of Diagonal Conducting Wall Generators Using Solid Propellants," AIAA J. 6, 1647-1651 (1968).

SECTION III

SELECTION OF A SOLID PROPELLANT

A. General Criteria for Solid Combustors

Deflagrating solid explosives or solid propellants, as used in this application, refers to a propellant in solid form containing the oxidizing material and fuel within the same matrix. This discussion will further be limited to the double-base matrix, as opposed to a composite system. This is due to the higher temperatures achievable with the double-base system. The double-base system is so named because, classically, it has as principle ingredients nitrocellulose (NC) as the fuel and an energetic plasticizer, usually nitroglycerin (NG), as the oxidizer. Various other materials are added such as aluminum to increase temperature and various plasticizers and burning rate modifiers. For MHD applications, it is also necessary to add metal salts as seed materials. These are usually added in the form of an oxidizing salt such as KNO_3 or $CsNO_3$. Composite propellants are made by embedding a finely divided solid oxidizer in a plastic, resinous or elastomeric matrix. This matrix usually provides the fuel for combustion of the propellant.

Solid fuels burn by parallel layers such that all burning surfaces regress in a direction normal to the burning surface. This allows the designer to predict the burning surface area as a function of time and allows the design of neutral burning surfaces. The burning rate of a solid fuel depends on the combustion pressure. In simplest form, this can be expressed as:

$$r = bp_c^n$$

where b and n are constants characteristic of the given fuel system and

p_c is the chamber pressure.

The mass flow of the fuel can be written as

$$\dot{m} = S\rho r$$

where S is the grain surface area, ρ is the fuel density and r is the regression rate. The mass flow rate can also be written as:

$$\dot{m} = p_c C_d A_t$$

where C_d is the discharge coefficient which depends only on composition and temperature of the exhaust gas, and A_t is the cross-sectional area of the throat. Under steady-state conditions which are reached very rapidly, these two equations are equal so that

$$p_c C_d A_t = S\rho r = S\rho b p_c^{\,n}$$

or

$$p_c = \left(\frac{S\rho b}{A_t C_d}\right)^{\frac{1}{1-n}}$$

The ratio of S/A_t is called K.

For an ideal gas with constant specific heats and no viscosity or thermal conductivity,

$$C_d = \frac{\gamma}{a_c}\left(\frac{2}{\gamma+1}\right)^{\frac{\gamma+1}{2(\gamma-1)}}$$

where a_c is the sound speed in the chamber and γ is the specific heat ratio for the gas. Aluminized rocket propellants usually have

$$a_c \sim 1100 \text{ m/s}$$

$$\gamma \sim 1.18$$

so

$$C_d \sim 6.6 \times 10^{-4} \text{ s/m}$$

In real situations, the values of r and K as functions of pressure are determined experimentally. Figure 3-1 shows the dependence of r and K on pressure for a specific propellant. A value of K is determined from the experimental data which yields the desired pressure and this, in turn, determines the burning rate. The mass flow rate can also be rewritten in another useful form as

$$\dot{m} = KA_t \rho r.$$

B. Special Considerations in Applying Solid Propellants

The combustion of solid propellants produces a gas together with aluminum and aluminum oxide droplets. The general treatment of a chemical reacting flow containing solids or liquids which participate in the chemistry and undergo phase changes throughout the flow is extremely complex. Condensation rate, particle growth, size distribution, and reaction rate all interplay with details of the flow such as velocity, temperature, and pressure gradients. Phenomena such as condensed phase temperature and velocity lag and chemical nonequilibrium can complicate the general analysis of such flows considerably.

In general, complications due to presence of condensed phases are pronounced in regions of high gradients and tend to become of minor importance where gradients are small or nonexistent. Large gradients are commonly present in boundary layers, shock waves, DeLaval nozzles and, occasionally, in combustion chambers, and consideration of the detailed effects of condensed phase loading is often necessary in these situations. On the other hand, in situations where there is moderate "run" at low gradient, near equilibrium conditions may be expected.

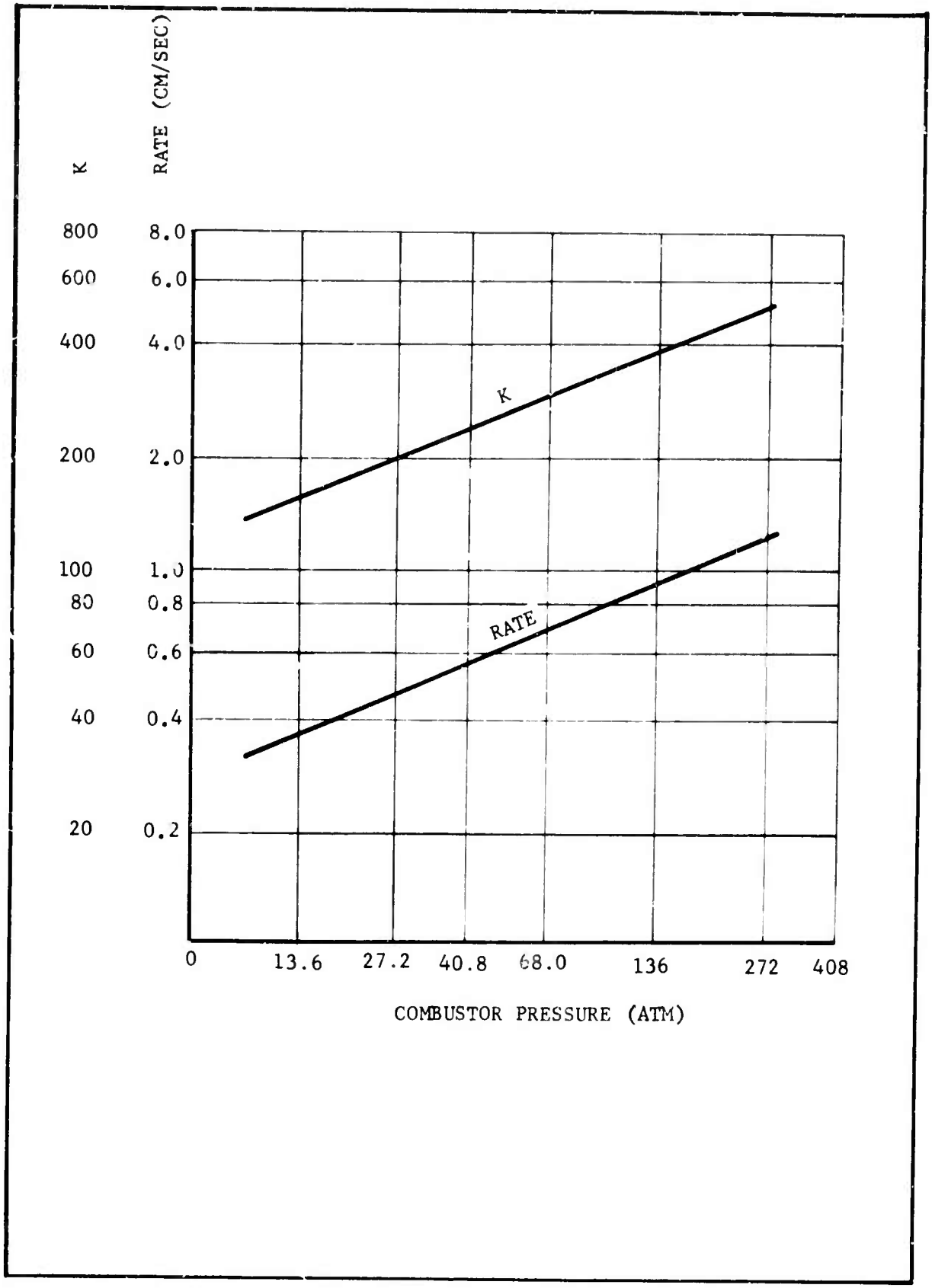

Figure 3-1. Plot of Burning Rate and Grain Surface Area to Throat Area (K) Versus Combustion Pressure

An MHD generator employing solid fuels usually operates at supersonic velocity so the generator working-fluid can pass through regions of high gradients prior to reaching the MHD channel. However, in practice, the regions of high gradient will be well upstream of the MHD generator because the expanding supersonic nozzle flow must match the expansion angle of the MHD generator at the channel entrance. This generator expansion angle is usually quite small (0-4°) so the nozzle expansion resembles that of a long wind tunnel nozzle designed to produce nearly parallel flow rather than the widely divergent propulsion nozzle commonly associated with solid propellant rocket motors. Since the gradients do turn out to be small, at least in the generator, the gas-condensed phase mixture can be treated as a single component continuum in most MHD applications.

C. Related IR&D Activities

During the past several years, Hercules has maintained an IR&D program, one of whose objectives was to formulate and evaluate MHD propellants. The propellants used for the present contract were developed under this IR&D program. The following is a summary of these activities as they relate to the present work.

1. Propellant Formulation

A major factor in obtaining the optimum performance from the MHD generator is selection of the optimum propellant formulations. The properties that are required to achieve the highest possible level of electric energy generation are:

(a) High conductivity of the exhaust gases

(b) High gas mixture velocity

In general, the velocity increases and the conductivity decreases as the exit pressure decreases at a constant chamber pressure. Propellant

characteristics that increase gas mixture velocity are high flame temperature and low molecular weight gases.

These requirements dictate the use of the highest possible binder energy consistent with processibility and mechanical property considerations. The high flame temperature requirement also dictates a high level of a metallic fuel such as aluminum.

Hercules has conducted a large number of calculations using a thermochemical computer code which has an electrical conductivity option to determine the propellant formulation parameters that give the necessary properties for obtaining maximum electrical power generation. The program used is primarily a "free energy" procedure for calculating equilibrium composition of complex gas mixtures; the basic premise being that chemical equilibrium in a gas mixture at a given temperature, and pressure is attained when its total free energy (Gibbs' function) is minimized. The theory on which the program is based has been extended by several authors to include the effect of condensed and ionized molecular species on equilibrium composition, and procedures based on this work are incorporated in the program.

The principal use of this program is the evaluation of rocket propellants by simulating their performance in a rocket motor by taking the theoretical specific impulse as a performance criteria. Chamber conditions in the motor are determined by assuming a balance between the heat of formation of the reactants and the enthalpy of the products of combustion. From these conditions, the entropy in the chamber can be determined. Taking this entropy as a base and assuming an isentropic process, the products of combustion are expanded to specified stations in an (ideal) nozzle. Conditions at these stations are then determined, and the theoretical specific impulse and product composition are calculated from the enthalpy difference between the chamber and the subject station.

The program also includes an optimization procedure and the capability of calculating equilibrium composition at a specified temperature and pressure. Transport properties for the mixture can be obtained from a separate program. An electrical conductivity option is available to modify this program giving the conductivity and gas mixture velocity at any specified station.

The parameters studied in these free energy runs were as follows:

(a) Level of electron generator. Potassium nitrate and cesium nitrate were the two electron generators studied with this program.

(b) Binder energy:

(1) Increasing nitrocellulose (NC) and the expense of nitroglycerin (NG).

(2) Increasing NG at the expense of the low energy polymer, polyethyleneglycol adapate (PGA).

(c) Aluminum level.

(d) Solid oxidizers in place of energetic binder.

(e) Trade-off between potassium and cesium nitrate to determine whether synergysm exists.

Each of these factors are discussed in the following paragraphs.

a. Electron Generators

Alkali metals are the obvious choice for an electron source because they readily give up an electron to form a complete orbital shell. The alkali metal that has the lowest ionization potential is cesium but potassium was also considered because of its substantially lower cost.

The logical manner to incorporate the alkali metal into

the propellant appears to be in its nitrate salt. The nitrate provides considerable energy and oxygen to the propellant without adding electron sink atoms such as the halogens. The pure metals are much too reactive to consider for use in propellants. Both potassium and cesium nitrate are commercially available and both are chemically compatible with other common double-base propellant ingredients.

A comparison of the conductivity σ and gas mixture velocity u, using the relationship σu^2, indicates that the cesium nitrate should outperform potassium nitrate by roughly 20 percent when $CsNO_3$ is substituted for KNO_3 (in the same propellant that was used at UTSI). Additional tailoring of the ingredients provides a further increase in the conductivity.

Because potassium nitrate is cheaper than cesium nitrate, a cost-effective advantage might be obtained by replacing part of the $CsNO_3$ with KNO_3. Also, the possibility of synergism between the two might result in higher performance from the mixture than could be achieved from either by itself.

Free energy equilibrium flow calculations indicate, however, synergism does not exist and a nearly linear reduction in conductivity occurs when replacing $CsNO_3$ with KNO_3. Cost effectiveness studies will be required at some future time to determine whether an advantage could be obtained from using some or all KNO_3 in place of the $CsNO_3$.

b. Binder Energy

One of the important properties in the gas stream that determines the conductivity and gas mixture velocity is the exit temperature. The energy of the binder (or heat of combustion) greatly affects the exit temperature; the higher the energy, the higher the temperature. Therefore, an important part of the development of a propellant is the development of

the highest energy binder that is attainable while retaining manageable mechanical properties, processibility, and low hazards.

The most energetic binder presently in use is the double-base binder. This binder, which is based on NC, NG, and a low energy plasticizer, triacetin (TA), can be made even more energetic by lowering the NC level and the amount of low energy compounds such as TA. One method for accomplishing this while retaining the good mechanical properties is to chemically crosslink the NC to make a continuous gelled polymer matrix throughout the entire propellant.

Figure 3-2 shows the changes in conductivity that are obtained by these adjustments in binder composition. Increasing the NG content by 4 percent at the expense of NC or by 2 percent at the expense of low energy organic compound such as TA increased the conductivity by a factor of 1.4 and 1.9 respectively, accompanied by slight increases in gas mixture velocity in both instances.

c. Aluminum Content

The oxidation balance of the gas mixture also markedly affects the conductivity of the exit gases. A propellant having an OMOX ratio of near 1.0 has the highest conductivity. (An OMOX ratio of 1.0 indicates that gas composition consists of metal oxide, CO, and H_2.) The most effective way to vary the OMOX ratio is to vary the aluminum level. Computation of the conductivity and gas mixture velocity versus OMOX are shown in Figure 3-3 in which the only change is varying the aluminum content at the expense of NG. The conductivity has a sharp maximum slightly below an OMOX of 1.0, whereas the gas mixture velocity continues to increase above an OMOX of 1.0. The product σu^2, however, achieves its maximum value very close to 1.0 so the aluminum level should

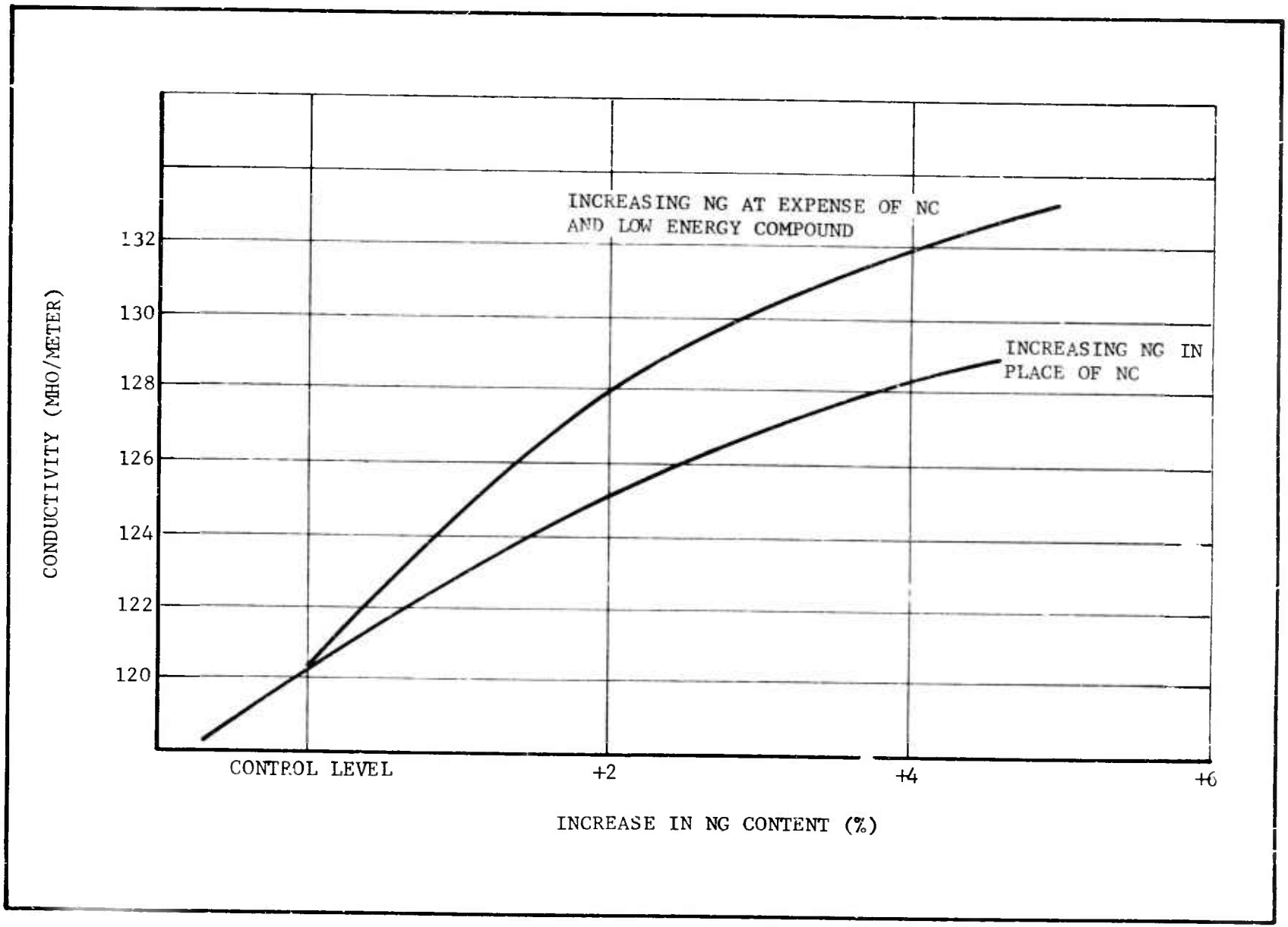

Figure 3-2. Effect of Binder Energy on Conductivity

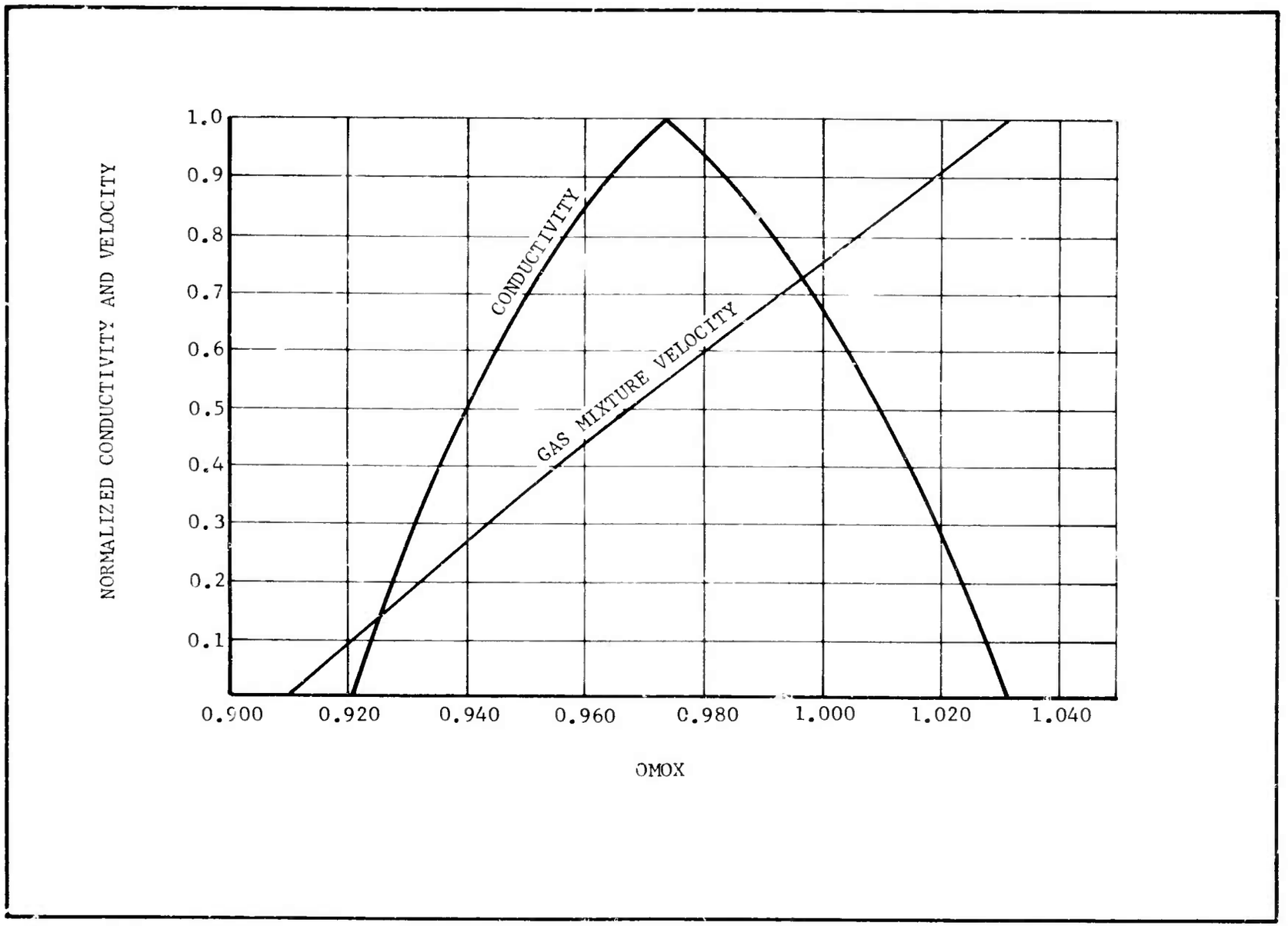

Figure 3-3. Effect of OMOX Ratio on Conductivity and Gas Mixture Velocity

be selected so that the propellant formulation is near an OMOX of 1.0.

d. Solid Oxidizer

The use of two different solid oxidizers has been investigated to determine if increased performance could be realized by replacing part of the binder with a solid. Cyclotetramethylene tetranitramine (HMX) and pentaerythrital tetranitrate (PETN) were selected because of availability, high energy, and because they contain no halogens which are electron sinks. In each case, replacing binder with either of these solid oxidizers lowered the conductivity and gas velocity.

The above discussions indicate that propellant development efforts should be concentrated on achieving

(1) High chamber temperature

(2) High binder energy

(3) OMOX ratio near 1.0

(4) $CsNO_3$ as the major electron source

2. Conductivity Measurements

A diagnostics channel (Figure 3-4) was used for measuring conductivity and pressure for various expansion ratios and combustion chamber pressures. The channel is constructed of copper discs insulated with sheets of zirconia. The channel has an inlet diameter of 5.1 cm, an outlet diameter of 8.4 cm and an active length of 40.6 cm. It is configured to handle mass flow rates of 0.5-4 kg/sec. In operation, a voltage is applied between the two end electrodes and the voltage distribution and pressure is monitored as a function of distance along the channel.

D. Solid Fuels Selected for Testing

Three of the fuels which were developed under the Hercules IR&D program

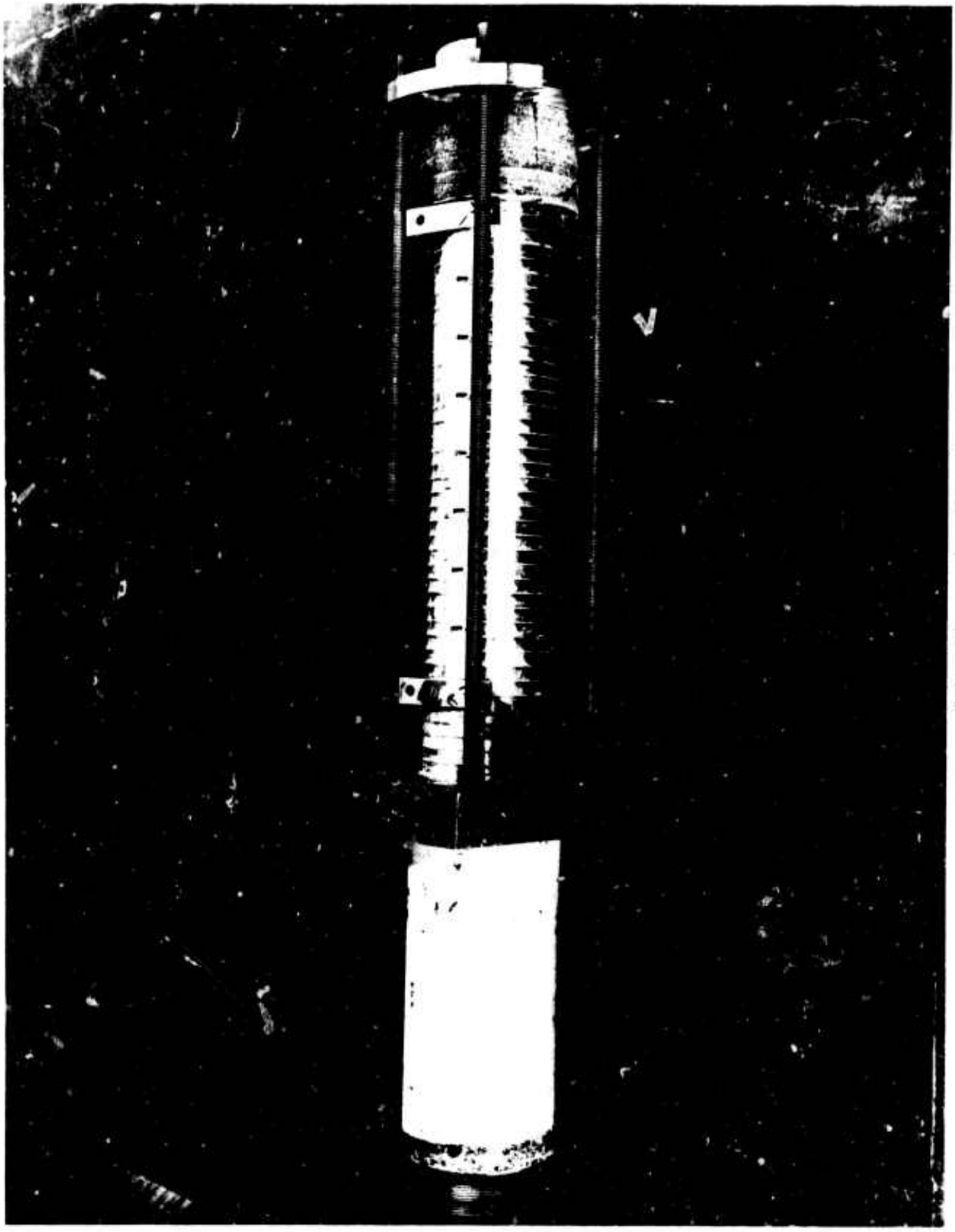

Figure 3-4. Diagnostics Channel

were found to meet the program requirements. The first of these fuels had 2% KNO_3 as a seed material while the other two used mainly $CsNO_3$. These latter fuels differed in the fact that one (VQX) utilized KNO_3 as an oxidizer and seed in addition to the $CsNO_3$ seed whereas the other (VQW) used only $CsNO_3$ seed. All testing performed on this program used either the 2% KNO_3 fuel or VQW.

1. 2% KNO_3 Fuel

The first fuel selected for testing was a double-base propellant with 2% KNO_3 seed added. Table 3-I lists the major ingredients of this propellant. Table 3-II gives a summary of the electrical properties of the 2% KNO_3 fuel.

2. VQW Fuel

The first cross-linked MHD fuel is designated VQW. It contains 7% cesium nitrate by weight as seed material. Table 3-III gives a list of the major ingredients of this propellant. Table 3-IV gives a summary of the electrical properties of the combustion products of this fuel.

3. VQX Fuel

The second cross-linked MHD fuel is designated VQX. This fuel also contains 7% cesium nitrate as seed material together with 10% by weight of potassium nitrate which replaces part of the HMX as an oxidizer. It has similar characteristics of VQW but has a 10% higher value for conductivity and a 75% lower value of $\omega\tau$.

E. Fuel Fabrication

Fuel grains up to 4.5 kg made from all three propellants have been fabricated and fired at Hercules on the previously discussed IR&D program. In addition, 18 kg grains of both the 2% KNO_3 fuel and VQW were cast as a part of this program. The processing of these propellants was the

TABLE 3-I

COMPOSITION OF 2% KNO_3 FUEL

Ingredient	Weight Percent
Aluminum	26.0
HMX	10.0
Nitrocellulose	15.0
Nitroglycerin	44.0
KNO_3	2.0
Miscellaneous Binder Ingredients	3.0

TABLE 3-II

SUMMARY OF CALCULATED 2% KNO_3 FUEL ELECTRICAL PROPERTIES

Chamber Pressure	48.0 Atm (705 psi)			
Parameter	σ	$\omega\tau/B$	u^*	ϵ^{**}
Chamber	49.9	0.016	--	--
Throat	53.2	0.027	1015	1.000
4 Atm	57.7	0.193	2070	2.809
2 Atm	54.5	0.393	2301	4.711
1 Atm	48.6	0.802	2496	8.090
0.8 Atm	46.2	1.00	2554	9.662
0.6 Atm	42.9	1.36	2624	12.17
0.4 Atm	37.8	2.06	2719	16.91
0.2 Atm	28.5	4.22	2862	29.86
0.1 Atm	21.0	8.53	2990	53.45

*In meters per second.

**Expansion ratio.

TABLE 3-III

COMPOSITION OF VQW FUEL

Ingredient	Weight Percent
Aluminum	22.5
HMX	25.5
Nitrocellulose	4.2
Nitroglycerin	26.4
$CsNO_3$	7.0
Miscellaneous Binder Ingredients	4.4

TABLE 3-VI

SUMMARY OF CALCULATED VQW ELECTRICAL PROPERTIES

Chamber Pressure	20.4 Atm (300 psi)				27.2 Atm (400 psi)				34.0 Atm (500 psi)				40.8 Atm (600 psi)				(47.6 Atm (700 psi)			
Parameter	σ	ωτ/B	u*	ε**	σ	ωτ/B	u	ε	σ	ωτ/B	u	ε	σ	ωτ/B	u	ε	σ	ωτ/B	u	ε
Chamber	84	.023			78	.017			73	.014			68	.012			65	.010		
Throat	95	.041			88	.031			83	.025			79	.021			75	.018		
4 Atm	109	.133	1695	1.566	103	.140	1829	1.879	98	.145	1923	2.179	93	.150	1995	2.472	88	.154	2060	2.769
2 Atm	109	.279	1987	2.478	99	.292	2094	3.039	91	.303	2173	3.572	84	.311	2234	4.088	77	.319	2286	4.610
1 Atm	99	.576	2222	4.105	87	.603	2313	5.093	77	.623	2380	6.027	68	.638	2435	6.931	61	.650	2478	7.845
0.8 Atm	95	.727	2313	4.858	81	.759	2377	6.041	71	.783	2441	7.161	62	.801	2493	8.244	55	.816	2533	9.339
0.6 Atm	88	.979	2374	6.056	74	1.021	2454	7.551	63	1.051	2515	8.964	54	1.074	2563	10.329	47	1.091	2603	11.710
0.4 Atm	77	1.486	2481	8.302	62	1.547	2554	10.377	52	1.589	2609	12.337	43	1.618	2655	14.232	37	1.639	2691	16.152
0.2 Atm	56	3.028	2643	14.365	43	3.128	2710	18.038	43	3.128	2755	22.105	43	3.128	2795	26.146	43	3.128	2844	30.184
Throat Area																				
10 kg/sec	74.9 cm^2				56.3 cm^2				45.1 cm^2				37.6 cm^2				32 cm^2			
25 kg/sec	187.3 cm^2				140.7 cm^2				112.8 cm^2				94.0 cm^2				80 cm^2			
50 kg/sec	374.5 cm^2				281.4 cm^2				228.5 cm^2				188.0 cm^2				160 cm^2			

*In meters per second.

**Expansion ratio.

same as cross-linked rocket propellants and no difficulties were encountered because of the use of cesium or potassium nitrates.

Firing these fuels also proceeded in the same way as firing rocket propellants. No special precautions were required and no difficulties were encountered.

SECTION IV

EXPERIMENTAL APPARATUS

This section gives a description of the hardware developed under the contract and includes the combustor, channel, diffuser, and magnet. A description of the load resistor bank, which was available from previous company programs, is also given.

A. Combustor

The solid fuel combustor is essentially a pressure vessel with nozzle containment on one end and a facility for loading the fuel grains on the other.

The original design which was used during the initial period of testing is shown in Figures 4-1 through 4-4. As can be seen in Figure 4-3, a four piece rectangular graphite nozzle was used which was machined to a very precise contour. A four piece design was used due to the problems and expense of machining the internal contours from a monolythic block. The reduced exterior dimensions were required by the necessity of using an external flange to attach the combustor to the channel.

As seen in Figure 4-4, the forward end which was used for loading the fuel grain contained a rupture disc that is designed to fail in the event that excessive pressure is generated in the combustor by nozzle blockage or grain fracture. It was also planned to hold this disc on with explosive bolts which could be cut on command to provide for emergency termination of the test. Due to problems in developing a fault sensing circuit, these were not used.

As a result of a failure in a thin-wall section of the nozzle during one of the early tests which resulted in channel damage, the nozzle design was changed to a washer concept embodying thicker wall sections. A copper

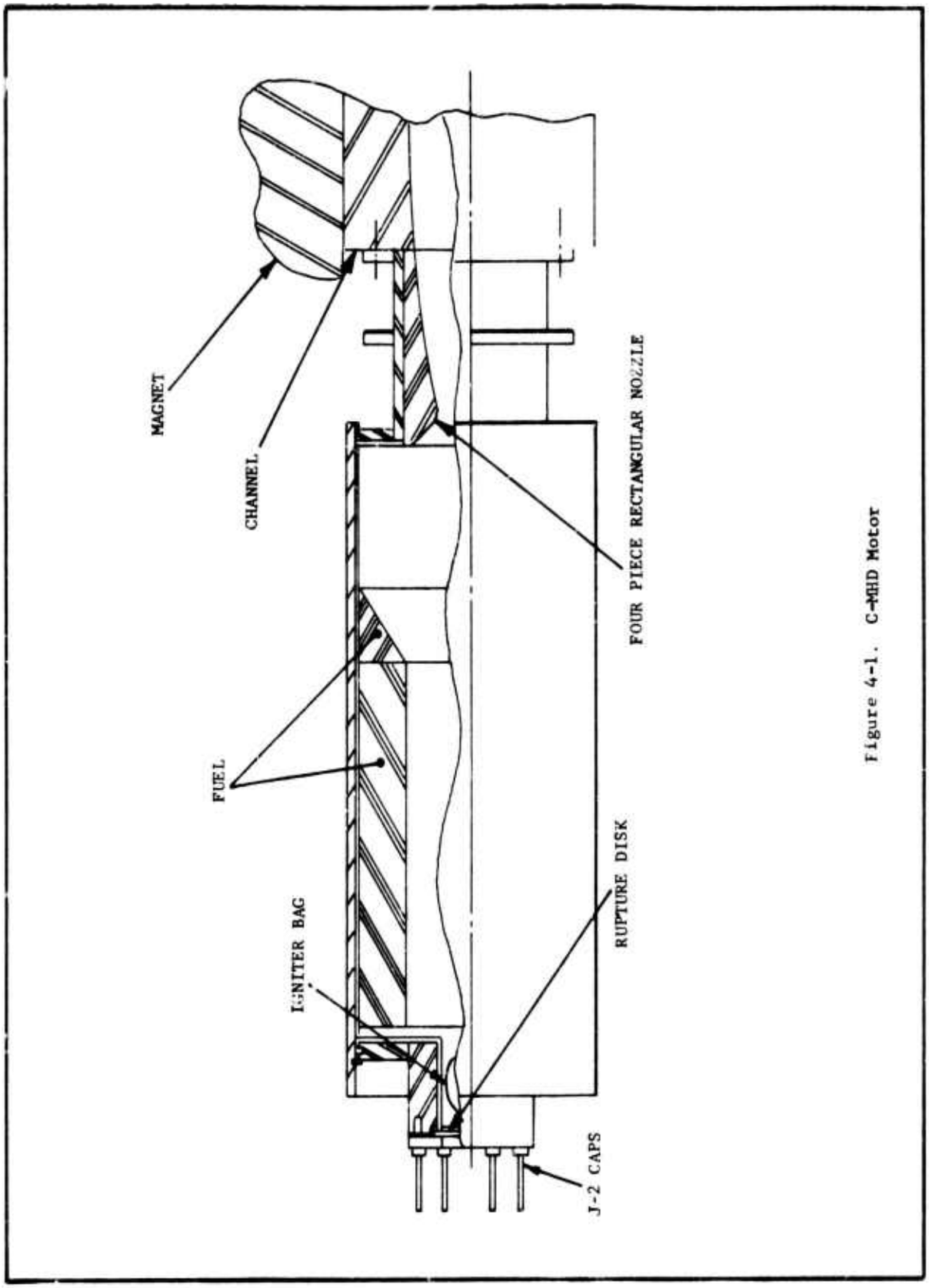

Figure 4-1. C-MHD Motor

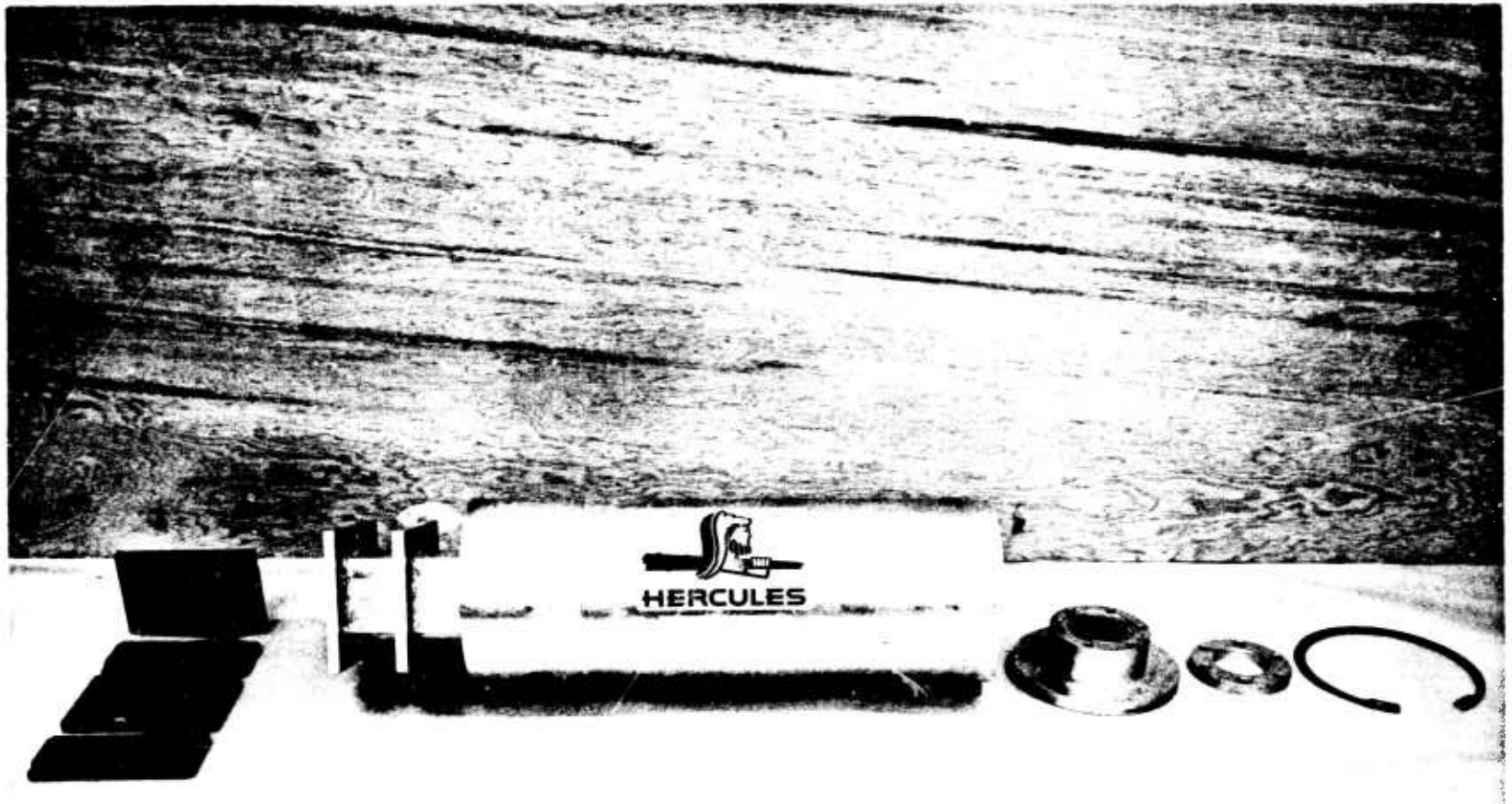

Figure 4-2. Overall View of Solid Combustion Chamber

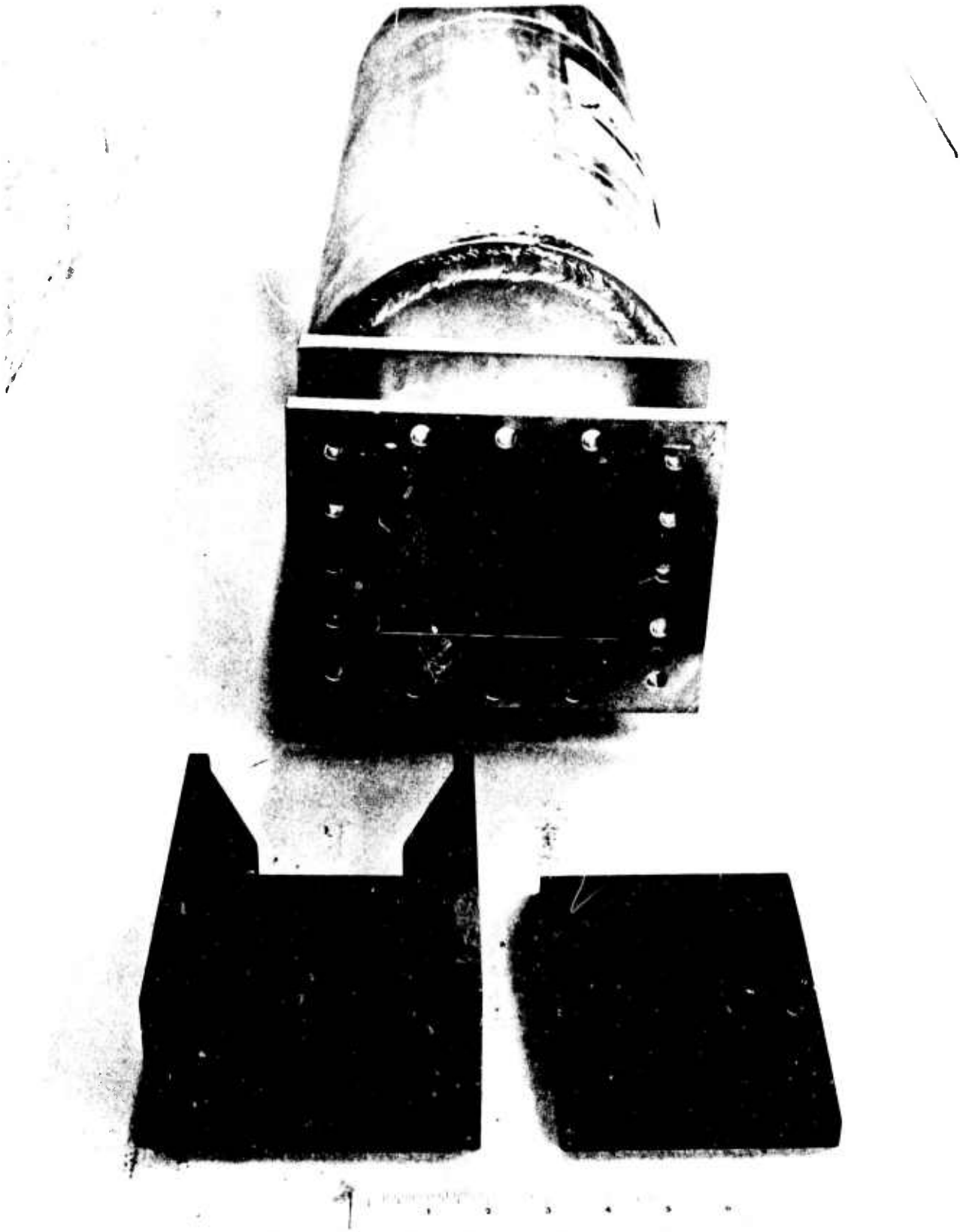

Figure 4-3. View of Nozzle End of Combustor

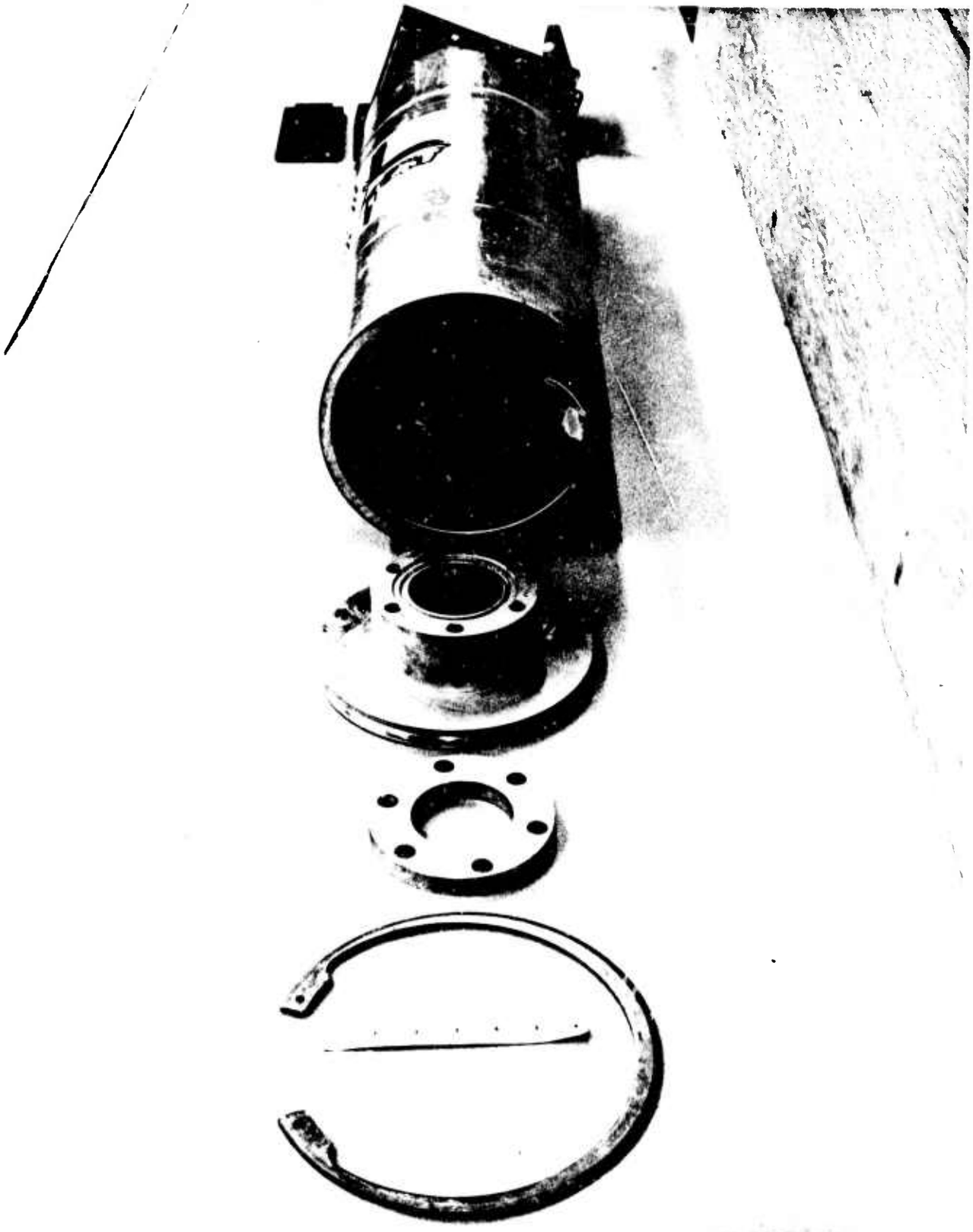

Figure 4-4. Ignitor End of Combustor

standoff flange was placed between the channel and combustor which allowed the dimensions of the nozzle container to be increased to the combustor diameter.

The new design is shown in Figure 4-5. The last 7.6 cm of the nozzle expansion ring is constructed of copper. The throat assembly was machined from a solid billet of HLM-85 graphite.

Detailed two-dimensional thermal and stress analyses were performed on the new nozzle design to insure that it would not fail as the earlier design did. The models used in these analyses represented 2-D cross sections at the throat and the exit of the nozzle, and because of symmetry, a one-fourth section was modeled in the finite-element grids. The nozzle material is HLM-85 graphite.

1. Thermal Analysis

The 2-D models used for the thermal analysis which are illustrated in Figures 4-6 and 4-7, neglect heat transfer in the third dimension (axial direction). This is expected to be a reasonable approximation because of the lower thermal gradients in this direction. Temperature distributions in the throat and exit sections at 1 second, 2 seconds, and 4 seconds (end of burn) are shown in Figures 4-8 through 4-13.

The backside temperatures of the HLM-85 graphire are below 530°K at the narrow side of the throat and below 810°K on the wide side of the throat at 4 seconds (see Figure 4-10). At the thinner exit plane section, the backside temperatures are between 810°K and 1370°K at 4 seconds, except for the corners which are between 530°K and 810°K (see Figure 4-13).

2. Stress Analysis

Two-dimensional (plane stress) analyses for thermal and

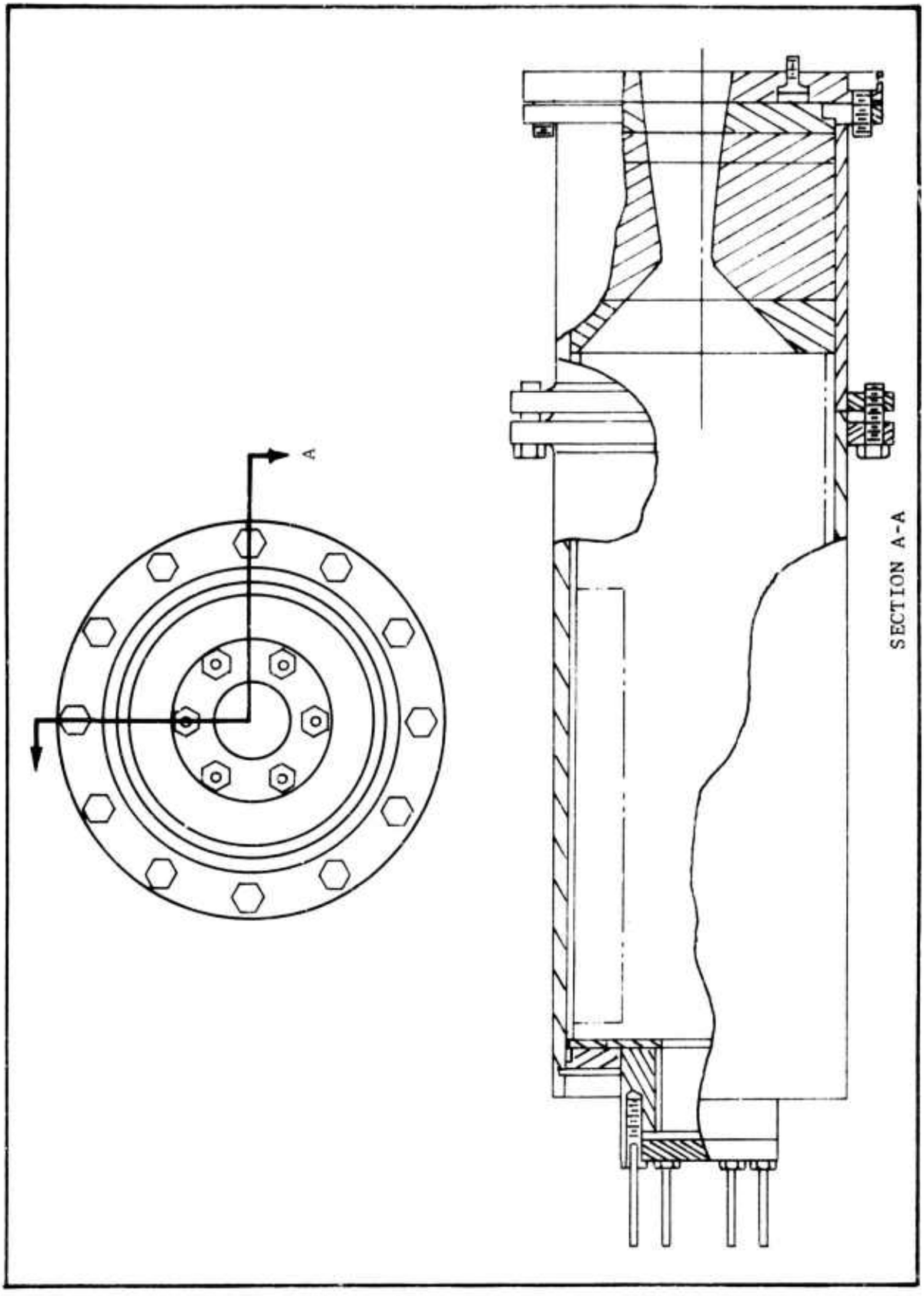

Figure 4-5. Modified Combustion Chamber

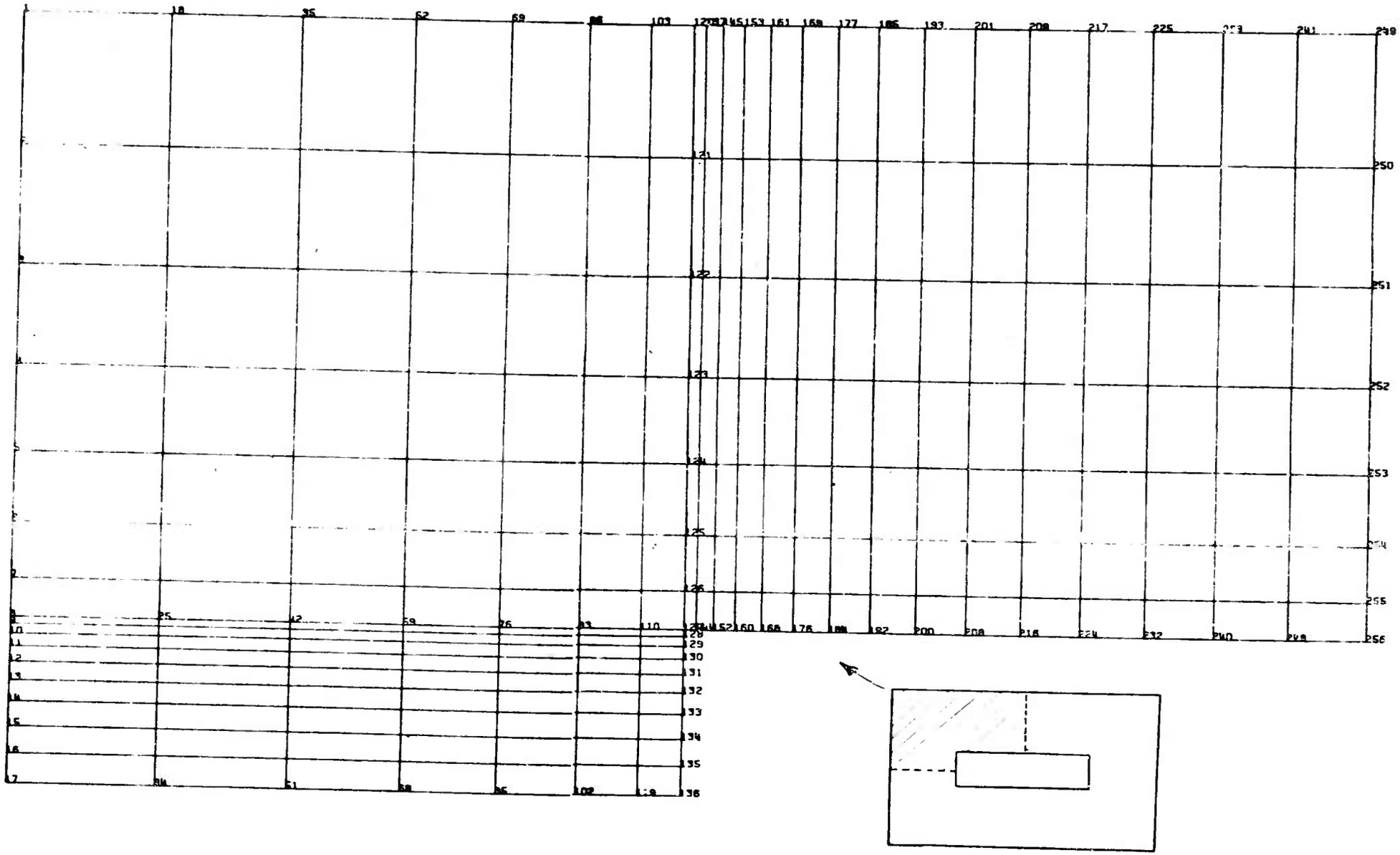

Figure 4-6. MHD Nozzle Throat Model

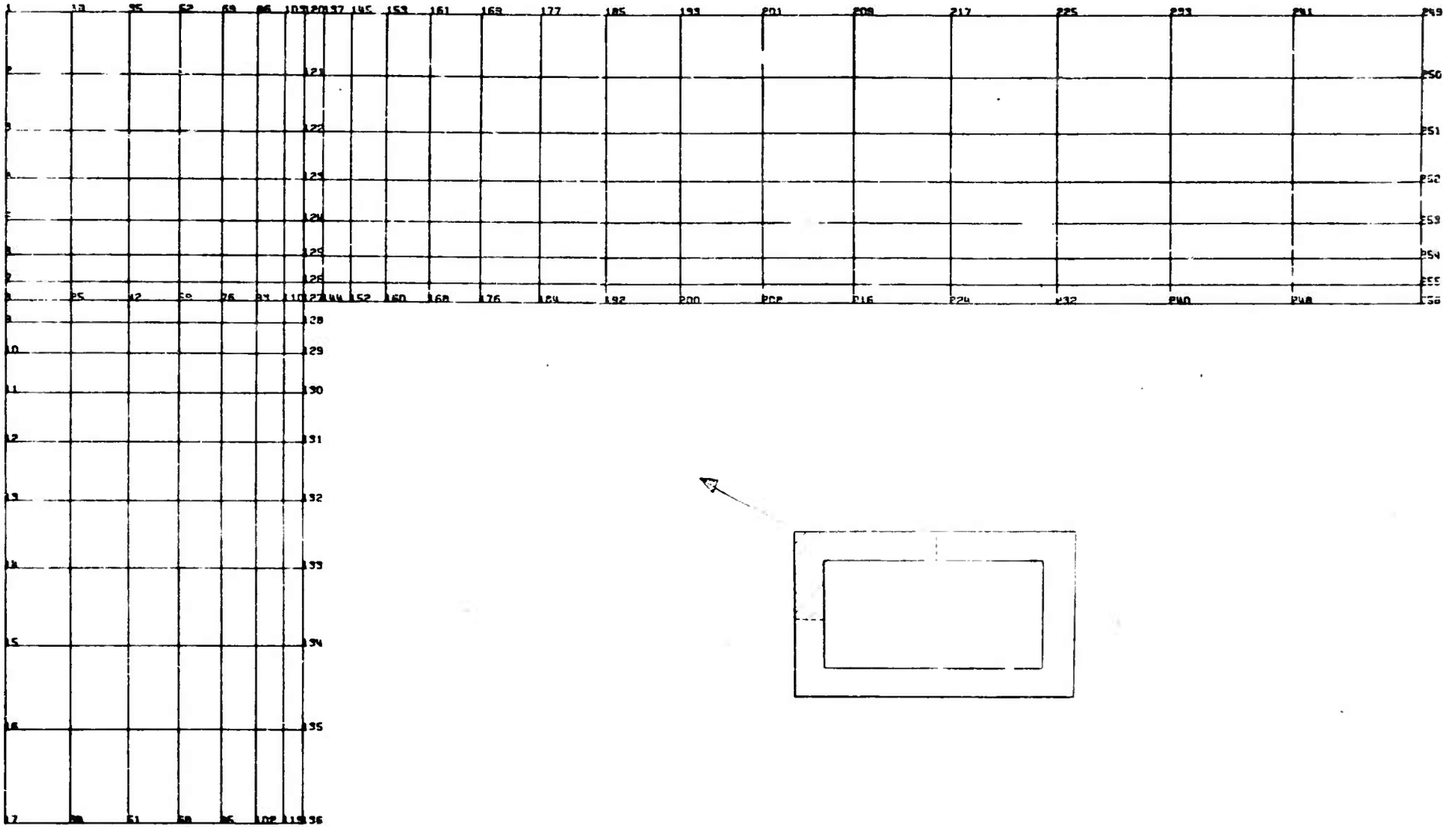

Figure 4-7. MHD Nozzle Exit Model

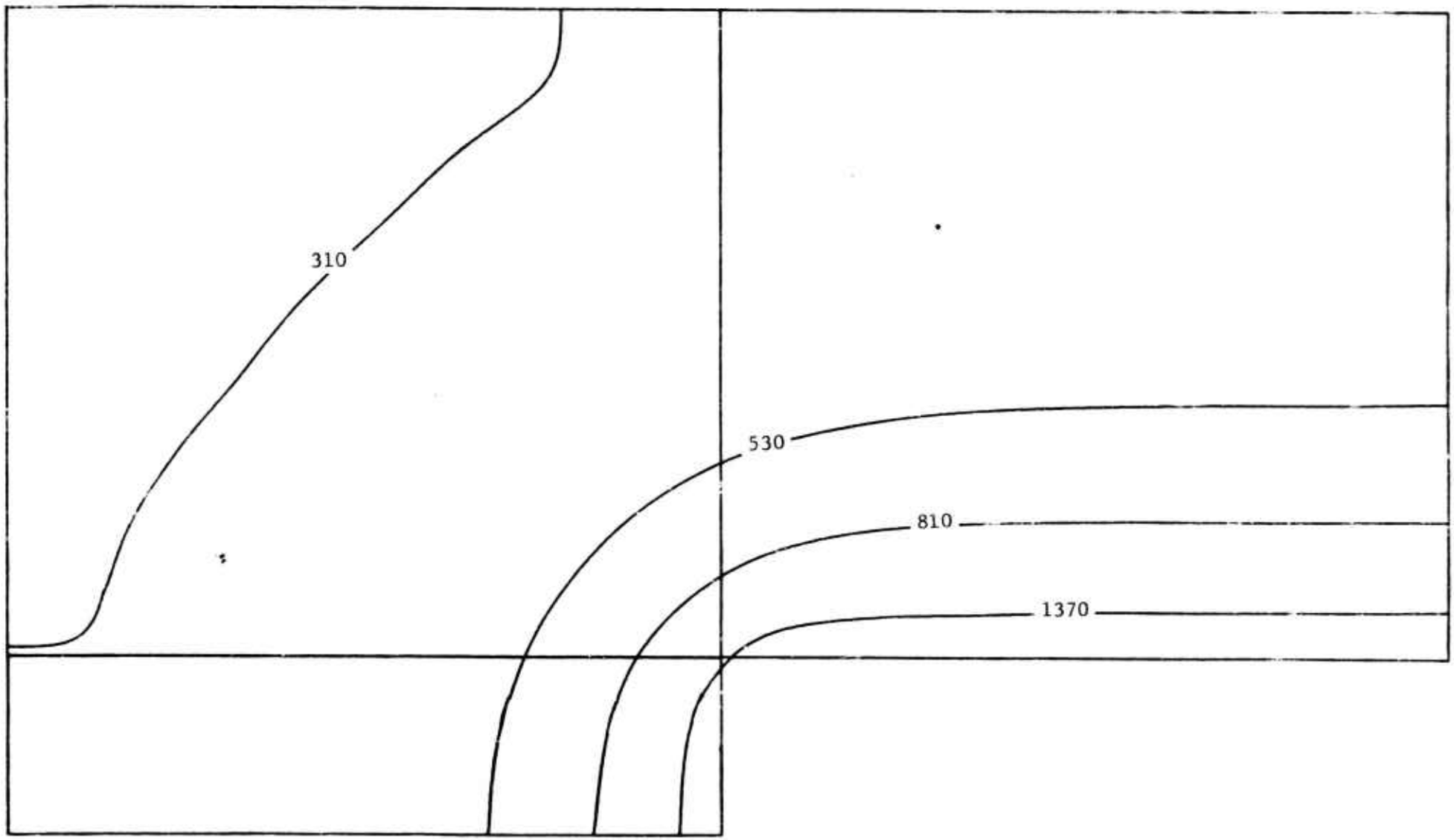

Figure 4-8. Temperature Distribution in MHD Nozzle Throat in °K, 1 Second

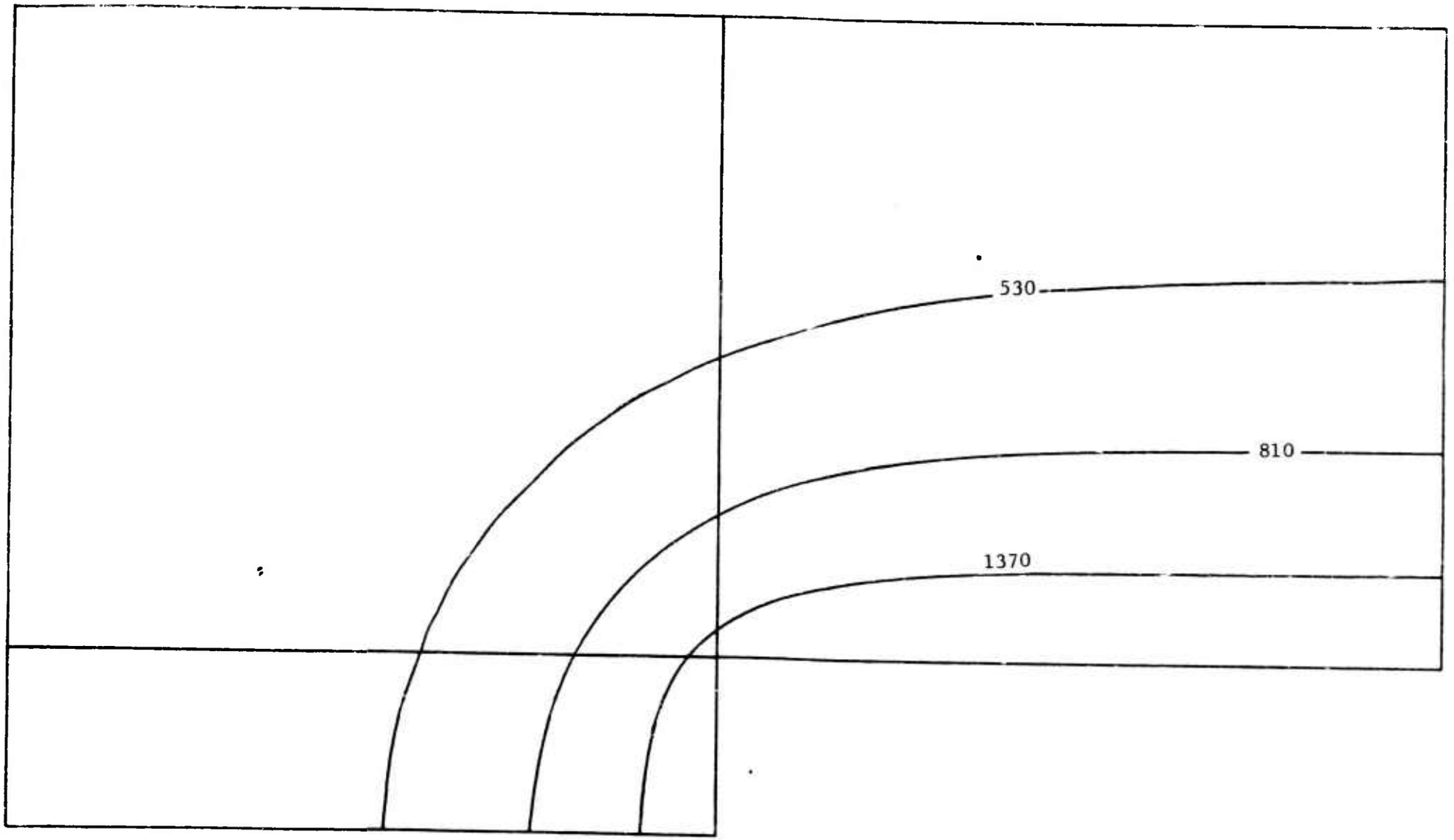

Figure 4-9. Temperature Distribution in MHD Nozzle Throat in °K, 2 Seconds

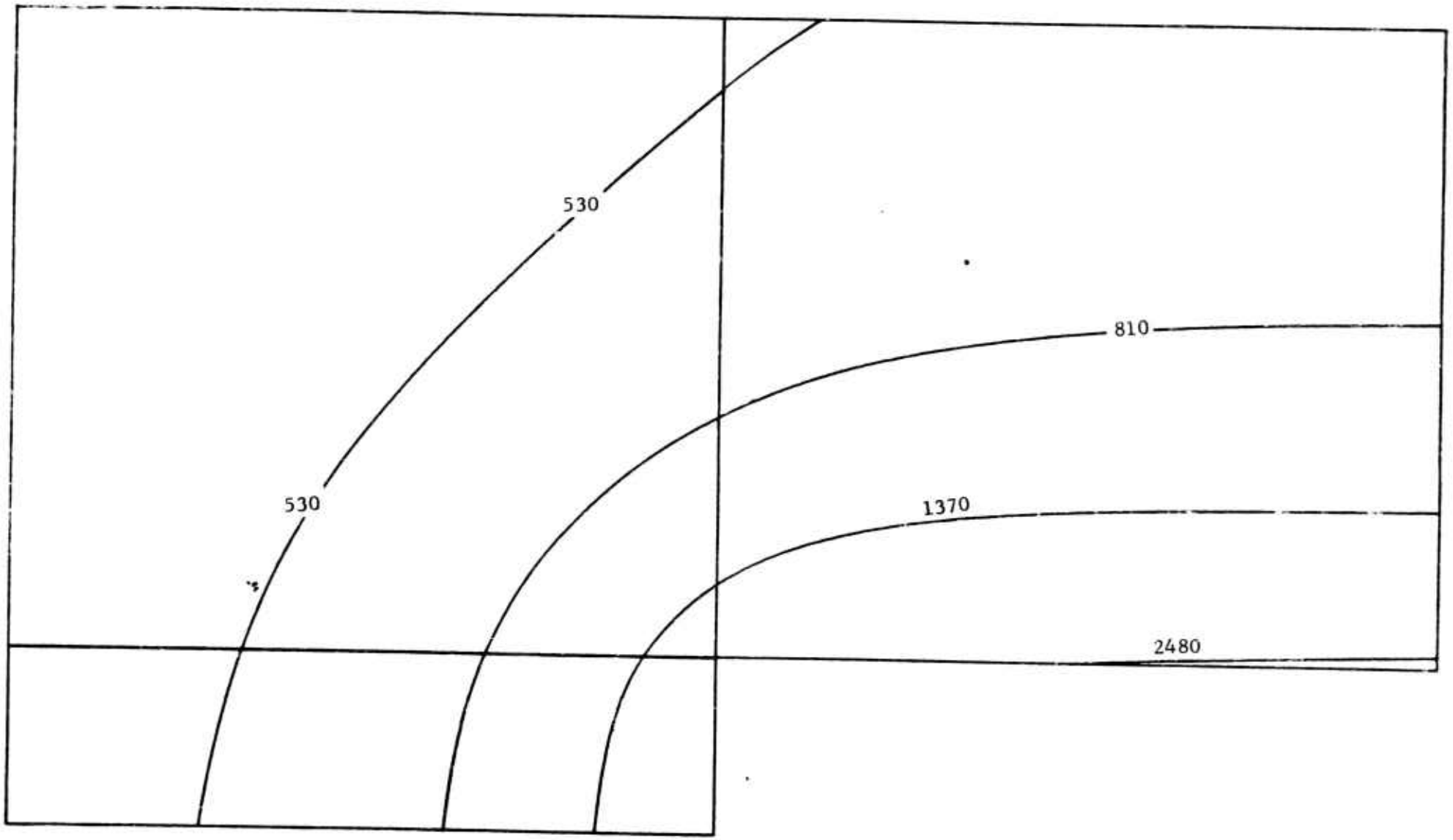

Figure 4-10. Temperature Distribution in MHD Nozzle Throat in °K, 4 Seconds

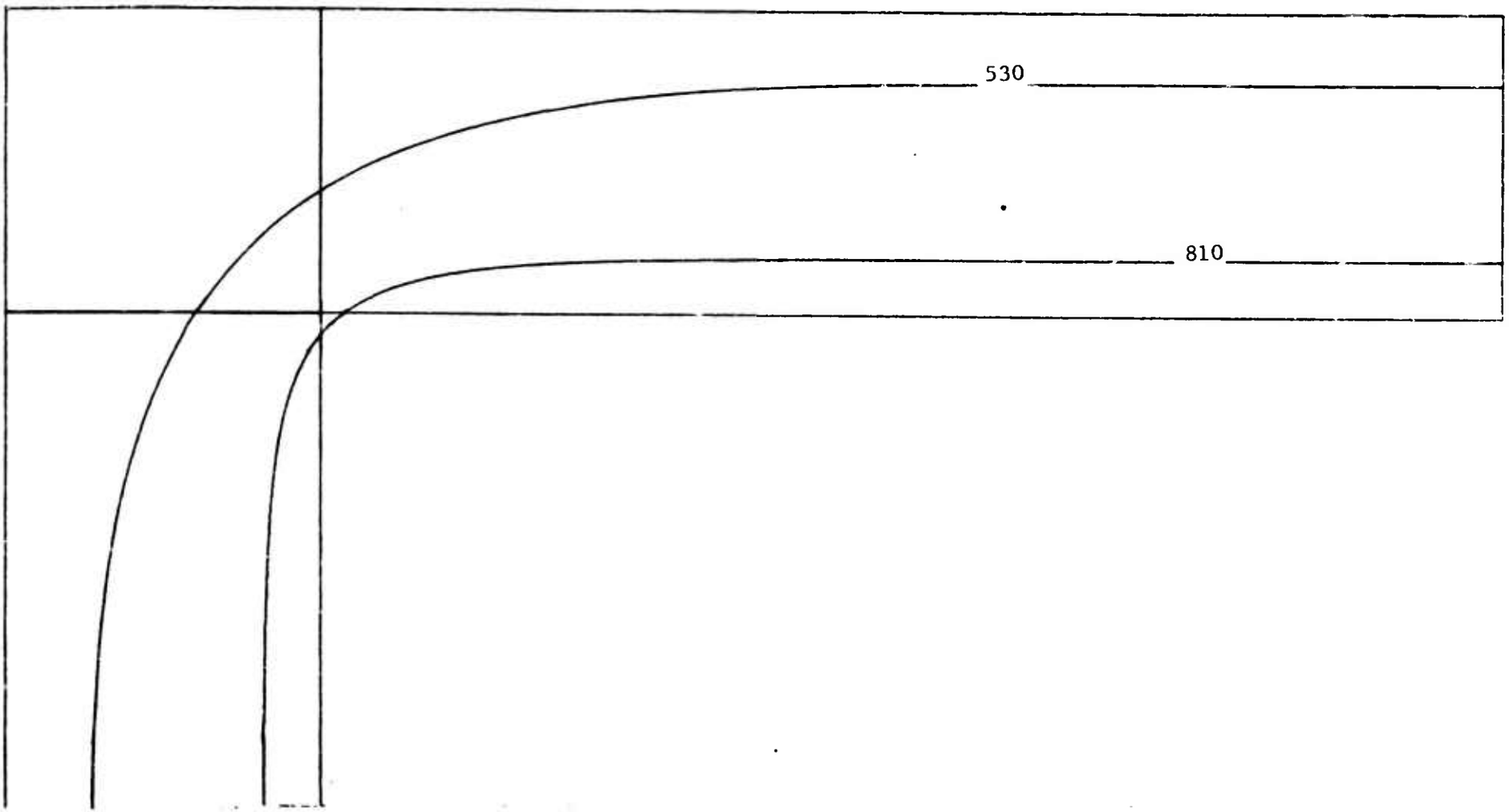

Figure 4-11. Temperature Distribution in MHD Nozzle Exit in °K, 1 Second

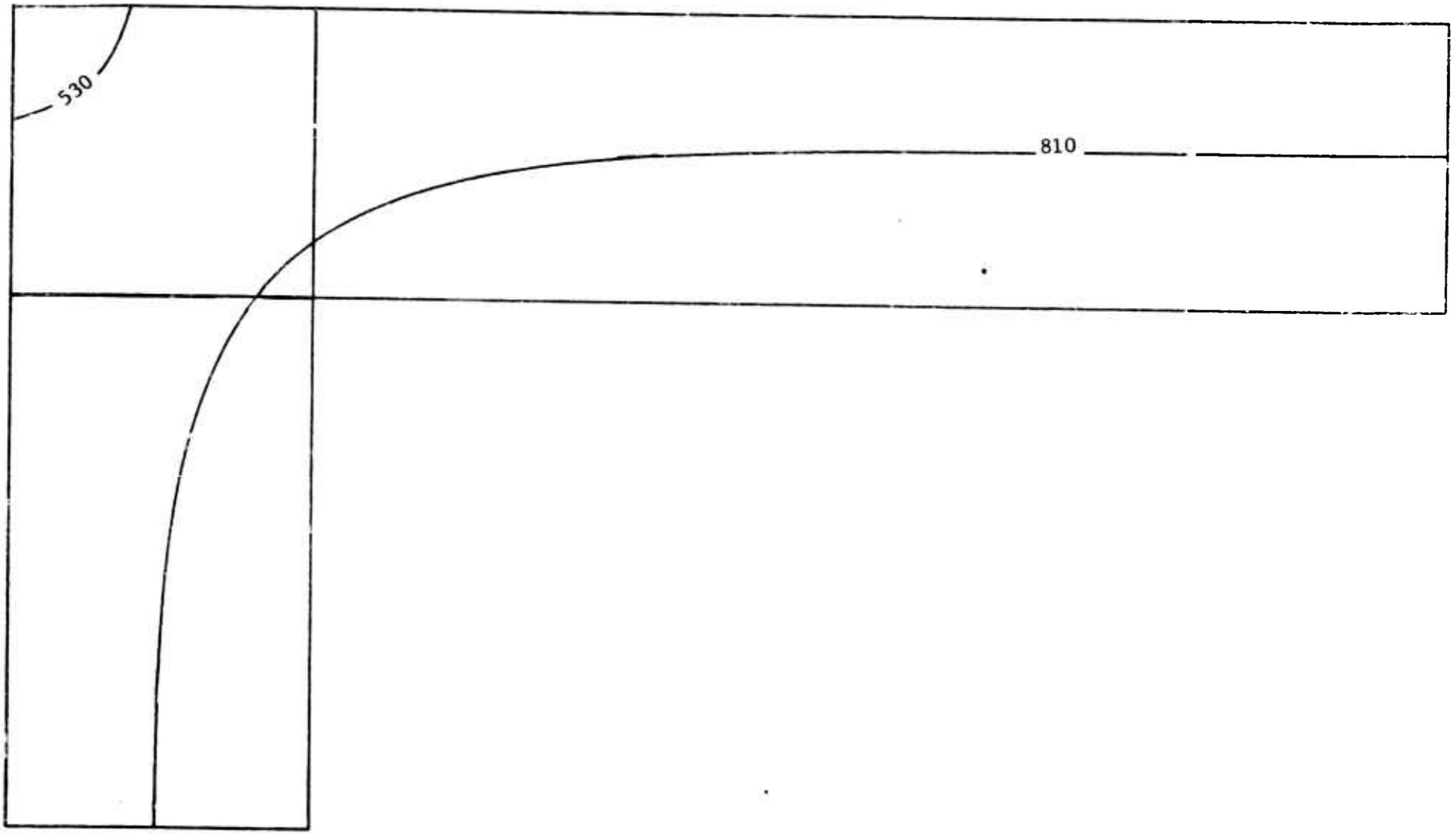

Figure 4-12. Temperature Distribution in MHD Nozzle Exit in °K, 2 Seconds

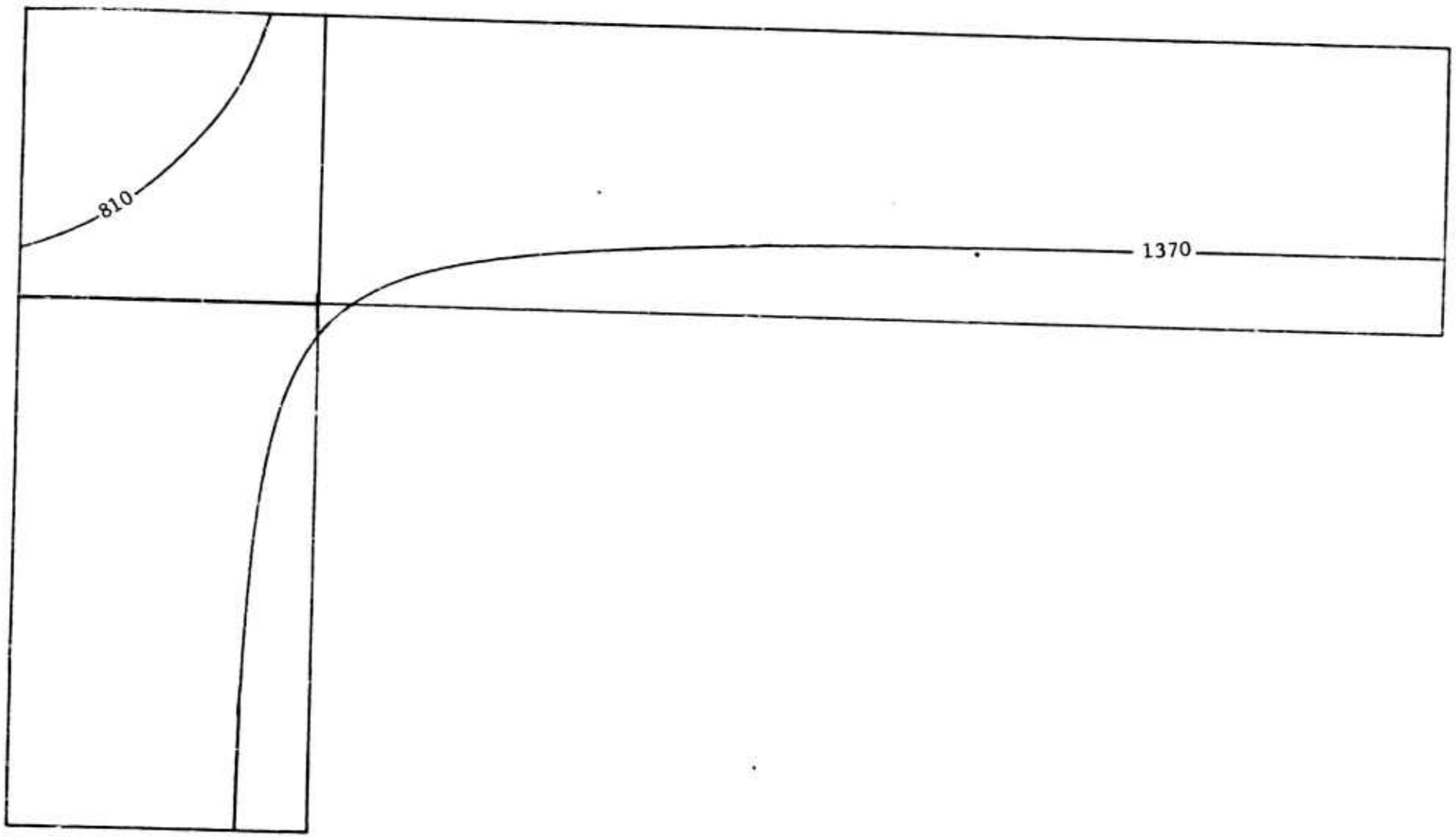

Figure 4-13. Temperature Distribution in MHD Nozzle Exit in °K, 4 Seconds

pressure loads were also performed on the exit section. The temperature gradients at 4 seconds (see Figure 4-13) and a pressure of 2.7 atm (40 psi) were used in the stress analyses (see Figure 4-14). Two conditions of backside restraint were modeled:

(a) A 0.127 mm gap between the HLM-85 nozzle and the steel housing (growth of the outside dimensions was limited to 0.127 mm).

(b) Free unrestrained growth of HLM-85

The maximum stresses (tension, compression and shear) conditions of restraint are shown in Figure 4-15. Also listed are the allowable stresses (strengths) of HLM-85. The results show the stresses are generally lower when the HLM-85 is unrestrained at the exit section. An exception is the tensile stress on the outside of the wide side which was higher when the HLM-85 was not restrained. The unrestrained growth of the narrow and wide sides was 2.11 to 2.39, and 1.09 to 2.06 mm, respectively.

Based on this analysis of the exit section and two restraint conditions, it appeared that complete restraint would cause compressive and/or shear cracks starting on the hot inside surfaces. No restraint would probably cause tensile cracks starting on the outside surfaces of the wide side. Thus the gap and restraint conditions between the graphite nozzle and the steel housing shown in Figure 4-16 were used.

B. Channel

Both the C-MHD and X-MHD channels used in this program were designed and fabricated by MEPPSCO, Incorporated under subcontract from Hercules. The X-MHD channel is discussed in Section IX.

The C-MHD design objective was to provide potential for achievement

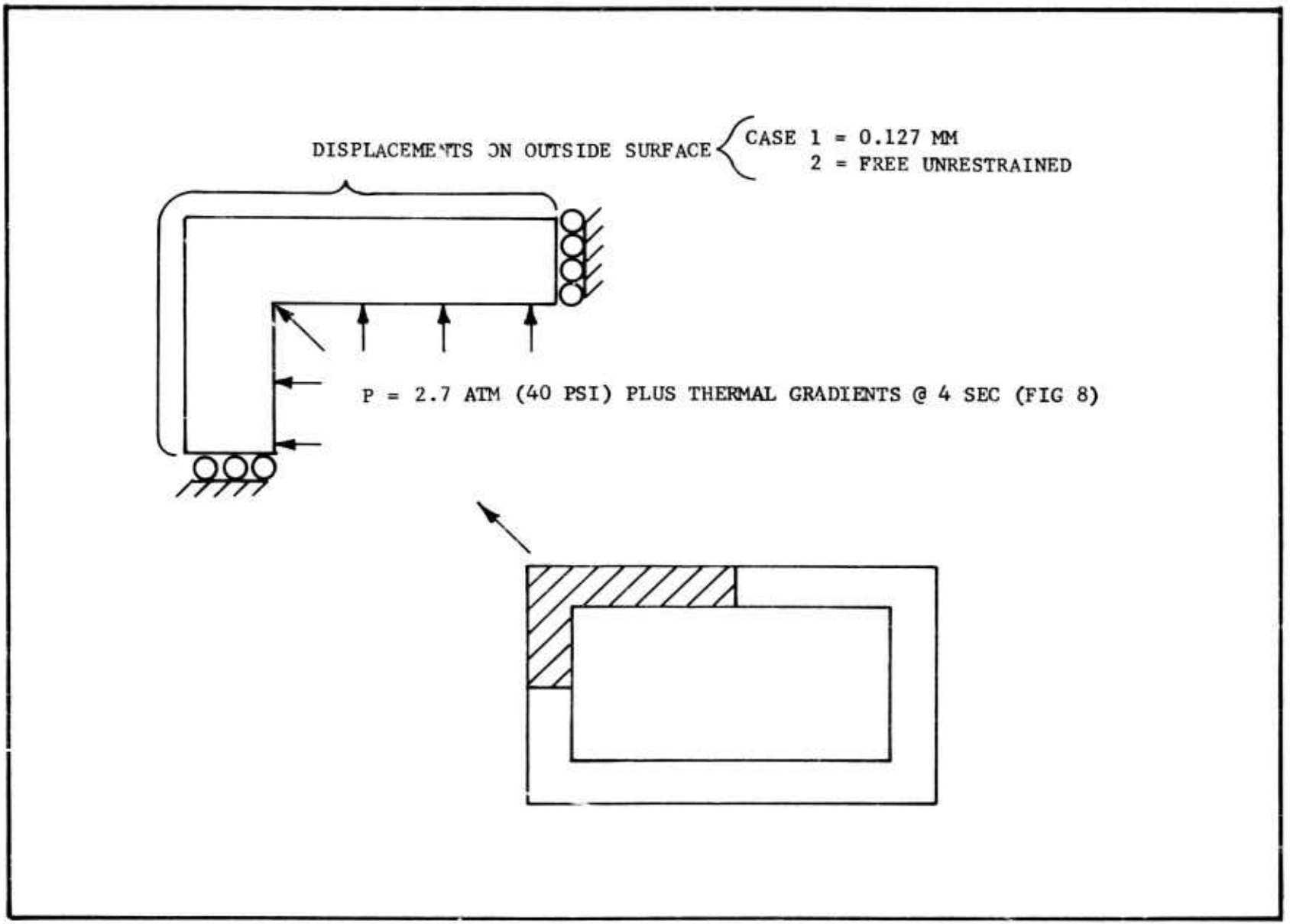

Figure 4-14. Plane Stress Model of MHD Nozzle Exit

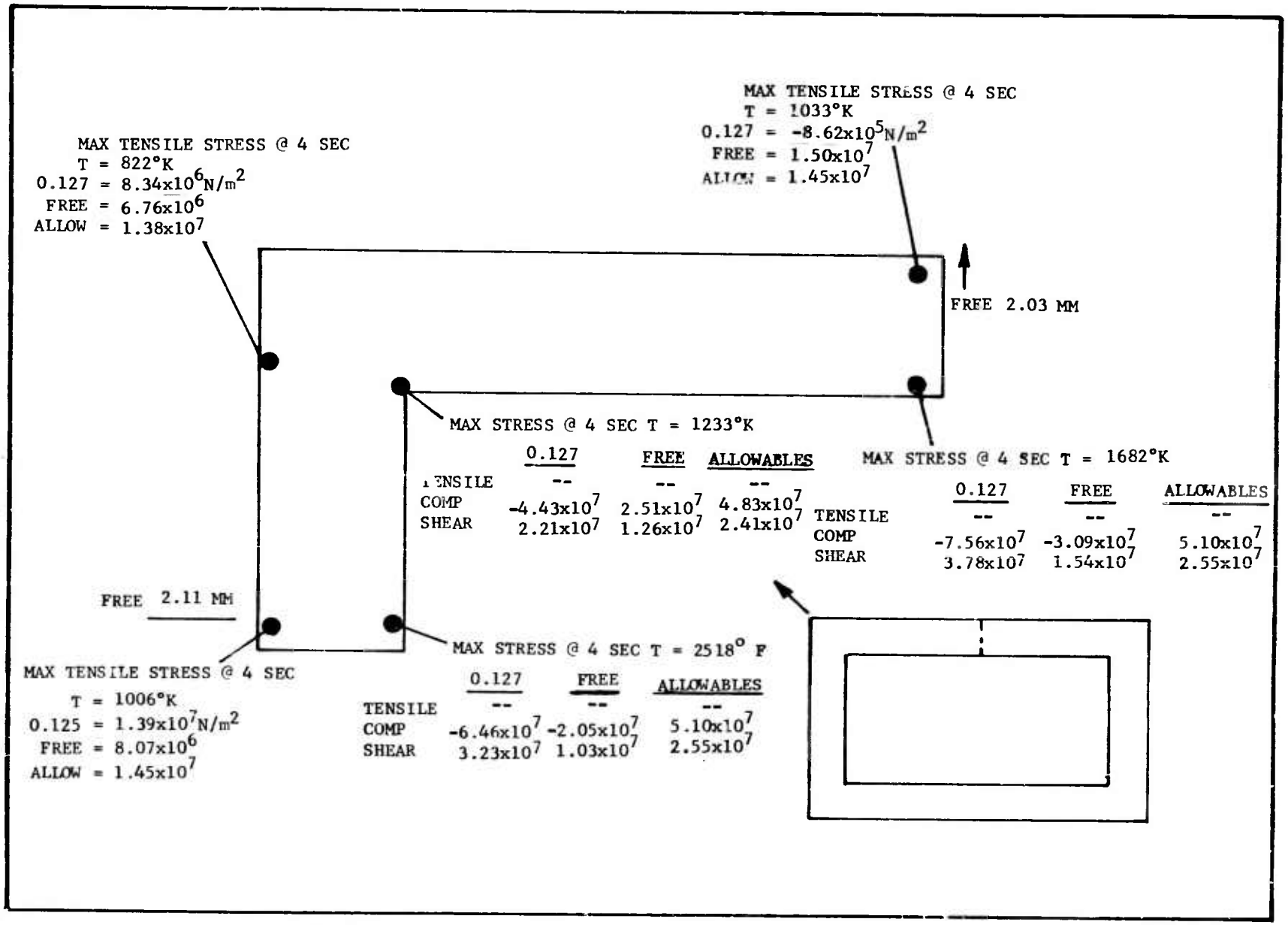

Figure 4-15. Location and Magnitude of Maximum Stresses in Exit Section of MHD Nozzle Pressure (27 atm) and Thermal Stresses at 4 Seconds

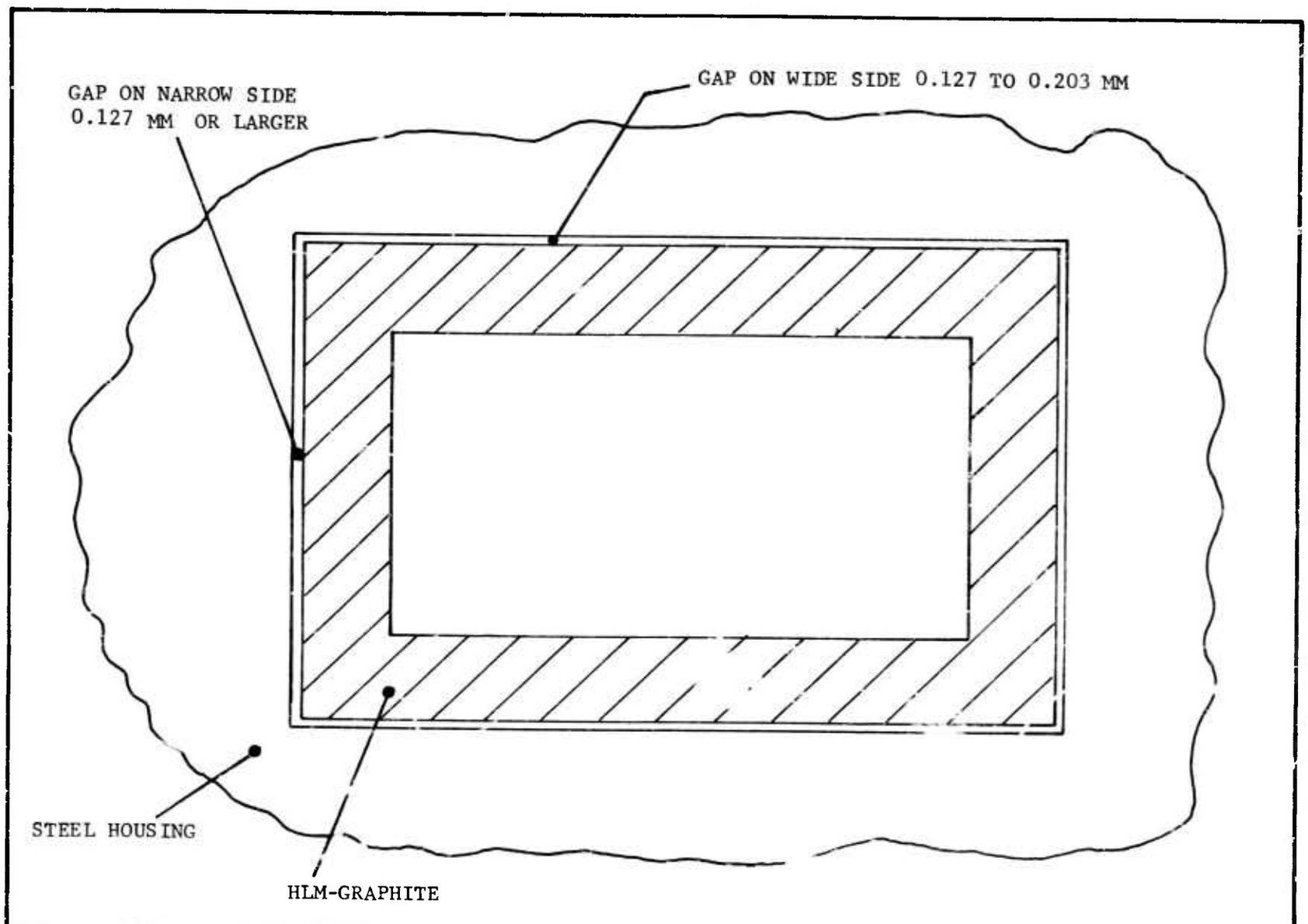

Figure 4-16. Restraint (Gaps) Between Graphite and Steel in MHD Nozzle Used in New Nozzle Design

of an energy extraction of one (1) MJ/kg. Since flight applications were of interest, compactness is important. Thus, operation near optimum power density, or more particularly power/unit length of channel, was required. Single circuit output was desirable since it was felt that the power dissipated on a complex set of bleeder resistors would, in fact, be unrecoverable in a practical, lightweight, power conditioning system. The highest energy extraction previously achieved is 0.62 MJ/kg with the original Mark V channel (1965), and recently duplicated in the Viking I. The highest single load output is 0.45 MJ/kg with the second Mark V channel, which was of the continuous electric Faraday (CEF) configuration. If compact C-MHD combustion chambers could be built at 10-12 atm combustion pressure, the CEF configuration could probably be considered for energy extraction in the 0.65 MJ/kg range using the high seed, low mobility propellants previously developed by Hercules.

Assuming a local overall equivalent turbine efficiency (including friction) in the 0.5 - 0.6 range, and an energy extraction of 1.0 MJ/kg, the available energy, A, at the generator inlet must be in the range of 1.7 - 2.0 MJ/kg. A is composed of two terms, an impulse term due to reduction in kinetic energy, and a reaction term due to expansion. If it is assumed that the flow can be decelerated to 80% of the inlet velocity without separation, the impulse term, A_i, may be written

$$A_i = (1.0^2 - 0.8^2)\ 1/2\ U_1^2 = 0.18\ U_1^2$$

where U_1 is the inlet velocity. The reaction term, A_r, is a function of the static pressure ratio across the channel under conditions that permit recovery to atmospheric pressure or higher. For the present design, the impulse and reaction terms with an inlet velocity of 2240 m/sec are about equal at 0.9 MJ/kg, and the static pressure ratio is 5.

The design equivalent stagnation pressure at the channel inlet is 30 atm (440 psi). The effective stagnation pressure ratio across the expansion nozzle in the high field is 1.5, and is calculated by assuming a CEF configuration in the nozzle.

The magnet is a constraint. The magnet was designed for dual use with both the C-MHD channel and the linear X-MHD configuration. With the predicted conductivity values, the channel inlet is in the high field region. The exit channel outside dimensions are constrained to fit in the 0.36 m x 0.36 m magnet aperture, but this is compatible with exit conditions permitting recovery to the atmosphere.

The channel could have been designed with greater length, but at the present length and at design energy extraction, the boundary layers are essentially merged at the exit and the momentum defect under full load conditions occupies almost 20% of the channel area.

The channel built for this program is a peg wall design with diagonalization of the electrodes provided externally. The pegs in the forward part of the channel are of copper whereas those in the aft section of the channel are aluminum. The electrodes and power removal box liners are of high density graphite. A castable ceramic was used between the electrodes and the pegs.

The channel nozzle and entrance area is fabricated from graphite. Since it is located at an axial station with near peak magnetic field, inlet pressure losses due to circulating eddy currents in the conducting nozzle have been estimated in order to adjust combustion pressure to compensate for these losses. The inlet losses were calculated by assuming that the nozzle flow was equivalent to that in a short circuited single electrode Faraday generator. The throat area was decreased from

the value that would be appropriate to the selected inlet conditions (equivalent to 30 atm combustion pressure) without losses until overall expansion length was reduced to 0.228 m to keep the losses in bound. As was mentioned above, it was found that a stagnation pressure ratio of 1.5 was required to compensate for the inlet losses. Therefore, the actual combustion pressure is 45 atm (660 psia) with an effective stagnation pressure of 30 atm at the beginning of the active region in the channel. The design operational characteristics of the channel are given in Table 4-I.

Figures 4-17 thru 4-25 give the design parameters of the channel as a function of axial distance. Figures 4-26 through 4-34 show the various operations performed while fabricating the channel.

The assembled channel is shown in Figure 4-35 with the lower external diagonal wires installed. Figure 4-36 shows the "as built" internal contours of the channel. Figure 4-37 shows the location of pressure taps in the peg walls and also the position of the first and last electrode on both the top and bottom of the channel.

The channel was damaged during a conductivity run which necessitated its disassembly. Figures 4-38 through 4-40 show the disassembled channel and entrance box. Figure 4-41 shows the repaired channel side wall. During the repair operation, the first few electrodes were replaced due to an erosion pattern developing at the point where the electrode caps are bolted to the aluminum electrodes. No measurable erosion was found anywhere else on the electrodes. No operational problems would have occurred by using the existing electrode caps but it was felt that they should be refurbished while the channel was disassembled. Originally,

TABLE 4-I

OPERATIONAL SUMMARY

Mass Flow: 4.07 kg/sec

Propellant Composition: 26% Al, 2% KNO_3, 10% HMX, 15% NC, 44% NG, 1% NDPA, 3% Miscellaneous Binder Ingredients

Combustion Pressure: 45 atm (660 psia)

Throat Dimensions: .070 (E) x .018 (B)

Channel Inlet Location: STA 22

Throat Location: STA 16

Channel Inlet Dimension: .052 (B) x .110 (E) meter (2.09" x 4.33")

Channel Inlet Wall Half Angles: Peg: 9.54°
Electrode: 3.75°

Channel Inlet Static Pressure: 2.9 atm

Channel Active Region Begins: STA 25 (.076 meter into channel)

Active Region Inlet Parameters:
- Static Pressure: 1.50 atm
- Velocity: 2240 m/sec
- Dimensions: .077 m x .115 meter
- Wall Half Angles: Peg: 7.2°
  Electrode: 0°
- Conductivity: 35.9 mho/m

Channel Active Region Ends: STA 64.375 (1 meter active length)

Active Region Exit Parameters
- Static Pressure: 0.32 atm
- Velocity: 1831 m/sec
- Dimensions: .254 (B) x .240 (E) (can be opened to .254 x - .254 m)
- Wall Half Angles: Peg: 1.6°
  Electrode: 8°
- Conductivity: 32.9 mho/m

Velocity Ratio: 0.82

Exit Recovery Pressure Including Boundary Layer: 1.54 atm

Recommended Diffuser Wall Half Angles: 0

Current Density: 12.9 - 2.4 amp/cm^2

Maximum Electric Field: x: 4380 v/m, y: 5692 v/m

Maximum Hall Coefficient: 3.5

Φ/D at Exit: .07

H_{inc} at Exit: 1.47

Exit Flange Face Location: STA 73.75

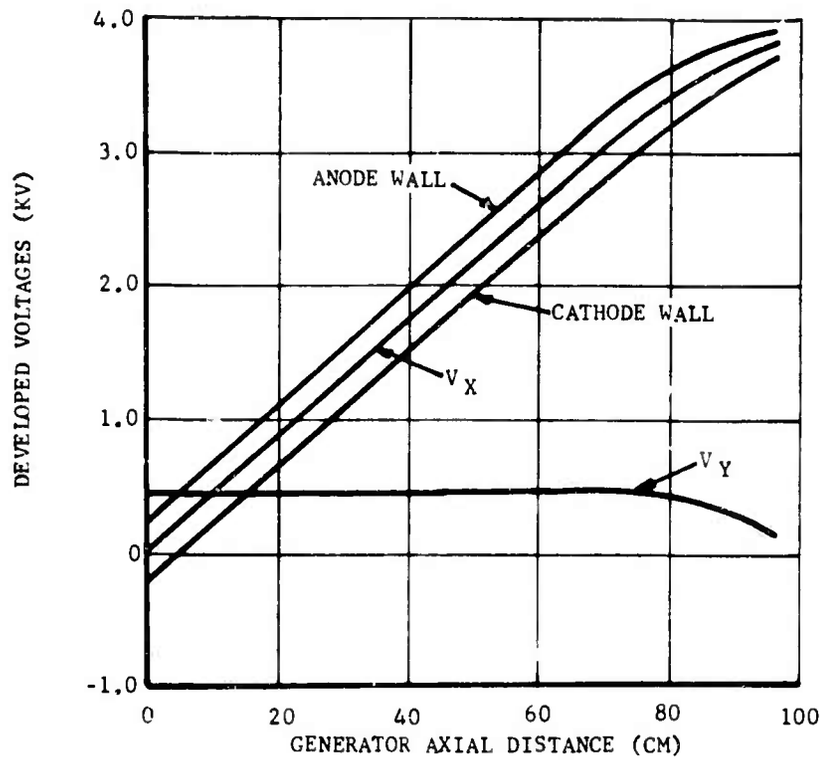

Figure 4-17

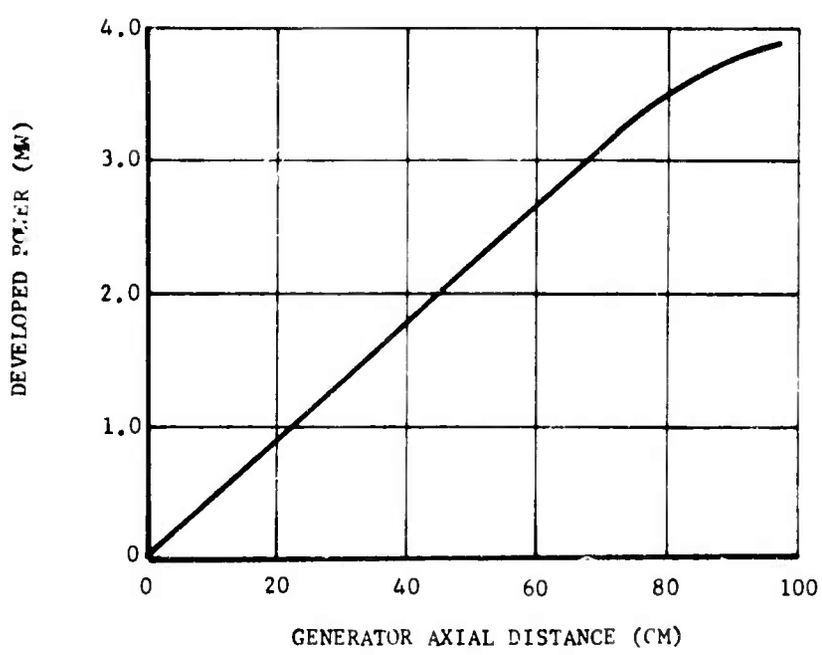

Figure 4-18

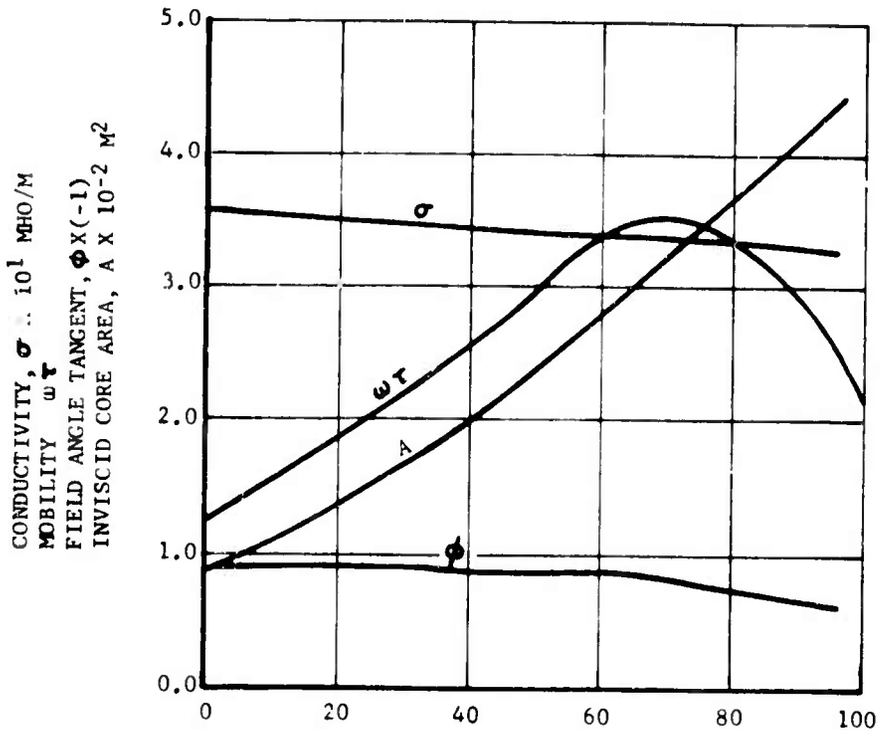

Figure 4-19

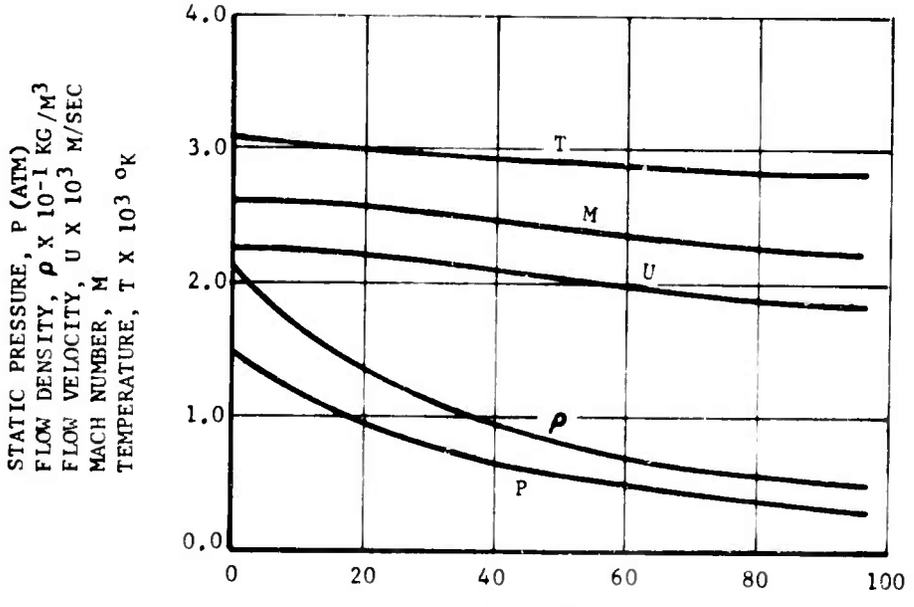

Figure 4-20

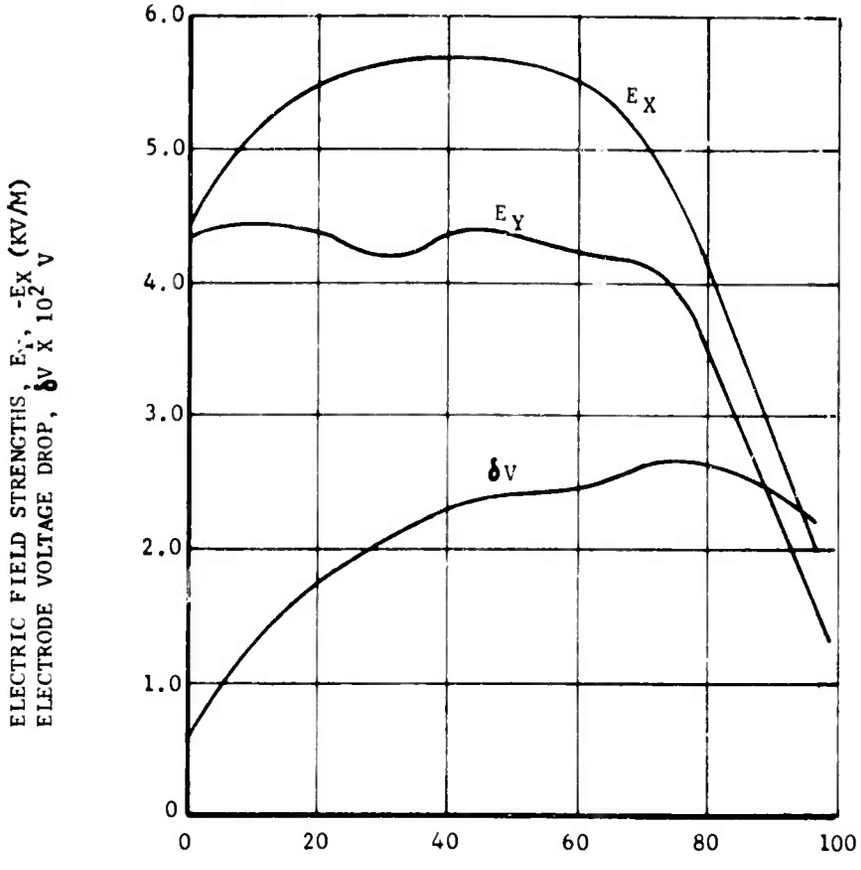

Figure 4-21

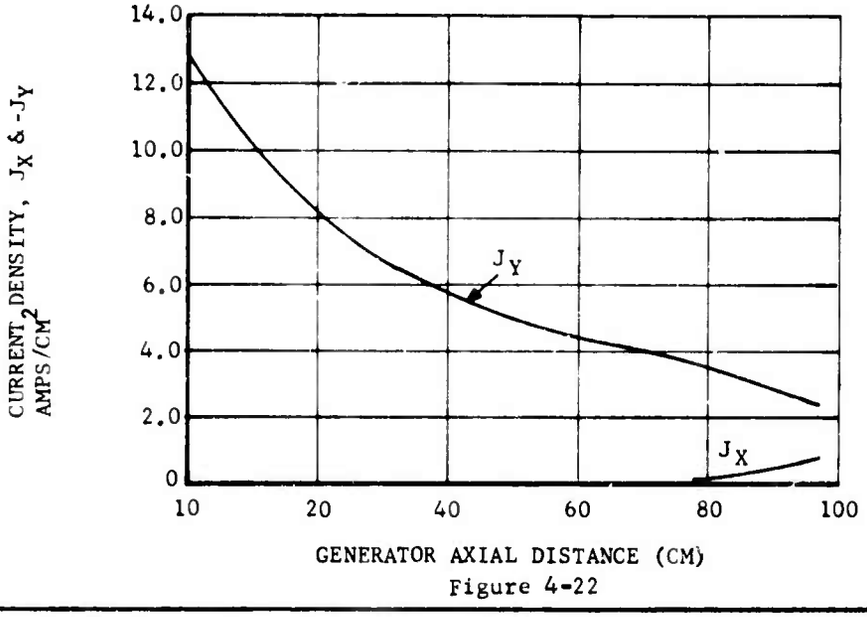

Figure 4-22

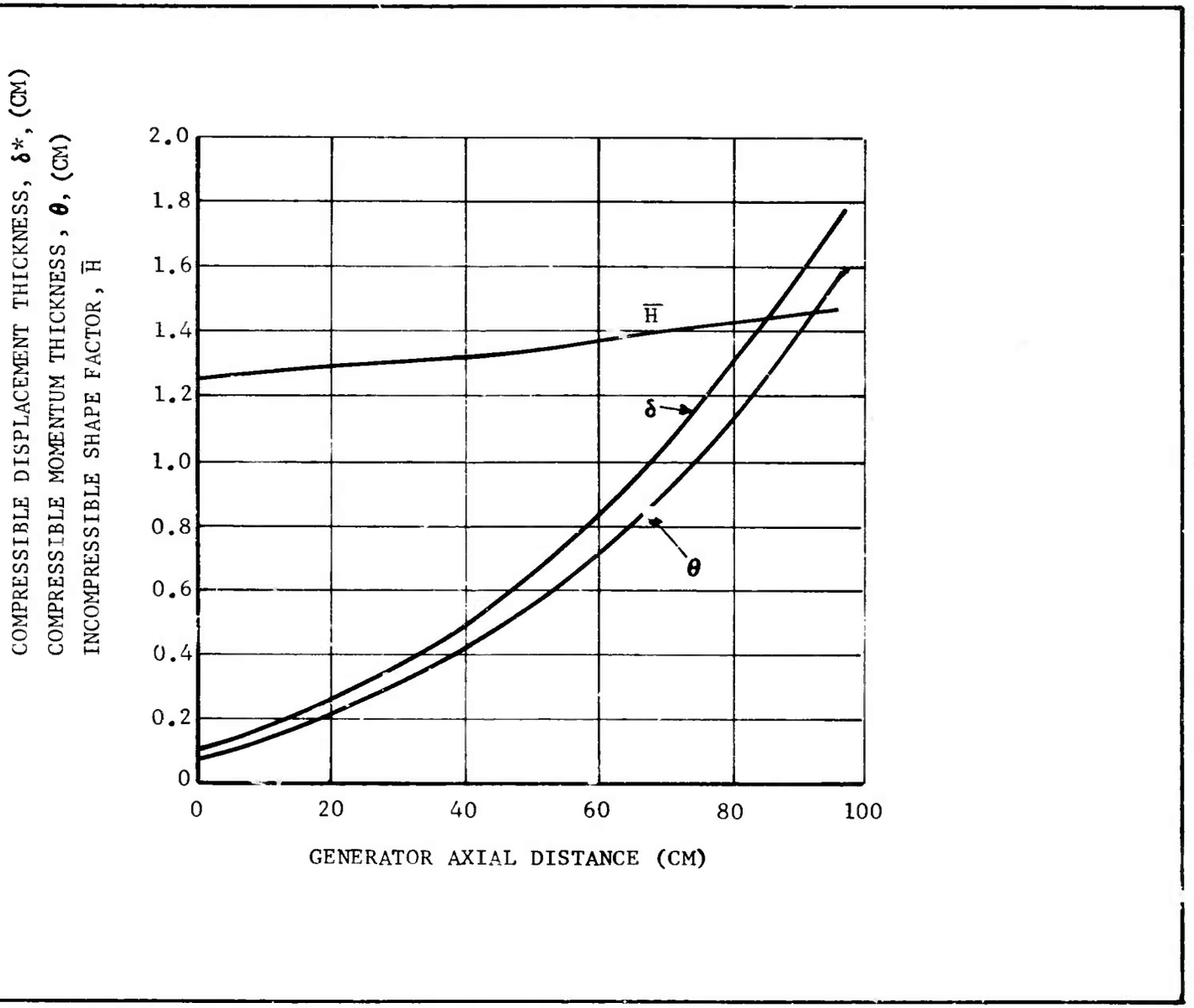
COMPRESSIBLE DISPLACEMENT THICKNESS, δ*, (CM)
COMPRESSIBLE MOMENTUM THICKNESS, θ, (CM)
INCOMPRESSIBLE SHAPE FACTOR, H̄
2.0
1.8
1.6
1.4
1.2
1.0
0.8
0.6
0.4
0.2
0
H̄
δ
θ
0
20
40
60
80
100
GENERATOR AXIAL DISTANCE (CM)

Figure 4-23

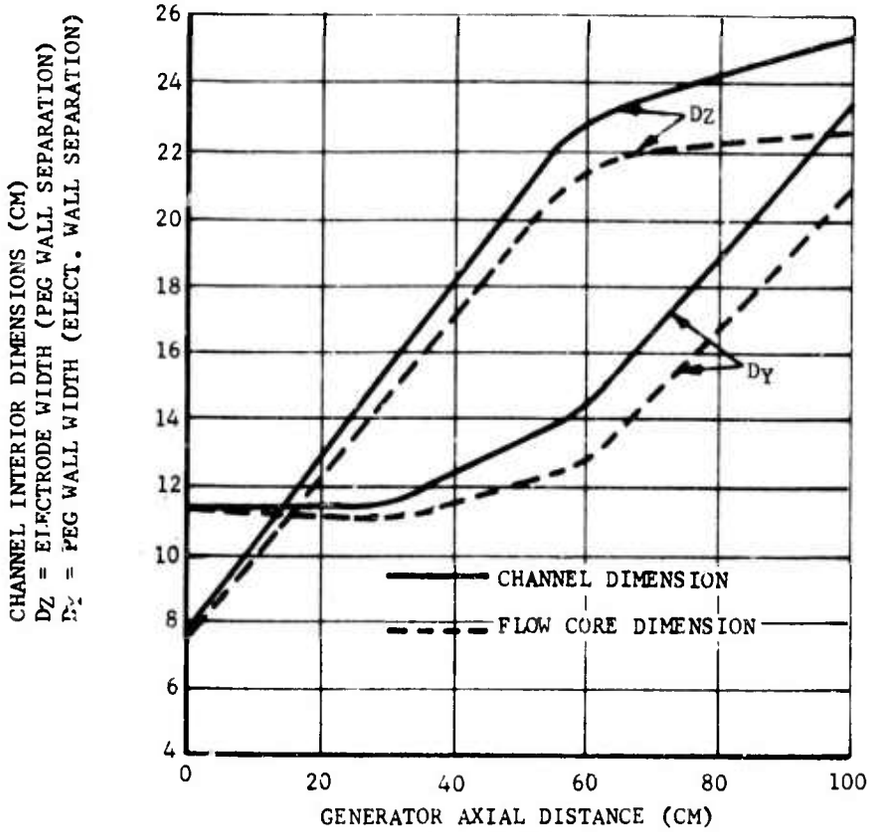

Figure 4-24

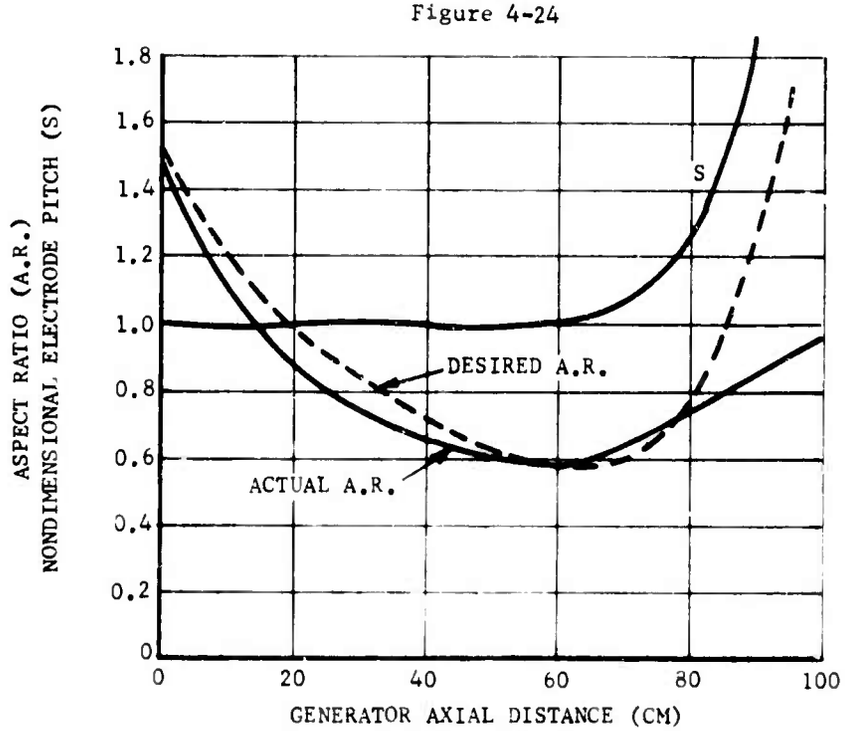

Figure 4-25

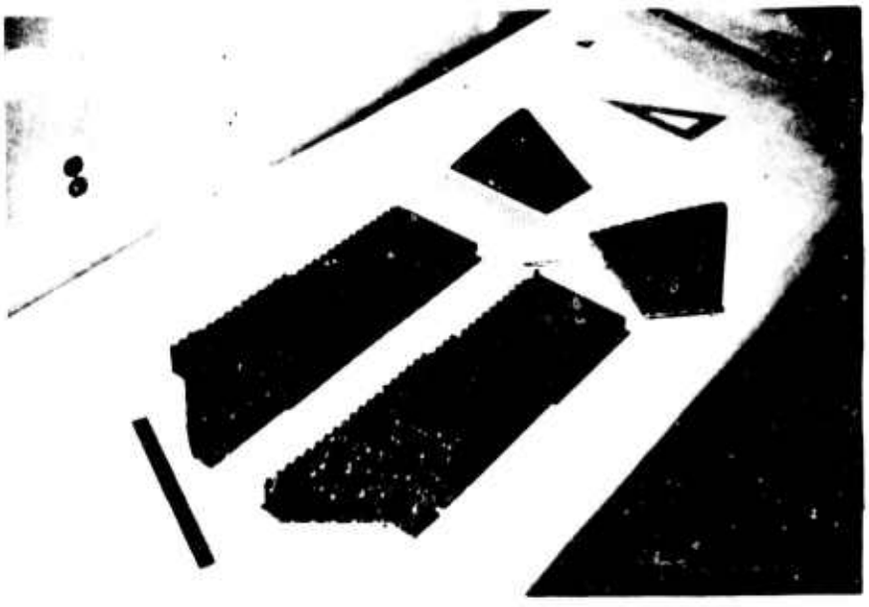

Figure 4-26

Partial assembly of peg boards; boards are bonded to side panels after assembly, packing with refractory and surface machining.

Figure 4-27

Completed exit flange-power takeoff. Made of aluminum, inside surface of exit and inlet flanges is lined with graphite to make good contact with the plasma for power takeoff.

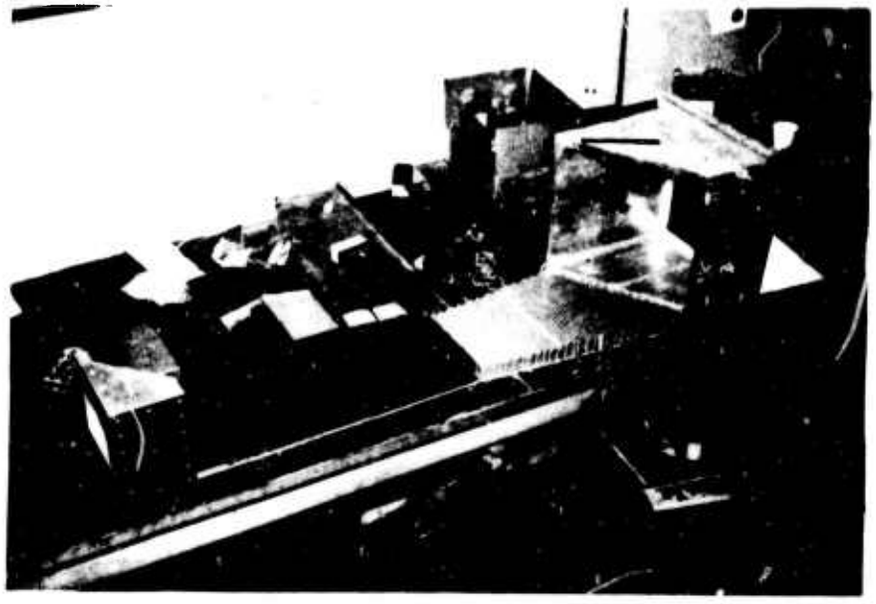

Figure 4-28

Pre-assembly for illustration showing mating of peg walls to exit flanges. Longer pegs (dark) at inlet of channel are of copper to accept high heat transfer rate. Shorter light colored pegs of aluminum are used in the downstream portions of the channel.

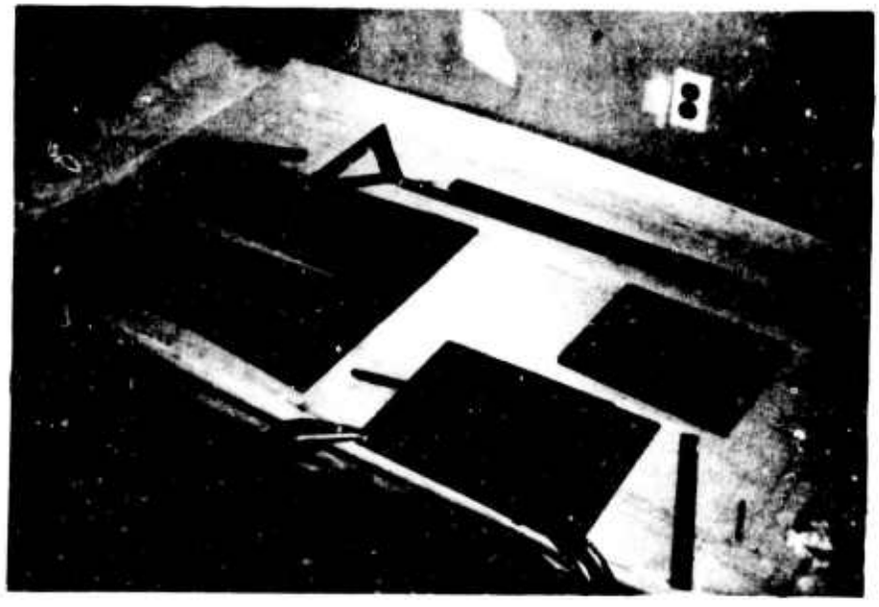

Figure 4-29

Electrode boards prior to mounting of electrodes. Bottom boards for bottom wall have "presserts " inserted for electrode mounting. Electrodes are demountable for channel repair in the event of an interelectrode breakdown.

Figure 4-30

Peg boards drying in floodlamp oven after packing with high alumina refractory. The boards are clamped to prevent distortion during drying.

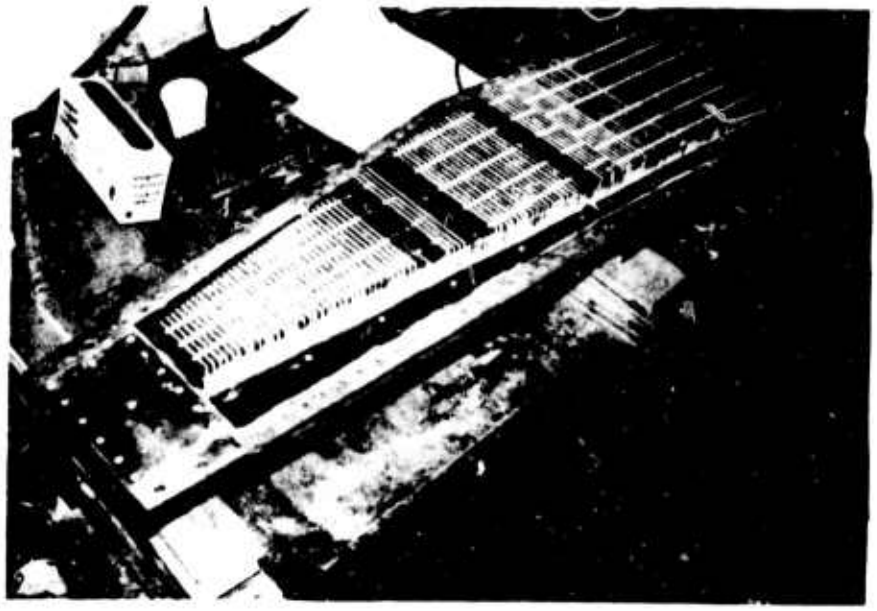

Figure 4-31

Nearly completed electrode wall. Several electrodes just installed to replace those broken during assembly are visible; the refractory cement has not yet been installed in the mounting holes for these electrodes, or between them.

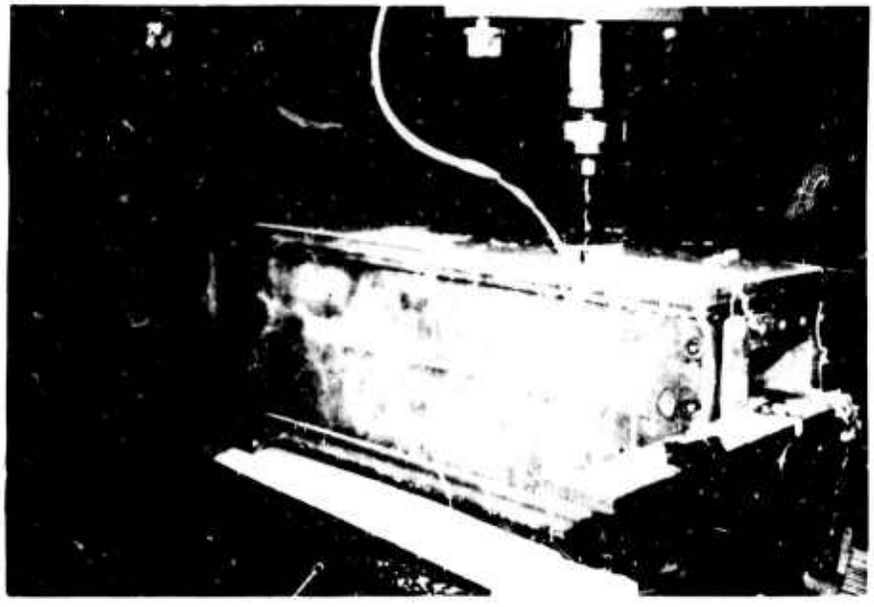

Figure 4-32a

Channel mounted on tape machine for drilling of tie rod holes. Channel has been assembled to the flanges for the match drilling of these holes. A water soluble cutting lubricant is being used.

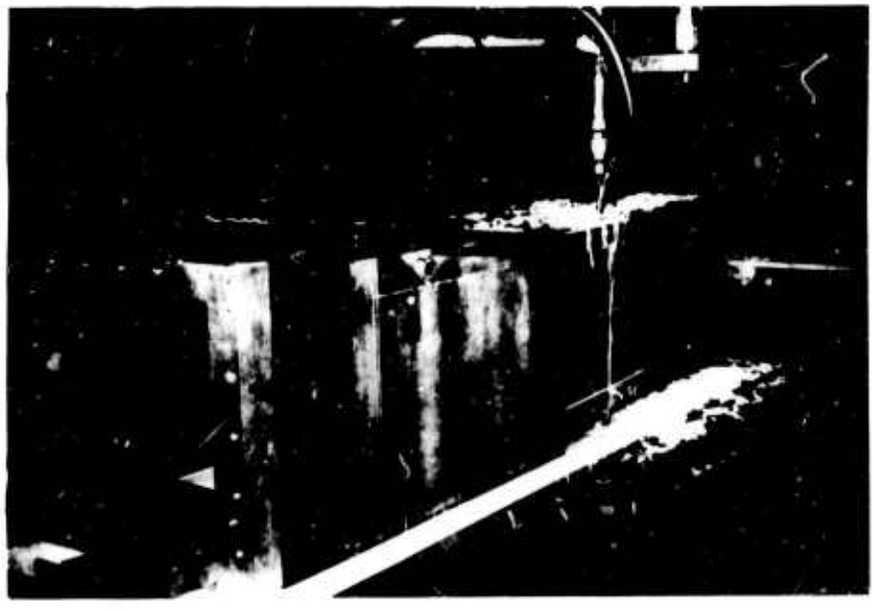

Figure 4-32b

Another view of the channel during tie rod hole drilling showing some details of the side panel mounting to the exit flange.

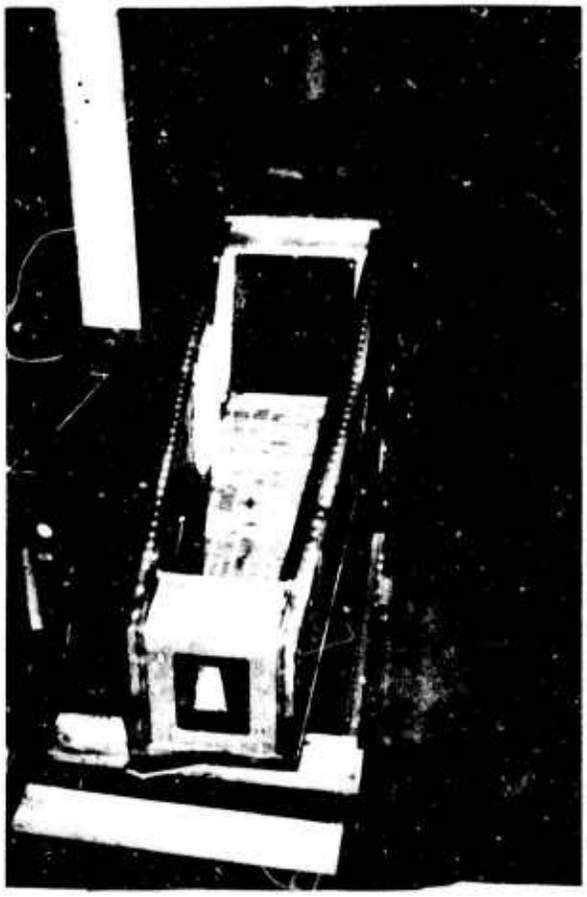

Figure 4-33

Channel during assembly shown in inverted position. Note graphite liner on inlet power takeoff. Peg board on left side is in process of fitting for clearance with electrode wall. Gun drilled tie rod holes are visible on top of peg walls.

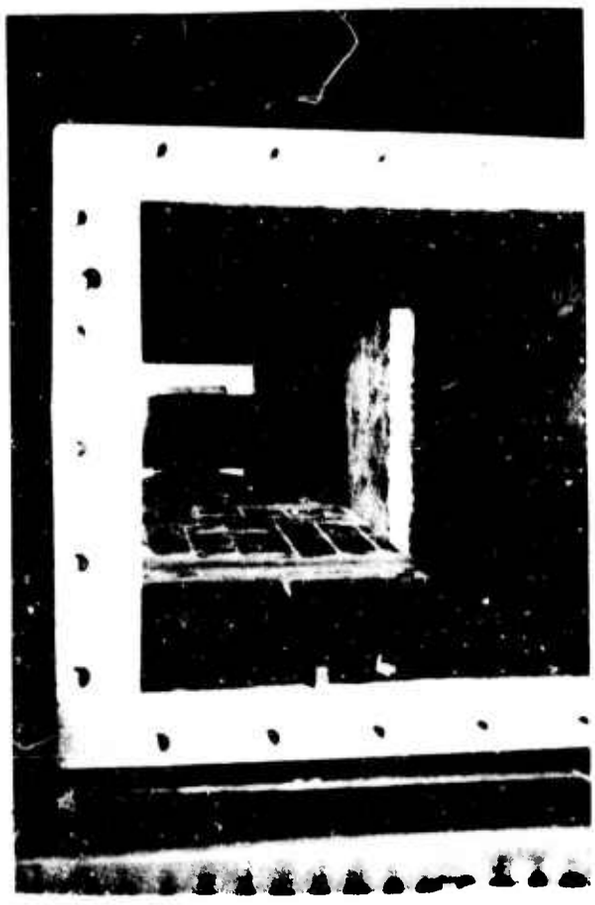

Figure 4-34

Another view of channel in same stage of assembly as in Figure 3. View is looking up through exit power takeoff, and shows the graphite lining. Graphite mounting holes and rib voids will be filled with alundum cement at final assembly.

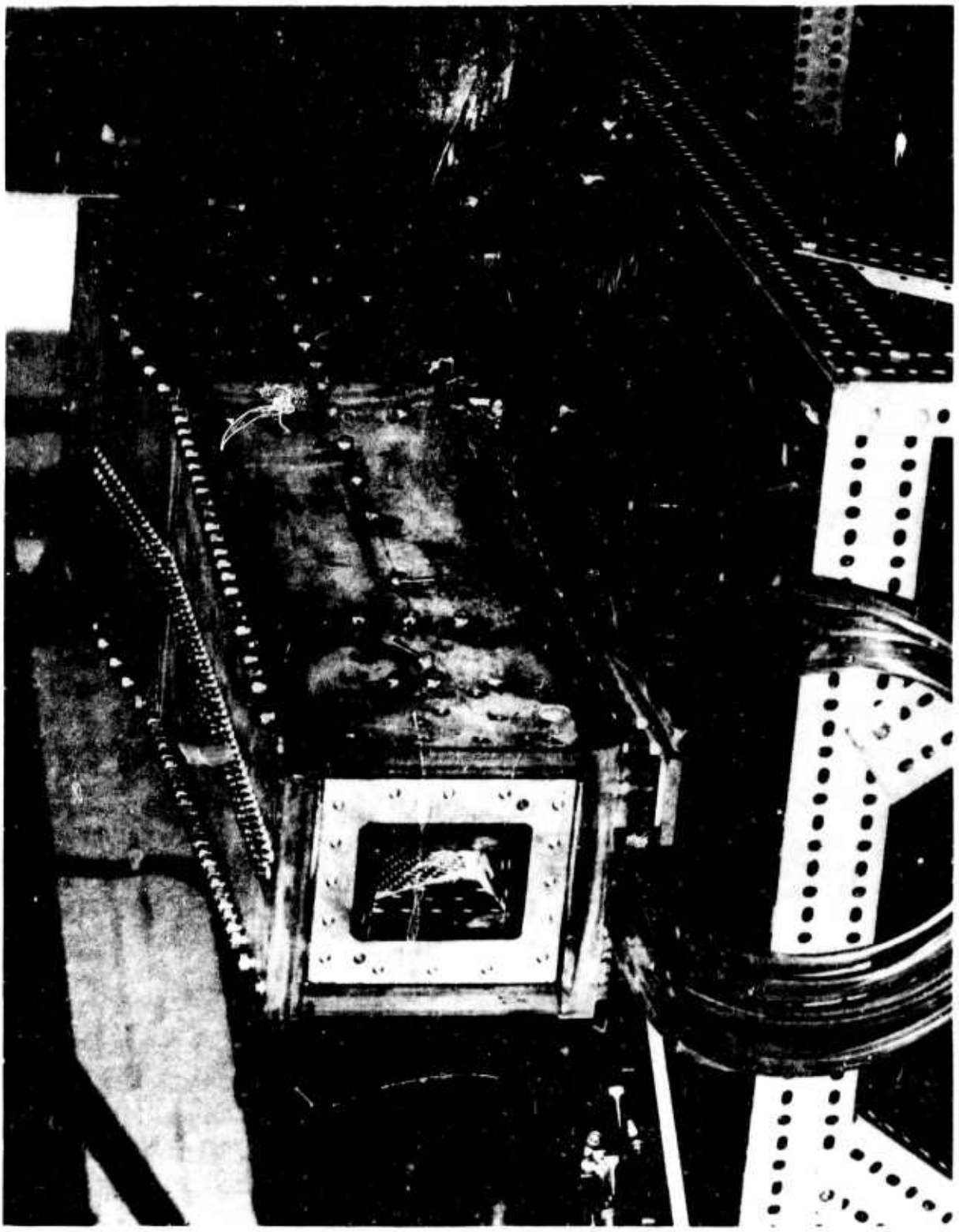

Figure 4-35. Photograph of 4 MW MHD Channel Viewed from Entrance

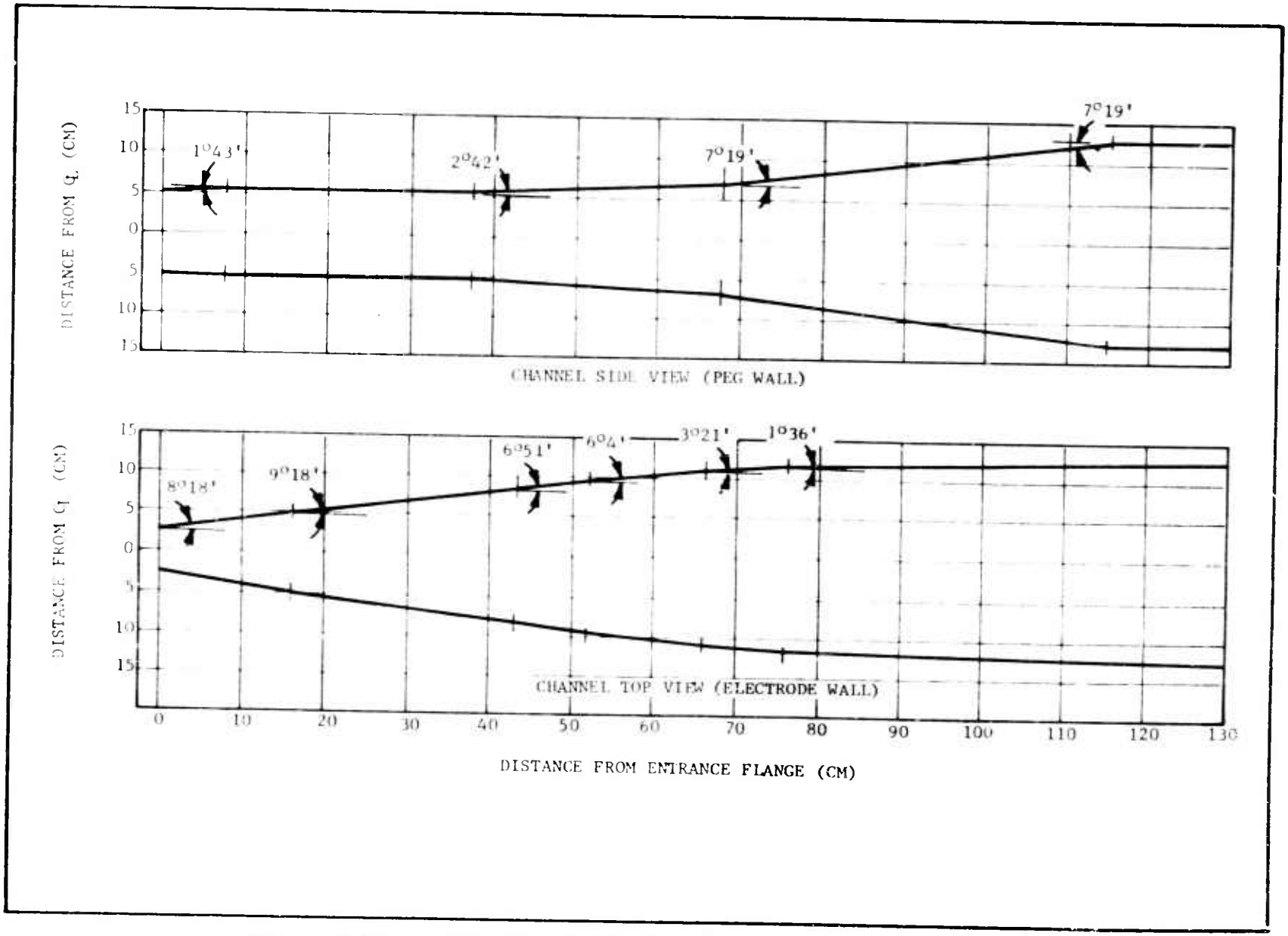

Figure 4-36. C-MHD Channel Showing "As Built" Internal Contours

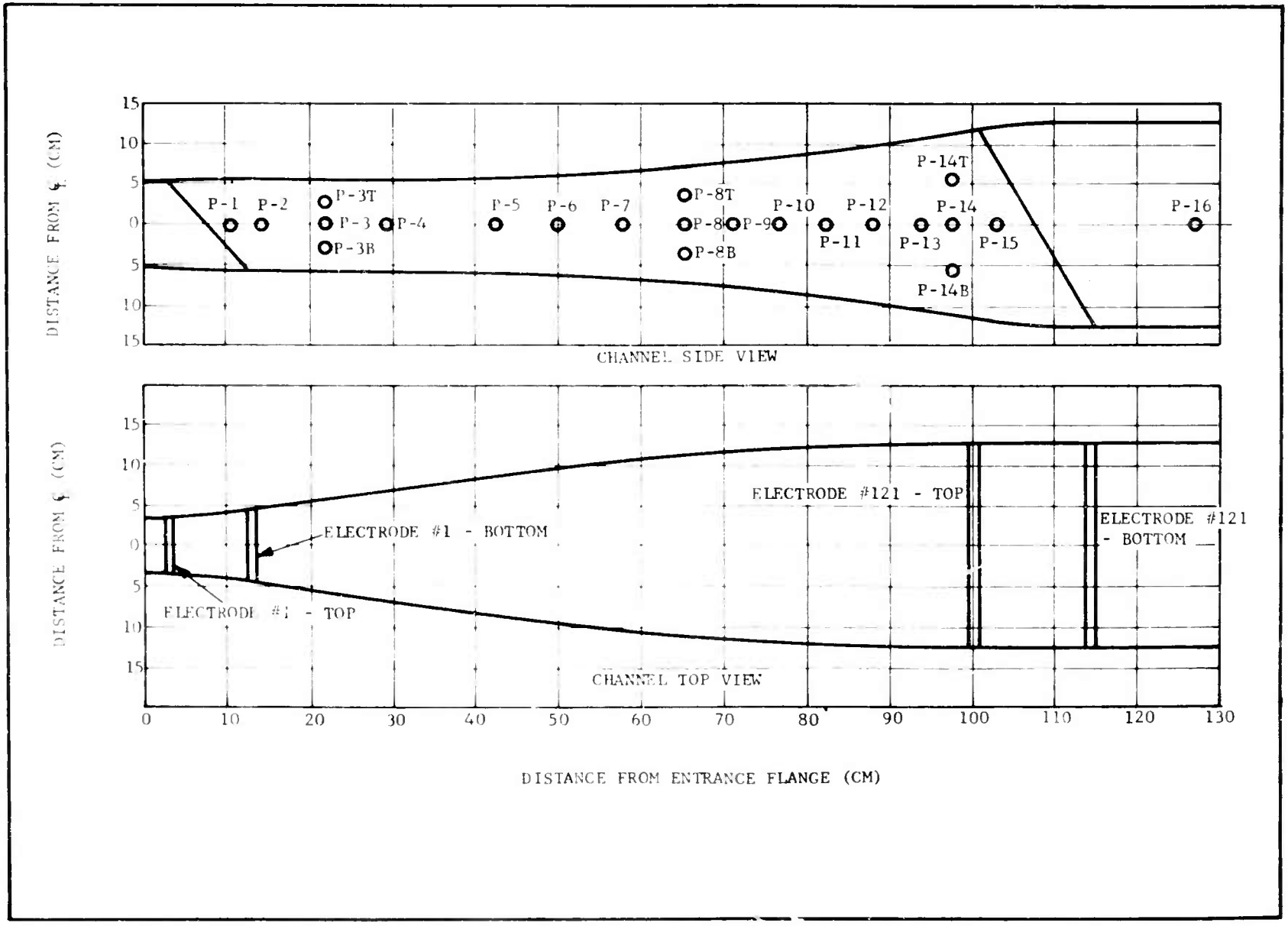

Figure 4-37. Location of Pressure Tap and End Electrodes in C-MHD Channel

Figure 4-38. View of Damaged Entrance Box

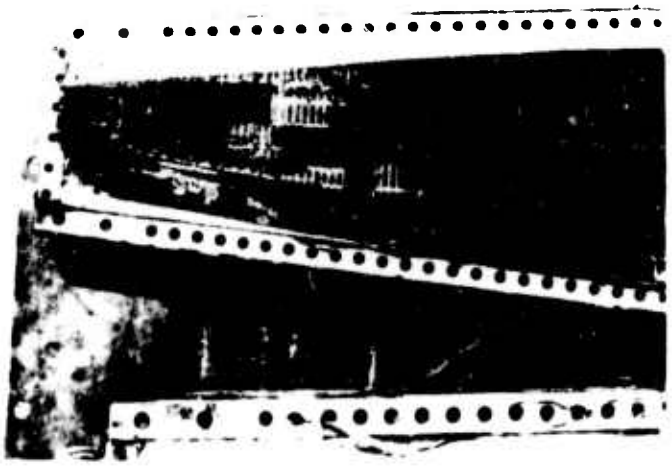

Figure 4-39. View of Disassembled Electrode Wall

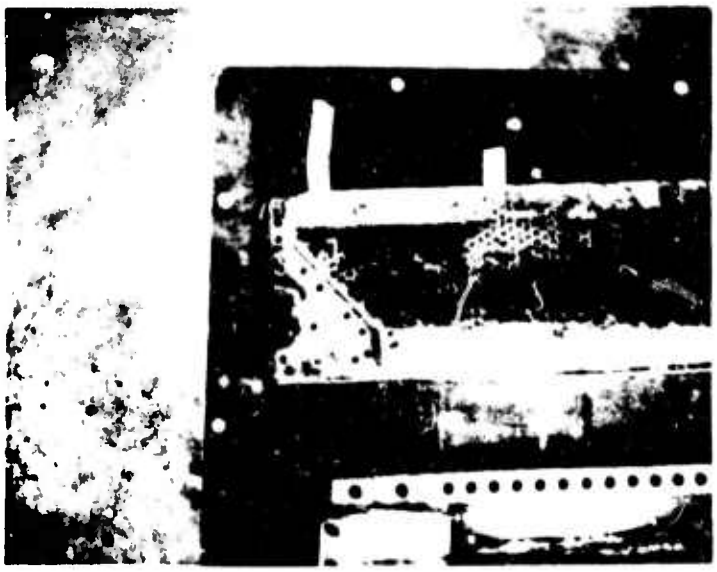

Figure 4-40. View of Disassembled Peg Wall

Figure 4-41. View of Repaired Peg Wall

a soft ceramic was used to fill the countersunk holes and came out very easily. A harder ceramic, Sauereisen No. 78, was used for repotting the assembly. In future designs, it would probably be worthwhile to stagger the bolts from electrode to electrode so that they are not aligned in the direction of flow.

C. Diffuser Design and Fabrication

The function of the diffuser is to increase the static pressure in the channel flow to atmospheric pressure or above so that the flow can be discharged into the atmosphere without causing a shock to form in the channel. Typically the supersonic MHD channel, with a Mach number of 2, will have a static pressure of one-third an atmosphere while the stagnation pressure is about 3 atmospheres. This means, in principle, if the flow could be decelerated isentropically to zero velocity, the static pressure would increase to three atmospheres. In supersonic flow, either a converging-diverging channel or a long constant area channel, or a combination of the two is generally used as a diffuser. In operation, a normal shock occurs in the diffuser, decelerating the flow to subsonic Mach numbers, with a concurrent recovery of pressure and an increase in entropy.

In this program there were three design flows which had to be considered: These were:

a) The Channel Proof Test. A static firing conducted outside of the magnet with no electrical loading.

b) Optimum Load Test. Conducted in the magnet with the designed load of 3.4 ohms.

c) Short Circuit Test. Conducted in the magnet with maximum

load current flow.

Of the above possibilities, the channel proof test places the most stringent requirements on the diffuser. Table 4-II lists the physical parameters for each of these tests. In the proof test the flow continues to accelerate as the channel expands, reaching M = 4 at the exit with a very low static pressure. In the power generation case the velocity is slower, M = 2.2 and the static pressure is about one-third atmosphere. In the short circuit case the flow is just barely supersonic, but the static pressure is almost atmospheric. From a theoretical basis, we can say that the required diffuser performance will depend upon the strength of magnetic induction, generator load and plasma conductivity. Since these parameters can vary widely, it is clear that the diffuser must be capable of operating efficiently over wide limits.

Two different supersonic diffuser designs have been evaluated; a converging-diverging nozzle and a constant-area pipe.

1. Converging-Diverging Nozzle

The design of the converging-diverging nozzle diffuser is based on the premise that a shock forming in the MHD channel will move through the generator and be swallowed by the diffuser throat. For most efficient operation, the design should be such that the equilibrium position of the shock is in the diffuser throat so that the shock occurs at the minimum possible Mach number in the diffuser. However, the most critical condition is starting, where the shock must move down the channel and through the converging section of the nozzle. The area ratio which will allow swallowing of the shock to be accomplished is called γ, and is given by the expression

TABLE 4-II

DIFFUSER FLOW PARAMETERS

Case	Condition	u_e (m/sec)	M	P (atm)	T (°K)	$\frac{4fL}{D}$	L/D	$P_{o_{exit}}$	υ
I	Proof Test	2965	4.0	0.100	2320	1.18	58	3.75	0.53
II	Optimum Load	1831	2.208	0.303	2813	0.60	30	15.0	0.725
III	Short Circuit	1000	1.03	0.60	3100	0.01	0.5		0.99

$$\nu(M) = \left(\frac{\gamma-1}{\gamma+1}\right)^{1/2} \left(\frac{2\gamma}{\gamma+1}\right)^{\frac{1}{\gamma-1}} \left(1 + \frac{2}{\gamma-1}\frac{1}{M^2}\right)^{1/2} \left(1 - \frac{\gamma-1}{2\gamma}\frac{1}{M^2}\right)^{\frac{1}{\gamma-1}} .$$

An isentropic diffuser would have a much larger area contraction ratio. Hence, if the diffuser is of fixed geometry; i.e., the area ratio cannot be changed after flow is started as is sometimes done in supersonic wind tunnels where the diffusers have movable walls, this form of diffuser has low efficiency. (Diffuser efficiency is expressed in terms of the fraction of the enthalpy recovered by the diffuser.) For subsonic and slightly supersonic diffusers, the experimentally determined efficiency is about 75%. For higher Mach numbers the diffuser efficiency is slightly higher than the efficiency of a normal shock occurring at the inlet Mach number.

The value of ν, the minimum area ratio for starting the diffuser, is shown in Table 4-II for the various test conditions. The short circuit experiment, Case III, requires only a small reduction in area ratio to start, whereas the channel proof test could use almost a 2 to 1 area ratio reduction. It is clear that each case would require an individually designed diffuser. Because of the uncertainty in the plasma conductivity and electrode voltage drops, the diffuser for Cases II and III would have to be designed with a suitable margin of safety to insure that supersonic flow would start under the most optimistic conditions. This would require less contraction than shown in Table 4-II. However, if design conditions were achieved, the result would be reduced pressure recovery. While this reduced pressure recovery could be tolerated, it illustrates the problem of operating the experiment with a fixed geometry converging-diverging nozzle.

2. Constant-Area Pipe Diffuser

It is known that friction slows a supersonic flow, and that if

the pipe is sufficiently long the flow will be decelerated to Mach number unity. At this point a normal shock will occur with static pressure recovery. This type of diffuser has the advantage that for velocities lower than the design Mach number the shock will move upstream in the diffuser to the appropriate station, thereby making the system much more flexible, i.e., it is in a way self-adjusting.

The conditions for the shock to occur in the diffuser are given by the relation

$$\frac{4fL}{D} = \left[\left(\frac{P_i}{P_e}\right)^2 - 1\right] - \ell n \left(\frac{P_i}{P_e}\right)^2$$

where P_i and P_e are the stagnation pressures at the inlet and the outlet. L is the length of the pipe, f is the friction factor, and D is the hydraulic radius. We can use the isentropic relations to present this equation in terms of the Mach number, M, and the specific heat ratio, γ, as follows:

$$\frac{4fL_{max}}{D} = \frac{(1-M_i)^2}{M_i^2} + \frac{\gamma-1}{2\gamma} \ell n \frac{\frac{\gamma+1}{2} M_i^2}{1 + \frac{\gamma-1}{2} M_i^2}$$

Because of the relatively low value of γ in the solid propellant flow stream (i.e., γ = 1.04 to 1.15), the L/D's required for a shock to occur are somewhat larger than is the case for air, where γ = 1.4

The appropriate L/D values for the three cases are shown in Table 4-II, under the assumption that f = 0.005, a value appropriate for supersonic flow over smooth surfaces where the Reynolds number is about 5×10^5. It may be seen that the L/D's required for the proof test are very high. For this test it would appear appropriate to use a fixed diffuser with the throat area ratio of 0.53, given in Table 4-II.

For the power generation experiment, Case II, it was decided that a combination pipe diffuser and diverging section be used as shown in Figure 4-42. The straight pipe should be about 9 diameters in length, and then diverge with a 3° half-angle. For proof tests, inserts were installed in the supersonic section to form a fixed area ratio diffuser. This design was fabricated as shown in Figure 4-43.

D. Magnet

The magnet utilized in this program was designed and fabricated by MCA, Incorporated under subcontract from Hercules and was designed for multiple use. That is, it was designed to handle both the combustion driven generator, which required the 0.36 m window and the explosive generator which, in some cases, could require access perpendicular to the bore. The magnet is shown in Figure 4-44 with the specifications given in Table 4-III. The power supply consists of 300 truck batteries tied in a configuration of 10 parallel connected elements of 30 batteries each, in series, to produce an unloaded voltage of approximately 360 volts. Under load, with the magnet, the battery bank delivers up to 11,000 amps at 200 volts. The bank is shown in Figure 4-45, with the batteries and magnet shown schematically in Figure 4-46.

The parametric analysis used to develop the magnet are given in Reference 1. Figure 4-47 gives a calculated plot of B field versus the axial distance. Figures 4-48 through 4-52 show the magnet under construction.

E. Load Bank

The resistive load bank consists of two identical sections, one of which is shown in Figure 4-53. Each section has 60 constantan strips of

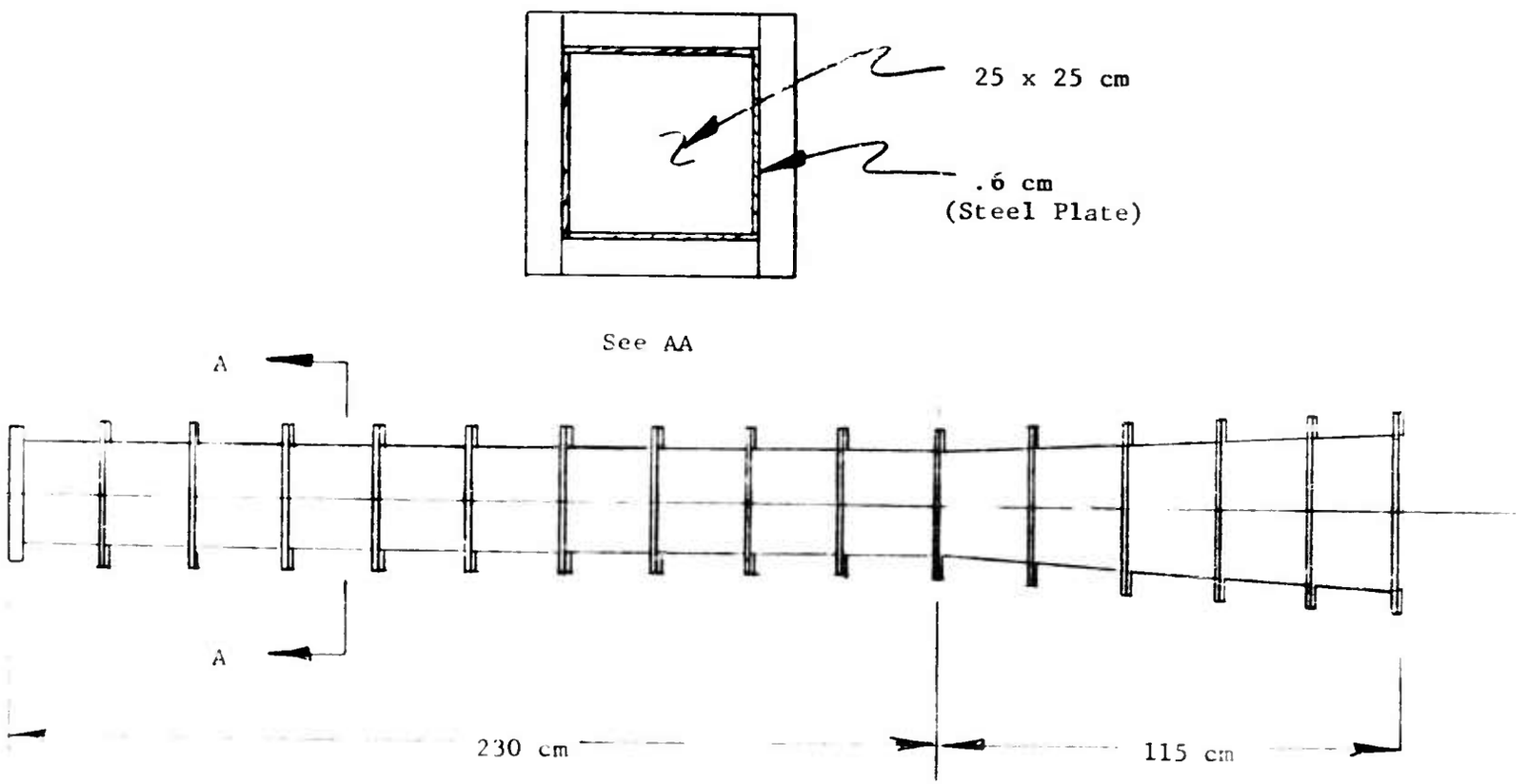

Figure 4-42. Supersonic and Subsonic Diffuser Sections

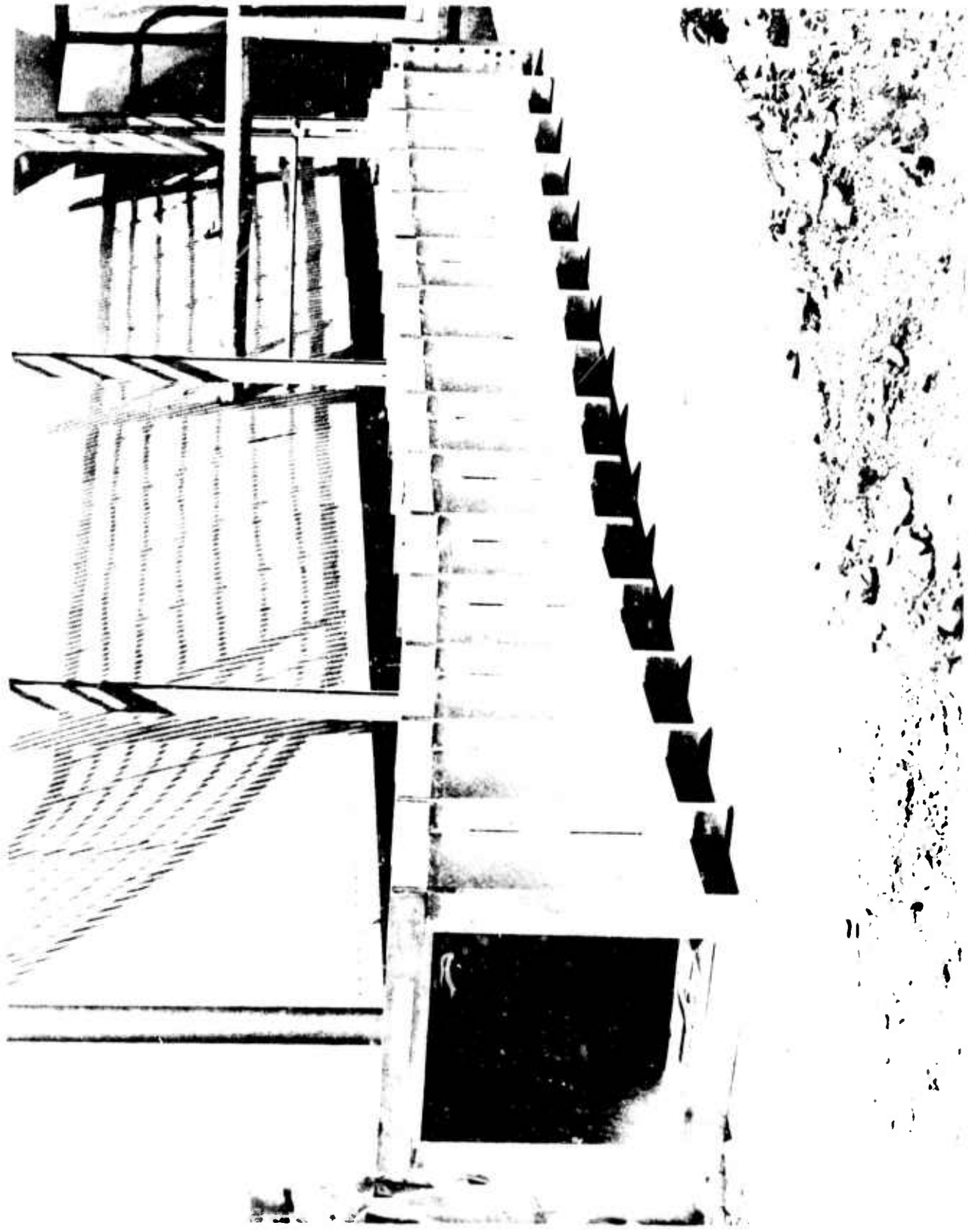

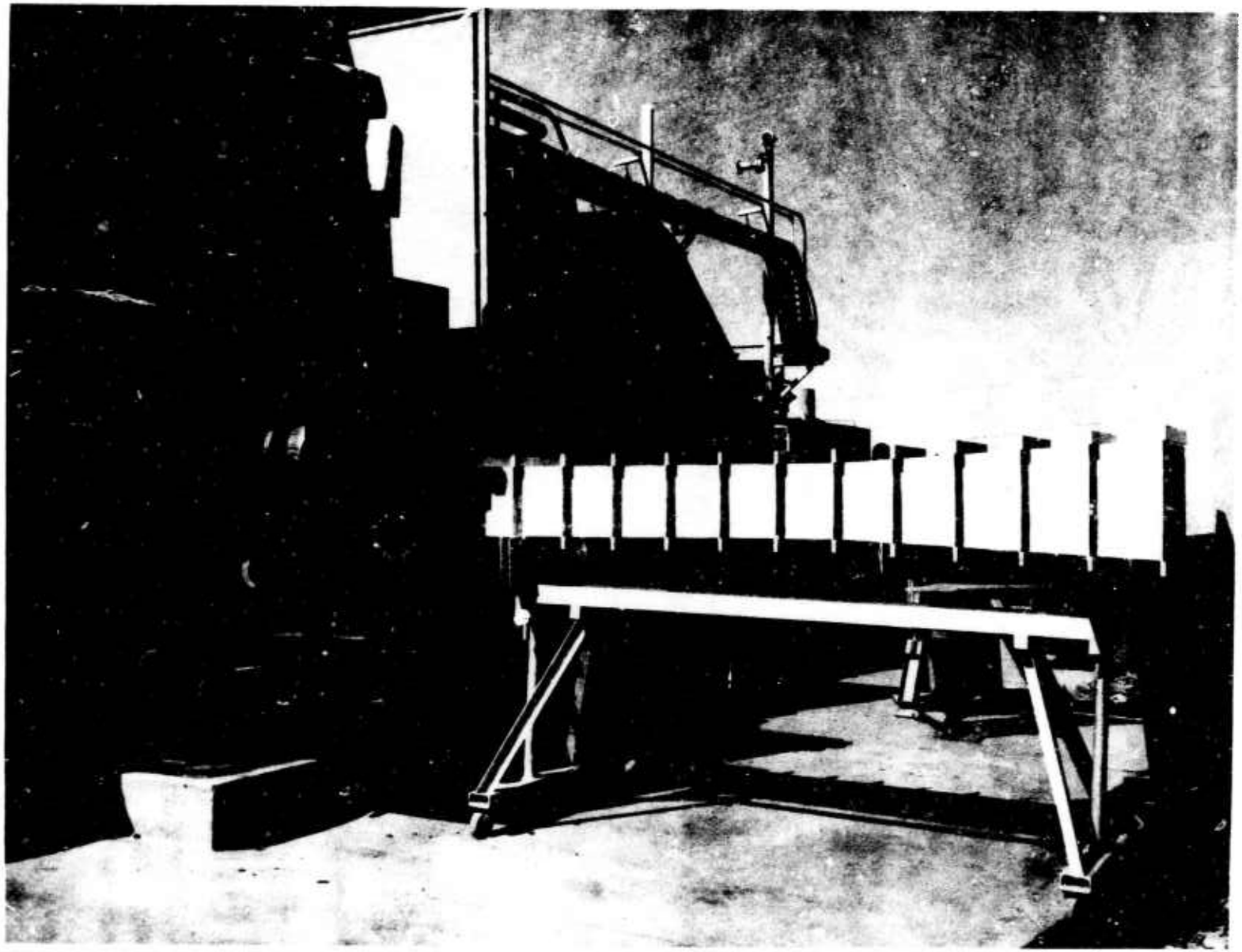

Figure 4-44. View of Magnet and Diffuser Assembly

TABLE 4-III

LINEAR CHANNEL MAGNET DESIGN SUMMARY

Operating Temperature (Initial)	300^{o} K
Working Time for 10% Resistance Change	25 sec
Total Central Magnetic Field	2.5 T
Power	2.54 MW
Current per Coil Half	5700 A
Coil Voltage	223 V
Connection	parallel
Conductor	2.08 cm (0.82") square
Turns per Coil Half	154
Resistance per Coil Half	39.2 mΩ
Total Inductance	95 mH
Copper Current Density	1380 A/cm^2
Transverse Force per Unit Length per Coil Half	1.53×10^6 N/m (8750 lb/in)
Compressive Force per Unit Length per Side	2.11×10^6 N/m (12,040 lb/in)
Compressive Stress	(6.6×10^6 N/m^2) (956 psi)
End Turn Force per Coil Half	1.5×10^6 N (3.35×10^5 lb)
Copper Weight	6950 kg (15,300 lb)
Iron Weight	35,900 kg (79,000 lb)
Bore Size	0.356 m × 0.356 m (14" × 14")
Length Between End Turns	1.63 m (64")
Iron Dimensions	1.63 m × 2.11 m × 1.57 m (64" × 83" × 62")

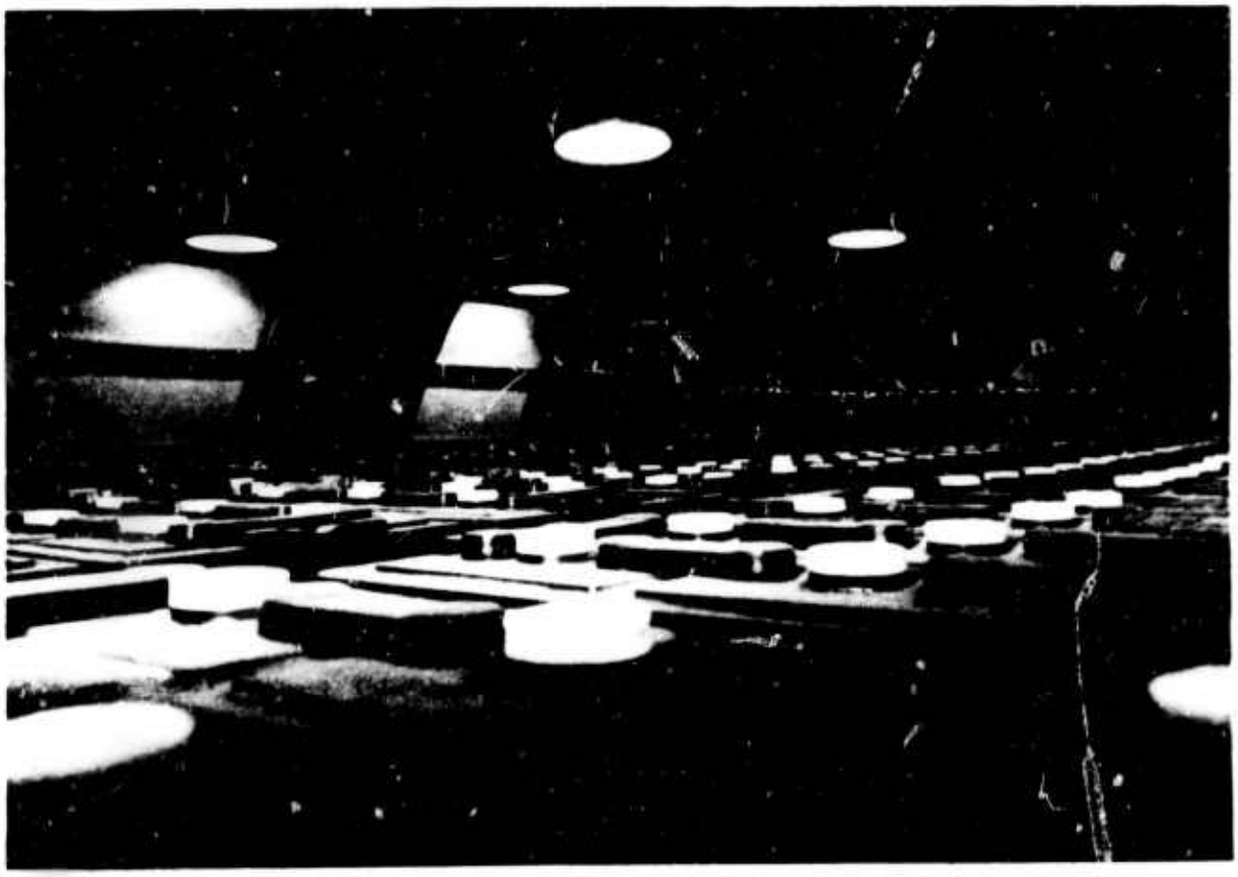

Figure 4-45. View of Battery Bank

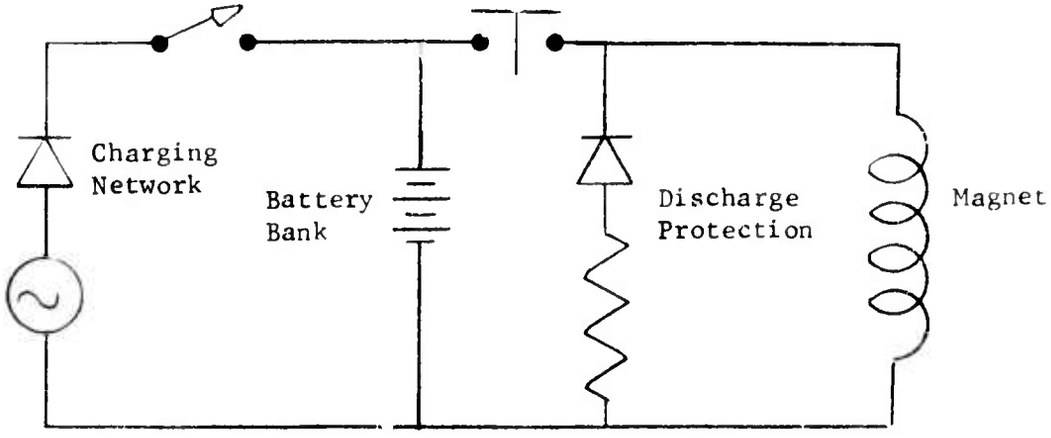

Figure 4-46. Schematic of Magnet System and Power Supply

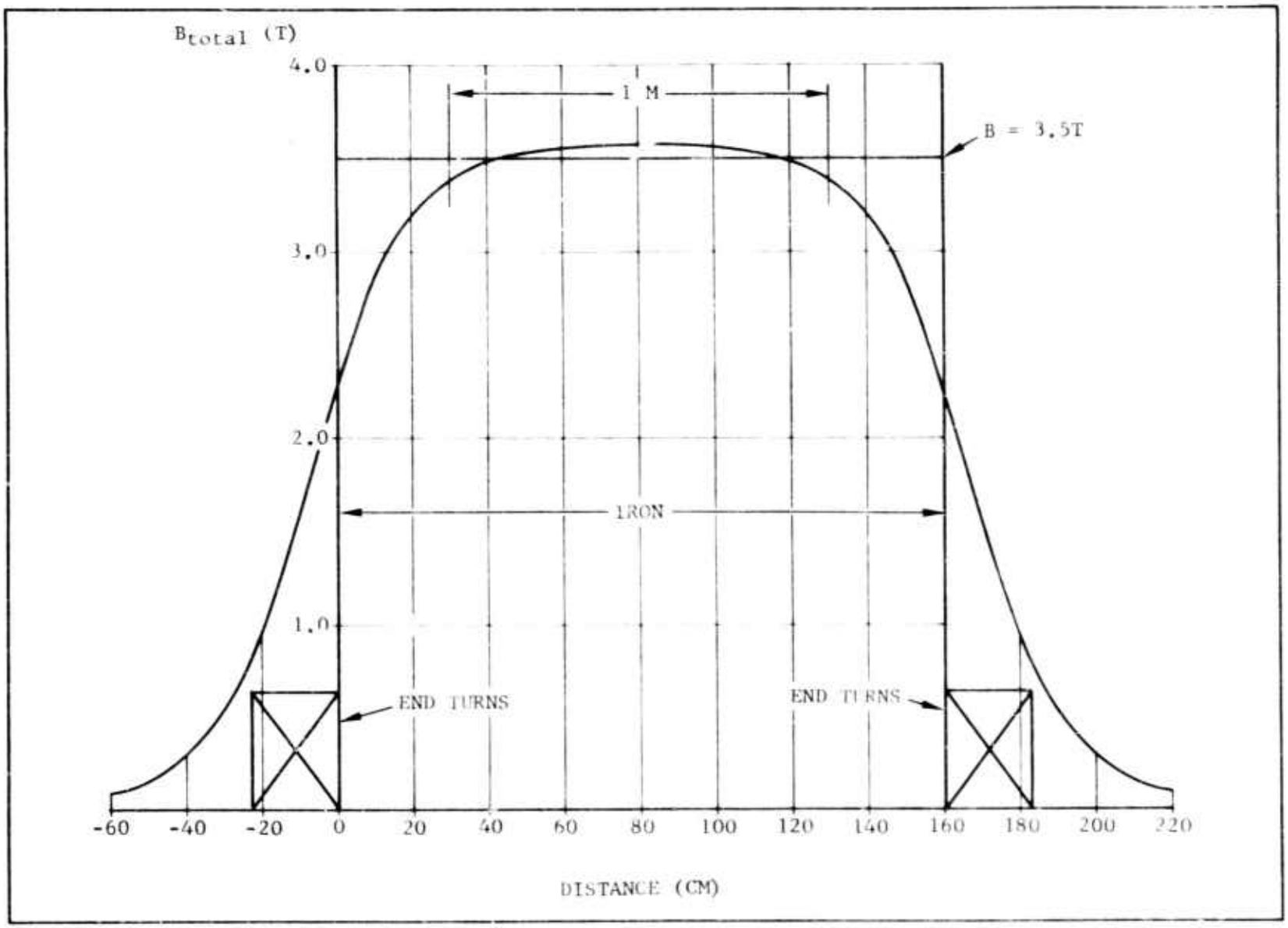

Figure 4-47. Plot of Total Magnetic Field Versus Axial Distance in Magnet

Figure 4-48. Inner Coil After Ground Wall Insulation

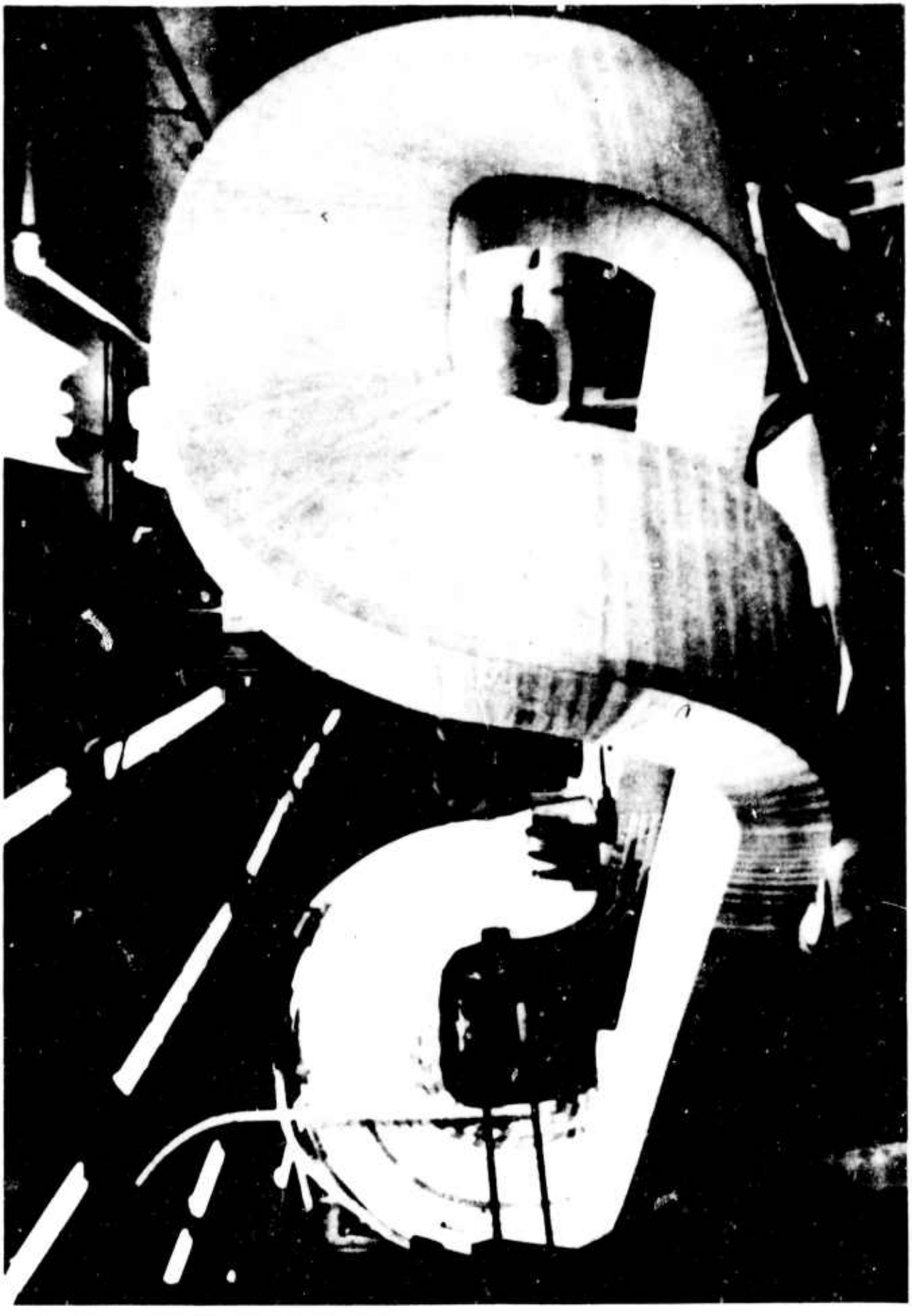

Figure 4-49. Insulation of Outer Coil

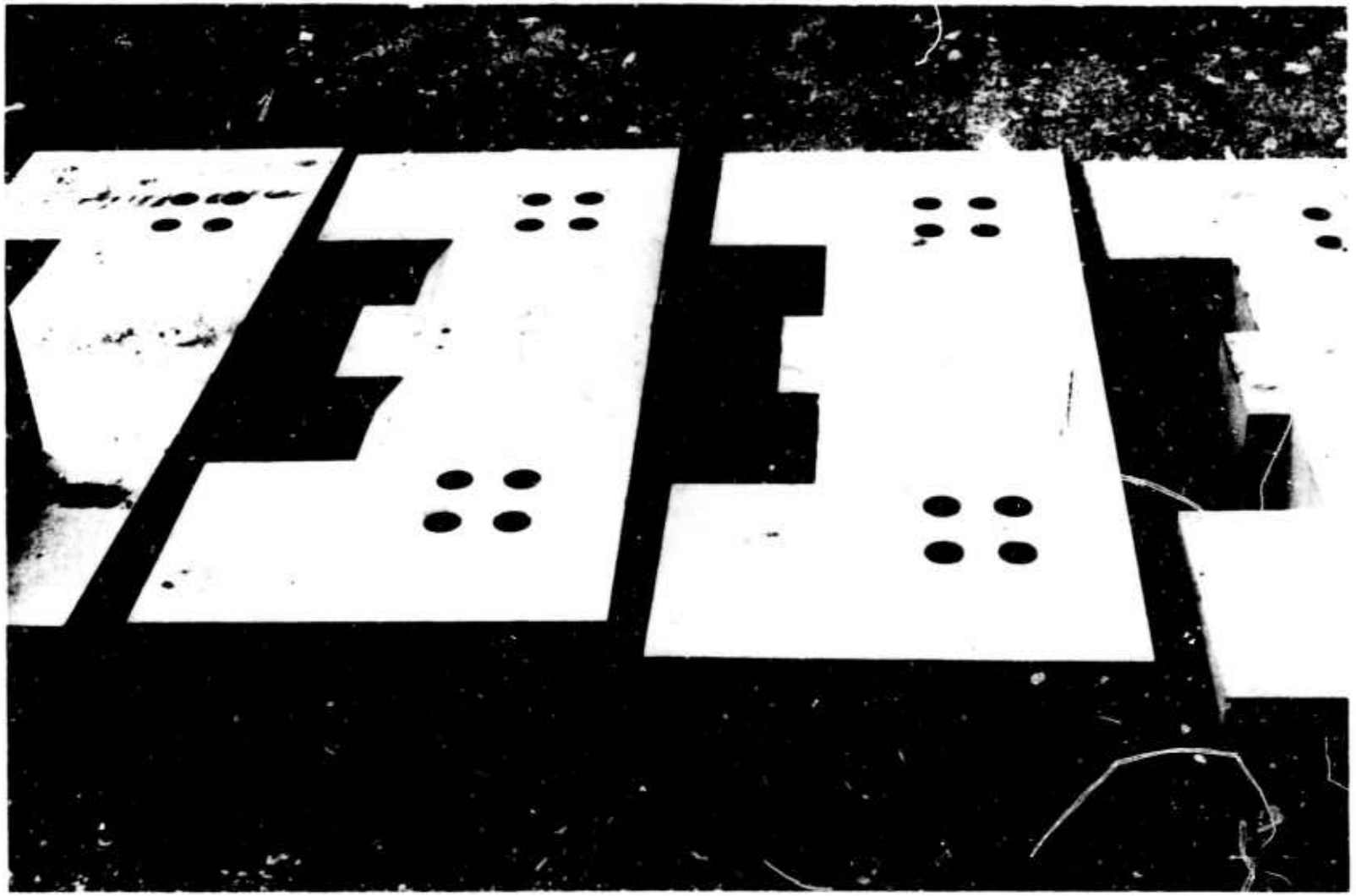

Figure 4-50 Close Up View of Sections

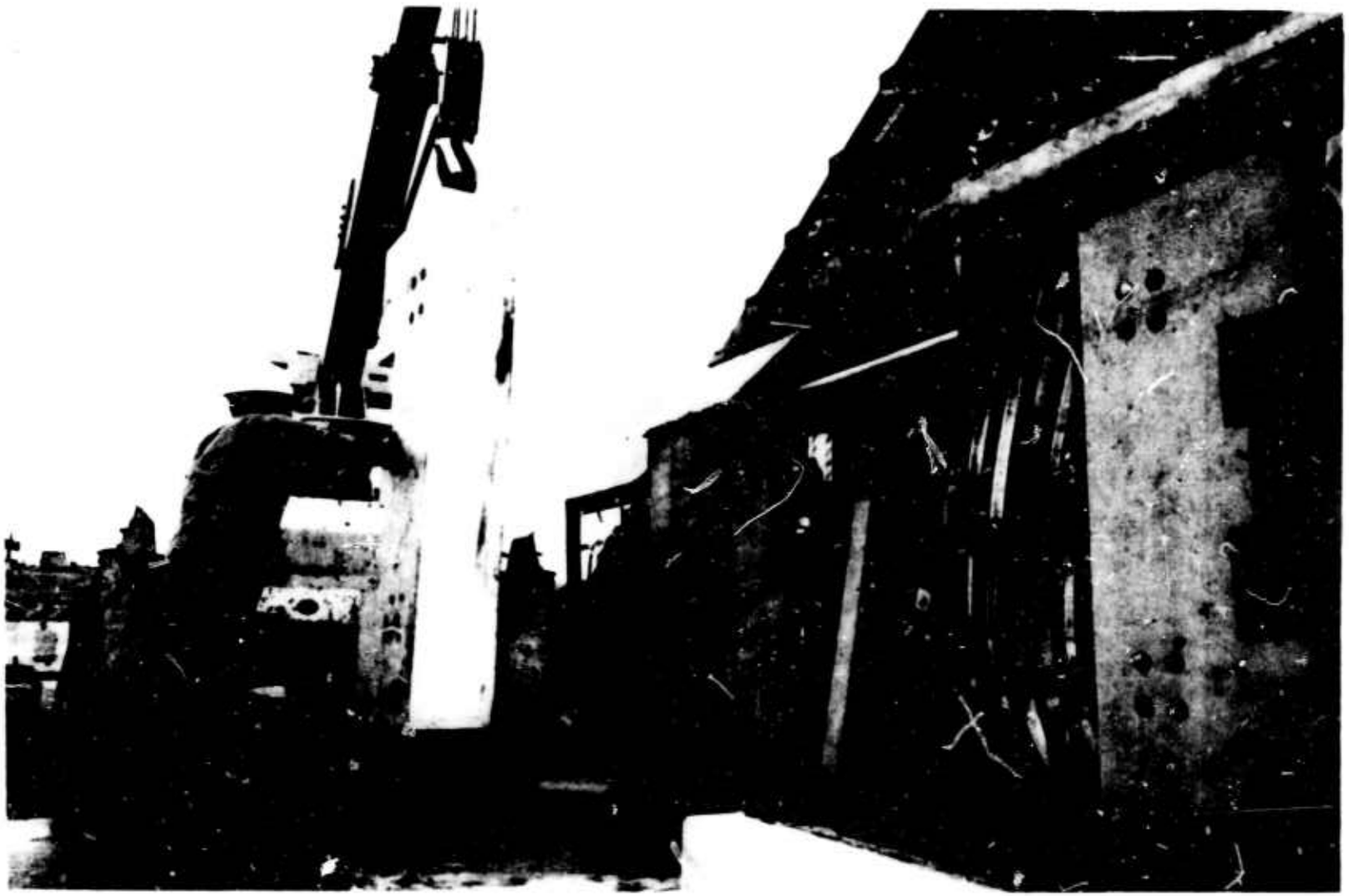

Figure 4-51. C-Sections Being Installed on Base Plates

Figure 4-52. Magnet Coil being Hoisted into Position

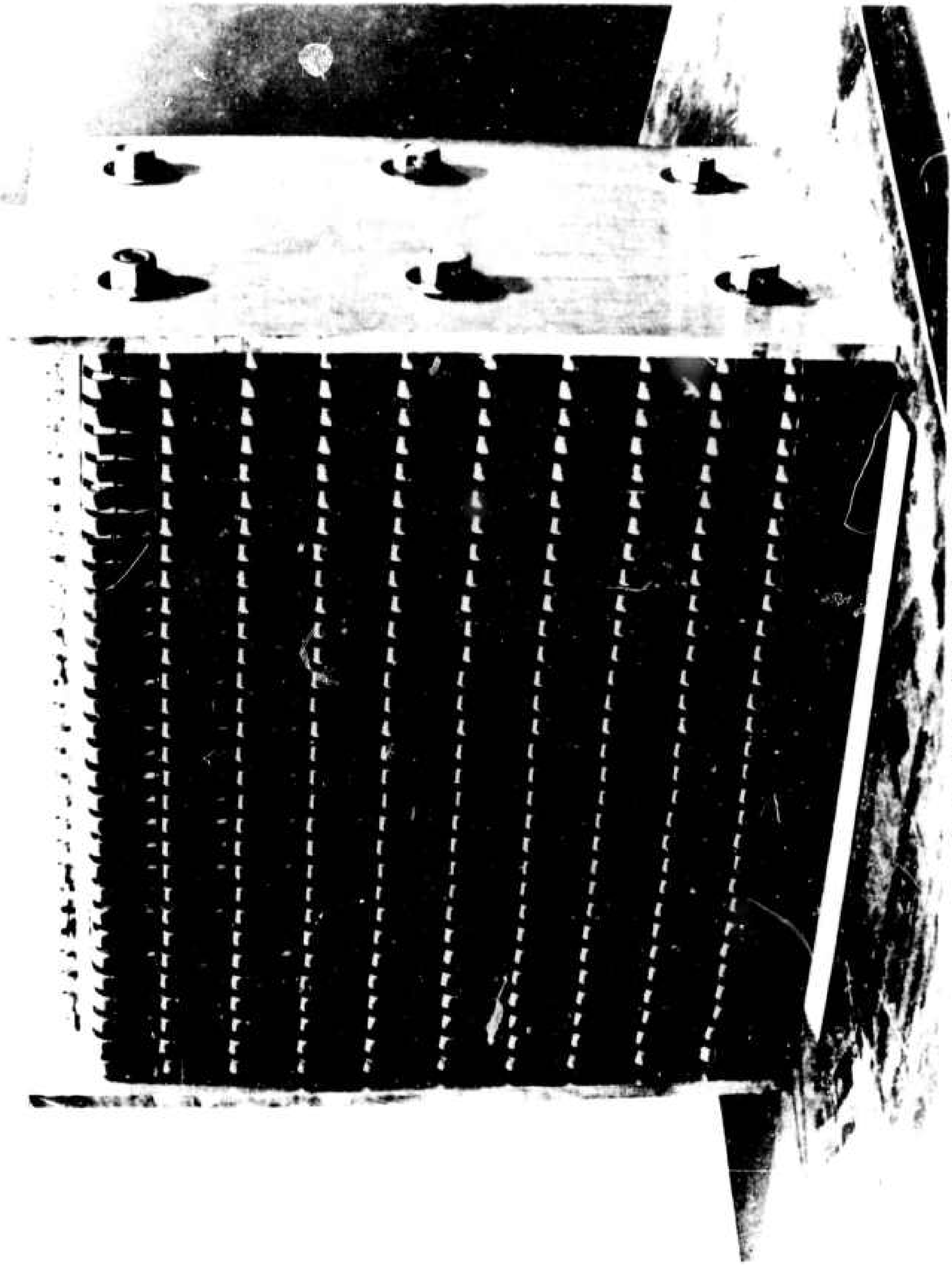

Figure 4-51. Photograph of Coil Bank

0.067 ohms resistance each. Various series parallel combinations can be utilized with a maximum of 4 ohms per section when all 60 strips are connected in series. Using both sections, a maximum of 8 ohms may be attained. In operation, the load banks are submersed in a tank of transformer oil to aid in cooling.

REFERENCES

1. C. D. Bangerter, L. R. West, T. R. Brogan, D. B. Sheldon, Z. J. J. Steklev and J. Farrh, Explosive Magnetohydrodynamic Program, Interim Technical Report No. AFAPL-TR-73-16, May 1973.

SECTION V

TEST RESULTS

This section covers experimental work completed in both conductivity measurement and power generation. Two fuels are discussed in each area, the original 2% KNO_3 fuel and the 7% $CsNO_3$ (VQW) fuel.

A. Conductivity Tests

The basic conductivity tests were made using the diagnostic channel shown in Figure 5-1. The channel is fabricated of 1.27 cm thick copper discs separated by sheet zirconia. It expands at a constant half angle of 2-1/2°. In operation, a DC voltage is applied across the ends of the channel. The current and axial voltage distribution are measured which yields a value of gas resistivity as a function of axial position. This is then converted to a value for conductivity.

Figures 5-2 and 5-3 give voltage distribution and conductivity as a function of channel position for the 2% KNO_3 fuel. As can be seen, the conductivity is about 20 mhos/meter at the entrance conditions of the power channel.

Two conductivity tests were made in the same manner using the 2% KNO_3 fuel in the large power channel. These tests yielded a conductivity slightly less or about 16 mhos/m at the channel entrance. A voltage of 100 volts DC was imposed across the channel in the axial direction. Figures 5-4 and 5-5 give the pressure and voltage profile, respectively, for test MHD-1 along the channel. Data are given for three different times with the note that the aft part of the nozzle broke up at about 0.8 seconds. The data for conductivity test MHD-4 is given in igure 5-14 (Section B below).

The pressure measurements were made along the insulator wall of the

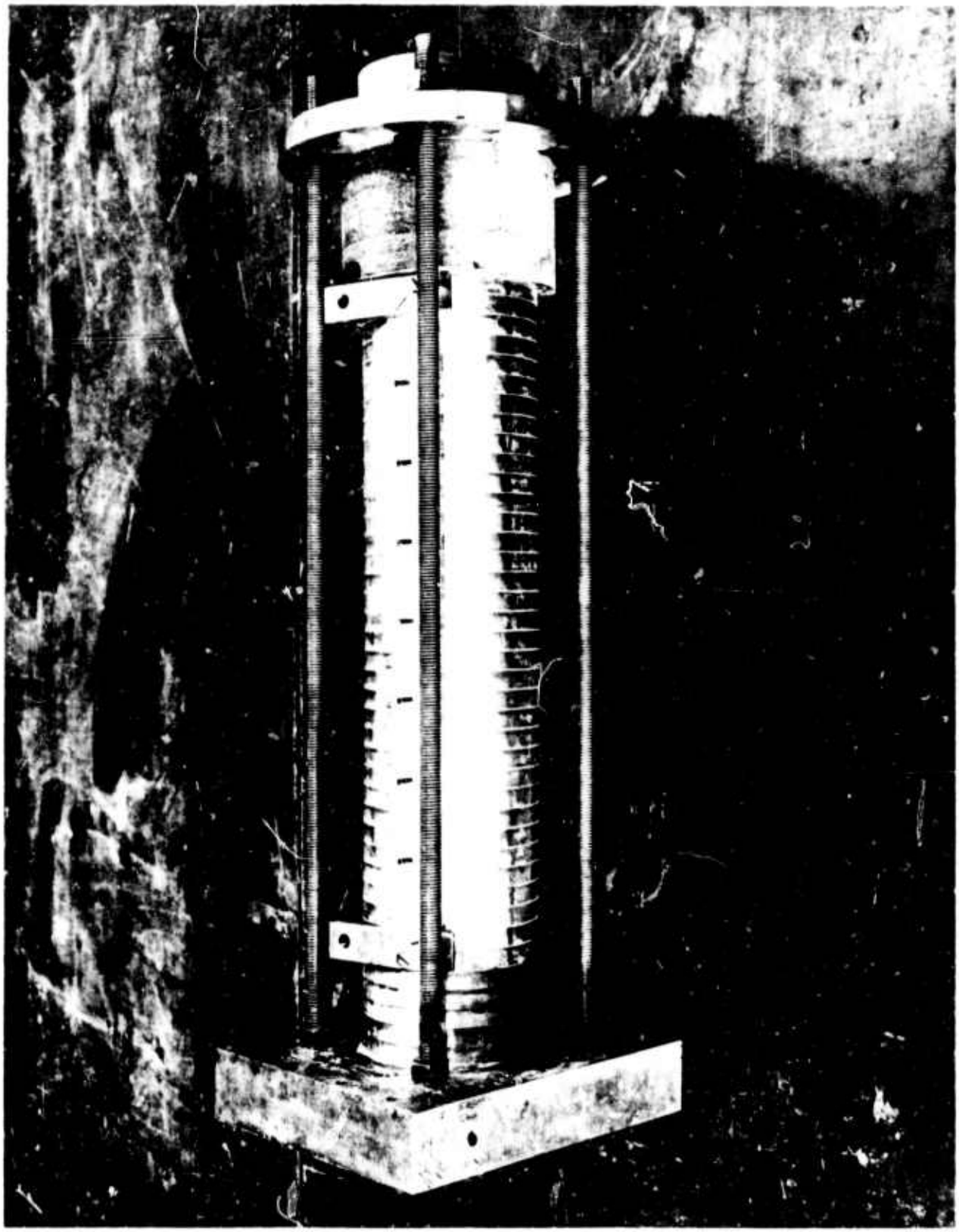

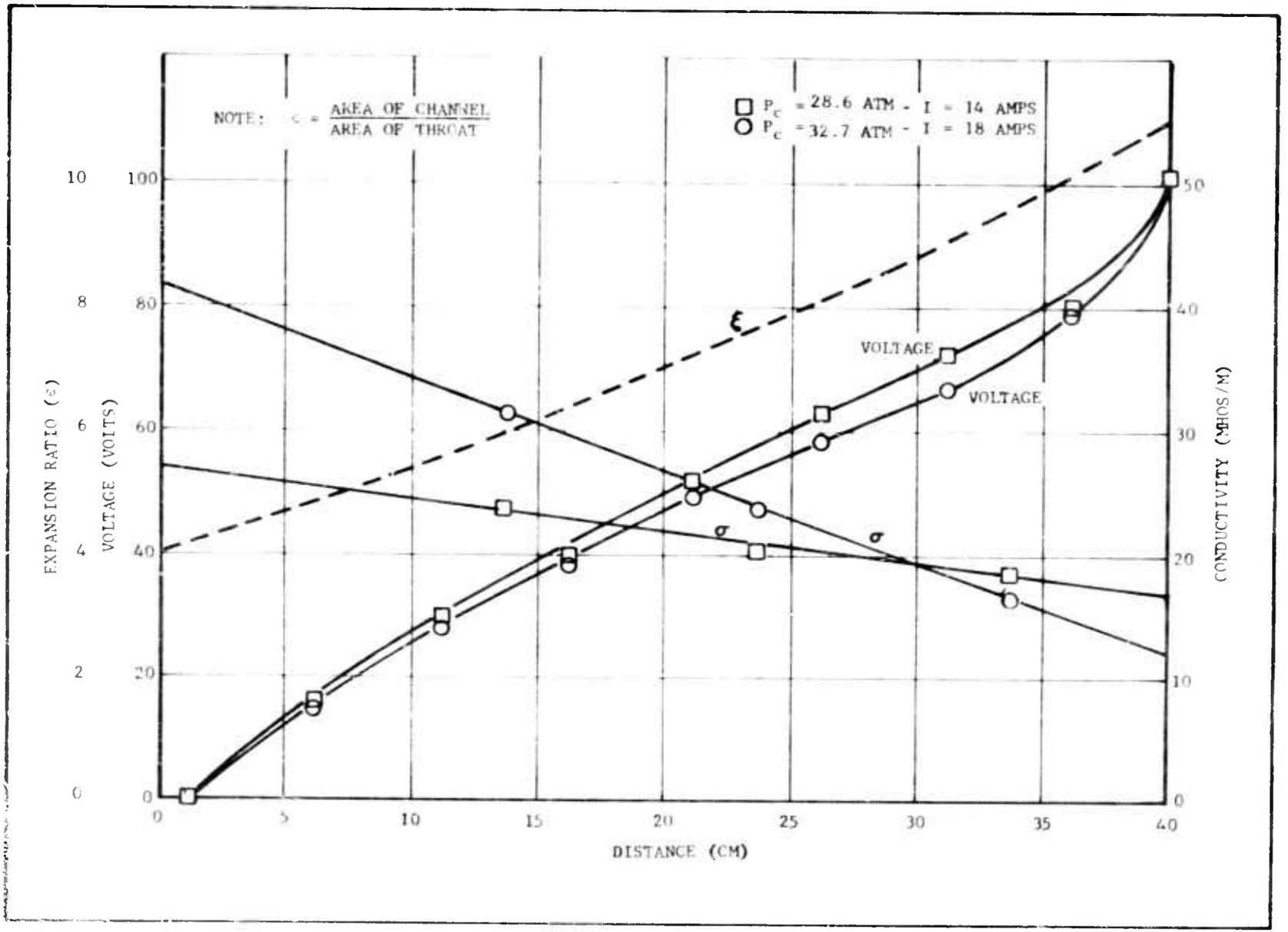

Figure 5-2. Data Plot of Diagnostic Test With Chamber Pressures of 28.6 and 32.7 Atm

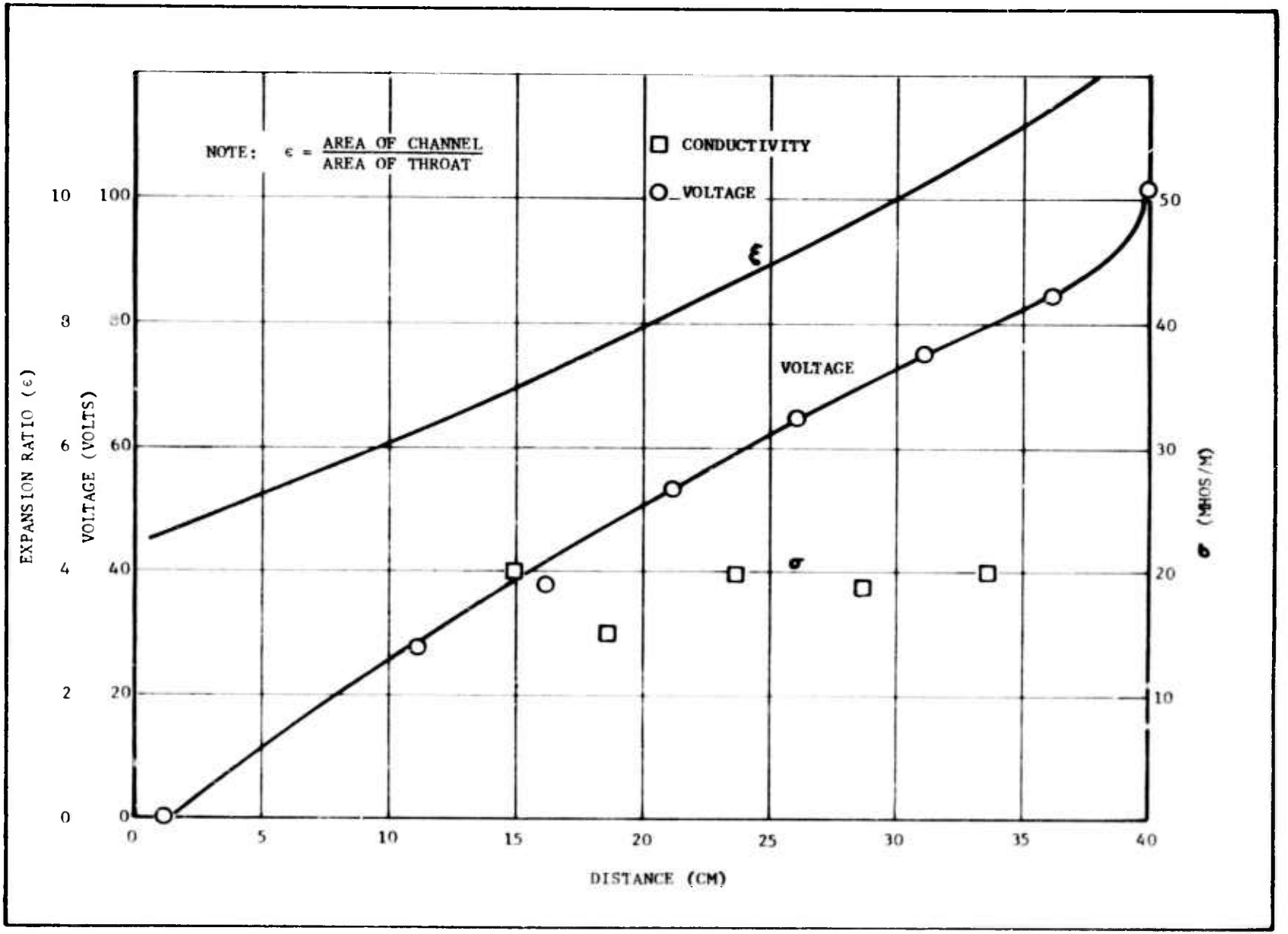

Figure 5-3. Data Plot of Diagnostic Test With Chamber Pressure of 57.8 atm

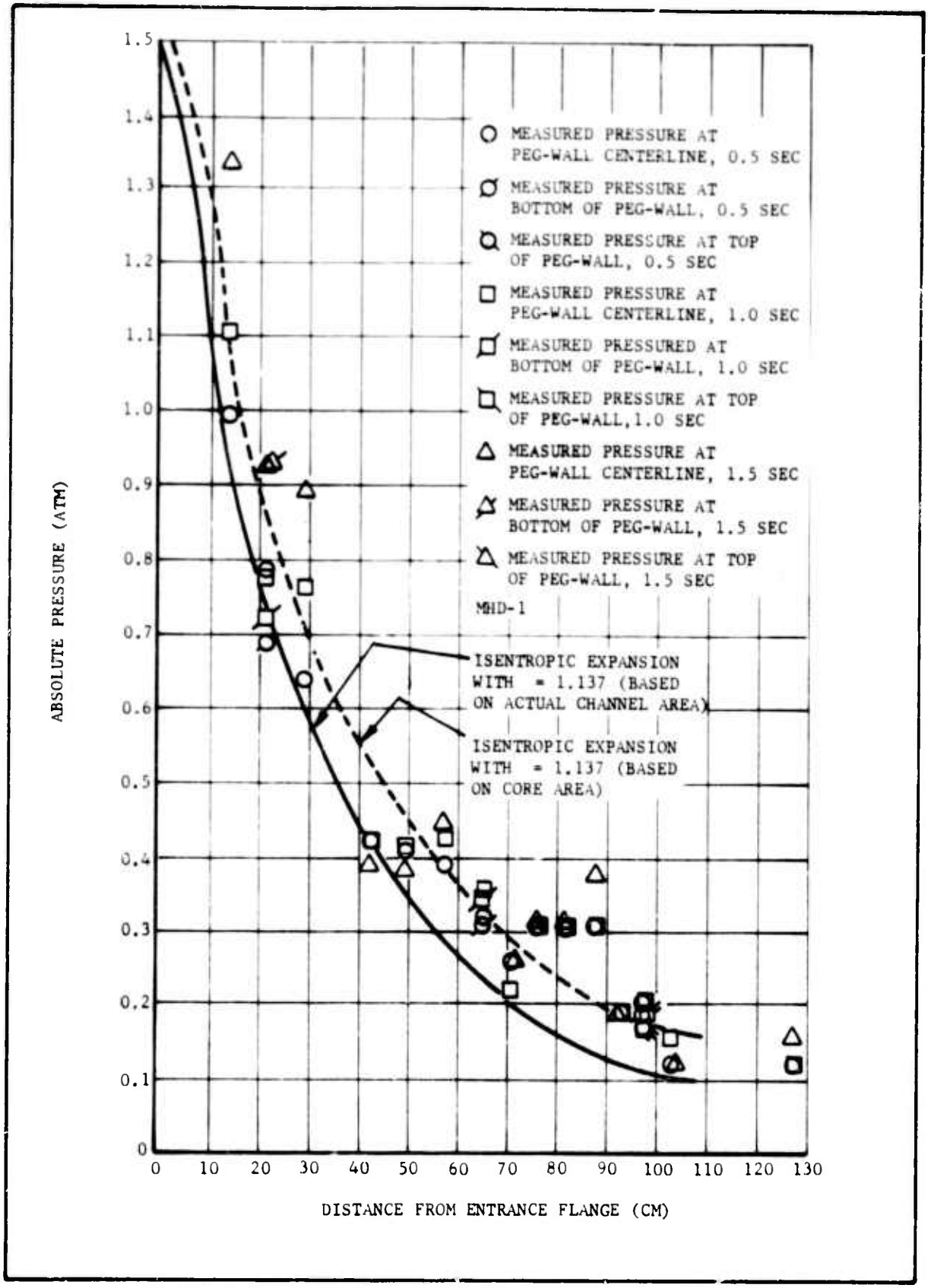

Figure 5-4. Plot of Pressure Versus Distance for Power Channel Test MHD-1.

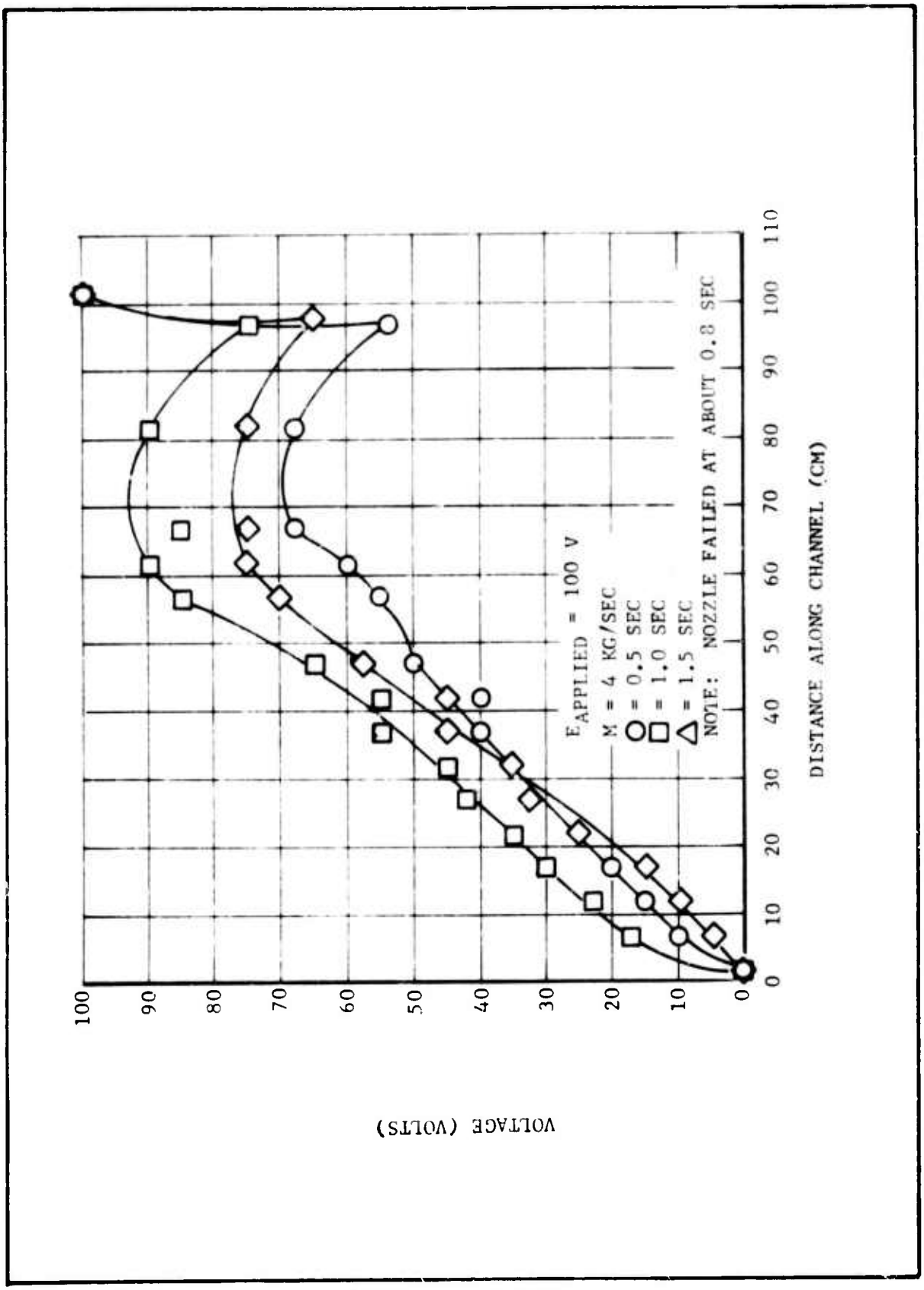

Figure 5-5. Plot of Voltage vs Distance

power channel while the voltages were taken from the cathode (upper electrode) wall. Note that significant pressure anomalies occurred in the last half of the channel.

When the VQW fuel became available, two conductivity tests were run again using the diagnostics channel. This data yields conductivities of about 40-50 mhos/meter at the planned channel operating conditions. Figure 5-6 shows a plot of conductivity for both the original fuel and the VQW.

B. Subscale Diffuser Tests

Prior to fabricating the full scale diffuser, a subscale model was tested on the diagnostic channel. This was felt to be necessary since certain operating conditions require pressure recovery from 0.14 atm. Figure 5-7 is a photograph of the subscale diffuser attached to the diagnostic channel which was fired with a exit-throat area ratio of 50 resulting in 0.17 atm at the diffuser entrance. The diffuser was scaled from the large system by utilizing a 10 diameter constant area supersonic section, followed by a 5 diameter (entrance) expanding subsonic section. Pressure measurements were made each 15 cm of diffuser length. These were taken by attaching 1/8" Teflon tubing between the ports shown in Figure 5-7 and absolute pressure gauges. These gauges were then photographed at 64 frames/second. Figure 5-8 shows a typical plot of pressure versus distance for 3 times during one run. The diffuser worked well, as is noted from Figure 5-8. Essentially the same parameters were noted in the full scale diffuser.

C. Channel Power Tests

Two conductivity tests and two power tests were run with the 2% KNO_3 fuel before the channel was damaged. In the first power test (MHD-2),

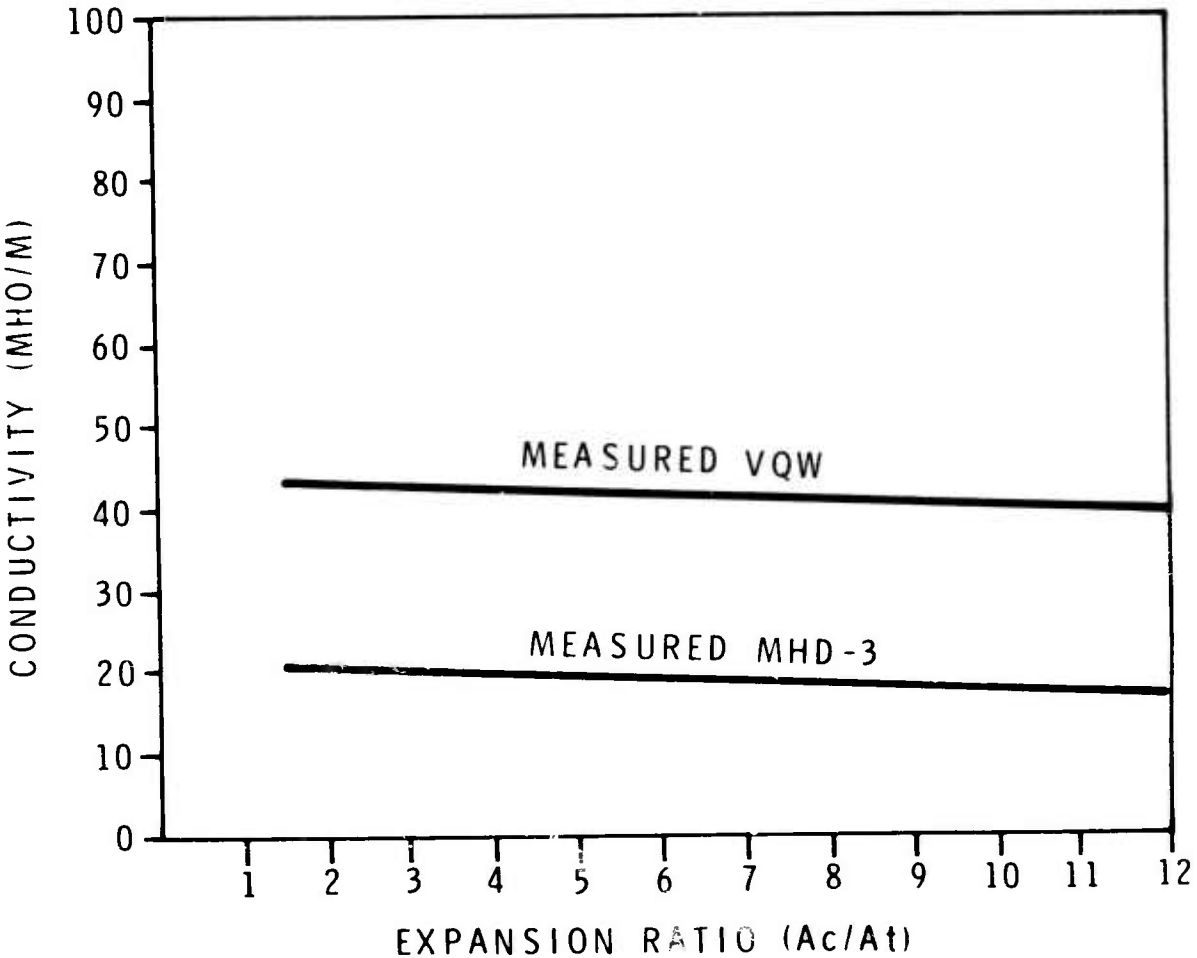

Figure 5-6. Comparison of Measured Conductivity of VQW and Original 2% KNO_3 fuel

Figure 5-7. Photograph of Scale Diffuser Attached to Diagnostic Channel

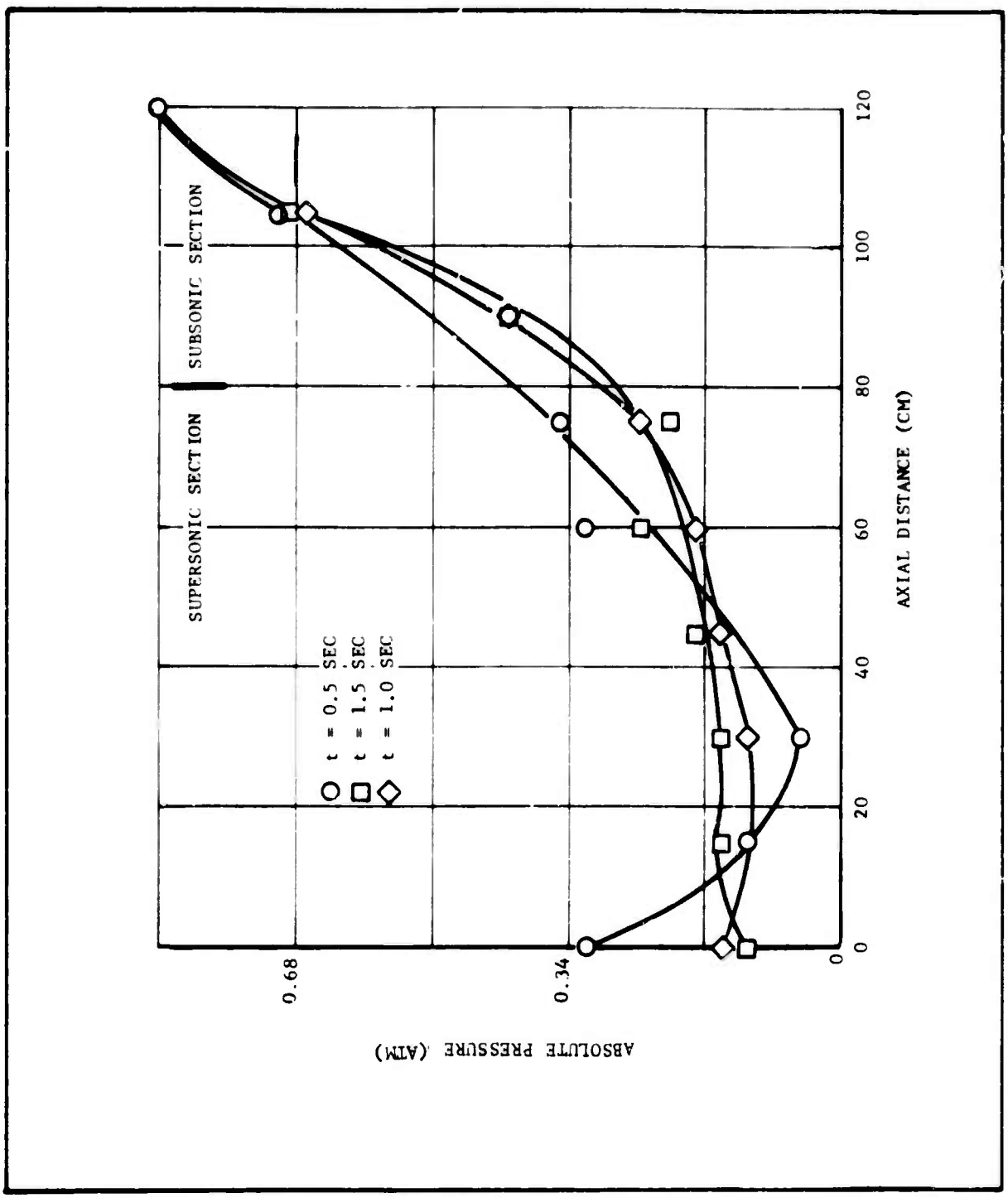

Figure 5-8. Plot of Pressure vs Axial Distance in Diffuser at Three Times

the channel was tested at a 1.8 second burn time using a 4.2Ω load. Stall had been predicted at load values in excess of 5.5 ohms, as shown in Figure 5-9.

Figure 5-10 shows a cathode voltage and centerline pressure data from MHD-2. As can be seen, a maximum of 1800 volts was reached at a point 65 cm from the channel inlet. This then decreased to 900 volts at the channel exit. The data again shows the pressure anomalies near the 65 cm position that were noted in MHD-1.

The second power test (MHD-3) was a 4 second burn using a 2Ω load for about 2.5 seconds and a short circuit for the remaining 1.5 seconds of the burn. Figure 5-11 shows a plot of the voltage distribution vs generator position for the 2Ω load portion of MHD-3. The developed load voltage is 1400 volts which corresponds to 1 MW of power delivered to the load. Figure 5-12 shows the voltage distribution after the load had been short circuited. Figure 5-13 shows the measured pressure distribution for both load conditions. As can be seen, the channel pressure and voltage distribution still show anomalies in the 65-90 cm region of the channel but the behavior was somewhat closer to that expected than was the 4.2Ω firing.

After a careful review of the data from the 2 power tests, it was concluded that the voltage and pressure variations observed after the 65 cm position were probably due to the gas conductivity being well below the channel design value of 33 mho/m. This was in accord with the results of firing MHD-1 at 0.5 sec., which showed an entrance conductivity of 16 mho/m. It was decided that another grain should be fired to remeasure the gas conductivity.

This conductivity firing (MHD-4) was normal for about 2.5 sec., after

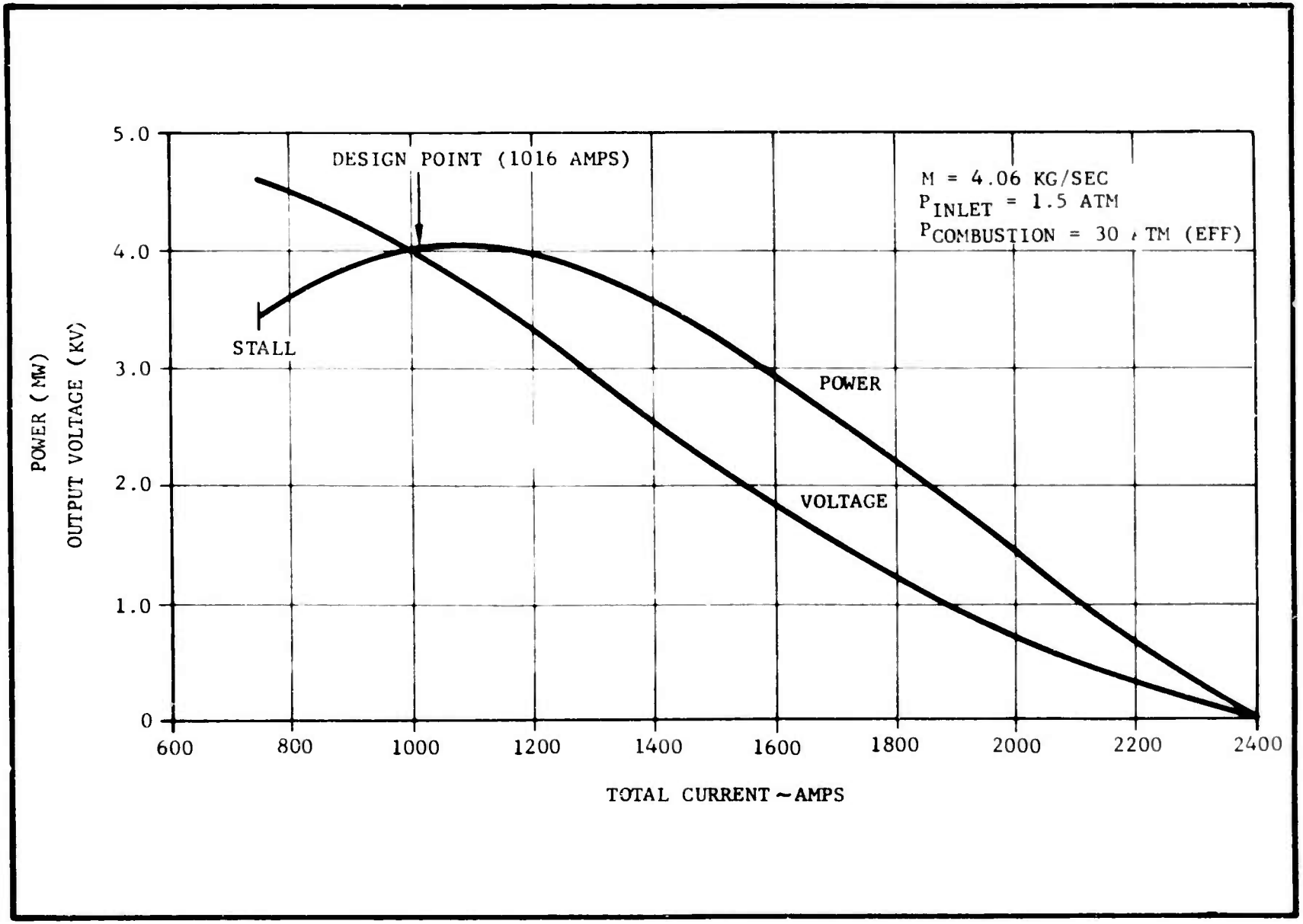

Figure 5-9. Nominal Predicted Electrical Characteristics Using 2 Percent KNO_3 Propellant

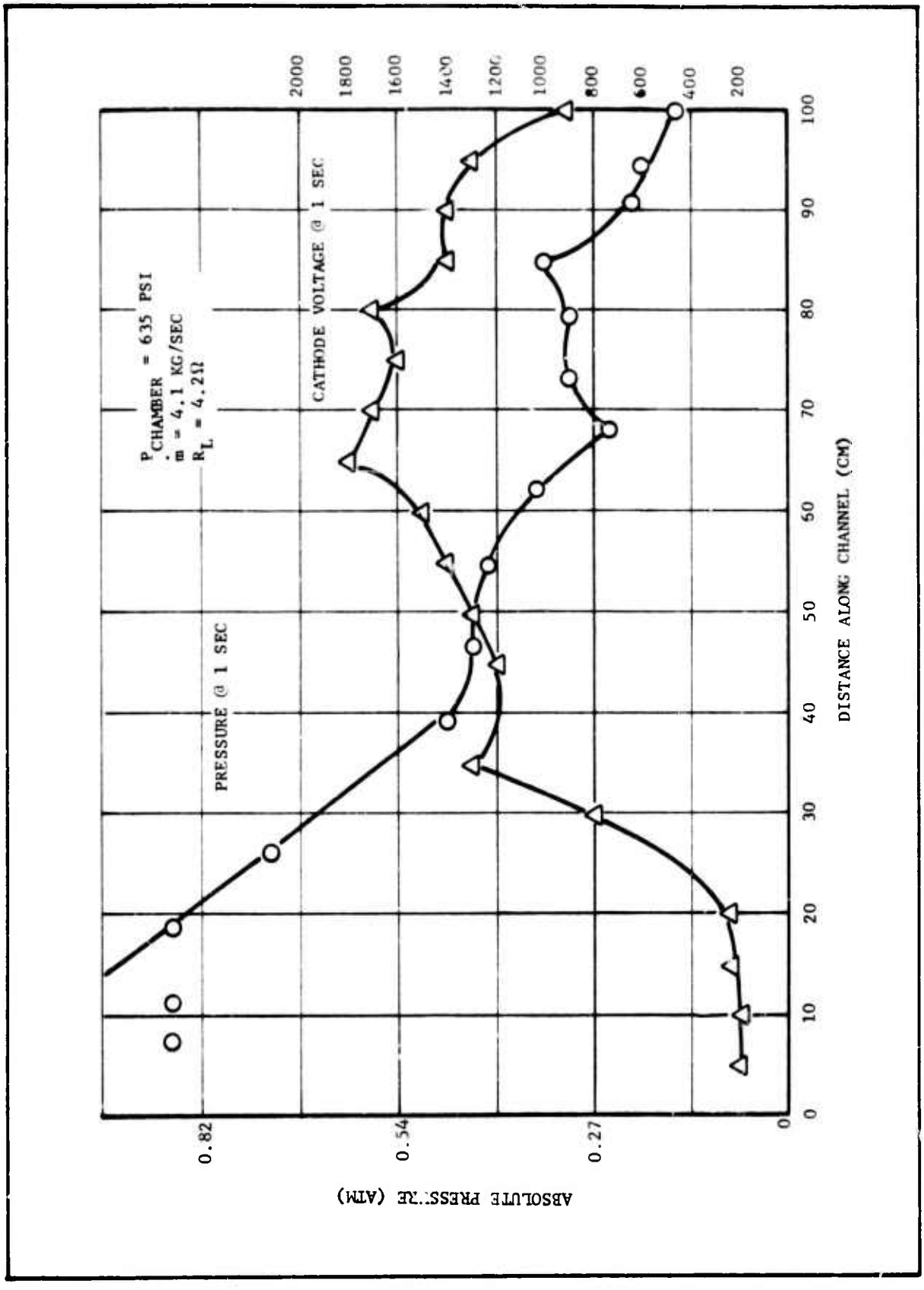

Figure 5-10. Plot of Pressure and Cathode Voltage MHD-2

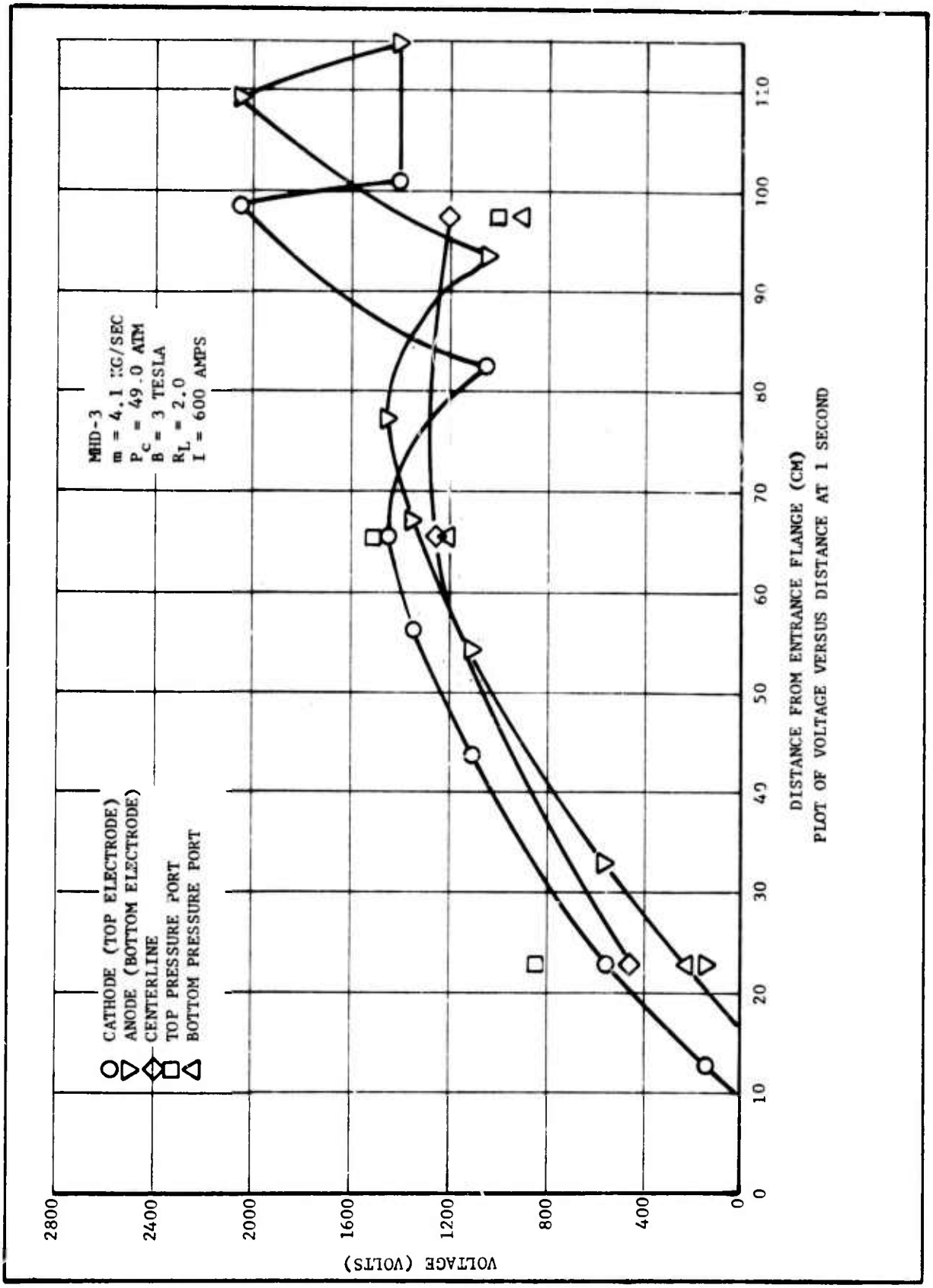

Figure 5-11. Voltage Distribution as a Function of Position for 2Ω Load

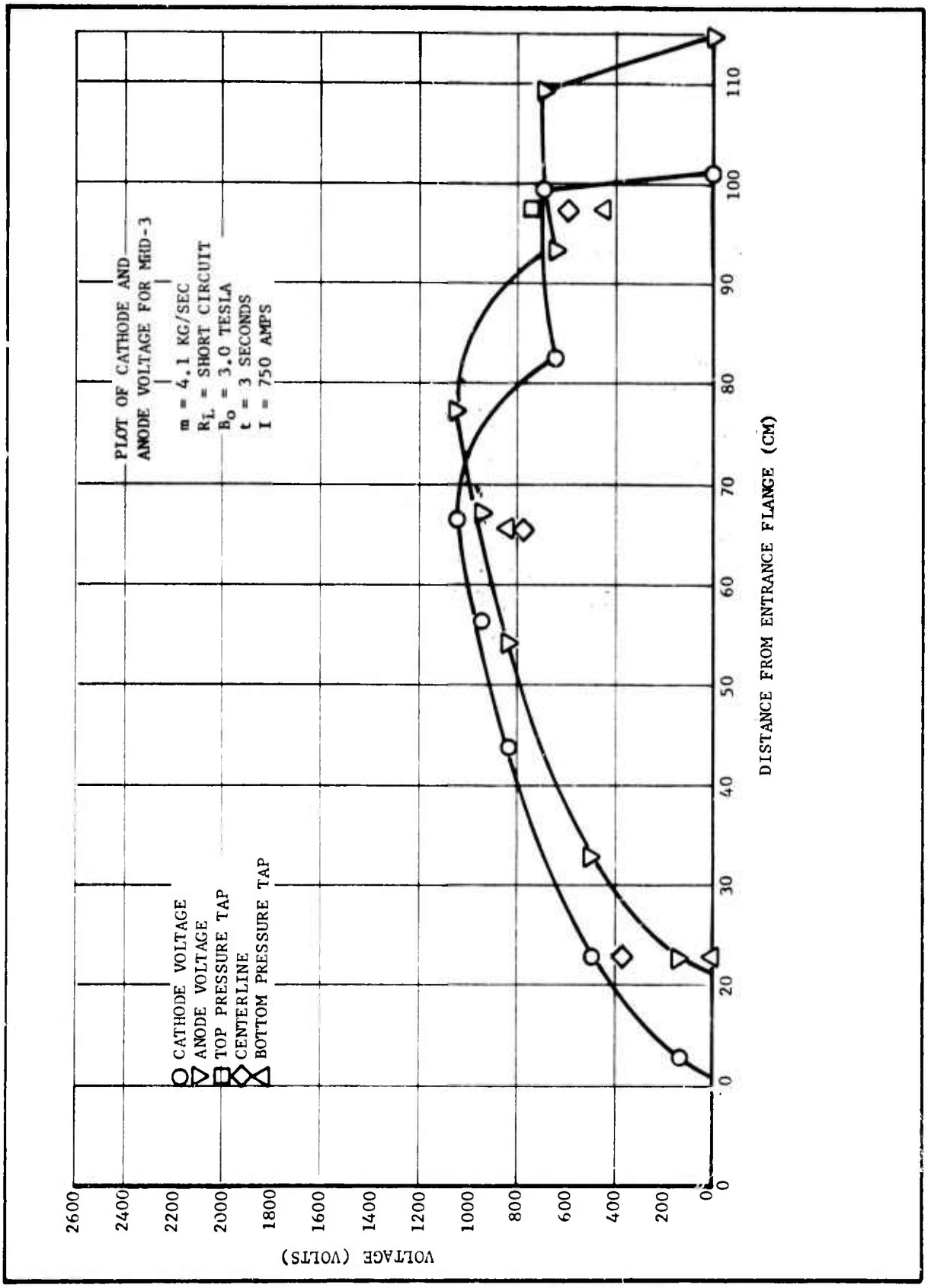

Figure 5-12. Voltage Distribution as a Function of Position for Short Circuit

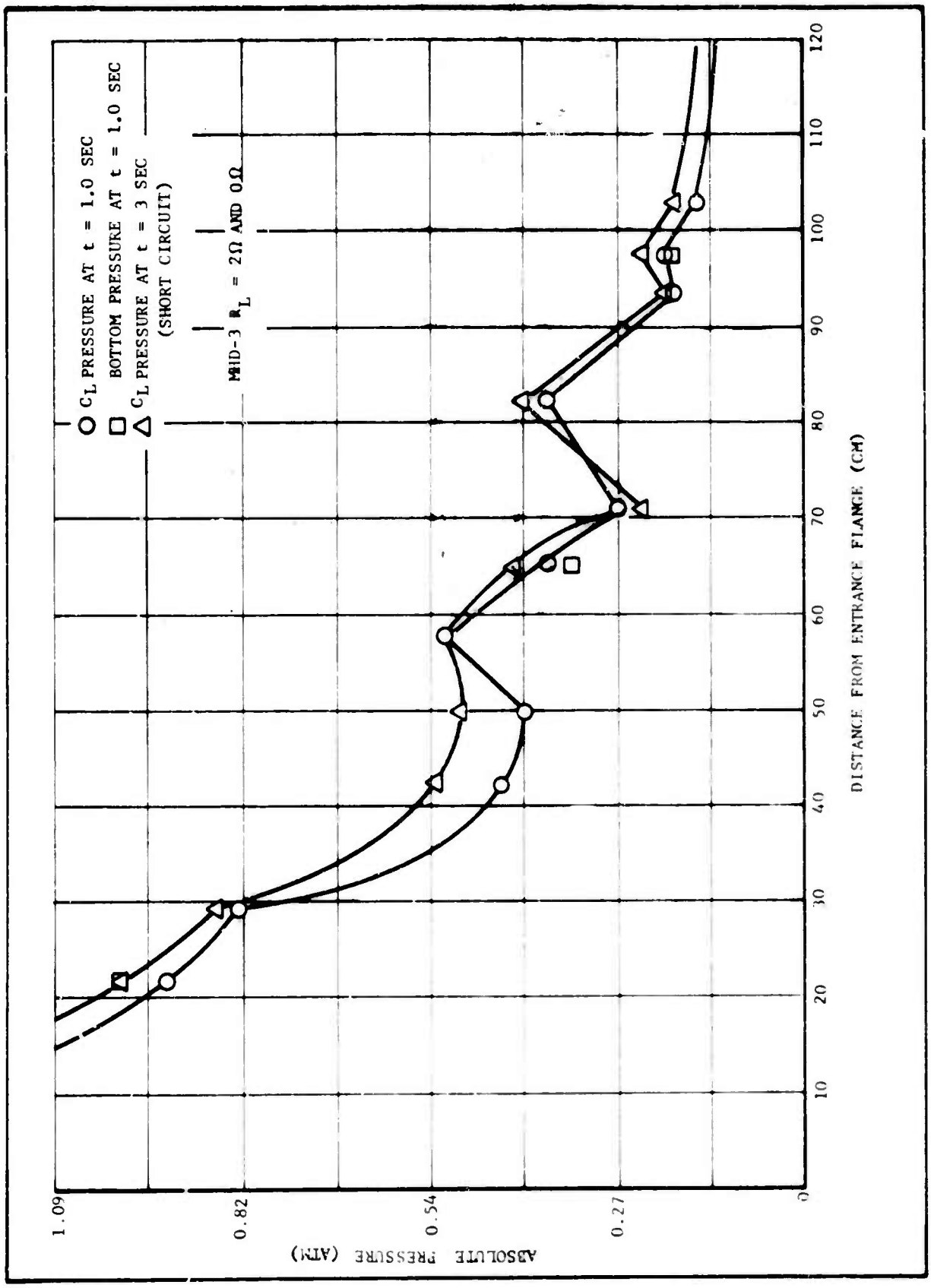

Figure 5-13. Pressure Distribution as a Function of Position

which an apparent failure of the nozzle exit cone caused the exhaust gas to burn through the side of the nozzle retention section in the combustor. The hot gases were also directed against the entrance flange of the channel, causing some damage. In addition, the channel wiring was destroyed and the insulation on the magnet coils was scorched by the hot exhaust gas. Some very minor erosion of one magnet pole piece also took place.

An examination of the nozzle parts indicated that the rear ring in the nozzle assembly may have cracked due to pressure and thermal stress. After cracking, pieces of the ring probably fell into the exhaust stream leaving the metal retention section unprotected. A post-firing examination showed that part of the failed ring had, in fact, moved into the exhaust stream deflecting the gas against the unprotected metal wall.

The main reason for failure of the last ring appears to have been insufficient wall thickness. This is supported by the fact that cracking of the last ring had been observed in other nozzles after firing, whereas the thicker rings in the upstream parts of the nozzle rarely showed cracks. The limitation on the wall thickness at the last ring was imposed by the need to make the nozzle retention section smaller than the bolt pattern on the channel entrance.

Figure 5-14 shows the voltage and conductivity data taken during MHD-4. The conductivity at the channel entrance is the same as was measured in MHD-1 and is substantially less than the 33 mho/m entrance value used in designing the channel.

Since it was apparent that the conductivity of the 2% KNO_3 fuel was much too low for the channel to operate as designed, a new fuel was required. This fuel (VQW) and its attendant conductivity measurements

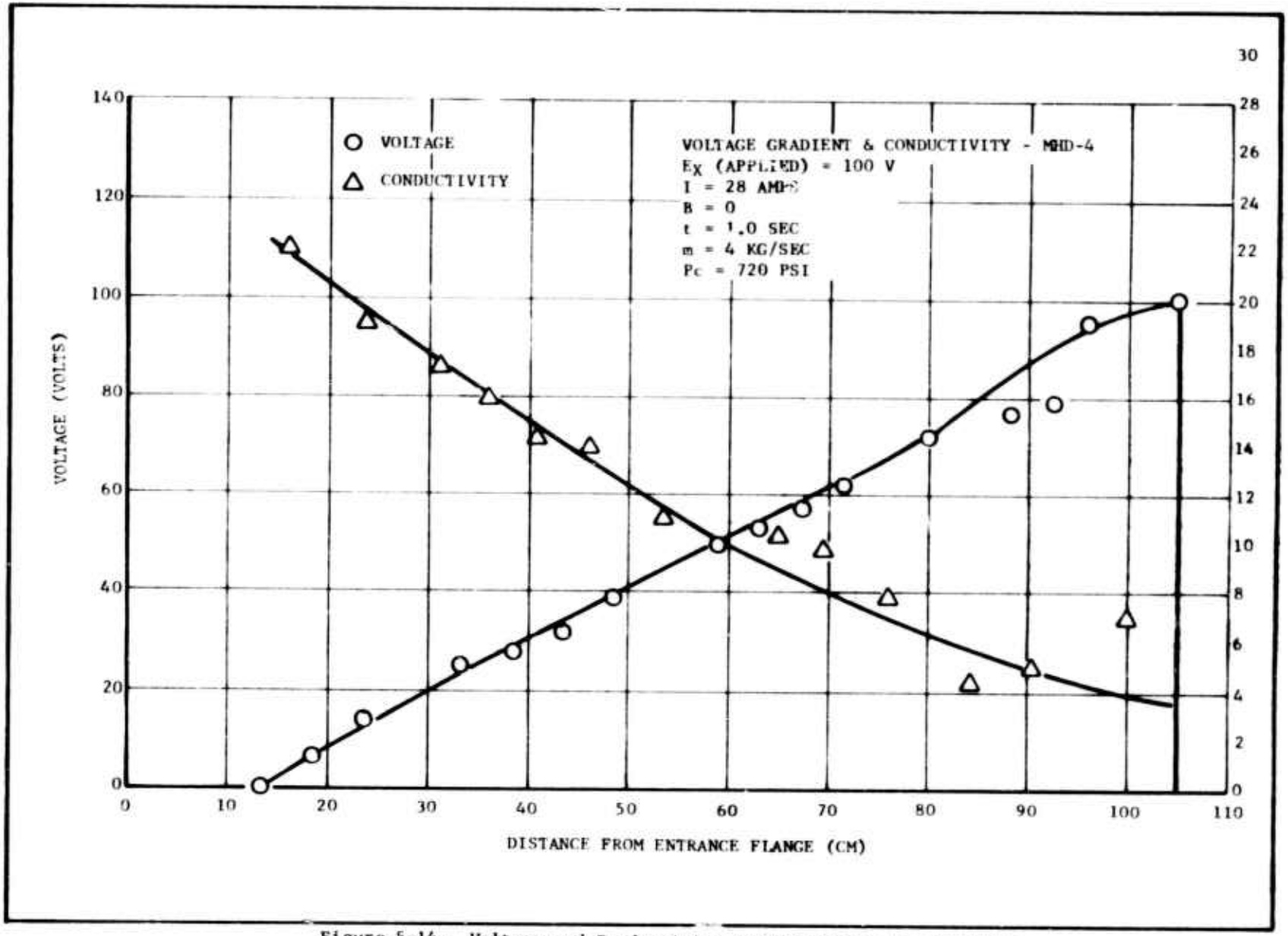

Figure 5-14. Voltage and Conductivity Distributions as a Function of Generator Position (MHD-4)

have been discussed previously. It was found after this fuel had been cast into full size grains that the burning rate was much lower than had been expected. This restricted the mass flow rate to 3.1 kg/sec in the grain geometry in which the fuel had been cast. This mass flow rate is compared to a design value of 4.1 kg/sec in the channel. The restriction in mass flow rate because of burn rate can be reasoned by referring back to Section III where it was shown that mass flow rate is determined by:

$$\dot{m} = \rho r A_s \quad .$$

where the density, ρ, and surface area, A_s, are fixed by the fuel composition and grain geometry, respectively.

Five power tests were made with the VQW fuel in spite of the reduced mass flow rate. The load resistance was varied from 3.9Ω to 8Ω. The first power test (MHD-5) resulted in an extremely low pressure burn due to the low burning rate and produced essentially no power.

Figure 5-15 shows a plot of voltage versus axial distance for the four remaining tests. It can be seen that the experimental data at 3.2 kg/sec generally follows the predicted curve at 4.1 kg/sec for the first 60 cm of channel length. After this point, the voltage curve is flat and no more power is being produced.

It should be noted that the power level shown is taken at 0.6 seconds for all tests except MHD-9. Tests MHD-6, 7 and 8 dropped to about one-half the power after this time. Data suggests that this occurred after a series of shocks moved out of the diffuser and into the channel. This did not occur on MHD-9, which remained at its original power level for the entire test.

Figure 5-15. Plot of Predicted Performance at 4.1 kg/sec Versus Experimental Performance at 3.2 kg/sec Mass Flow Rate (VQW)

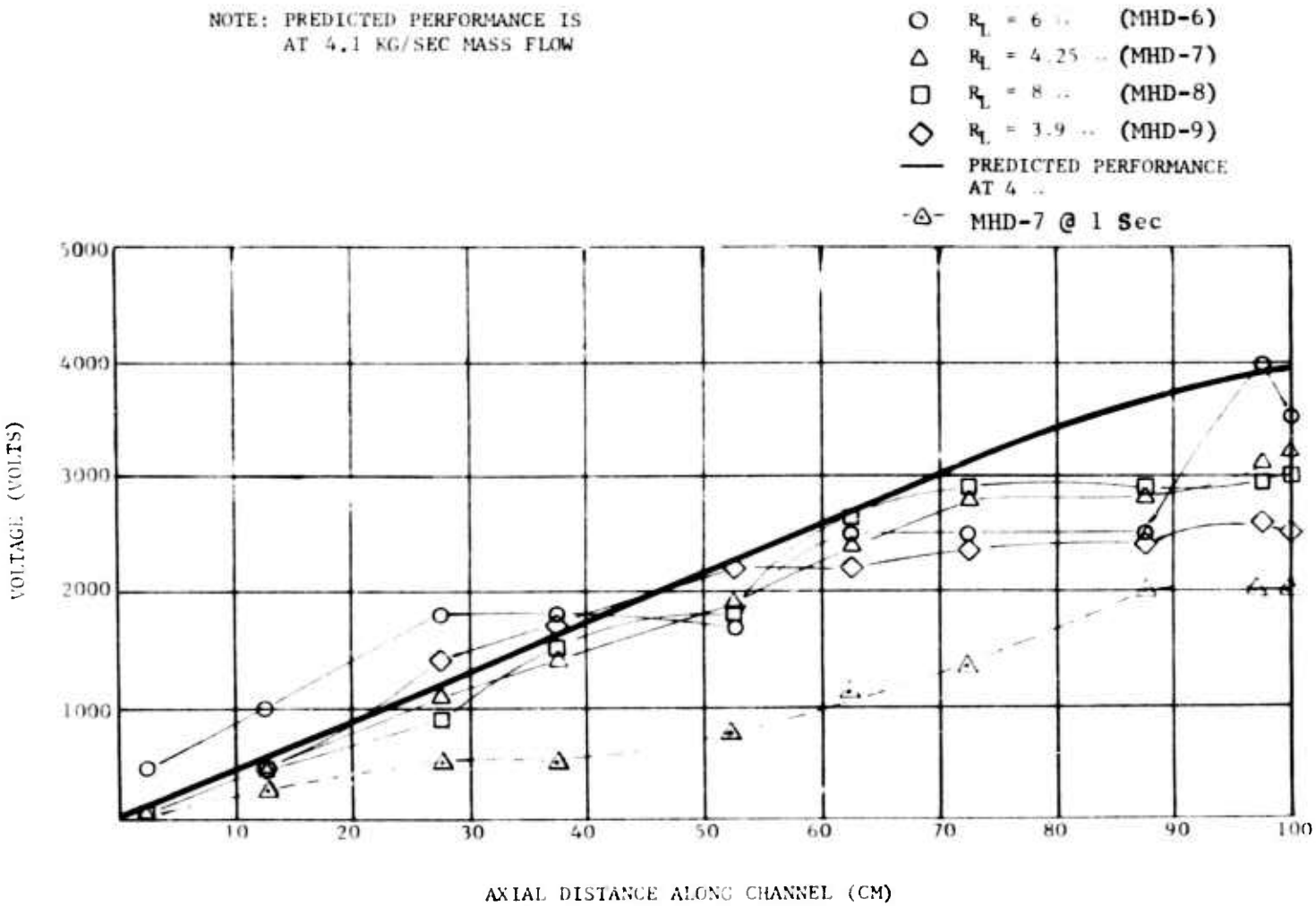

Current data taken in the diagonal wires indicates areas of extremely high current (> 150 amps) occurred at various locations in the downstream end of the channel. It is not clear what caused this, but it is believed that this occurred from shocks inside the channel. It is further believed that these shocks occurred because the diffuser was not able to recover the pressure at the reduced mass flow rate. It should be remembered that the diffuser is required to recover from about 0.17 atm with full mass flow. Table 5-I shows the diagonal current as a function of position and time on MHD-9. During any test in excess of 2 seconds, the wires used to make the diagonal connections burned up, again suggesting the locally high current value. It should be noted that this never occurred on any tests with the low conductivity fuel, even though they burned for up to 4 seconds.

Plans were made to increase the surface area on the remaining five grains of VQW to raise the mass flow rate to the design value of 4.1 kg/sec. Present funding did not allow this, however.

Test MHD-7 produced 2.4 megawatts during the first 0.6 seconds for an "efficiency" of 0.74 megawatts per kg/sec of mass flow and a power density of 80 MW/m^3.

TABLE 5-I

DIAGONAL WIRE CURRENT FOR MID-9

X(Dist. from Ent. Flange, cm)		14.25	19.17	24.1	33.9	43.8	53.6	63.4	73.3	83.1	93.0	102.8	107.7	130.0
	Time (sec)	I_1 (amp)	I_2 (amp)	I_3 (amp)	I_4 (amp)	I_5 (amp)	I_6 (amp)	I_7 (amp)	I_8 (amp)	I_9 (amp)	I_{10} (amp)	I_{11} (amp)	I_{12} (amp)	P (Atm Abs)
	0.04									143.0				
	0.18									> 150.0				
	0.25	0	2.9	2.9	2.9	0	0	0	0	> 150.0	0	0		
	0.32	2.9	7.1	5.7	7.1	0	11.4	2.9	2.9	> 150.0	0	0	0	0.721
	0.39	2.9	14.3	5.7	7.1	0	40.0	2.9	4.3	> 150.0	0	0	0	0.721
	0.46	2.9	20.0	5.7	7.1	0	62.9	2.9	7.1	> 150.0	0	0	0	0.687
	0.53	2.9	28.6	10.0	10.0	0	65.7	2.9	15.7	> 150.0	0	0	0	0.68
	0.56	2.9	40.0	11.4	11.4	0	71.4	2.9	17.1	> 150.0	0	0	0	0.687
	0.60	2.9	40.0	11.4	11.4	0	--	2.9	25.7	> 150.0	0	0	0	0.680
	0.67	2.9	41.4	11.4	11.4	17.1	0	5.7	42.9	> 150.0	--	2.9	0	0.680
	0.70	7.1	41.4	15.7	14.3	17.1	100.0	7.1	42.9	> 150.0	--	2.9	0	0.646
	0.74	7.1	45.7	15.7	14.3	17.1	150.0	7.1	38.6	> 150.0	--	4.3	0	0.565
	0.76	7.1	45.7	15.7	17.1	17.1	142.9	7.1	38.6	> 150.0	--	4.3	0	0.565
	0.81	7.1	51.4	15.7	17.1	17.1	85.7	7.1	28.6	> 150.0	--	7.1	0	0.565
	0.85	7.1	48.6	15.7	17.1	17.1	91.4	7.1	25.7	> 150.0	0	8.6	0	0.565
	0.88	7.1	42.9	15.7	17.1	28.6	104.3	7.1	25.7	> 150.0	--	8.6	0	0.565
	0.92	7.1	40.0	15.7	17.1	28.6	128.6	7.1	25.7	> 150.0	--	8.6	0	0.544
	0.94	7.1	37.1	15.7	17.1	42.9	142.9	7.1	25.7	> 150.0	0	8.6	0	0.544
	0.97	7.1	31.4	15.7	17.1	57.1	> 150.0	7.1	25.7	> 150.0	--	8.6	0	0.544
	1.00	7.1	30.0	15.7	17.1	> 150.0	142.9	5.7	22.9	> 150.0	--	7.1	0	0.531
	1.01	7.1	28.6	15.7	15.7	> 150.0	142.9	5.7	20.0	> 150.0	--	7.1	0	0.531
	1.04	7.1	28.6	15.7	15.7	> 150.0	134.3	5.7	20.0	> 150.0	5.7	5.7	0	0.517
	1.06	7.1	25.7	15.7	15.7	> 150.0	122.9	4.3	17.1	> 150.0	8.6	5.7	0	0.497
	1.08	7.1	25.7	15.7	15.7	> 150.0	102.9	4.3	17.1	> 150.0	14.3	5.7	0	0.497
	1.11	7.1	22.9	15.7	15.7	142.9	85.7	4.3	15.7	> 150.0	47.1	5.7	0	0.510
	1.14	7.1	21.4	15.7	15.7	102.9	74.3	4.3	15.7	> 150.0	0	4.3	0	0.490
	1.15	7.1	21.4	15.7	15.7	100.0	68.6	4.3	14.3	128.6	8.6	4.3	0	0.490
	1.18	7.1	17.1	15.7	15.7	150.0	57.1	4.3	14.3	85.7	60.0	4.3	0	0.476
	1.22	7.1	17.1	15.7	15.7	150.0	45.7	2.9	11.4	45.7	45.7	2.9	0	0.456
	1.24	7.1	17.1	15.7	15.7	150.0	42.9	2.9	10.0	42.9	42.9	2.9	0	0.456
	1.26	7.1	17.1	15.7	15.7	150.0	34.3	2.9	8.6	14.3	97.1	2.9	0	0.442
	1.29	7.1	17.1	15.7	15.7	150.0	28.6	2.9	7.1	0	105.7	2.9	0	0.442
	1.36	7.1	14.3	15.7	15.7	150.0	48.6	2.9	5.7	0	74.3	2.9	0	0.422
	1.43	7.1	14.3	14.3	14.3	150.0	42.9	1.4	5.7	0	45.7	1.4	0	0.361
	1.50	7.1	14.3	14.3	14.3	150.0	34.3	1.4	4.3	0	21.4	1.4	0	0.361
	1.57	7.1	14.3	14.3	14.3	150.0	22.9	1.4	4.3	0	5.7	1.4	0	0.361
	1.64	7.1	14.3	14.3	14.3	150.0	14.3	1.4	2.9	0	--	0	0	0.361

TABLE 5-I (Cont'd)

X(Dist. from Ent. Flange, cm)		14.25	19.17	24.1	33.9	43.8	53.6	63.4	73.3	83.1	93.0	102.8	107.7	130.0
	Time (sec)	I_1 (amp)	I_2 (amp)	I_3 (amp)	I_4 (amp)	I_5 (amp)	I_6 (amp)	I_7 (amp)	I_8 (amp)	I_9 (amp)	I_{10} (amp)	I_{11} (amp)	I_{12} (amp)	P (Atm Abs)
	1.71	7.1	14.3	14.3	14.3	150.0	11.4	1.4	1.4	0	--	0	0	0.320
	1.78	7.1	14.3	11.4	11.4	150.0	48.6	1.4	1.4	0	2.9	0	0	0.320
	1.81	7.1	14.3	11.4	10.0	150.0	54.3	1.4	1.4	0	0	0	0	0.313
	1.85	7.1	14.3	11.4	8.6	150.0	48.6	1.4	1.4	0	--	0	0	0.286
	1.92	7.1	14.3	11.4	7.1	150.0	41.4	1.4	1.4	0	--	0	0	0.265
	1.99	7.1	14.3	8.6	7.1	150.0	28.6	1.4	1.4	0	--	0	0	0.252
	2.06	7.1	14.3	8.6	7.1	150.0	20.0	1.4	1.4	0	--	0	0	0.252
	2.10	7.1	14.3	8.6	10.0	150.0	28.6	1.4	1.4	0	0	0	0	0.252
	2.13	7.1	14.3	8.6	10.0	150.0	71.4	1.4	1.4	0	0	0	0	0.252
	2.15	7.1	14.3	7.1	10.0	150.0	150.0	1.4	2.9	0	0	0	0	0.252
	2.17	7.1	14.3	7.1	10.0	150.0	142.9	1.4	2.9	0	0	0	0	0.252
	2.20	7.1	14.3	7.1	10.0	14.3	142.9	1.4	2.9	0	--	0	0	0.252
	2.21	7.1	14.3	7.1	10.0	14.3	150.0	1.4	2.9	0	--	0	0	0.252
	2.26	7.1	14.3	7.1	11.4	150.0	128.6	0	1.4	0	--	0	0	0.252
	2.29	7.1	14.3	7.1	11.4	150.0	142.9	0	1.4	0	--	0	0	0.252
	2.33	7.1	17.1	4.3	11.4	0	150.0	0	1.4	0	--	0	0	0.252
	2.36	7.1	17.1	4.3	11.4	0	135.7	0	1.4	0	--	0	0	0.252
	2.40	7.1	25.7	4.3	11.4	150.0	125.7	1.4	1.4	0	--	0	0	0.286
	2.47	7.1	31.4	4.3	11.4	150.0	97.1	1.4	1.4	14.3	--	0	0	0.286
	2.54	7.1	40.0	4.3	10.0	> 150.0	82.9	1.4	1.4	97.1	--	1.4	0	0.286
	2.56	7.1	40.0	4.3	10.0	150.0	74.3	1.4	1.4	85.7	--	1.4	0	0.299
	2.58	7.1	40.0	4.3	10.0	150.0	75.7	1.4	1.4	150.0	--	1.4	0	0.299
	2.61	7.1	37.1	4.3	10.0	150.0	74.3	1.4	1.4	131.4	--	1.4	0	0.299
	2.68	7.1	28.6	4.3	10.0	150.0	64.3	2.9	1.4	71.4	--	1.4	0	0.320
	2.75	7.1	10.0	2.9	5.7	150.0	51.4	2.9	1.4	40.0	--	0	114.3	0.320
	2.82	7.1	14.3	4.3	10.0	150.0	34.3	2.9	1.4	14.3	--	1.4	> 150.0	0.320
	2.89	7.1	10.0	2.9	5.7	150.0	22.9	2.9	1.4	7.1	--	0	> 150.0	0.320
	2.96	7.1	7.1	2.9	5.7	150.0	14.3	1.4	1.4	7.1	0	0	> 150.0	0.320
	3.03	7.1	5.7	1.4	4.3	150.0	11.4	1.4	0	7.1	0	0	> 150.0	0.320
	3.10	?	4.3	1.4	2.9	150.0	5.7	1.4	0	7.1	0	0	> 150.0	0.320
	3.17	?	2.9	1.4	2.9	142.9	4.3	1.4	1.4	5.7	2.9	0	> 150.0	0.320
	3.24	?	0	0	1.4	121.4	1.4	1.4	1.4	2.9	2.9	0	> 150.0	0.320
	3.31	?	0	0	1.4	97.1	0	1.4	1.4	0	1.4	0	142.9	0.320
	3.38	?	0	0	1.4	78.5	0	1.4	1.4	0	1.4	0	114.3	0.320
	3.45	?	0	0	1.4	60.0	0	1.4	1.4	0	1.4	0	85.7	0.320
	3.51	?	0	0	0	50.0	0	0	0	0	0	0	60.0	0.320
	3.75	?	0	0	0	0	0	0	0	0	0	0	0	0.320

SECTION VI

CONCLUSIONS

The goal of the deflagrating explosive investigation was to develop the technical base to allow for the design and construction of lightweight, multimegawatt deflagrating explosive driven MHD generators with a wide range of operating parameters. It cannot be claimed that this program has fully satisfied this goal, but it did produce some very positive steps toward the desired end. As was mentioned at the close of the last section, test MHD-7 produced 2.4 MW during the first 0.6 seconds for a power extraction of 0.74 MW/(kg/s) and a power density of 80 MW/m^3. This is a 19% improvement over the previous maximum power extraction, 0.62 MW/(kg/s) produced on the Viking I program. In addition, the channel proved to be mechanically sound, showing very little erosion after 9 firings with rocket-type propellants which produce a very erosive exhaust stream with a high weight fraction of liquid aluminum oxide.

The channel (and other hardware) were designed to produce 4 MW at a power extraction of 1.0 MW/(kg/s) and a power density of 130 MW/m^3. Unfortunately neither test series really satisfied the conditions assumed in the design of the channel. The 2% KNO_3 propellant only had half the conductivity assumed for the design. The tests with VQW propellant had a mass flow rate about 3/4 of the design value. Thus these tests cannot be considered a complete evaluation of the channel design.

The pressure anomalies noted in the last half of the channel with the KNO_3 fuel and their relationship to the reduced voltage in this same section remain to be explained. Raising the conductivity by the use of VQW fuel brought the voltage profile very close to the predicted value in the first

65 cm of the channel. The last 35 cm still showed no voltage gain and furthermore the whole channel voltage dropped by roughly a factor of 2 after 0.6 second of firing time in 3 of the last 4 firings. It is likely that the flat voltage distribution is related to low mass flow rate, as was suggested in Section V, but with the limited data at hand it is certainly not possible to rule out flow separation or some other problem. The sudden change in performance at 0.6 second is probably related to burn-out of the diagonalizing wires, but again, other problems cannot be completely ruled out

Clearly one of the most immediate needs for future development of solid propellant MHD is to fully characterize the channel that was constructed for this investigation. A program for doing this is suggested in Section VII. This one step would make a considerable contribution to the technical base needed to design and build lightweight solid propellant MHD generators in the 10-20 MW range.

SECTION VII

RECOMMENDATIONS FOR FUTURE DEVELOPMENT OF SOLID PROPELLANT MHD

As was mentioned at the end of Section VI, the first step in the development of C-MHD should be to complete the characterization of the channel used in the present program. This should be done in more depth than simply firing VQW at 4.1 kg/s. Once this has been completed, attention should be given to designing and fabricating a lightweight channel with about the same power output as the present system. After the lightweight channel has been constructed and thoroughly tested with a single pulse combustor, it may be desirable to consider a multipulse combustor with this lightweight channel. The following paragraphs discuss these phases in somewhat more detail.

A. Phase I - Characterization of the Existing Channel

This phase would involve a test sequence of 62 successful firings. Throughout this phase, diagnostics and instrumentation would be developed to the extent possible, as needed. The parameters to be varied to characterize the channel include:

(a) Chamber pressure

(b) Load impedance

(c) Magnetic field level

(d) Fuel variation (ϕ and ΔT)

(e) Electrode trimming resistors

(f) Slant angle

The test matrix would consist of a baseline composed of 24 tests at 8 load conditions with the other parameters set at the design conditions. This diagnostic series of tests would be run first to show any basic

problems in the channel design. Single variations would then be made at selected loads to determine off-design operating characteristics. This places load resistance as the prime independent variable at each condition. The matrix is shown in Table 7-I.

The two additional fuels shown in Table 7-I would be formulated after the baseline tests are run. This would allow the fuels to be designed within the characteristics of the channel. They would also be designed to be compatible with the existing slant wall configuration.

B. Phase II - Lightweight Channel Development

A design would be developed for an MHD generator channel based on the concept of using stacked graphite washers overwrapped with filament epoxy composite. The channel would be designed for a 4 kg/sec flow (~4 Mw power output) and use with the existing magnet. The channel would be designed to operate continuously for 4 sec, at the 4 kg/sec flow rate without external cooling and be capable of continuous operation for 16 seconds. Cooling would be accomplished by forced convection using water for this longer run time.

After the channel has been fabricated, it should be subjected to a complete characterization program with emphasis on determining its wear characteristics.

C. Phase III - Development of Multipulse Combustor

As stated previously, the purpose of this portion of the program would be to develop a combustor-fuel combination for multiple pulse operation. The first task would be to conduct an analytical study of either a multiple wafer design or a multiple shot cartridge system. The results of this study would then be compared to mission requirements since

TABLE 7-I

TEST MATRIX - PHASE I

	Load Resistance							
	0	1Ω	2Ω	3Ω	4Ω	5Ω	6Ω	10Ω
Baseline Tests	3	3	3	3	3	3	3	3
P_c - 650 psi								
B - 3.5 Tesla								
Fuel - 7% $CsNO_3$								
Slant Angle - Existing								
Pressure Variation								
P_c - 500 psi	1				1			1
P_c - 800 psi	1				1			1
B - 3.5 Tesla								
Magnetic Field Variation								
P_c - 650 psi								
B - 2.5 Tesla	1		1		1			1
B - 1.5 Tesla	1		1		1			1
Fuel Variation								
P_c - 650 psi								
B - 3.5 Tesla								
Fuel #2	1	1	1	1	1	1	1	1
Fuel #3	1	1	1	1	1	1	1	1
Slant Angle Variation								
$\varphi = 30°$	1		1		1		1	
$\varphi = 70°$	1		1		1		1	

NOTE: Numbers indicate number of successful tests at that condition.

each has areas of pulse length/power level dominance. One system would then be selected for further development.

A fuel system would be designated using fuel requirement data, such as ignition requirements and burn rate, conductivity, and thermodynamic requirements. A computer study would then be undertaken to provide the basic candidate fuel to be made.

After the combustor design and the fuel had been selected, the combustor could be fabricated and tested. This testing would, of course, include firings with and without the lightweight channel.

In addition to the above channel and combustor development phases, it is assumed that parallel work would be done on a superconducting magnet. This would allow testing of a complete 4 MW lightweight solid propellant generator prior to making a commitment to scaleup.

PART II

DETONATING EXPLOSIVE MHD STUDIES

SECTION VIII

INTRODUCTION

The detonating explosive magnetohydrodynamic (X-MHD) generator was conceived and studied during the early and mid-1960's as a compact source of intense electrical impulses of from 10 microseconds to 1 millisecond duration. This early work was carried out at MHD Research, Incorporated and at Hercules Incorporated, Bacchus Works, Utah.[1-5] Peak power output of 280 megawatts and energy output of 25 kilojoules were attained at Hercules[5] using a sheet of 0.45 kilogram of Composition C-4 detonated by a plane wave generator and seeded on the surface with cesium picrate. These experiments were carried out with an X-MHD channel of cross section dimensions 0.20-0.15 meters in a 2.8T magnetic field. The channel was evacuated to a pressure of approximately 1.3×10^3 newton/m^2 prior to detonation of the explosive. The performance corresponds to 1.5% conversion of explosive chemical energy to electrical output. The present program was conducted to improve X-MHD conversion efficiency as well as study fundamental X-MHD processes under controlled conditions.

For efficient and practical operation of the X-MHD, two factors become of prime importance and are interrelated. First, the conversion of explosive chemical energy to electrical output should be maximized in order to minimize the amount of explosive as well as reduce stress and heat loads on the generator. And second, the X-MHD channel should provide acceptable performance with residual or purge gas pressure equal to ambient pressure in order that heavy, bulky and power consuming vacuum pumping equipment will not be required.

This part of the report details the work completed on the detonating explosive MHD generator portion of Contract No. F33615-72-C-1394 since

the publication of Technical Report AFAPL-TR-73-16, dated May 1973.[6] That report covered the theoretical studies associated with the X-MHD channel design, magnet design, and the experimental work completed on containment of 1 kilogram detonating charges. Coverage of this earlier work is not repeated in this document.

The following sections of this report contain a description of the experimental apparatus with descriptions of each component. The test data is then presented in its entirety with an analysis of the results and a description of problem areas. The final section contains a discussion of the future outlook for explosive MHD along with a suggested development program to be pursued.

REFERENCES

1. Jones, Malcolm S., Jr., V. H. Blackman, R. C. Brumfield, E. E. Evans, C. N. McKinnon, Research on the Physics of Pulsed MHD Generators, MHD Research, Inc., Final Report No. 646, Dec. 1963.

2. Jones, M., "Explosion Driven Linear MHD Generators," Proceedings of The Conference on Megagauss Magnetic Field Generation by Explosives, Frescati, Italy, Sept. 1965.

3. Multimegajoule, Pulsing, Explosive Driven MHD Feasibility Study, AFAPL-TR-71-11, Nov. 1971.

4. Explosive Magnetohydrodynamics, AFAPL-TR-65-61, April 1965.

5. Explosive Driven MHD Generator for Laser Pumping, Technical Report AFAPL-TR-65-256, Nov. 1965.

6. C. D. Bangerter, L. R. West, T. R. Brogan, D. B. Sheldon, Z. J. J. Stekly and J. Farrh, Explosive Magnetohydrodynamic Program, Interim Technical Report No. AFAPL-TR-73-16, May 1973.

SECTION IX

EXPERIMENTAL APPARATUS

A. Magnet

The magnet utilized in this program was developed under the contract, as was discussed in Section IV. This magnet was designed for multiple use. That is, with the combustion driven generator, which required the 0.36 m window, and with the explosive generator which, in some cases, requires access perpendicular to the bore. The magnet is shown in Figure 4-42 with the specifications given in Table 4-III. The power supply consists of 300 truck batteries tied in a configuration of 10 parallel connected elements of 30 batteries each, in series, to produce an unloaded voltage of approximately 360 volts. Under load, with the magnet, the battery bank delivers up to 11,000 amps at 200 volts. The design features of the magnet are given in Reference 1. The design magnetic field is 3.5 Tesla at a current of 12,000 amperes.

B. Channel

The generator channel used for this part of the program utilizes two identical channel sections. They are placed on opposite sides of a detonation chamber or driver and utilize the bi-directional nature of the gas flow out of the chamber. The channel-driver configuration is shown schematically in Figure 9-1 and photographically in Figure 9-2. The channels are fabricated of stainless steel with an internal liner of phenolic. The aluminum electrodes are set into the phenolic liner and attached to the stainless steel through a series of bolts. The bolts used for the upper electrodes are insulated from the case. Beryllium copper

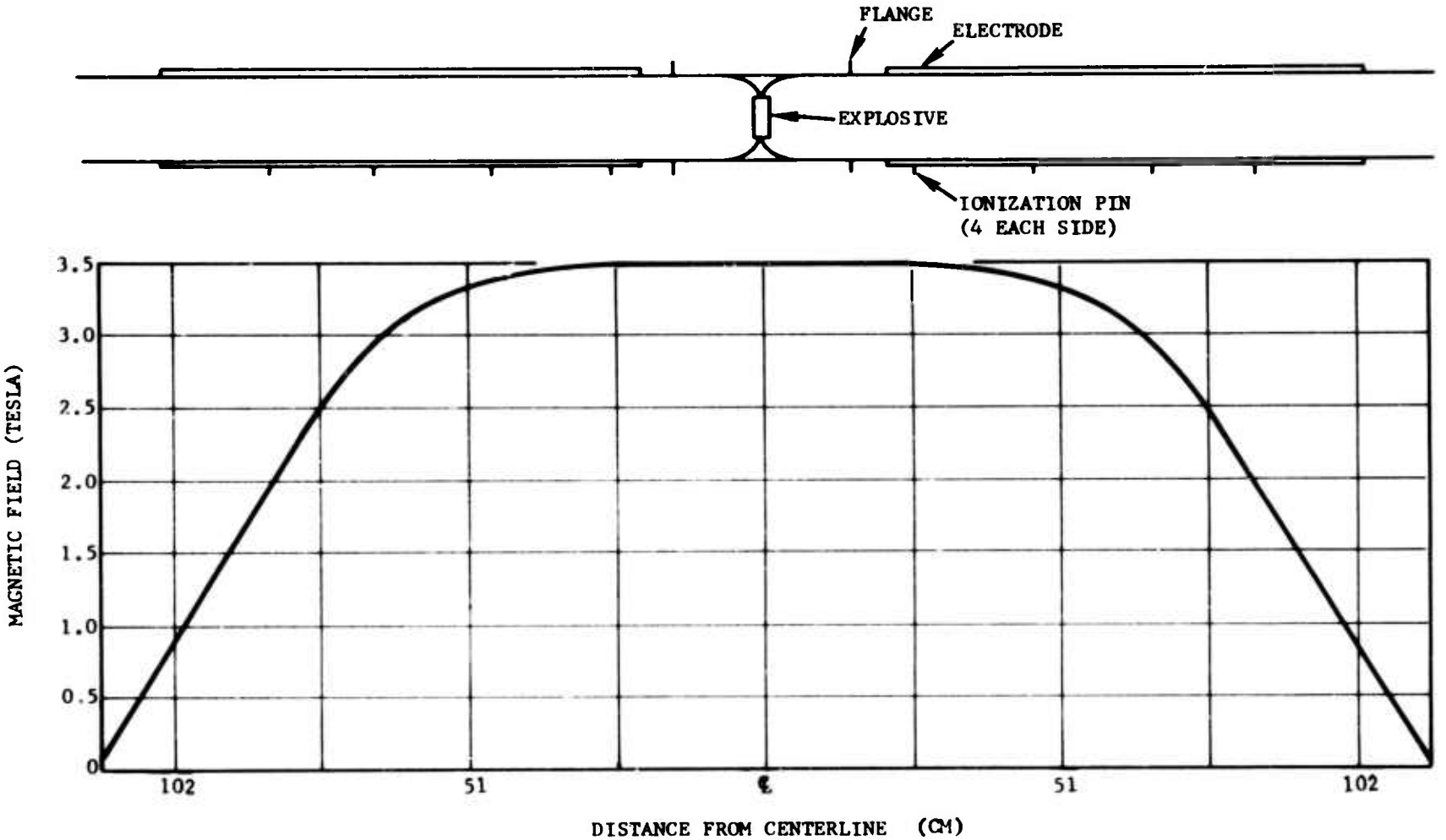

Figure 9-1. X-MHD Channel Schematic with Magnetic Field Profile

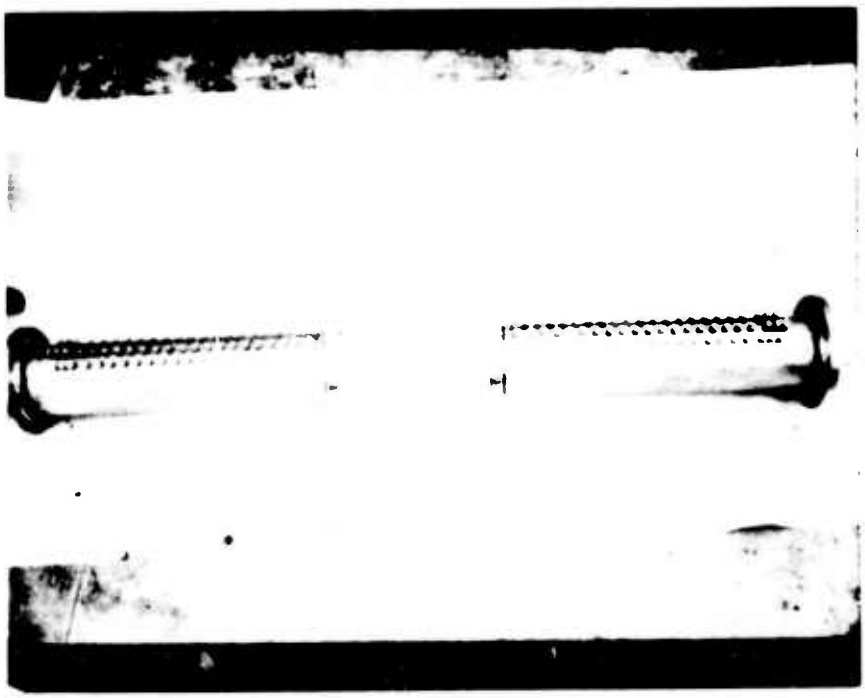

Figure 9-2. Photo of X-MHD Channel and Driver

bolts are used at the end of the channel for power removal.

The detonation section of the explosive channel is shown in Figure 9-3. Firings were conducted using 0.1 kg charges of Composition C-4 explosive. The explosive was shaped with a cylindrical disk with diamond shaped edges, as shown in this figure. The explosive was bonded into a split ring of stand-off material made of EA 946 epoxy and glass microbeads. The steel blast ring and deflector plates direct the gases down the channel. The steel blast ring was used for three or four shots before it required replacement. The phenolic liners, used to prevent shorting of the gases across the channel, were used two or three times before requiring replacement.

C. Instrumentation

The instrumentation for the explosive MHD firings consisted of a voltage divider and a Rogowski coil for voltage and current measurements on each MHD channel. In addition, the west channel was fitted with four pairs of ionization pins for the purpose of determining the velocity of the conducting layer.

1. Voltage Measurements

The voltage output of each X-MHD channel was measured with a high impedance voltage divider placed across the applied load. The schematics for the dividers are shown in Figure 9-4. The cables connecting the dividers to the scopes were approximately 40 meters of RG58AU coaxial cable. Each cable was terminated with a 50Ω resistor in parallel with the scope. In many cases, a 10 to 1 attenuator was inserted in a line just

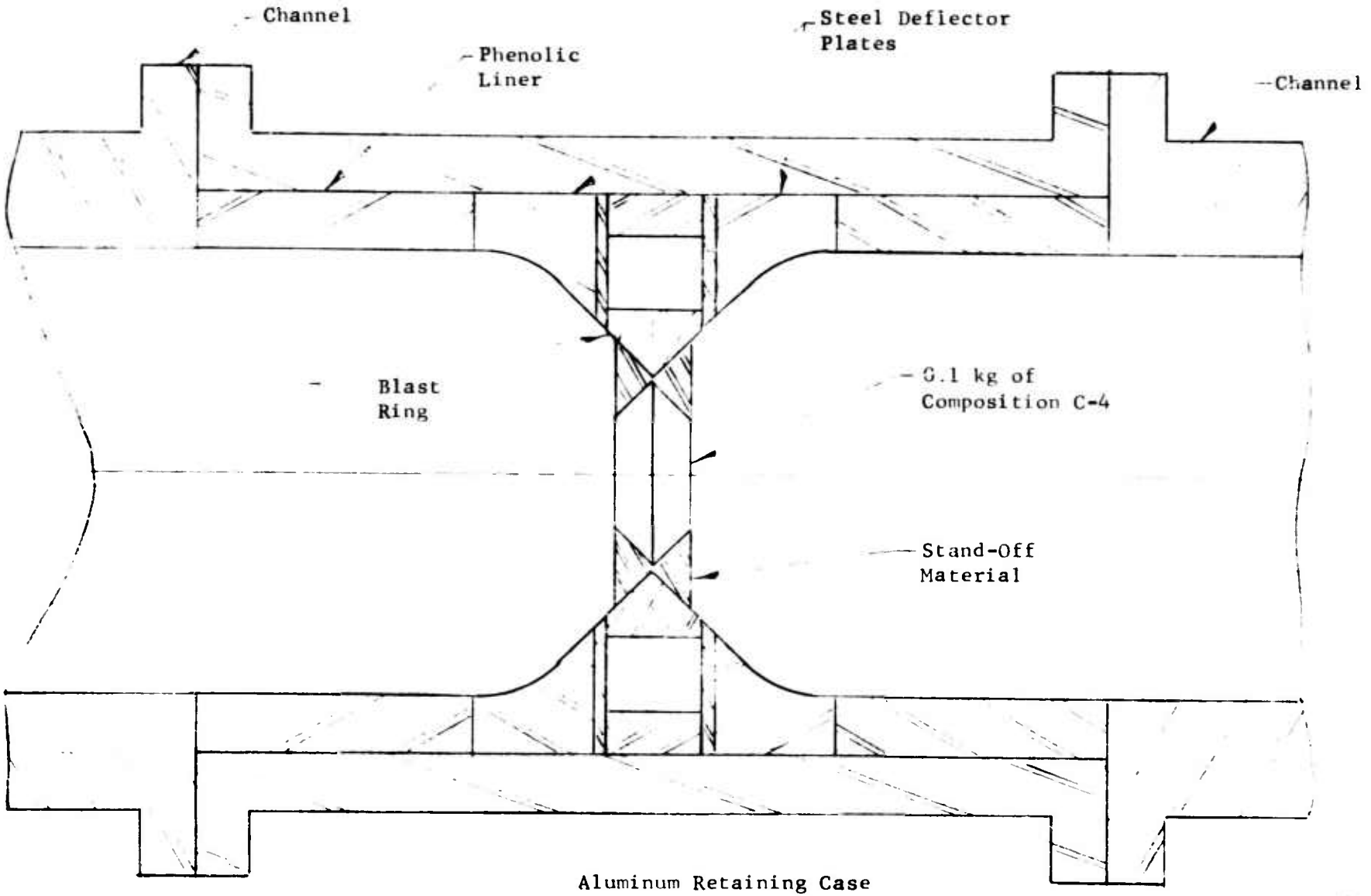

Figure 9-3. Detonation Chamber for Dual Linear MHD Channel

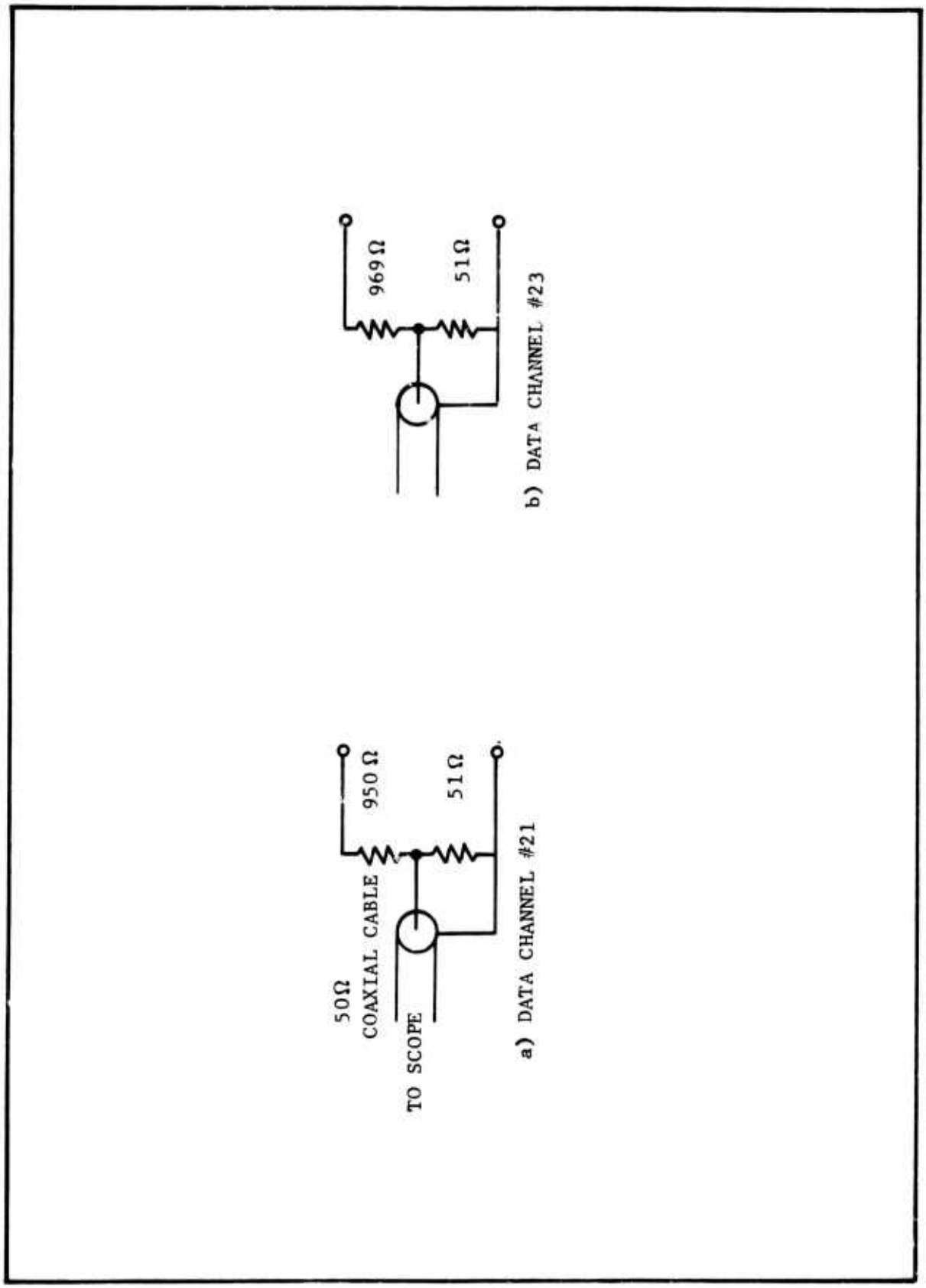

Figure 9-4. Divider Schematic

before the termination resistor.* Figure 9-5 shows a schematic diagram of the voltage measuring circuit with the termination in place.

The system was calibrated by applying a known DC voltage to the voltage divider and observing the oscilloscope output. The resulting calibration factors for both data channels used are given in Table 9-I. The rise time response of the system was checked by applying a 10μs long square pulse to the divider and recording the oscilloscope trace. The rise time of the system, defined as the time between 10% and 90% of final amplitude, was found to be 0.1μs, which is well below any requirements of X-MHD.

2. Current Measurements

The current output of each X-MHD channel was measured with a Rogowski coil. The coils were constructed by stripping the ground shield of a length of RG-11 coaxial cable back a few inches from the end, attaching a fine wire to the shield and winding approximately 720 turns on the exposed dielectric. At the end of the turns, the coil wire was connected to the center conductor of the cable. In use, the end of the cable with the wire winding is bent around the current path to form a closed loop and taped in position. This functions like a continuous coil but it can be placed in position without breaking the load circuit.

The Rogowski coil must be used with an integrator since its output is the time derivative of the current passing through the loop. An RC integrator was used in this work to perform the necessary integration.

---

*This attenuator still provided a 50Ω termination for the coaxial cable.

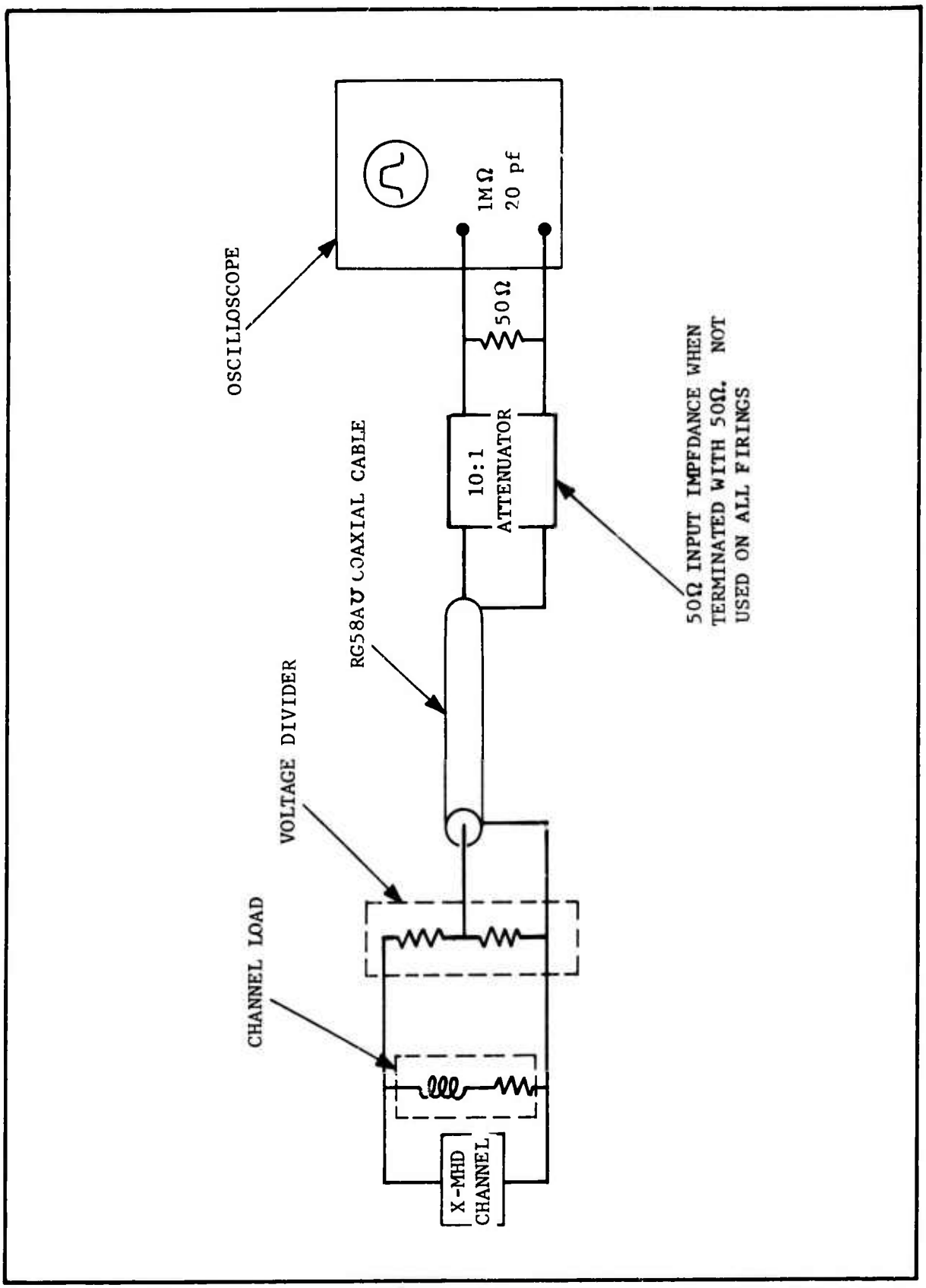

Figure 9-5. Voltage Measuring Circuit

TABLE 9-I

CALIBRATION DATA

Data Channel #21:	$v = 45.1\ v_m$
Data Channel #23:	$v = 45.0\ v_m$
Data Channel #24:	$i = (10.5 \times 10^3\ A/V)[v_o + (10^3/s)\int_o^t v_o d\tau]$
Data Channel #25:	$i = (10.4 \times 10^3\ A/V)[v_o + (10^3/s)\int_o^t v_o d\tau]$

v_m = voltage divider output as measured by scope.

v_o = integrator output as measured by scope.

Approximately 40 meters of RG58AU coaxial cable was used to transmit the signal from the coil to the integrator. Appendix A gives a detailed discussion of the circuit used and its calibration. A schematic of the circuit is shown in Figure 9-6. The relationship between oscilloscope voltage and X-MHD channel current for each data channel is given in Table 9-I with the voltage calibration factors.

3. Ionization Pins

The ionization pins shown in Figure 9-7 were installed to determine the velocity of the conducting sheet in the generator. They were connected electrically, as shown in Figure 9-7. Basically, the circuit involves a capacitor for each pin which is charged to a negative 50 volts DC. As the pin is shorted out by the conductive layer, a path is provided which allows the capacitor to discharge through the plasma to ground. The current flow through this circuit is monitored on the oscilloscope. Ideally, one should be able to determine conductivity and sheet thickness from examination of the voltage level and wave shape. This has not been possible, however, because the ionization pins appear to have been triggered by the shock which precedes the conducting sheet. The data is, however, useful for determining velocity of the conductive sheet.

D. Test Procedure

As seen in Figure 9-3, the system has four flanges. Under the present test setup, all of these must be disconnected to reload the detonation chamber.

The detonation chamber is loaded at a separate location from the channel using the following steps:

1. The molded explosive charge is cemented into place using

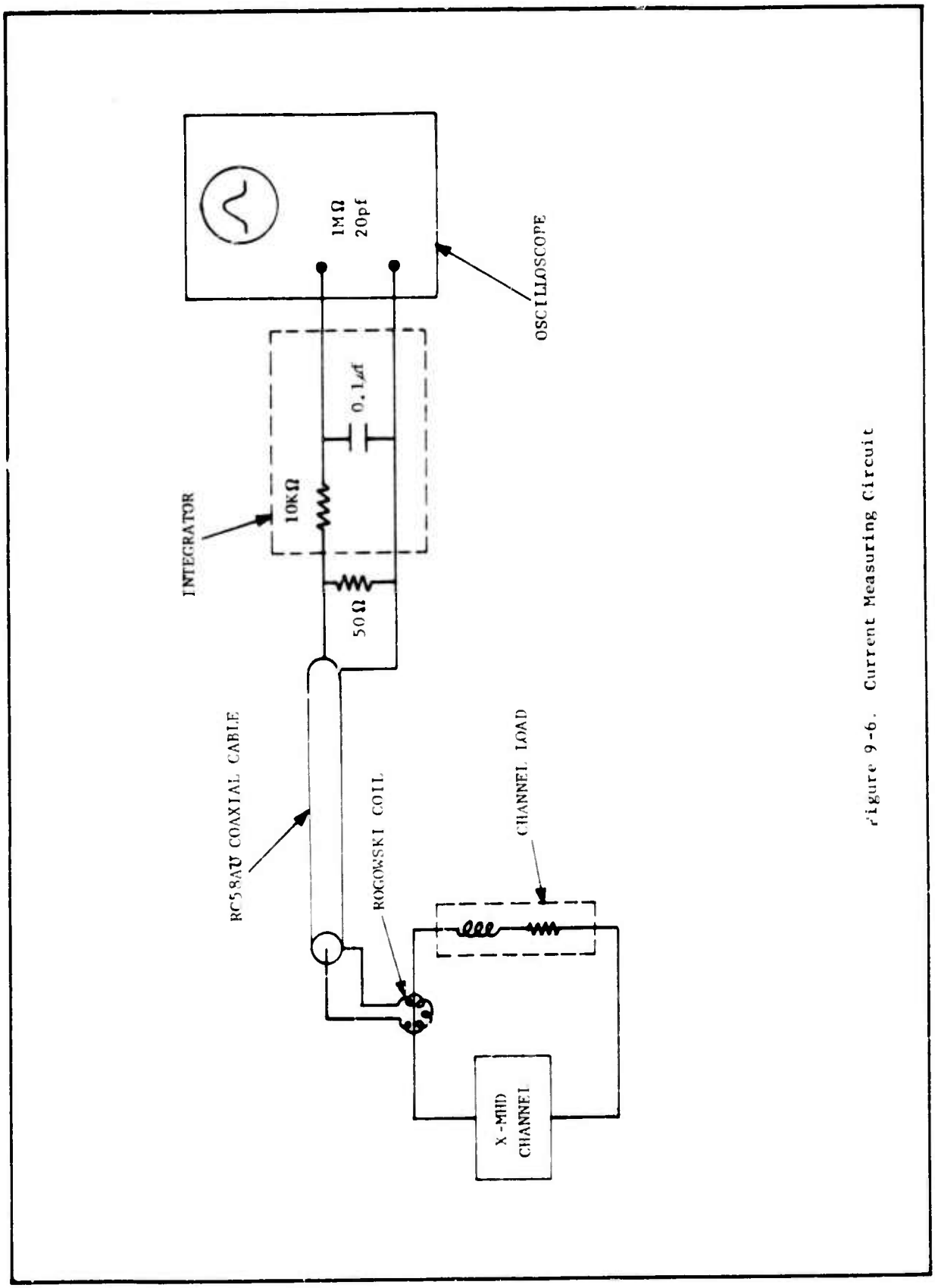

Figure 9-6. Current Measuring Circuit

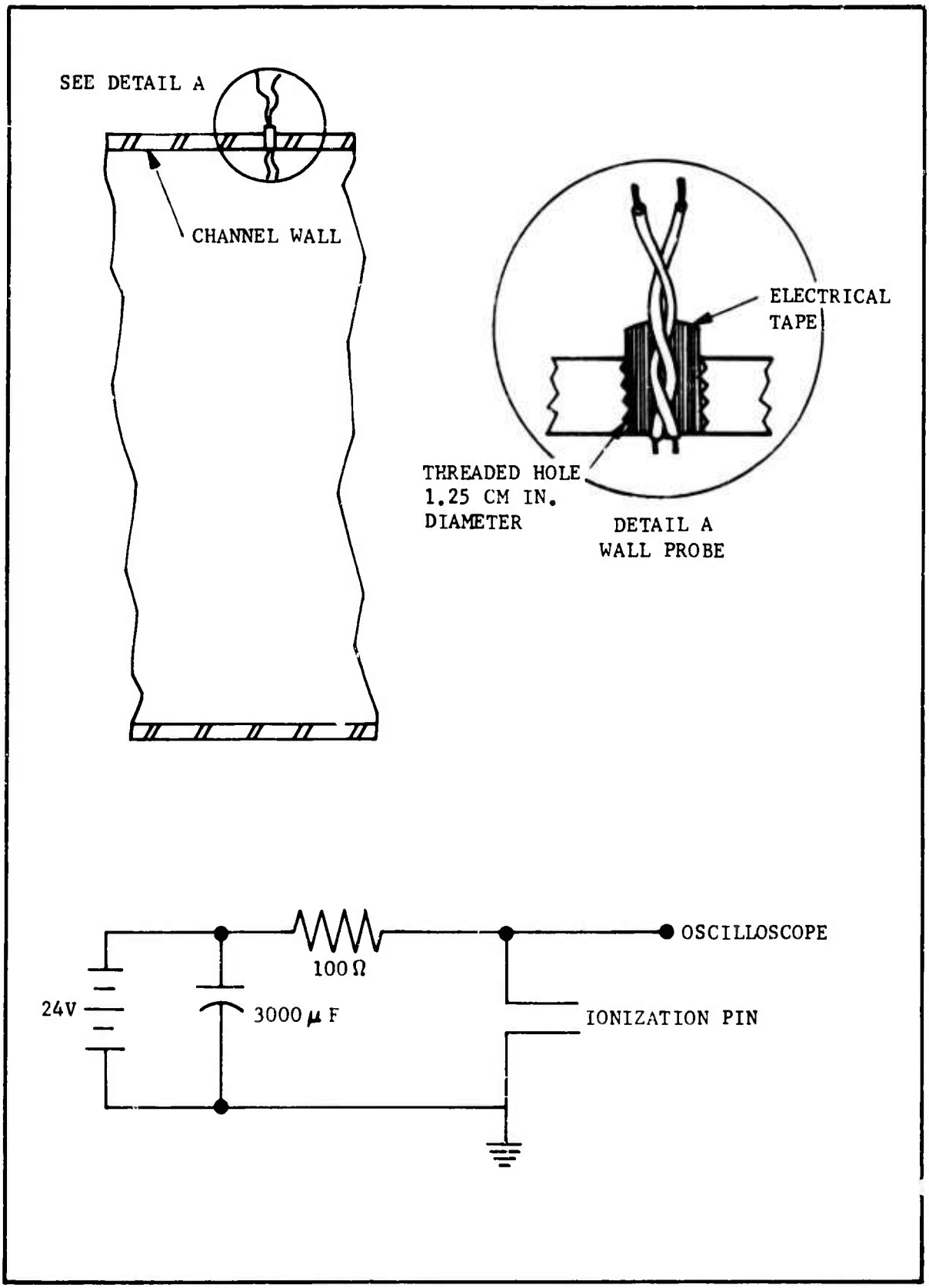

Figure 9-7. Schematic and Circuit Diagram of Ionization Pins

one standoff spacer and Eastman 923 cement.

2. A paste composed of $CsNO_3$ and cellulose dissolved in Methyl-1-Ethyl-Ketone is then spread on the face of the explosive and the plane wave generator.

3. The explosive detonator is cemented to the plane wave generator cone, which is then placed inside the second standoff spacer.

4. The standoff spacer containing the plane wave generator is then cemented to the charge holder.

5. The charge holder assembly is placed in the detonation chamber along with the deflector plates. The detonator leads and scope trigger pin leads* are connected to the electrical lead-outs, which completes the assembly of the detonation chamber.

The detonation chamber is mounted between the two channels using a rubber gasket seal between the flanges. The entire assembly is then slid into the magnet and the exhaust tubes attached with Mylar diaphragms placed between the flanges. This allows a vacuum to be drawn on the channel. Load resistors and Rogowski coils are mounted to each channel and the current and voltage leads connected.

The channel is evacuated and flushed with the fill gas to be used and then evacuated to the pressure desired. The magnet is brought up to full field and the detonator fired.

---

*A pair of ionization pins were inserted into the explosive to provide a trigger signal for the oscilloscopes which record current and voltage.

REFERENCES

1. C. D. Bangerter, L. R. West, T. R. Brogan, D. B. Sheldon, Z. J. J. Stekley and J. Farrh, Explosive Magnetohydrodynamic Program, Interim Technical Report No. AFAPL-TR-73-16, May 1973.

SECTION X

TEST RESULTS

A total of 19 X-MHD firings were made under this program. The complete raw data from each firing is included in Appendix B. Appendix C shows the measured currents, voltages and the energy output for firings X-MHD-13 thru X-MHD-19 as derived from the raw data.

There are several general observations that can be made about the data. First, the voltage traces for all shots show an inductive overshoot at the beginning and end of the current flow. The loads used were constructed to be low inductance but the inductance was measured to be on the order of 0.1 μh. With a load current rising from 10 to 100 kA in 40 μs, as was the case in some of the better firings, the voltage appearing across the inductive part of the load would be

$$\Delta v = L \frac{di}{dt} \sim (10^{-7}\ \text{h}) \frac{90\times10^{3}\ \text{A}}{40\times10^{-6}\ \text{S}} = 230\ \text{volts}.$$

This is about 10% of the total voltage appearing across the load. In principle, this should not cause a problem in evaluating the energy delivered to the load, provided that the load inductance is constant. This can be seen as follows:

$$W = \int_{T_1}^{T_2} vidt = \int_{T_1}^{T_2} i^2 Rdt + L\int_{T_1}^{T_2} i \frac{di}{dt}\, dt$$

$$= \int_{T_1}^{T_2} i^2 Rdt + \frac{1}{2} L \left[i^2(T_2) - i^2(T_1) \right] \qquad = \int_{T_1}^{T_2} i^2 Rdt.$$

Here W is the energy delivered to the load and it is assumed that the times T_1 and T_2 are chosen so that $i(T_1) = i(T_2)$. This would be true, for example,

if T_1 and T_2 were the times at which current was 10% of the peak current on rise and fall, respectively. In practice, this equality between $\int vidt$ and $\int i^2Rdt$ was found to be approximately true for data taken on the west channel but the east channel data showed $\int vidt$ was generally much larger than $\int i^2Rdt$.

The discrepancy in west channel data might be explained as a departure of the load inductance from constancy but this seems unlikely because two of the load resistors were used on both channels with no change in the relation between these integrals. Another hypothesis that can be advanced to explain this observation is that some ground loop or other internal currents may have been flowing in the east channel. This is supported by the observation of voltage variations during open circuit tests that look like inductive overshoots even though no current should have been flowing in the system. Between shots X-MHD-14 and X-MHD-15, the system was changed to provide a more positive grounding of both channels but this did not solve the problem. It was also suggested that the true resistance of the load might be higher than that measured with a Wheatstone bridge. These "effective load resistances" are considered in Section XI but are also shown to be an unsatisfactory explanation to the phenomena.

Another observation about the data is that X-MHD-14 shows much better performance than X-MHD-13, even though the load resistances were the same. One difference between these two firings was careful sanding of all surfaces used to connect the loads to the channel. This was done to reduce the contact resistance (which could be on the order of milliohms without sanding) down to a level below the load resistance. Although this did improve the agreement between the vi and the iR products, it did not resolve the discrepancy completely. For the purposes of this report, energy calculations were made

by integrating vi as well as i^2R but the latter are considered more reliable because of the problem with the voltage measurement.

A third important observation is that the performance of the channel containing the driver is much worse than the one without it. The low performance of the channel with the driver is probably due to the fact that the blast products from the main charge propagates into the relatively dense products of combustion of the plane wave generator, and must accelerate them as well as the residual gas. Since the mass of the plane wave generator is nearly 20% that of the total charge, this is not too surprising. On run X-MHD-19, a cap and small piece of Deta Sheet in the center of the charge was used to fire the round. While the front produced by this method of firing the explosive probably jets in the center and is far from plane, it is likely to be symmetric with respect to the two channels, or nearly so. The data from X-MHD-19 indicate that this is so. In fact, the output of the east channel was greater than that of the west channel, although well below that of the non-driver channel when the charge is fired by the usual plane wave generator. The obvious solution to this problem is to split the main charge in half and put the plane wave generator in between.

Finally, it is to be noted that decay time for the current pulse is much longer than the rise time. It is probably due to the drop in applied magnetic field as the current sheet travels down the channel, which causes the current to fall with a characteristic time somewhat longer than the inductive decay time. The observed decay time is too long to be due to thickening of the conducting sheet. It also could not be due to interaction with rarefaction waves propagating thru the explosion products* because the ionization pin measurements suggest a nearly constant sheet

*See Section VI of Reference 1.

velocity.

Table 10-I gives a summary of the firing results for the last six firings. The most important result is that the channel without the driver achieved more than 4% efficiency in 3 of the 6 shots. On shot X-MHD-14, the efficiency of the best channel exceeded 5%. The average efficiency of the best channels on shots X-MHD-14 and X-MHD-15, which have approximately the same load, is just under 5%.* Note also that the efficiency for the 4.89 mΩ load on shot X-MHD-16 is nearly as good as the average of the 2 previous shots.

All efficiency calculations were based on the heat of explosion of the charge material, Composition C-4. This parameter was computed by two different methods. The first method was a simple weighing of the heats of explosion for each of the components of the material. The second method was a free energy calculation similar to that of Reference 2. The results of this calculation are given in Table 10-II.

It should be noted that heat of explosion is not the only yardstick that could have been used to judge the efficiency of the generator. One such parameter is the "ballistic potential" of an explosive. This is the amount of work done by the explosion products in an adiabatic reversible expansion process from the Chapman-Jouguet point to ambient pressure (areas $A_1 + A_2 + A_3 + A_4$ in Figure 10-1). A somewhat more accurate measure of the explosion energy can be obtained by deducting Areas $A_1 + A_3$ from the ballistic potential. This is suggested by the formula

$$Q = (e_{CJ} - e_o) - \frac{1}{2}(p_{CJ} + p_o)(\frac{1}{\rho_o} - \frac{1}{\rho_{CJ}})$$

*The reason for the discrepancy between the two energy outputs with approximately the same load appears to be due to increased internal resistance in the later shot (see Section XI). The loading on the opposite channel was not the same in both cases (open circuit for X-MHD-14 and 8.42 mΩ for X-MHD-15), but there should be little connection between channels on a given shot.

TABLE 10-I

SUMMARY OF IMPORTANT RESULTS

Shot No.	Fill Gas	Initial Pressure (Torr)	Charge Mass (kg)	Driver Location	East Channel					West Channel					
					Load (mΩ)	Pulse Energy* (kj)	Eff.** (%)	Rise Time† (μs)	Pulse Length†† (μs)	Load (mΩ)	Pulse Energy* (kj)	Current Sheet Speed (m/s)	Eff.** (%)	Rise Time† (μs)	Pulse Length†† (μs)
XMHD-14	He	3.0	0.10	East	Open	--	--	--	--	8.42	11.8	5140	5.7	40	70
XMHD-15	He	2.5	0.10	East	8.42	1.20	0.6	60	40	8.22	8.50	5670	4.1	25	100
XMHD-16	80% He-20% Ar	3.5	0.10	East	8.42	1.69	0.8	65	50	4.89	8.86	4520	4.3	40	90
XMHD-17	80% He-20% Ar	270	0.14	East	8.42	0.22	0.08	80	30	8.22	2.44	4890	0.8	70	35
XMHD-18	80% He-20% Ar	270	0.14	West	8.42	--	--	--	--	8.22	0.52	3660	0.2	70	55
XMHD-19	80% He-20% Ar	3.0	0.10	Not Used	8.42	5.05	2.5	55	55	8.22	2.33	5168	1.1	60	45

*Energy = $\int i^2 R dt$ where the integration is from the time where current exceeds 10% of its peak value to the time where it drops back to 10% of its peak value.

**Efficiency is based on the assumption that one-half of the charge explosion energy is available to each channel. The calculated heat of explosion for the Composition C-4 charge material is 4.13 MJ/kg.

†Defined as the time required for current to rise from 10% to 90% of its peak value.

††Defined as the time over which the current exceeds 90% of its peak value.

TABLE 10-II

PROPERTIES OF COMPOSITION C-4

	Calculated Heat of Explosion
Weighted Composition Method*	4.10 MJ/kg
Free Energy Method	4.16 MJ/kg
Average	4.13 MJ/kg

*Composition C-4 components are as follows:

RDX	91.00%
Polyisobutylene	2.10
Motor Oil	1.60
Di-(2-ethylhexyl) sebacate	5.30

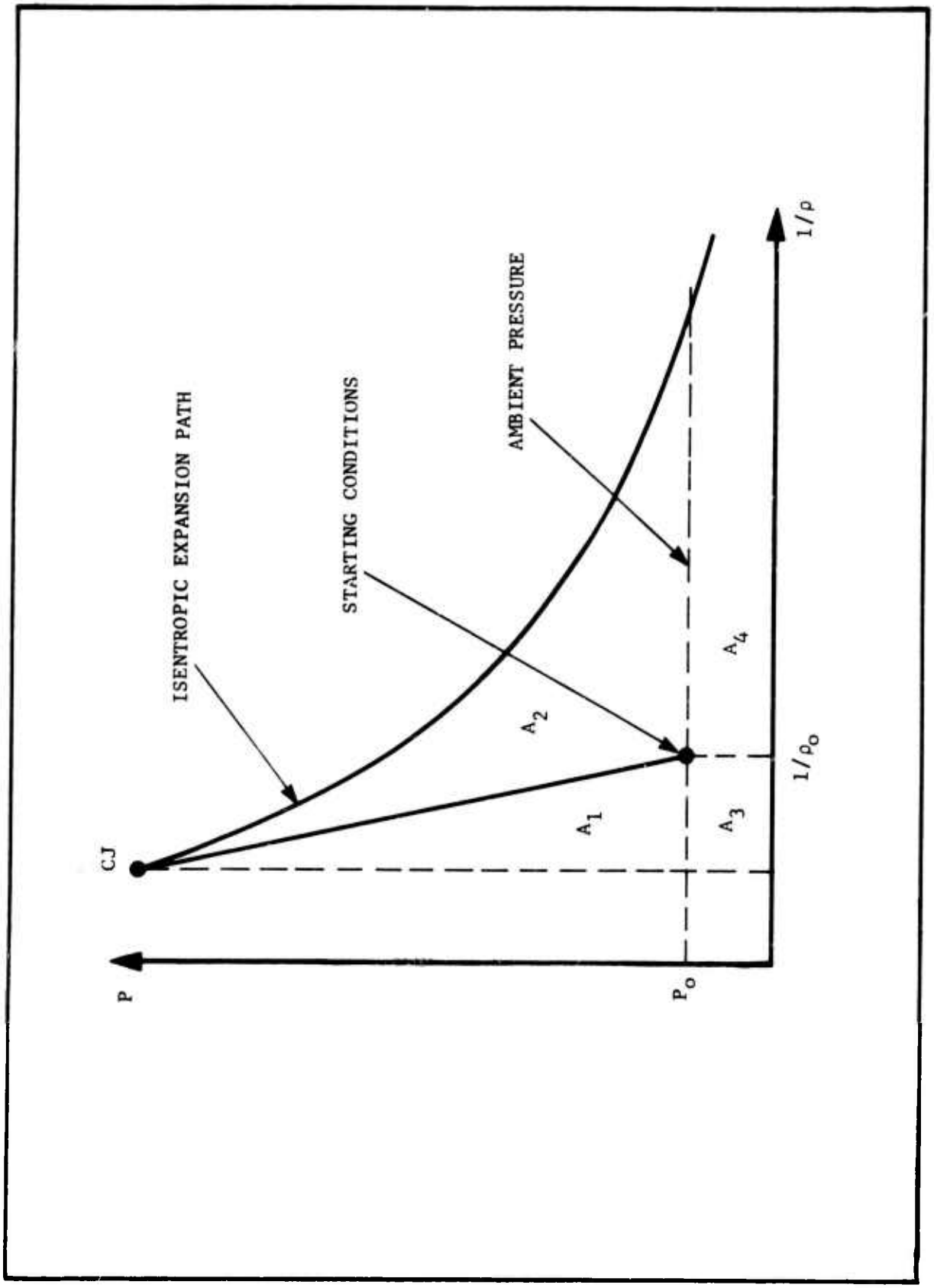

Figure 10-1. Detonation Energy and Mechanical Work

which relates the explosion energy, Q, to the internal energies, e, pressures, p, and densities at the Chapman-Jouguet point (subscript CJ) and starting conditions (subscript o). Note that the second term on the right is just the sum $A_1 + A_3$. Normally A_4 can be neglected compared to A_2. The value of the area A_2 for Composition C-4 is calculated to be

$$A_2 = 3.59 \text{ MJ/kg}$$

which is not greatly different from the calculated heat of explosion. Heat of explosion has the added advantage, however, of being subject to relatively simple experimental determination.

Table 10-III gives data taken from ionization pin pairs placed in the west channel. The pins were only used on the last five firings in the program. Figure 10-2 shows x-t diagrams of the pin response for these firings. Of particular interest is the fact that the front velocity increases somewhat from the beginning of the electrode to Pin No. 2 (0.46 meter) and then becomes essentially constant. This was found in earlier tests with the 0.4 m channel and reported in Reference 1. This is probably due to a high-speed center core jet which imparts energy to the outer edge in an attempt to become planar.

An examination of the current duration suggests the ionization pins were triggered by the shock rather than the conducting sheet formed at the contact surface between the explosion products and the inert fill gas. A shock with a Mach number of 8 or less, as indicated by the ionization pin response, would produce at most 6300°K, so neither helium nor argon would be expected to have significant ionization behind the shock. It is very likely that the residual cesium seed material left on the walls from the previous shot provided enough ionization to trigger the pins even

TABLE 10-III
IONIZATION PIN DATA

Position	Distance From Face of Charge	3 Torr Helium		3.5 Torr 80% He-20% Ar	270 Torr 80% He-20% Ar		3 Torr 80% He-20% Ar
		X-MHD-14 (8.42 mΩ)	X-MHD-15 (8.22 mΩ)	X-MHD-16 (8.89 mΩ)	X-MHD-17 (8.22 mΩ)	X-MHD-18* (8.22 mΩ)	X-MHD-19** (8.22 mΩ)
Front of Electrode	0.200 m	22 μs	20 μs	--	21 μs	25 μs	22 μs
Pin #1	0.248	30	30	31	33	--	32
Pin #2	0.456	60	57	67	63	80	61
Pin #3	0.664	90	80	100	92	120	89
Pin #4	0.842	114	104	127	118	152	114

*Driver in same channel as pins.

**No driver.

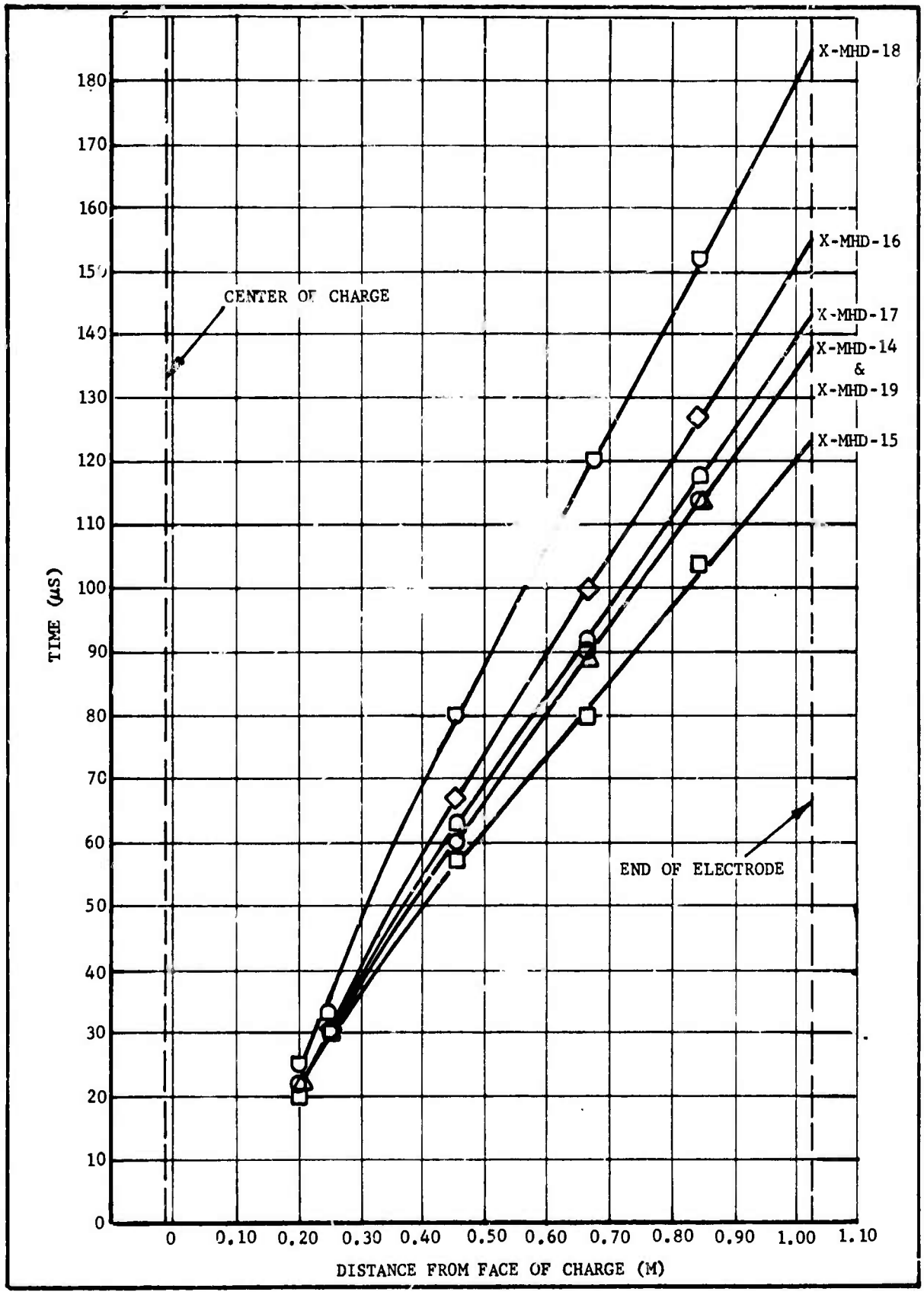

Figure 10-2. x-t Diagram of Ionization Pin Response

when the fill gas was helium. No special effort was made to clean the channel walls between shots so some cesium was undoubtedly present. This assumption allows a much better reconciliation of the estimated conducting sheet speed and the pulse length.

The conducting sheet speed listed in Table 10-I was calculated by assuming the shock speed was constant after contacting the electrodes with the average value taken for the whole electrode length. The indication at the front of the electrode is weighted about equal to Pins 1 and 2 together because all of the indications could have some time delay and the higher field strength across the electrodes should make the delay smaller for the electrodes. The sheet speed was assumed to be constant and equal to the gas velocity just behind this shock. For the purposes of this calculation, the sound speed and specific heat ratio for the fill gases used were as follows:

Fill Gas	Sound Speed (m/s)	Specific Heat Ratio (γ)
He	1020	1.667
80% He-20% Ar	924	1.667

The average shock speeds used in the calculations were as follows:

Test No.	Average Shock Speed (m/s)	Average Shock Mach Number
X-MHD-14	7010	6.87
X-MHD-15	7690	7.54
X-MHD-16	6160	6.67
X-MHD-17	6639	7.19
X-MHD-18	5054	5.47
X-MHD-19	7010	7.59

The use of these average speeds allows a relatively simple determination of generator internal resistance and inductance, as is shown in Section XI.

During the course of the experimental program, several problems occurred which hindered the recovery of data from the tests. First and foremost of

these was data loss when the oscilloscopes were either off scale or failed to trigger. This problem was eliminated as experience in firing the channel increased. Midway through the testing program, the diode protective system on the magnet began to arc. On examination of the diode system it was found that a carbon buildup, probably due to smoke from previous firings, had occurred on the Micarta standoff insulators, which had initiated the arcing. It was necessary to completely disassemble the diode system for cleaning. It was then reassembled with new Micarta standoff sheets and reinstalled on the magnet. No further arcing problems were experienced.

REFERENCES

1. C. D. Bangerter, L. R. West, T. R. Brogan, D. B. Sheldon, Z. J. J. Stekly and J. Farrh, Explosive Magnetohydrodynamic Program, Interim Technical Report No. AFAPL-TR-73-16, May 1973.

2. M. A. Cook, The Science of High Explosives (Reinhold Publishing Co., New York, 1958), Ch. 4.

SECTION XI

ANALYSIS OF CHANNEL PERFORMANCE

The physical operation of the X-MHD generator has been assumed to be that presented in Section III of Reference 1 for the purposes of this discussion. No further gas dynamic analyses of this type presented in Reference 1 has been done for this report. The starting conditions just after detonation of the charge are so complicated that they are difficult to model with any greater accuracy than was done in the original report. Thus there was little to be gained from additional numerical calculations.

The analysis of generator inductance has been improved and the inductance for the linear channels used in our experiment has been determined. The effective internal resistance of the generator has also been determined from the inductance analysis. A rough evaluation of the major energy losses in this generator is given in the last part of this section.

A. Effective Resistance of the Loads

As was mentioned in the previous section, the terminals used for mounting the load resistors were sanded on the later firings to reduce contact resistance. In spite of this precaution, the agreement between measured voltage and the product of maximum current and resistance is still rather poor. We could assume that this is due to some change in the load resistance due to high current flow and define the effective resistance of the load, R_{eff}, by

$$R_{eff} = v/i_{max}$$

where i_{max} and v are the maximum current and corresponding voltage measured at the load. The results of this analysis are shown in Table II-I for the voltage-current data from several firings.

The use of these effective resistances generally improves the agreement between $\int vidt$ and $\int i^2 R_{eff} dt$ as is shown in Table II-II. The

TABLE 11-I

EFFECTIVE RESISTANCE OF LOADS

Test No.	East Channel (mΩ)		West Channel (mΩ)	
X-MHD-6	53.8	(25.0)*	--	--
X-MHD-12	1.46	(4.89)	--	--
X-MHD-13	--	--	7.53	(8.42)*
X-MHD-14	--	--	8.40	(8.42)
X-MHD-15	36.2	(8.42)	10.2	(8.22)
X-MHD-16	32.1	(8.42)	6.71	(4.89)
X-MHD-17	16.3	(8.42)	10.9	(8.22)
X-MHD-18	--	--	10.0	(8.22)
X-MHD-19	22.9	(8.42)	9.89	(8.22)

*The numbers in parentheses are the load values measured on a Wheatstone Bridge.

TABLE 11-II

COMPARISON OF $\int$ vidt WITH $\int i^2 R_{eff}\, dt$

Test No.	East Channel $\int$ vidt	East Channel $\int i^2 R_{eff}\, dt$	West Channel $\int$ vidt	West Channel $\int i^2 R_{eff}\, dt$
X-MHD-6	5.79 kJ	4.95 kJ	--	--
X-MHD-12	1.08	0.55	--	--
X-MHD-13	--	--	6.52 kJ	5.77 kJ
X-MHD-14	--	--	12.7	11.8
X-MHD-15	5.36	5.16	10.9	10.6
X-MHD-16	6.16	6.42	12.0	12.2
X-MHD-17	0.67	0.42	3.09	3.24
X-MHD-18	--	--	0.73	0.62
X-MHD-19	12.6	13.7	3.26	2.80

exceptions to this statement are tests X-MHD-12 and X-MHD-13, where the effective resistance is less than the nominal value. It is tempting to leap to the conclusion that these effective resistances are the proper ones to use in evaluating energy, especially since it would give total energy outputs of 15.8 kJ, 18.6 kJ and 16.5 kJ for shots X-MHD-15, X-MHD-16, and X-MHD-19. The corresponding total efficiencies would be 3.8%, 4.5% and 4.0%, respectively. Nevertheless, it is very difficult to see how the same 8.42 mΩ resistor had very close to its nominal value on the west channel and from 2 to 4 times its nominal value on the east channel. In addition, the voltage divider was connected to the resistor rather than to the channel so contact resistance between the resistor and its channel connections would not have been counted in the voltage measurement. For the purposes of this report, we will not use these effective resistances.

B. Inductance and Internal Resistance

The inductance and internal resistance of the generator were obtained from a 2 parameter fit of the measured current-time history to Equation (14) of Appendix D. The inductance of the generator was taken to be of the form

$$L(t) + L_L$$

where L_L is a constant and includes the inductance of the load. The time variable part of the inductance, L(t), was assumed to be due to the variation in magnetic flux passing through a current loop formed by the two electrodes, the current sheet and the flange at the end of the channel (see Figure 1 of Appendix D). One of the electrodes was connected to the channel shell but the $\vec{J} \times \vec{B}$ force still keeps the current flow opposite the insulated electrode.

The two parameters in the fitting procedure are, therefore, L_L and the internal resistance of the generator, R_c. The velocity-time history for the conducting sheet, which is needed for the fit, was taken from the simplified wave diagram shown in Figure 11-1. As was mentioned in Section X. this has been assumed constant through its residence time in the electrodes. The space variation in magnetic field due to the position of the channel relative to the magnet was also included in the calculation.

Figure 11-2 shows a plot of the current-time history of test X-MHD-14, with both the experimental measurements and the calculated current with L_L = 0.11 μh and R_c = 21 mΩ. Figure 11-3 shows a plot of the variation of inductance with time. Table 11-III lists the values R_c obtained from the last 6 firings by this same method using L_L = 0.11 μh. Note that the internal resistances obtained in this manner have a considerable range of variation. This may be due to variations in mixing at the contact surface, causing variation in the amount of seed material that is heated by the shocked helium. The internal resistance for X-MHD-18 is expected to be much higher than that of the other firings because of the lower shock velocity and consequent lower heating of the seed material.

The magnetic Reynolds number for the system can be estimated from the internal resistance by the relation

$$Rm_a = \mu_o \sigma u a$$

where μ_o is the magnetic permeability of vacuum, σ is the sheet conductivity, u is the sheet velocity, and a is the sheet thickness. If D is the diameter of the duct,

$$Rm_a = \mu_o \left(\frac{\sigma D a}{D}\right) u \ ,$$

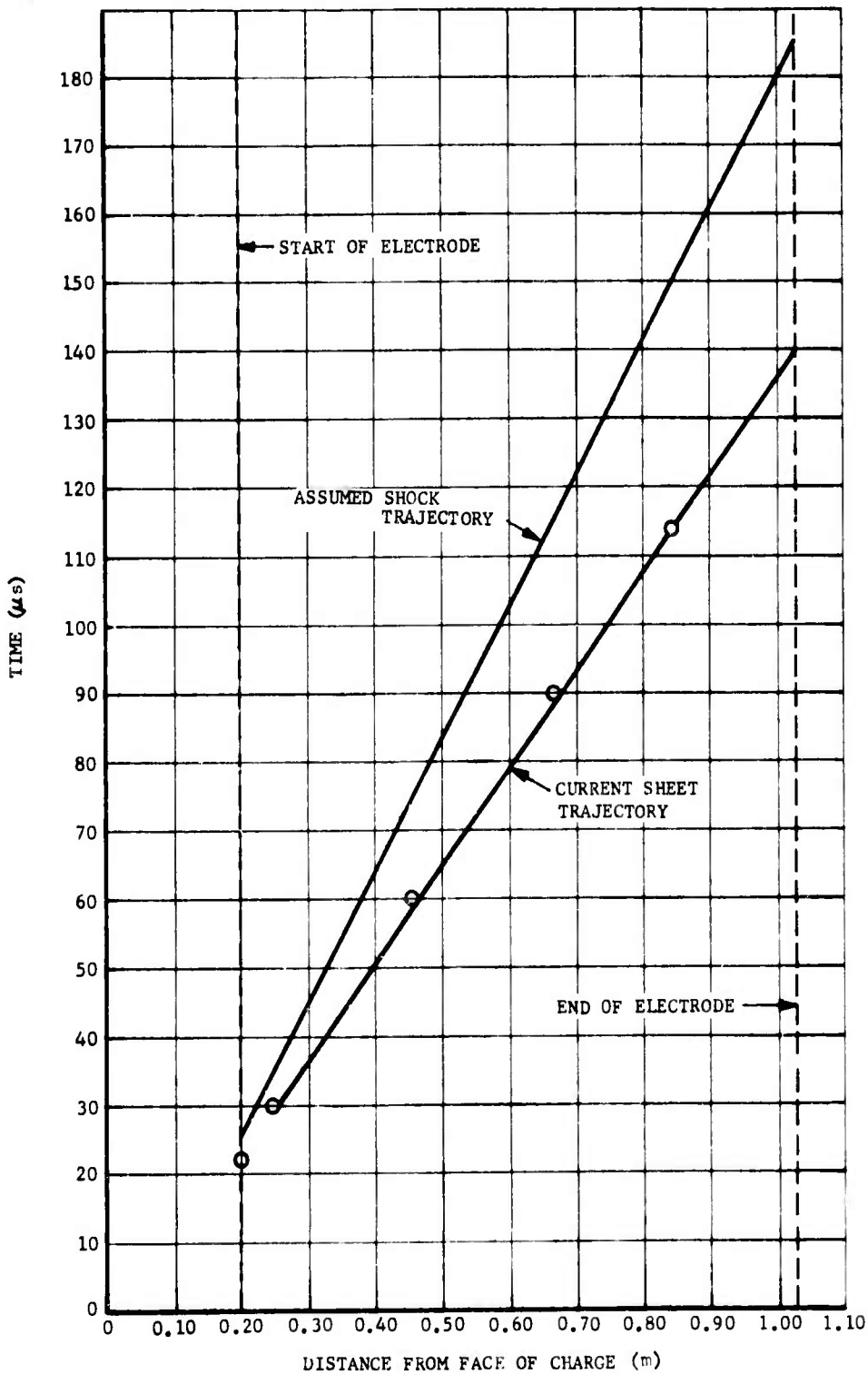

Figure 11-1. Simplified Wave Diagram for X-MHD-14

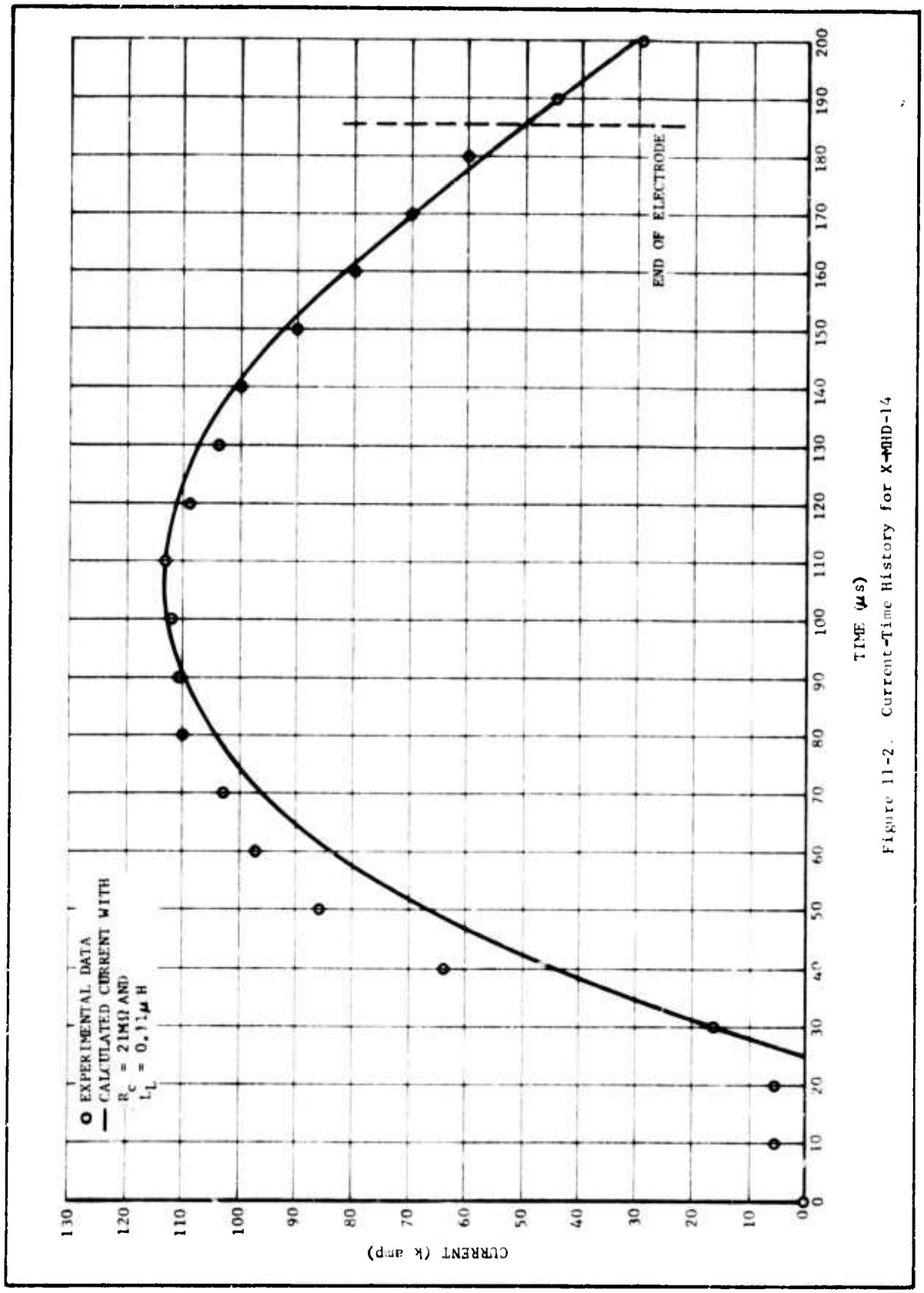

Figure 11-2. Current-Time History for X-MHD-14

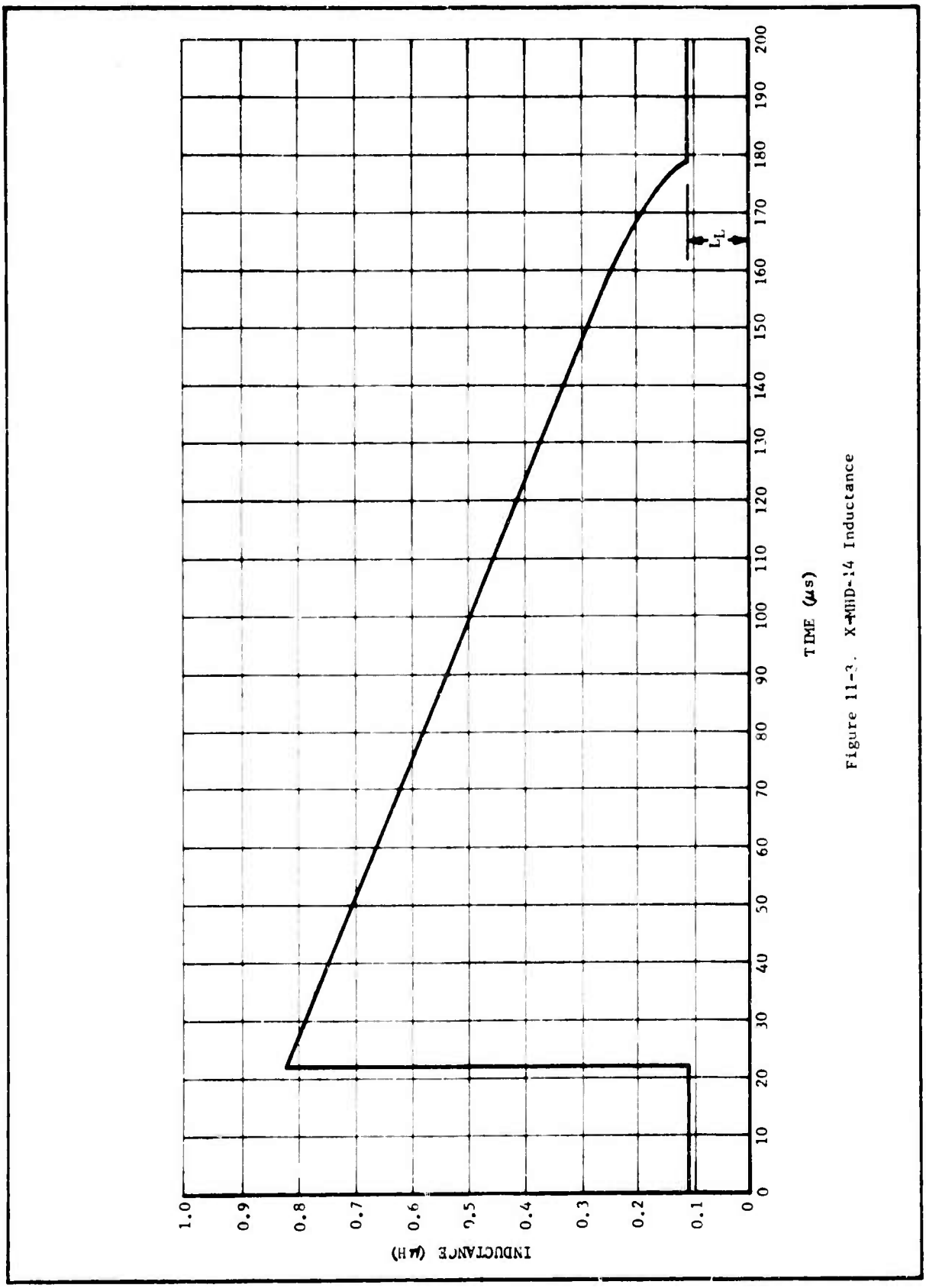

Figure 11-3. X-MHD-14 Inductance

TABLE 11-III

INTERNAL RESISTANCE OF GENERATOR
(Load Inductance of 0.11 μH)

X-MHD-14	21×10^{-3} Ω
X-MHD-15	35×10^{-3} Ω
X-MHD-16	20×10^{-3} Ω
X-MHD-17	54×10^{-3} Ω
X-MHD-18	$> 150 \times 10^{-3}$ Ω
X-MHD-19	72×10^{-3} Ω

$$= \frac{\mu_o u}{R_c} = \frac{(4\pi \times 10^{-7}\ \text{H/m})(5140\ \text{m/s})}{21 \times 10^{-3}\ \Omega}$$

$$Rm_a = 0.31$$

This is about a factor of 2 smaller than had been expected for these experiments (see Section VB of Reference 1). A significant improvement in the generator performance could be obtained by increasing Rm_a to 1.5 or 2.0.

C. Losses

The major losses in the present X-MHD tests were the residual kinetic and internal energy contained in the explosion products after the conductive sheet leaves the generator. These losses are difficult to assess accurately either experimentally or theoretically. Nevertheless, order of magnitude estimates of these quantities can be made by assuming density is independent of position when the conducting sheet leaves the generator. At this time the explosion gases* occupy 456 times their original volume and the average density is

$$\rho_{av} \sim 3.44\ \text{kg/m}^3.$$

The average of the gas velocity squared can be estimated as (1/3) of the square of sheet velocity so the kinetic energy is**

$$\text{Kinetic Energy} \sim \frac{1}{2}\ \rho_{av}\ \frac{(u_{sheet})^2}{3}\ V$$

$$\sim \frac{1}{6}\ (3.44\ \text{kg/m}^3)(5140\ \text{m/s})^2\ \frac{\pi}{4}(0.155\ \text{m})^2(1.0\ \text{m})$$

$$\sim 290\ \text{kJ}.$$

where V is the volume of the channel and u_{sheet} is the conducting sheet velocity.

The residual internal energy in the explosion products can be

*Including the standoff and seed materials.

**Using data from X-MHD-14.

estimated as

$$\text{Internal Energy} \sim c_v(T-300°K)\ \rho_{av}V$$

$$\sim 0.246\ \frac{cal}{g°K}\ (454°K-300°K)(65\ g)(\frac{4.184\ J}{cal})$$

$$\sim 10\ kJ.$$

The values of c_v and temperature were obtained from a thermochemical calculation of the explosion product expansion. As with density, the temperature has been assumed constant through the generator for this calculation.

Most of this energy will be exhausted from the machine since the products occupy 1440 times their original volume when the pressure is at 1 atmosphere. This means only a small part of this energy (less than 1/3) would remain in the channel for eventual transfer to the walls as heat. In ordinary blast waves in air only about 15% of the explosion energy is expected to remain with the products. Since 2/3 of the products end up outside of the channel, it is possible that as little at 5% of the explosion energy might remain inside for eventual heating of the channel.

The vaporization of seed and standoff materials does not contribute to the losses of the system because of the oxygen available in these materials. In fact, there is a calculated 2 kJ gain in energy due to combustion of these materials.

The residual kinetic and internal energy of the helium fill gas is very small, 0.2 kJ each. The heat loss from the shocked helium is even smaller. This can be roughly estimated by using gun ballistics techniques.[2] Reynolds' analogy is used for the heat transfer coefficient, h,

$$h = \frac{1}{2}\ \lambda c_p \rho u$$

where c_p is the specific heat of helium at constant pressure, λ is a dimensionless friction factor, and u is the gas velocity. If the diameter of the channel, D, is in centimeters, then

$$\lambda = \frac{1}{(13.2 + 4 \log_{10} D)^2}$$

$$= \frac{1}{(13.2 + 4 \log_{10} 15.5)^2} = \frac{1}{323} \quad .$$

with a shocked helium density of 2.41×10^{-3} kg/m^3,

$$h = 100 \text{ W/m}^2 \text{ °K}.$$

The total heat transfer as the gas moves down the channel is thus

$$Q = \int_0^{t_f} h\pi D(U-u)t(T-T_w)dt$$

where U is the shock velocity, T is the gas temperature, T_w is the wall temperature and t_f is the time at which the helium leaves the channel. Evaluating Q gives

$$Q \sim 7J$$

Thus the main losses in the generator are associated with the explosion products, at least under the operating conditions used here.

REFERENCES

1. C. D. Bangerter, L. R. West, T. R. Brogan, D. B. Sheldon, Z. J. J. Stekly and J. Farrh, Explosive Magnetohydrodynamic Program, Interim Technical Report No. AFAPL-TR-73-16, May 1973.

2. R. N. Jones, H. P. Hitchcock and D. R. Villegas, Interior Ballistics of Guns, AMC Engineering Handbook No. 150.

SECTION XII

CONCLUSIONS

The goal of the detonating explosive MHD studies was to evaluate the feasibility of multikilowatt, high-repetition-rate X-MHD generators. The authors believe that the results of this program show that these devices are feasible at the present time. The achievement of 11.8 kJ electrical output from a single channel, at an efficiency of 5.7% with a 0.1 kg charge shows that high power output can be obtained from a device of modest dimensions. The use of symmetrical charge initiation together with a more uniform space distribution of the applied magnetic field would make a very significant contribution toward this end.

There are, of course, significant problems that must be solved before the X-MHD generator could be considered a fully developed power source. Not the least of these problems is providing for high repetition rate pulsing of the device. Section XIII shows how this could be done for ten 0.1 kg charges at a repetition rate of 100 shots per second. Demonstrating this concept together with solving some of the other problems that contribute to reduced performance of the X-MHD generator will require a significant development program. A suggested outline for such a program is presented in Section XIII.

SECTION XIII

RECOMMENDATIONS FOR FUTURE DEVELOPMENT OF EXPLOSIVE MHD

In viewing the future of explosively driven MHD as a viable energy source, a number of items must be examined. Of prime importance is the application to which this power source will be directed. The load has a direct bearing on the efficiency of the generator inasmuch as its ability to use the energy directly or the requirements that it presents for pulse shaping and power conditioning will effect both weight and total efficiency. Ideally, the generator likes a purely resistive load. The off-design effects of feeding a load with either inductance or capacitance must be examined in greater detail.

To date, the system has met most expectations and it appears that a total energy conversion efficiency (heat of explosion to electrical output) of 8% can be achieved upon solution of the problem areas now exposed.

A brief discussion follows on the areas which require further definition.

A. Energy Losses

The scope of energy loss mechanisms in the X-MHD generator is complex and not completely understood. They can, however, be divided into internal and external losses. Internal losses to be considered are: Low interaction parameter (low magnetic Reynolds number), internal impedances, nonuniformities in velocity and magnetic field, wall friction, heat loss, and the slowing of shock velocity by ambient gas backpressure. External losses arise when coupling into a load which has a complex impedance and when any power conditioning is required to meet voltage and wave shape requirements. Losses have been covered rather extensively in Reference 1. One area which developed during the course of the experimental program

was the asymmetry of the detonation wave when the detonation was being driven from one side. The channel on the plane wave generator side of the detonation chamber produced less than half the energy of the opposite channel. Removing the plane wave generator produced more energy on the low channel but less on the channel which had previously produced high power. It is apparent that work will have to be conducted to change the charge/driver geometry to give symmetric waves.

B. Vacuum Requirements

As seen from the experimental data, and from Reference 1, the effect of residual gas density is very crucial in the efficiency of the system. The most desirable condition would be to operate the X-MHD generator with a residual gas pressure equal to ambient pressure to avoid the use of a high-capacity vacuum system for repetitive pulse operation. For this to be practical, the backpressure imposed on the conducting front by the shocked residual gas must be minimized to achieve maximum velocity. At the same time, it is necessary to achieve the 8000°K or better temperature requirement. As both backpressure and shocked gas enthalpy for a strong shock are proportional to the square of the shock Mach number, these requirements are contradictory.

Optimum X-MHD performance can be attained by purging with monatomic gases. Monatomic gases available for purging are helium, neon, and argon. Neon is rejected because of very high cost. The most practical purging gases are helium or mixtures of helium and argon.

Even at 9000°K in a monatomic gas, little ionization occurs, and near perfect gas conditions apply in the shocked gas. Therefore, a unique relationship exists between the required shock Mach number and the initial temperature of the residual gas to achieve a specified temperature in the shocked residual. If the residual gas pressure is fixed at $8.29 \times 10^{4} n/m^{2}$

there is also a unique relationship between the backpressure imposed on the conducting front and the initial temperature of the residual gas for final temperature. These relationships are shown in Figure 13-1 for a gas heated to 9000°K by the shock.

The effect of preheat in reducing backpressure requirements is dramatic. For instance, an ambient pressure monatomic gas preheated to 2200°K and shocked by the blast to produce a temperature of 9000°K will impose a backpressure identical to that imposed in the previous high-power Hercules experiments by air at 10 mm Hg (1.32×10^3 n/m^2), that is 10 atm. On the other hand, at ambient temperature, a Mach 10 shock is required and a backpressure of 124 atm will be imposed. These two extremes correspond to a very significant 20 percent difference in interface velocity.

Low-repetition-rate X-MHD generators should be designed for channel purging by a preheated monatomic gas. Specific recommendations are preheat temperature capability of 1250°K and helium/argon mixtures. The mole fraction of argon need not exceed approximately 15 percent. These recommendations are arrived at on the basis of preliminary X-MHD gas dynamic calculations described in Reference 1.

At low repetition rate, the helium expenditure to purge is not a significant factor, and the time between shots permits a thorough purge. With hot helium purge, a very low backpressure and high interface velocity is achieved, and σ_a values approaching 200 mho may be expected.

At high repetition rate (100 pps), the hot helium purge is probably not practical. Helium expenditure would be substantial, and the 10 msec period might prevent a thorough purge. Turbine engine exhaust or combustion bleed gases are a possibility; however, the spent explosion products from the previous round would seem to be the most attractive

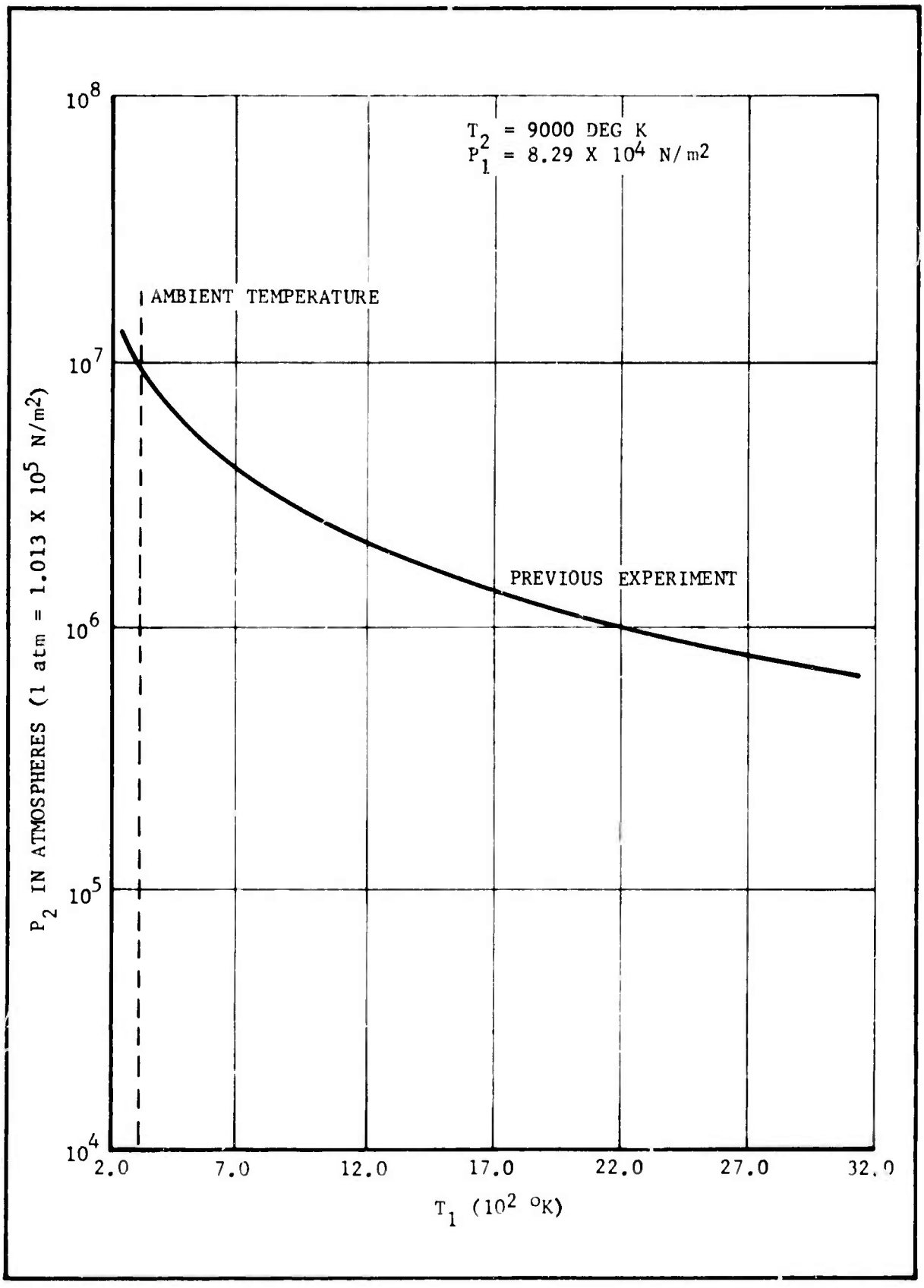

Figure 13-1. Backpressure vs Initial Temperature of Monatomic Residual Gas

purge gas.

When the explosion products from an X-MHD round have completely expanded, the barrel will be at a pressure of one atmosphere. Mixing with external ambient gases will be minimal during the 10 msec period. The spent explosion product temperature, T_1, is, at the very least, the temperature which would result from an isentropic expansion from explosion conditions to one atmosphere. The temperature is probably somewhat greater than this value, since all phases of the expansion are not completely isentropic. Using the isentropic expansion, the residual gas temperature will be approximately one fifth of the explosion temperature and the sound speed approximately 45 percent that of the value of the initial explosion products.

Under these conditions, shock-heated residual gas temperatures of 6000° to 7000°K and interface velocities of approximately 5500 m/sec should result. Since the conductivity of the conducting interface is proportional to the 1.5 power of the temperature of the shock-heated gases (Spitzer conductivity with seed), σa products of approximately 100 mho may be expected. While this value of σa is below that obtainable with hot helium purge, good X-MHD performance can still be obtained.

With spent explosion products as the residual gas, the back-pressure will increase to 100-125 atm, as compared with about 25 atm using hot helium. This accounts for the decrease in interface velocity.

With hot helium purge in the low-repetition-rate generator; a thorough and complete purge would be required in order to achieve the high values of σa predicted. With spent explosion products as the residual gas, impurities do not present a problem since they are unlikely to be more of an energy sink holding the shock temperature rise than are the explosion

products themselves. Thus, while the performance, though acceptable, is somewhat below that of the low-repetition-rate generator, very little can occur to reduce performance below that expected.

One other point is the influence of magnetic Reynolds number, Rm_a, effects. A low-repetition-rate, high-energy-per-pulse generator will be of large diameter, with the conducting zone thickness small by comparison. With this thickness-to-diameter ratio, the Rm_a effects predicted on the infinite sheet basis can be a good approximation. High-repetition-rate X-MHD for lower energy per pulse will lead to thickness-to-diameter ratios of order unity. Under these circumstances, low Rm_a approximations will be valid to substantially higher values of Rm_a, probably approaching two. For this reason, low Rm_a approximations can be utilized in calculations for the high-repetition-rate devices.

C. Power Conditioning

As noted previously, any power conditioning required will effect the total efficiency of the generator. The two areas where power conditioning apply are wave shaping and impedance matching.

The voltage output of a direct coupled X-MHD generator is limited by the size since the sustained voltage gradient is limited to about 25 kV/meter under load. For a channel of the size being tested in this program, this would yield 3 kV per channel or 6 kV if the two channels were tied in series. This voltage would be increased by the square root of the power for larger generators. For applications requiring larger voltages than this, one if left with the choice of inductively coupling, in which the current sheet acts as the primary winding of a transformer or designing a transformer type load. The effect of load inductance is covered in Reference 1.

D. Proposed Program for Development of X-MHD

Future X-MHD development is aimed at low volume, lightweight systems with a minimum of complexity. Prototype design goals are to obtain a proven power density (based on total generator volume) of 1-2 kW/cm^3 and a specific energy output of 250 J/g.

Studies, conducted as part of the current program, indicate that the explosive containment concept will enable achievement of rates up to 100 pulses per second (pps) using feed mechanism designs developed for high rate-of-fire cannons.

The future program should be directed toward demonstrating 100 pps operation for a 10 pulse train. From that point, the necessary cooled channels, cartridge magazines, and prototype feed mechanisms could be developed for longer pulse trains.

The X-MHD device offers a method of producing multi-MW average power at modest pulse rates without the complexity, weight, and volume of power conditioning for most applications. This may be the only practical method of obtaining high energy pulses in the 50 to 100 microsecond range.

1. Technical Discussion

The X-MHD is a unique direct prime power source of high energy electrical impulses at the multi-MW average power level without the need for power conditioning equipment. Thus, X-MHD can be an optimum selection for applications requiring repetition rates up to 100 Hz at pulse energies to 50 kJ.

The basic principles and potential of the X-MHD have been described in Reference 1. This report shows that the ideal linear X-MHD geometry with essentially complete confinement and utilization of the explosion products should lead to energy extraction in the 5-10 percent

range while operating into ambient backpressure so that vacuum equipment to evacuate the channel is not required. As a part of the current program, an experimental dual linear 0.155 m diameter X-MHD geometry has been evaluated. In order to provide baseline data, the 0.155 m channels are of constant cross-section along the channel, and 0.1 kg charges are utilized.

The areas of prime importance to be addressed in future development programs are as follows:

a. Efficiency and power generation effects related to firing into residual detonation products.

b. Synchronizing detonation firing circuits to insure detonation while the charge is in line with the channel.

c. Determining channel heat loads under high rate conditions.

The first area is covered quite extensively in Reference 1 with respect to pressure, temperature, density and molecular weight of the detonation products.

The second area involves the development of a fail-safe means of detonating the charges which takes into account detonation delay times, charge velocity and the problems of electromechanical contacts for initiation.

It is expected that the present channel design could handle the heat loads generated during a 10 pulse test without additional cooling.

A proposed baseline mechanism for firing ten (10), 0.1 kg charges at the rate of 100 per second is shown in Figure 13-2. As indicated in Figure 13-2, the charges to be fired are mounted in a rigid slider plate and connected to a large air cylinder. A roller release system prevents the motion of the plate while the drive cylinder is pressurized to about

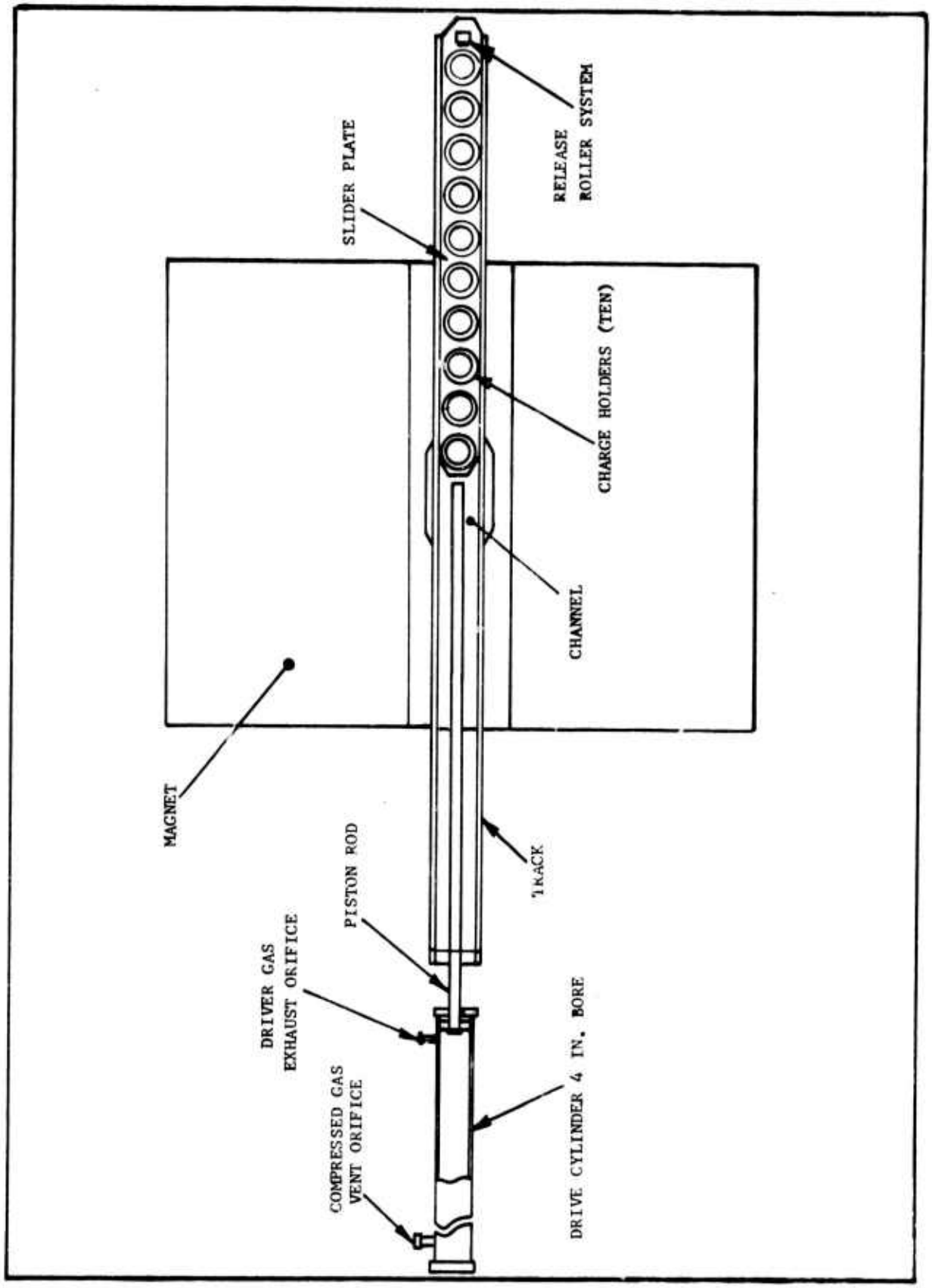

Figure 13-2. Proposed Explosive MHD Feed System

$3.5 \times 10^6 N/m^2$. To initiate the test, an air cylinder is used to pull the roller release system thus allowing the 2.2×10^4N load (applied by the air cylinder) to accelerate the charge holder and slider plate. The delay between application of voltage and charge detonation is less than 30 μs. During this time the charge moves about 0.5 mm so no major problems are anticipated with timing of the detonations.

By the time the center of the first charge coincides with the center of the channel, the system will have attained a velocity of about 15 m/s. At this time the piston has advanced to the point that the exhaust orifice is uncovered and the driving gas is vented. As the piston continues its travel down the cylinder, the gas in front of the piston is compressed to prevent additional acceleration of the system. By proper sizing of the exhaust orifice and vent orifice, it should be possible to attain a nearly constant velocity of the charge holders.

As the charges approach the center of the channel, electrical contact is made with the firing line thus detonating the charges as they pass the center of the channel.

After the last charge is fired, the piston passes the vent orifice and begins to compress the remaining gas in the cylinder. The compression of this gas decelerates the system and brings it to rest.

Although a significant amount of testing would be required to insure that the feed mechanisms operates properly, it appears feasible to build and demonstrate the apparatus with components that could either be purchased or fabricated within a reasonable length of time.

E. Program Plan for Further Development of X-MHD

1. Objective

The objective of the proposed program would be to demonstrate

that an explosive generator can be operated at a pulse rate up to 100 Hz with a pulse energy up to 50 kJ and a pulse width of 50 μs.

2. Work Statement

The work to be accomplished during the proposed program would consist of detonation chamber design, fabrication and testing followed by complete testing of the system for power characterization. The development of a more detailed program plan would take place during the initial part of the program.

a. Detonation Chamber Development

The detonation chamber and charge holder would utilize the basic designs developed under the present X-MHD program but would be modified to allow repetitive operation. The detonation chamber development would proceed as follows:

1) Task 1

Design a breech and feed system to provide explosive pulses at a rate of 50 to 100 Hz for approximately 10 pulses. The breech and feed system would be designed to utilize the explosive containment rings developed for the current X-MHD program. This system would be designed specifically for use with the channels and magnet that were used on the present X-MHD program.

2) Task 2

Fabricate the equipment designed in Task 1 above.

3) Task 3

Test the breech hardware both separately and mated with the channel and magnet.

b. Channel

Channel work would be restricted to liner replacement in

the channels that are being used in the current explosive MHD program.

c. Testing

Testing would start with the breech and feed system hardware alone and proceed to complete testing of the system for power characterization under repetitive pulse conditions. This testing would include a demonstration of up to 50 kJ per pulse electrical power output at a pulse repetition rate of 50 to 100 Hz for approximately 10 pulses.

3. Program Schedule

The proposed program would be carried out over a 12 month period, as shown in Figure 10-3. This consists of a 9 month technical effort followed by a 3 month period allocated for preparation of a technical report.

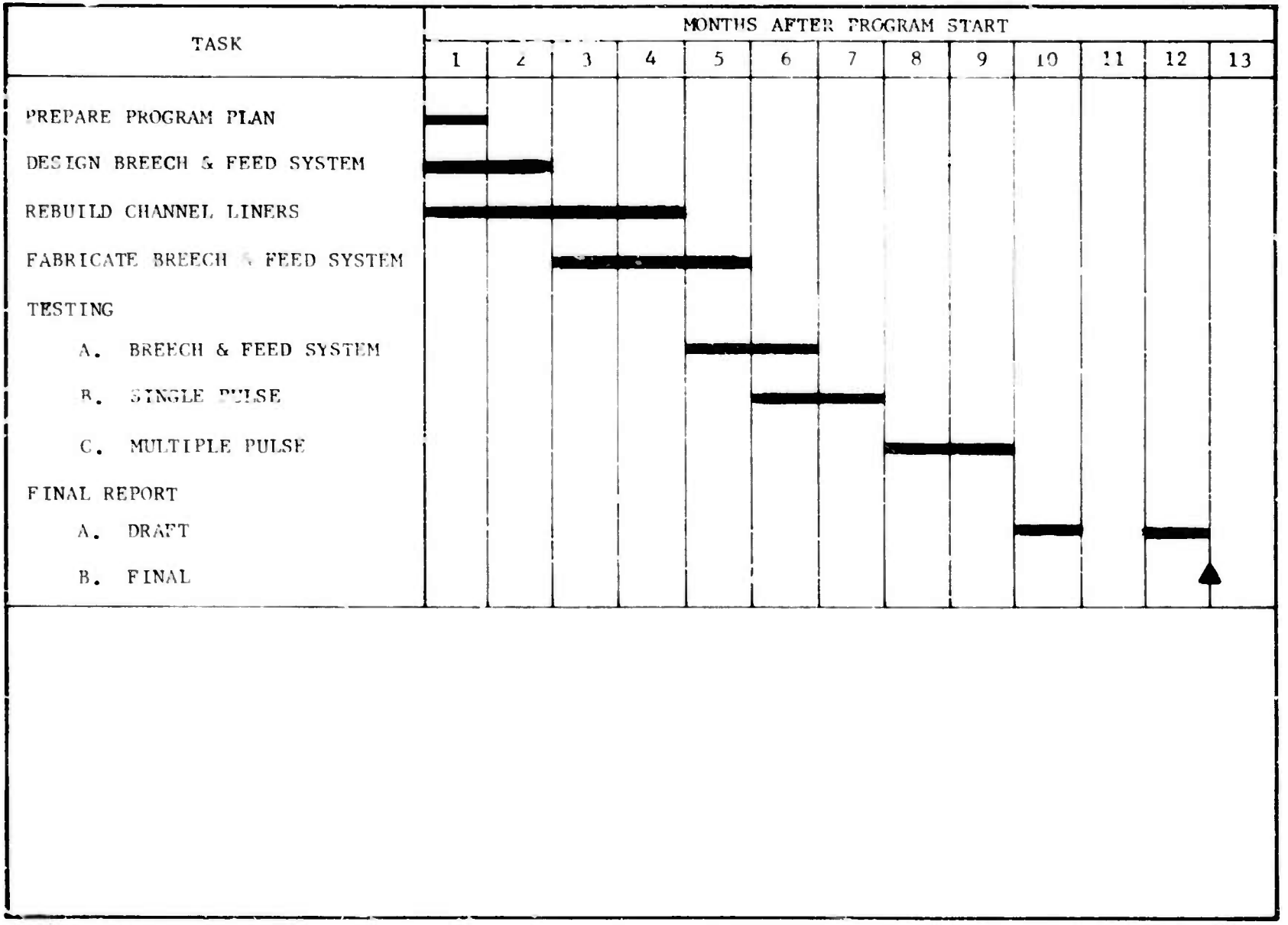

Figure 13-3. Program Schedule

REFERENCES

1. C. D. Bangerter, L. R. West, T. R. Brogan, D. B. Sheldon, Z. J. J. Stekley and J. Farrh, Explosive Magnetohydrodynamics, Interim Technical Report No. AFAPL-TR-73-16, May 1973.

APPENDIX A

CALIBRATION OF ROGOWSKI COILS

The Rogowski coils used for current measurements were constructed by stripping the ground shield of a length of RG-11 coaxial cable back a few inches from the end, attaching a fine wire to the shield and winding the wire around the exposed dielectric. At the end of the exposed section the coil wire was connected to the center conductor of the cable. In use, the end of the cable with the wire winding is bent around the current path and taped in position. This functions just like a solid coil but it can be placed in position without removing the load.

The theory of Rogowski coils is well known (see Reference 1), but it will be briefly repeated here. If a current i(t) passes thru a circular contour, C, at its center, the magnetic flux

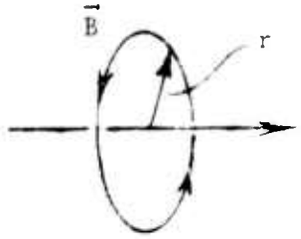

Figure 1. Magnetic Flux Density Around Current Path

density is given by

$$B(t) = \frac{\mu i(t)}{2\pi r} \qquad (1)$$

where μ is the permeability of the material along path C, and r is the radius of C. Note that the displacement current parallel to i has been neglected. If we have windings around the contour C so that each turn has its plane essentially perpendicular to C, then the voltage gain for

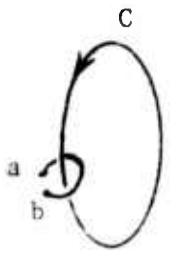

Figure 2. A Typical Turn Around Path C

each turn is given by

$$e_{ba} = \frac{d}{dt}(BA)$$

where A is the area of the turn. For N turns the voltage gain is

$$v_i = NA\frac{dB}{dt} = \left(\frac{N\mu A}{2\pi r}\right)\frac{di}{dt} \quad . \tag{2}$$

This can be written in terms of the self-inductance of the coil, L_c, as

$$v_i = \left(\frac{L_c}{N}\right)\frac{di}{dt} \tag{3}$$

where[2]

$$L_c = \frac{N^2\mu A}{2\pi r} \quad .$$

The Rogowski coil must be used with an integrator since its output is the time derivative of the current. An RC integrator is suitable for this purpose.[3] The circuit used in this work was as shown in Figure 3.

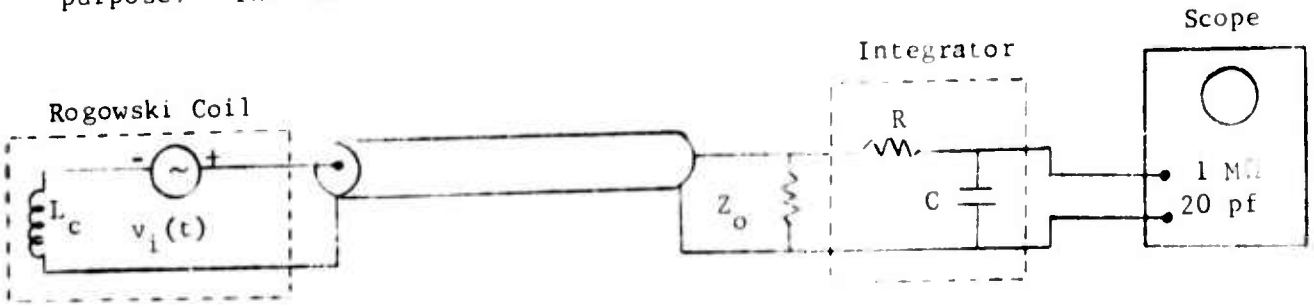

Figure 3. Schematic of Current Measuring Circuit

Since the coaxial cable is approximately terminated in its characteristic impedance, Z_o, the current in the left hand loop, i_1, satisfies

$$L_c \frac{di_1}{dt} + i_1 Z_o \cong v_i = \frac{L_c}{N} \frac{di}{dt} . \tag{4}$$

This equation can be solved to yield

$$i \cong \frac{N}{L_c} \left(Z_o \int_o^t i_1 d\tau + L_c i_1 \right) \tag{5}$$

where it has been assumed that $i_1 = 0$ at $t = 0$.

The right-hand circuit representing the terminating resistor, the integrator and the scope can be solved approximately by noting that when $C = 0.1\ \mu f$ and the time scale for current changes is 100 μs or less, the impedance of the integrating capacitor is

$$Z_c \sim \frac{\Delta t}{2\pi C} \sim \frac{10^{-4} s}{2\pi \times 10^{-7} f} = 160\ \Omega .$$

This is much less than the scope resistance so we can neglect the scope current. R is 10 kΩ so we can consider i_1 to flow thru Z_o only. Therefore, the right-hand circuit is approximately as follows:

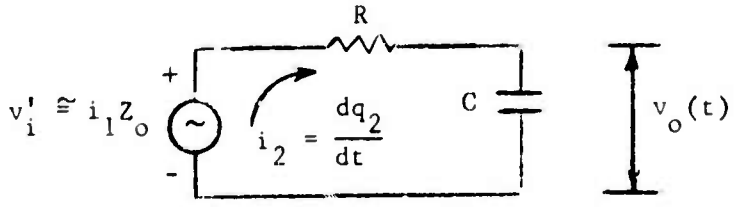

Figure 4. Simplified Representation of Integrator Circuit

The charge flowing in this circuit satisfies

$$R \frac{dq_2}{dt} + \frac{q_2}{C} = v_i' \cong i_1 Z_o \quad . \tag{6}$$

The voltage, v_o, measured by the scope is

$$v_o = \frac{q_2}{C}$$

so (6) can be written as

$$i_1 \cong \frac{1}{Z_o} \left(v_o + RC \frac{dv_o}{dt} \right) . \tag{7}$$

Substituting (7) into (5) we have

$$i \cong \frac{N}{L_c} \left[\int_o^t v_o d\tau + (RC + \frac{L_c}{Z_o}) v_o + RC(\frac{L_c}{Z_o}) \frac{dv_o}{dt} \right] \tag{8}$$

where it has been assumed that $v_o = 0$ at $t = 0$. In most systems,

$$\frac{L_c}{Z_o} \ll RC$$

so

$$i \cong \frac{NRC}{L_c} \left[v_o + (\frac{L_c}{Z_o}) \frac{dv_o}{dt} + \frac{1}{RC} \int_o^t v_o d\tau \right] . \tag{9}$$

For well designed systems, the second and third terms will be small compared to the first so a simple proportionality will exist between observed voltage and current. With rapidly changing or long pulses, this will not be the case and it will be necessary to carry one or both of these extra terms.

The system used at Hercules for the X-MHD testing had $Z_o = 50\Omega$, $k = 10k\Omega$, $C = 0.1\mu f$, and

$$L_c = \begin{cases} 96\ \mu h & \text{Coil \#25} \\ 102\ \mu h & \text{Coil \#24} \end{cases}$$

Thus, if changes take place in a time greater than $(10\ L_c/Z_o) \cong 20$ μs, we can neglect the second term in Equation 9. Similarly, if we are interested in pulse lengths shorter than $(RC/10) = 100$ μs, the third term in Equation 9 can be neglected.

Calibration of the coils was accomplished by detecting the current flowing thru a small resistor during a capacitor discharge. The discharge circuit was as follows:

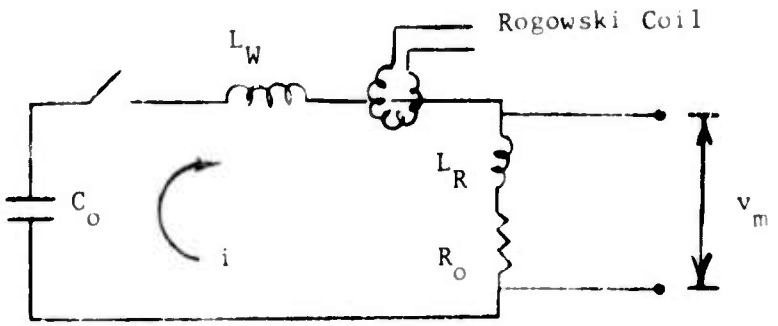

Figure 5. Capacitor Discharge Circuit

The current flow during discharge is governed by

$$(L_W + L_R)\frac{di}{dt} + R_o i + \frac{q}{C_o} = 0. \tag{10}$$

For convenience of notation, the inductance of the resistor, L_R, and the inductance of the remainder of the circuit, L_W, will be lumped together as L,

$$L = L_R + L_W. \tag{11}$$

Differentiating (10) and using (11) gives

$$\frac{d^2i}{dt^2} + \frac{R_o}{L}\frac{di}{dt} + \frac{1}{LC_o}\,i = 0. \tag{12}$$

Solving for i gives

$$i = Ae^{m_+ t} + Be^{m_- t} \tag{12}$$

where

$$m_+ = -\frac{R_o}{2L}\left(1 + \sqrt{1 - \frac{4(L/R_o)}{R_o C_o}}\right) \tag{13a}$$

and

$$m_- = -\frac{R_o}{2L}\left(1 - \sqrt{1 - \frac{4(L/R_o)}{R_o C_o}}\right) \tag{13b}$$

At $t = 0$, $i = 0$ so $B = -A$. In addition, at $t = 0$

$$L \left.\frac{di}{dt}\right|_{t=o} = V_o$$

where V_o is the initial voltage on the capacitor. Thus

$$i = \frac{V_o}{L(m_+ - m_-)}\left(e^{m_+ t} - e^{m_- t}\right)$$

or

$$i = \frac{V_o\left(e^{m_+ t} - e^{m_- t}\right)}{R_o\sqrt{1 - \frac{4(L/R_o)}{R_o C_o}}} \tag{14}$$

The voltage, v_m, measured across R_o and L_R is given by

$$v_m = iR_o + L_R \frac{di}{dt}$$

$$= \frac{V_o}{\sqrt{1 - \frac{4(L/R_o)}{R_o C_o}}}\left[\left(1 + \frac{m_- L_R}{R_o}\right) e^{m_- t} - \left(1 + \frac{m_+ L_R}{R_o}\right) e^{m_+ t}\right]. \tag{15}$$

Since $|m_-| < |m_+|$, the $e^{m_+ t}$ portion of both current and measured voltage will become small after sufficient time and the current and measured voltage will decay as $e^{m_- t}$. When this is true, the current is given by

$$i = \frac{v_m}{R_o\left(1 + \frac{m_- L_R}{R_o}\right)} . \tag{16}$$

The parameter m_- can be determined by plotting v_m vs t on a semi-log plot for large times. Then m_- can be calculated from

$$m_- = \frac{1}{(t_2 - t_1)} \ln \left(\frac{v_{m2}}{v_{m1}}\right) \tag{17}$$

where v_{m2} and v_{m1} are voltages measured in the linear region of the plot. (L_R/R_o) is somewhat more difficult to determine. Direct measurement of L_R gave

$$L_R \lesssim 1.5\ \mu h$$

with the uncertainty due to stray inductances in the measurement setup. With $R_o = 0.700\Omega$,

$$\frac{L_R}{R_o} \lesssim 2.1\ \mu s. \tag{18}$$

Another way of determining (L_R/R_o) is to measure the time, t_p, at which v_m reaches its maximum. According to (15) this satisfies

$$\frac{dv_m}{dt} = 0 = \frac{V_o}{\sqrt{1 - \frac{4(L/R_o)}{R_o C_o}}} \left[m_-\left(1 + \frac{m_- L_R}{R_o}\right) e^{m_- t_p} - m_+\left(1 + \frac{m_+ L_R}{R_o}\right) e^{m_+ t_p} \right].$$

Solving for (L_R/R_o),

$$\frac{L_R}{R_o} = \left[\frac{m_+ e^{(m_+ - m_-)t_p} - m_-}{m_-^2 - m_+^2 e^{(m_+ - m_-)t_p}} \right] . \tag{19}$$

m_- is known from measurements of v_m and (17) and m_+ can be found as follows: Solve (13b) for (L/R_o) to get

$$\frac{L}{R_o} = \left(\frac{- m_- R_o C_o - 1}{m_-^2 R_o C_o} \right) \tag{20}$$

and then substitute this result into (13a).

The procedure for calibrating Rogowski coils with a capacitive discharge can be summarized as follows:

1. Plot v_m as a function of time on a semi-log plot,
2. Calculate m_- from Equation (17);
3. Calculate (L/R_o) from Equation (20);
4. Calculate m_+ from Equation (13a);
5. Calculate (L_R/R_o) from Equation (19);
6. Calculate i at times $t >> (-1/m_+)$ from Equation (16);
7. Determine the calibration factor from Equation (9) in the form

$$\text{Cal. Factor} = \left(\frac{NRC}{L_c}\right) = \left[\frac{i}{v_o + \left(\frac{L_c}{Z_o}\right) \frac{dv_o}{dt} + \frac{1}{RC} \int_o^t v_o d\tau} \right] . \tag{21}$$

The system parameters that must be known in order to make these calculations are

$$R_o,\ C_o,\ t_p,\ L_c,\ Z_o,\ R,\ C.$$

Tables I and II show calibration voltages taken from oscilloscope displays of capacitor discharge data. All parameters necessary for arriving for the cal. factor are also recorded on the tables. Figures 6 and 7 show semi-log plots of both v_m and v_o for the purpose of determining m_-. It is worth noting that in both figures the "best-fit" lines thru the v_m and v_o data were drawn parallel even though v_o has a slightly larger slope than v_m. This was done because the theory given above requires that for times much greater (L_c/Z_o) but much less than RC, v_m and v_o must have the same time dependence. In both figures, a compromise was made between the two actual slopes to arrive at an appropriate average slope.

Table III gives the calculated parameters for calibration of both Rogowski coils used in this program. It is to be noted that (L_R/R_o) is different for the two coils even though the same load was used for both tests. This 8% variation would, however, only cause a 1% variation in the calibration factor so it can be regarded as unimportant.

TABLE I

CALIBRATION OF CHANNEL #24

Time (μs)	v_m (volts)	v_o (volts)
9	643	0.128
11	551	0.112
13	505	0.100
15	459	0.089
17	422	0.076
19	367	0.066
21	321	0.057
23	275	0.054
25	252	0.046
27	220	0.039
29	188	0.036
31	170	0.029
33	152	0.026
35	138	0.024
37	119	0.020
39	101	0.018

R_o = 0.700 Ω
C_o = 27 μf
t_p = 3.1 μs
L_c = 102 μh

Z_o = 50 Ω
R = 10 kΩ
C = 0.1 μf

TABLE II

CALIBRATION OF CHANNEL #25

Time (μs)	V_m (volts)	V_o (volts)
9	648	0.120
11	561	0.105
13	497	0.093
15	440	0.082
17	389	0.072
19	350	0.063
21	302	0.055
23	268	0.050
25	250	0.043
27	216	0.038
29	194	0.033
31	173	0.029
33	151	0.025
35	134	0.022
37	121	0.020
39	108	0.018

R_o = 0.700 Ω $\quad$ Z_o = 50 Ω

C_o = 27 μf $\quad$ R = 10 kΩ

t_p = 2.5 μs $\quad$ C = 0.1 μf

L_c = 96 μh

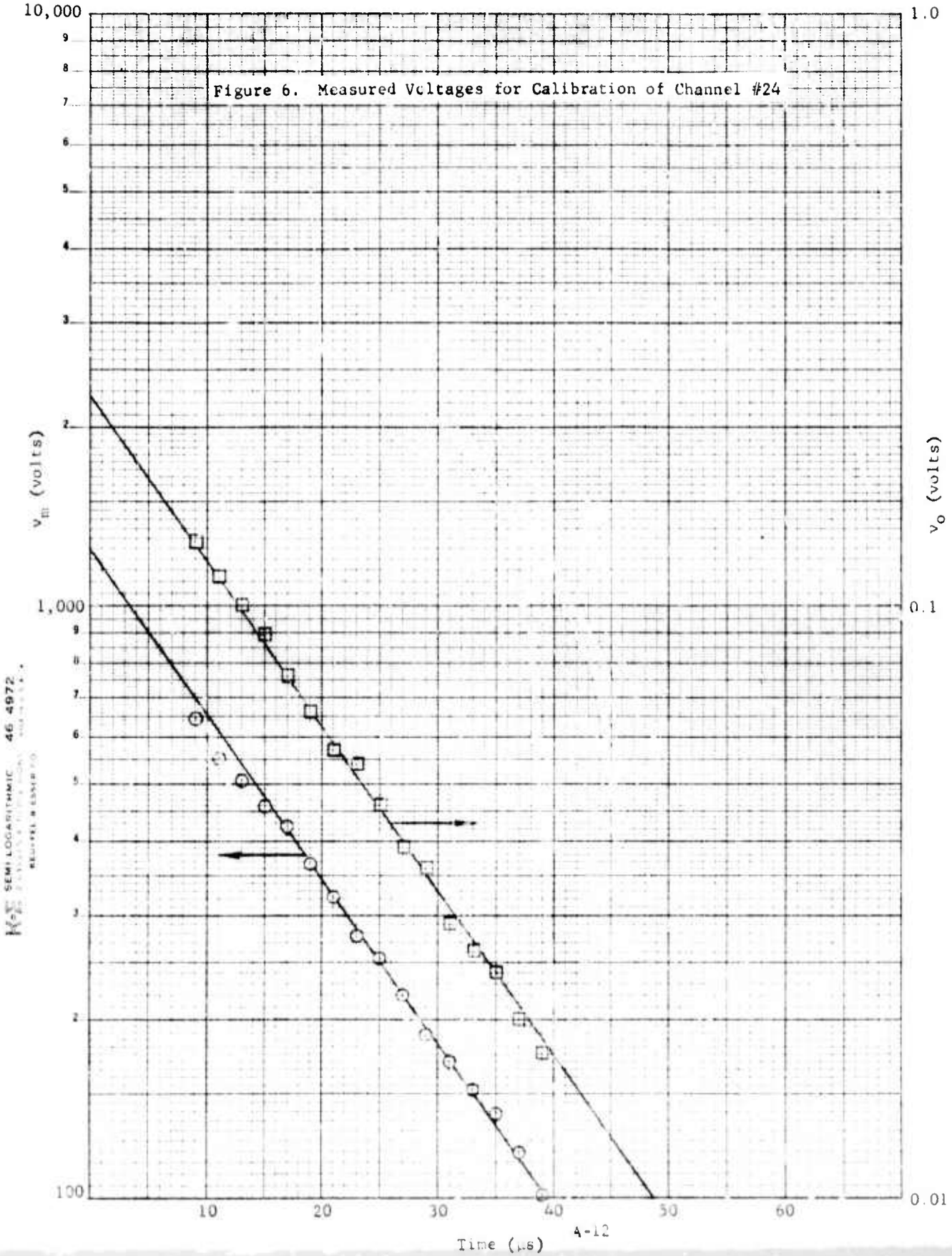

Figure 6. Measured Voltages for Calibration of Channel #24

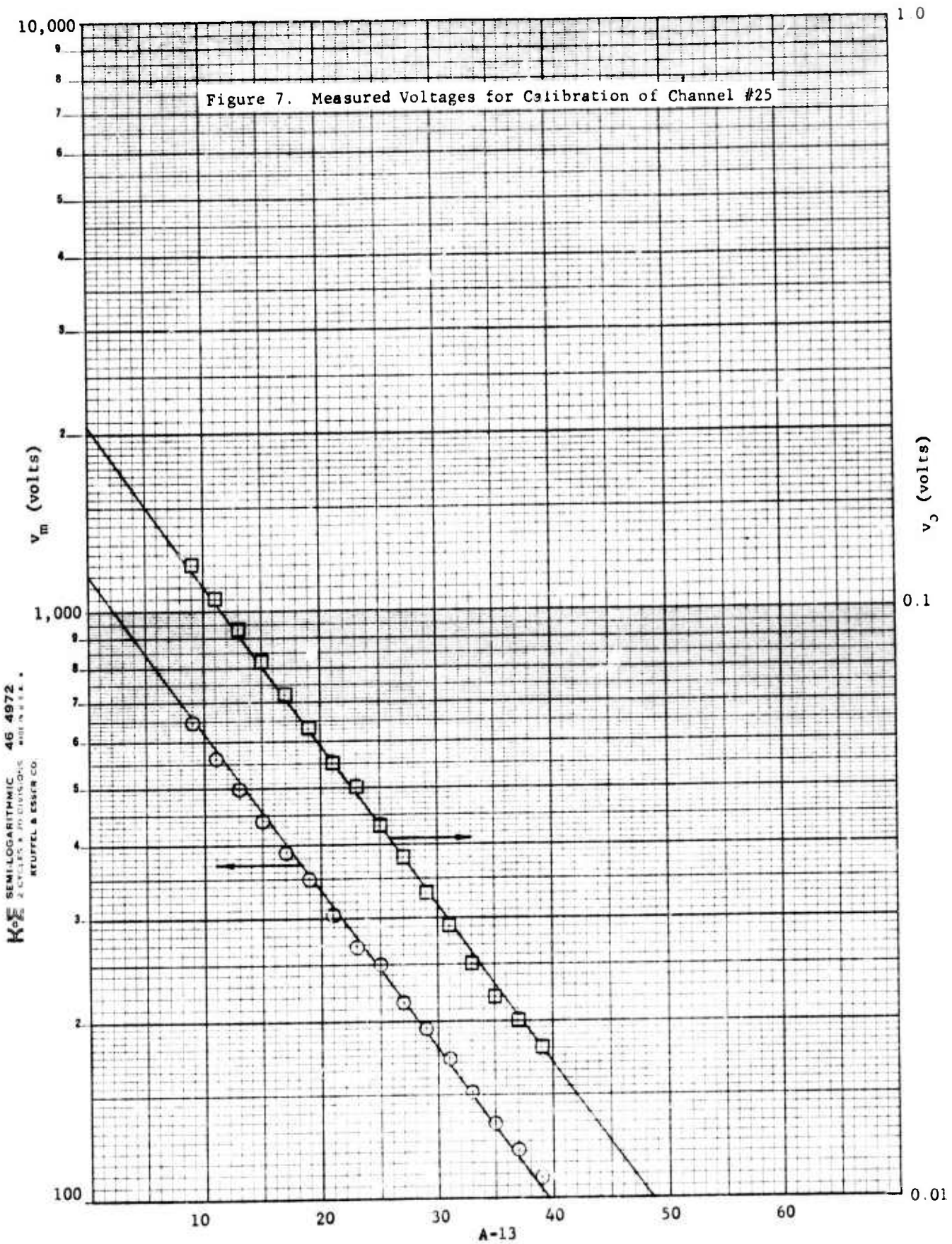

Figure 7. Measured Voltages for Calibration of Channel #25

TABLE III

CALIBRATION PARAMETERS

Parameter	Channel #24	Channel #25
m_-	- 1/15.6 μs	- 1/16.2 μs
(L/R_o)	2.69 μs	2.33 μs
m_+	- 1/3.25 μs	- 1/2.72 μs
(L_R/R_o)	2.00 μs	1.85 μs
Cal. Factor = $(\frac{NRC}{L_c})$	10.5×10^3 amp/volt	10.4×10^3 amp/volt

REFERENCES

1. A. J. Schwab, High-Voltage Measurement Techniques (The M.I.T. Press, Cambridge, Mass., 1972), p. 180.

2. V. Del Toro, Electromechanical Devices for Energy Conversion and Control Systems (Prentice-Hall, Inc., Englewood Cliffs, N.J., 1968), p. 40.

3. Ref. 1, p. 183.

APPENDIX B

RAW DATA FROM X-MHD TESTS

Firing No. X-MHD-1 Date June 4, 1974

Charge Specifications:

Composition C-4 Weight: 97.3 gm

Seed ($CsNO_3$) Weight: 3.0 gm (bulk)

Standoff Material: 17 gm (west), 21.4 gm (east)

Driver Location: East Channel

Fill Gas: Air . Initial Pressure: 40 Torr.

Magnet Current: 11,000 amps.

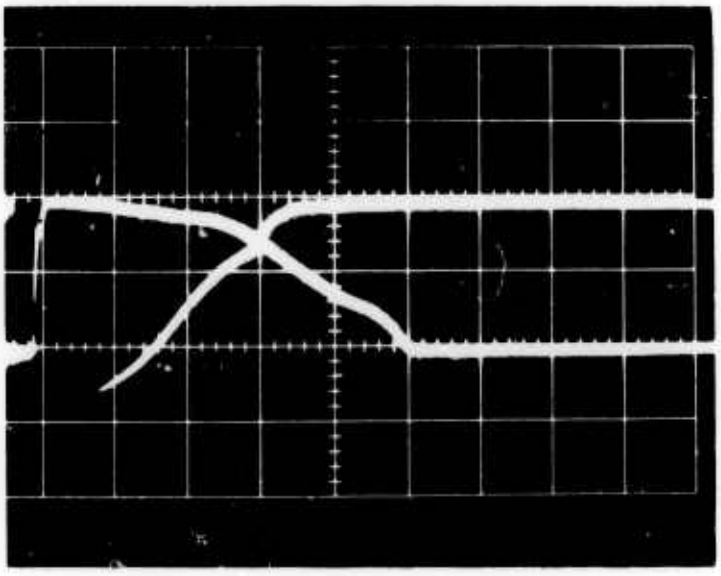

Upper Trace: West Channel Voltage, 1000 Ω Load

Vertical Deflection 20 v/cm

Horizontal Deflection 50 μs/cm

Data Channel *

Lower Trace: East Channel Voltage, 1000 Ω Load

Vertical Deflection 20 v/cm

Horizontal Deflection 50 μs/cm

Data Channel *

X-MHD-1 (Continued)

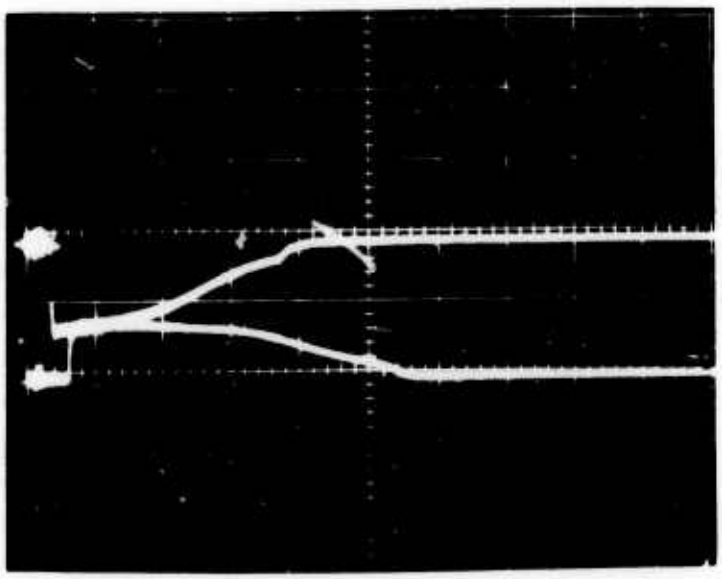

Upper Trace: West Channel Voltage, 1000 Ω Load

Vertical Deflection 10 v/cm

Horizontal Deflection 50 μs/cm

Data Channel * (10X attenuation)

Lower Trace: East Channel Voltage, 1000 Ω Load

Vertical Deflection 10 v/cm

Horizontal Deflection 50 μs/cm

Data Channel * (10X attenuation)

Notes:

*Data channel not recorded. Use $v = (44.0)v_m$ as conversion factor.

Firing No. X-MHD-2 Date June 11, 1974

Charge Specifications:

Composition C-4 Weight: 97.3 gm

Seed ($CsNO_3$) Weight: 2.7 gm (bulk)

Standoff Material: 12.5 gm each side

Driver Location: East Channel

Fill Gas: Air . Initial Pressure: 10 Torr.

Magnet Current: 11,000 amps.

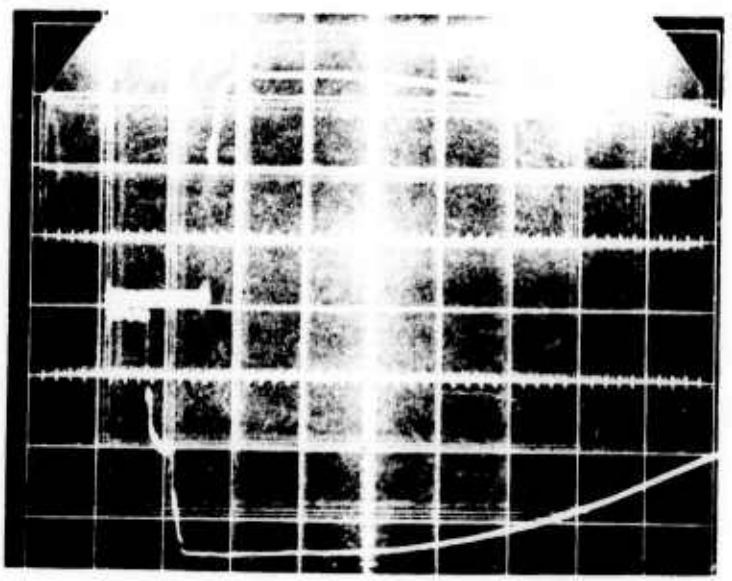

Upper Trace: East Channel Voltage, 975 Ω Load

Vertical Deflection 20 v/cm

Horizontal Deflection 10 μs/cm

Data Channel 21

Lower Trace: West Channel Voltage, 994 Ω Load

Vertical Deflection 20 v/cm

Horizontal Deflection 10 μs/cm

Data Channel 23

Firing No. X-MHD-3 Date June 11, 1974

Charge Specifications:

Composition C-4 Weight: 97.3 gm

Seed ($CsNO_3$) Weight: 2.7 gm (bulk)

Standoff Material: 12.5 gm each side

Driver Location: East Channel

Fill Gas: Air . Initial Pressure: 10 Torr.

Magnet Current: 11,000 amps.

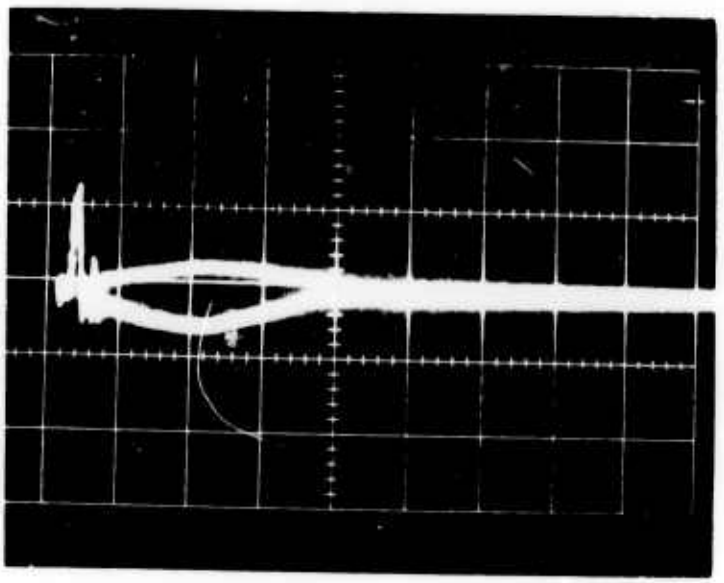

Upper Trace: East Channel Voltage, $25 \times 10^{-3}\ \Omega$ Load

Vertical Deflection 20 v/cm

Horizontal Deflection 50 μs/cm

Data Channel 21

Lower Trace: West Channel Voltage, $25 \times 10^{-3}\ \Omega$ Load

Vertical Deflection 20 v/cm

Horizontal Deflection 50 μs/cm

Data Channel 23

X-MHD-3 (Continued)

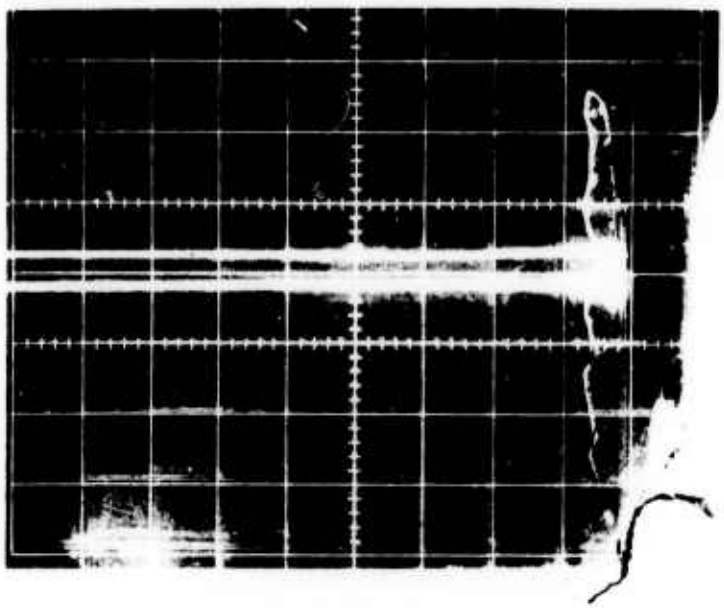

Upper Trace: _____ Channel Current, $25 \times 10^{-3} \Omega$ Load

Vertical Deflection 10 v/cm

Horizontal Deflection 50 μs/cm

Data Channel *

Lower Trace: _____ Channel Current, $25 \times 10^{-3} \Omega$ Load

Vertical Deflection 10 v/cm

Horizontal Deflection 50 μs/cm

Data Channel *

Notes:

*Scopes displaying current did not trigger at correct time.

Firing No. X-MHD-4 Date June 13, 1974

Charge Specifications:

Composition C-4 Weight: 100 gm

Seed ($CsNO_3$) Weight: 2.7 gm/side (surface)

Standoff Material: 12 gm

Driver Location: East Channel

Fill Gas: Air . Initial Pressure: 10 Torr.

Magnet Current: 11,000 amps.

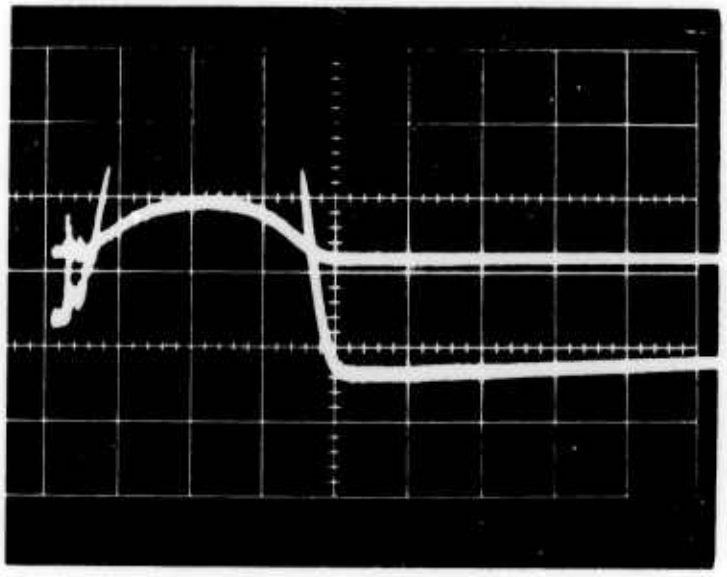

Upper Trace: West Channel Current, shorted Load

Vertical Deflection 20 v/cm

Horizontal Deflection 50 μs/cm

Data Channel 25

Lower Trace: West Channel Current, shorted Load

Vertical Deflection 2 v/cm

Horizontal Deflection 50 μs/cm

Data Channel 25

X-MHD-4 (Continued)

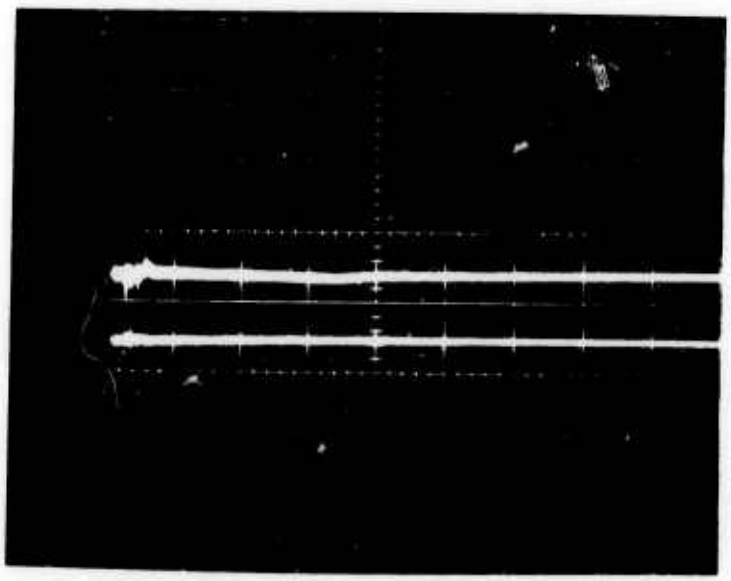

Upper Trace: West Channel $\frac{di}{dt}$, shorted Load

Vertical Deflection 20 v/cm

Horizontal Deflection 50 μs/cm

Data Channel 25 with 1000X attenuation

Lower Trace: East Channel $\frac{di}{dt}$, shorted Load

Vertical Deflection 20 v/cm

Horizontal Deflection 50 μs/cm

Data Channel 24

Notes:

X-MHD-4 (Continued)

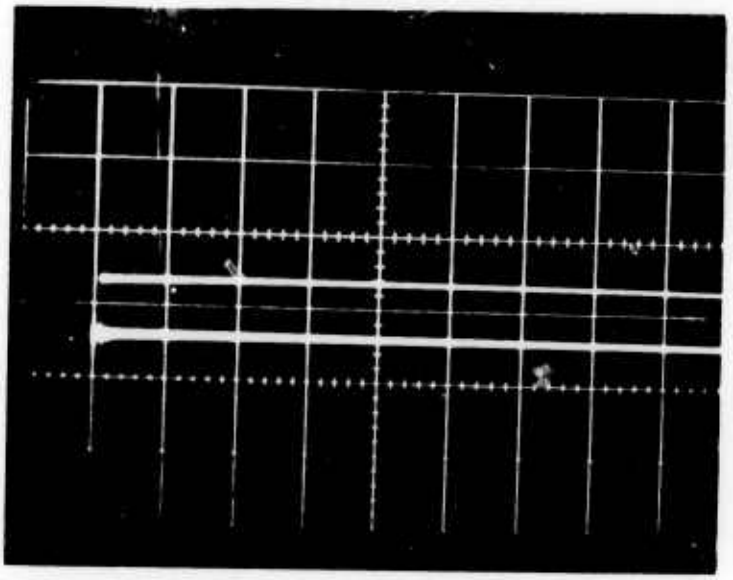

Upper Trace: East Channel Current, shorted Load

Vertical Deflection 20 v/cm

Horizontal Deflection 50 μs/cm

Data Channel 24

Lower Trace: East Channel Current, shorted Load

Vertical Deflection 2 v/cm

Horizontal Deflection 50 μs/cm

Data Channel 24

Notes:

No current was observed on east channel due to internal short in channel.

Firing No. X-MHD-5 Date June 20, 1974

Charge Specifications:

Composition C-4 Weight: 200 gm

Seed ($CsNO_3$) Weight: 2.7 gm/side (surface)

Standoff Material: 12 gm/side

Driver Location: East Channel

Fill Gas: Air . Initial Pressure: 10 Torr.

Magnet Current: 11,000 amps.

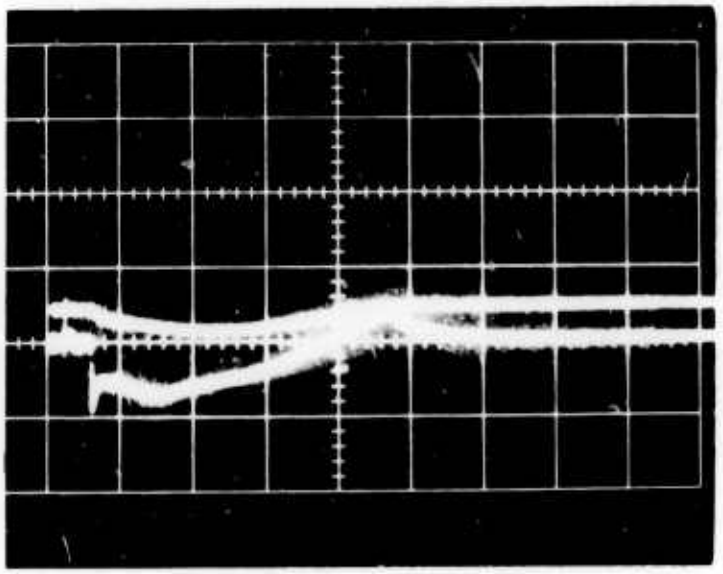

Upper Trace: East Channel Current, $25 \times 10^{-3}\ \Omega$ Load

Vertical Deflection 10 v/cm

Horizontal Deflection 50 μs/cm

Data Channel 25

Lower Trace: West Channel Voltage, $4.89 \times 10^{-3}\ \Omega$ Load

Vertical Deflection 20 v/cm

Horizontal Deflection 50 μs/cm

Data Channel 21

X-MHD-5 (Continued)

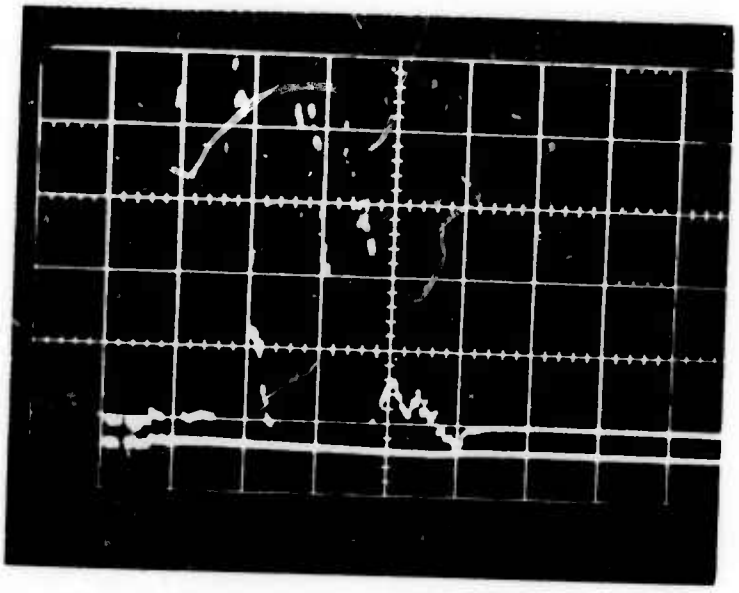

Upper Trace: West Channel Ionization Pins

4.89×10^{-3} Load, * Pin Spacing

Vertical Deflection 10 v/cm

Horizontal Deflection 50 μs/cm

Data Channel 22

Lower Trace: _____ Channel Ionization Pins

_____ Load, _____ Pin Spacing

Vertical Deflection ____ v/cm

Horizontal Deflection ____ μs/cm

Data Channel _____

Notes:

*Pin No. 1 located 24.8 cm from scope trigger pin.
Pin No. 2 located 20.8 cm from pin No. 1.
Pin No. 3 located 41.6 cm from pin No. 1.
Pin No. 4 located 59.4 cm from pin No. 1.

Firing No. X-MHD-6 Date June 24, 1974

Charge Specifications:

Composition C-4 Weight: 100 gm

Seed ($CsNO_3$) Weight: 2.7 gm/side (surface)

Standoff Material: 12.6 gm/side

Driver Location: East Channel

Fill Gas: Helium . Initial Pressure: 5 Torr.

Magnet Current: 11,000 amps.

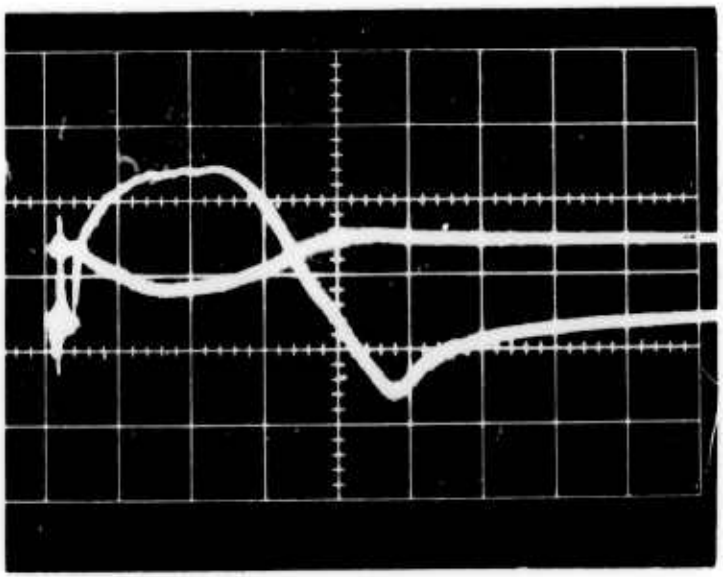

Upper Trace: East Channel Current, $25 \times 10^{-3}\ \Omega$ Load

Vertical Deflection 5 v/cm

Horizontal Deflection 50 μs/cm

Data Channel 25

Lower Trace: East Channel Voltage, $25 \times 10^{-3}\ \Omega$ Load

Vertical Deflection 20 v/cm

Horizontal Deflection 50 μs/cm

Data Channel 23

X-MHD-6 (Continued)

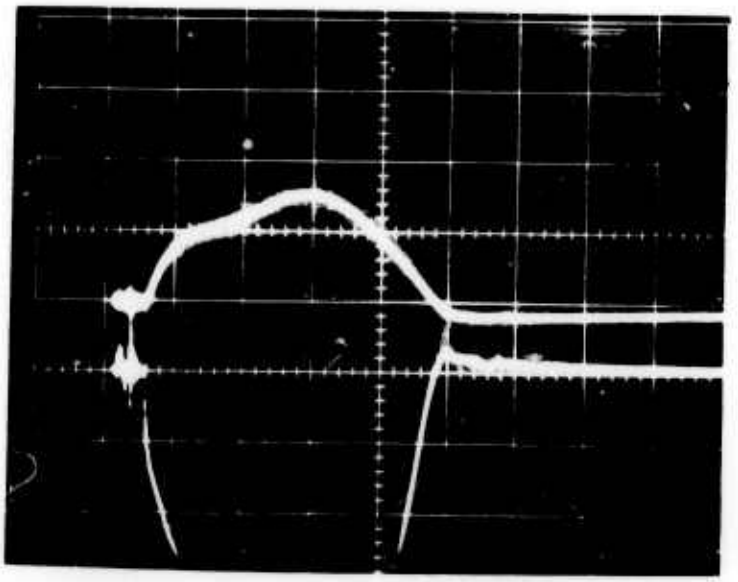

Upper Trace: West Channel Current, $4.89 \times 10^{-3}\Omega$ Load

Vertical Deflection 5 v/cm

Horizontal Deflection 50 μs/cm

Data Channel 24

Lower Trace: West Channel Voltage, $4.89 \times 10^{-3}\Omega$ Load

Vertical Deflection 20 v/cm

Horizontal Deflection 50 μs/cm

Data Channel 21

Notes:

Voltage across 4.89 mΩ load is larger than voltage across 25 mΩ load. This could indicate voltage leads were incorrectly identified.

X-MHD-6 (Continued)

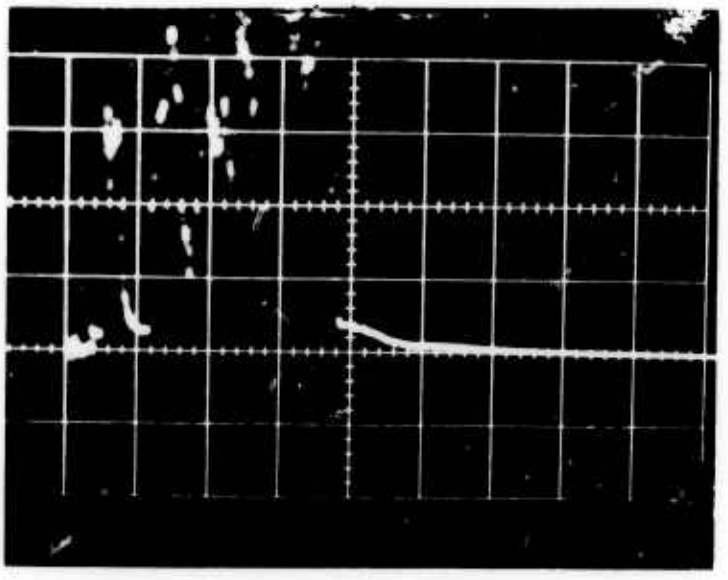

Upper Trace: West Channel Ionization Pins

$4.89 \times 10^{-3}\ \Omega$ Load * Pin Spacing

Vertical Deflection ____ v/cm

Horizontal Deflection 50 μs/cm

Data Channel 22

Lower Trace: _____ Channel Ionization Pins

_____ Load, _____ Pin Spacing

Vertical Deflection ____ v/cm

Horizontal Deflection ____ μs/cm

Data Channel _____

Notes:

*Refer to Test No. 5.

Firing No. X-MHD-7 Date June 24, 1974

Charge Specifications:

Composition C-4 Weight: 100 gm

Seed ($CsNO_3$) Weight: 2.7 gm/side (surface)

Standoff Material: 12.5 gm/side

Driver Location: East Channel

Fill Gas: Helium . Initial Pressure: 650 Torr.

Magnet Current: 11,000 amps.

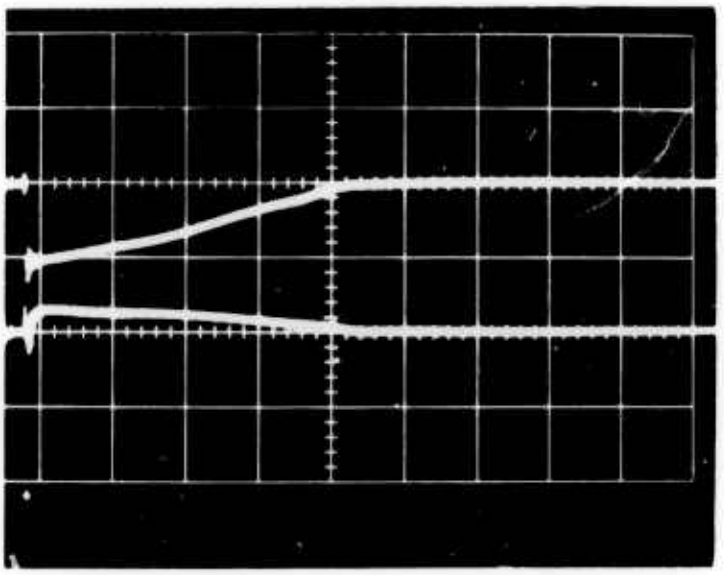

Upper Trace: West Channel Voltage, 975 Ω Load

Vertical Deflection 5 v/cm

Horizontal Deflection 50 μs/cm

Data Channel 21 with 10X attenuation

Lower Trace: East Channel Voltage, 994 Ω Load

Vertical Deflection * v/cm

Horizontal Deflection 50 μs/cm

Data Channel 23 with 10X attenuation

*Vertical deflection uncalibrated, correction factor of 2.8 times the setting of 5 v/cm should be used.

X-MHD-7 (Continued)

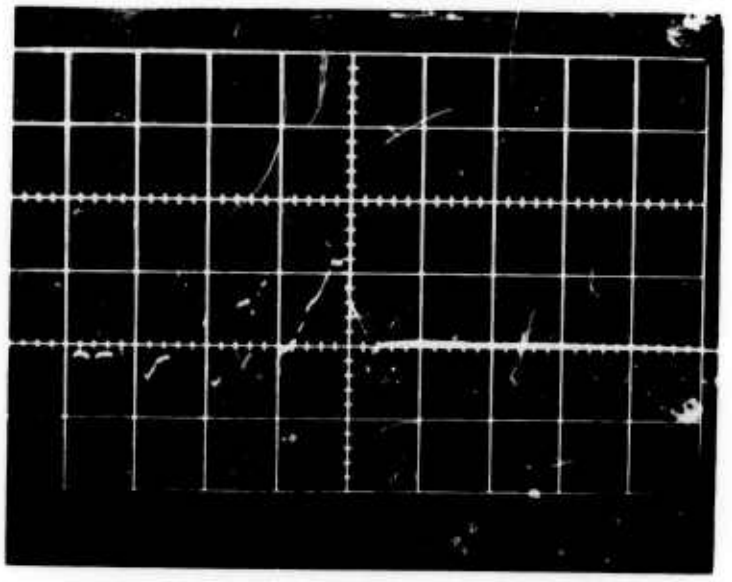

Upper Trace: West Channel Ionization Pins
975 Ω Load, * Pin Spacing
Vertical Deflection ____ v/cm
Horizontal Deflection 50 μs/cm
Data Channel 22

Lower Trace: _____ Channel Ionization Pins
_____ Load, _____ Pin Spacing
Vertical Deflection ____ v/cm
Horizontal Deflection ____ μs/cm
Data Channel _____

Notes:

*Refer to test No. 5.

Firing No. X-MHD-8 Date June 24, 1974

Charge Specifications:

Composition C-4 Weight: _____

Seed ($CsNO_3$) Weight: _____

Standoff Material: _____

Driver Location: _____ Channel

Fill Gas: Helium . Initial Pressure: 5 Torr.

Magnet Current: 11,000 amps.

No data obtained due to failure of scopes to trigger properly.

Upper Trace: _____ Channel _____ 1000 Ω Load

Vertical Deflection ____ v/cm

Horizontal Deflection ____ μs/cm

Data Channel ____

Lower Trace: _____ Channel _____ 1000 Ω Load

Vertical Deflection ____ v/cm

Horizontal Deflection ____ μs/cm

Data Channel ____

Firing No. X-MHD-9 Date June 25, 1974

Charge Specifications:

Composition C-4 Weight: 100 gm

Seed ($CsNO_3$) Weight: 2.7 gm/side (surface)

Standoff Material: 12.5 gm/side

Driver Location: East Channel

Fill Gas: Helium* . Initial Pressure: 11 Torr.

Magnet Current: 11,000 amps.

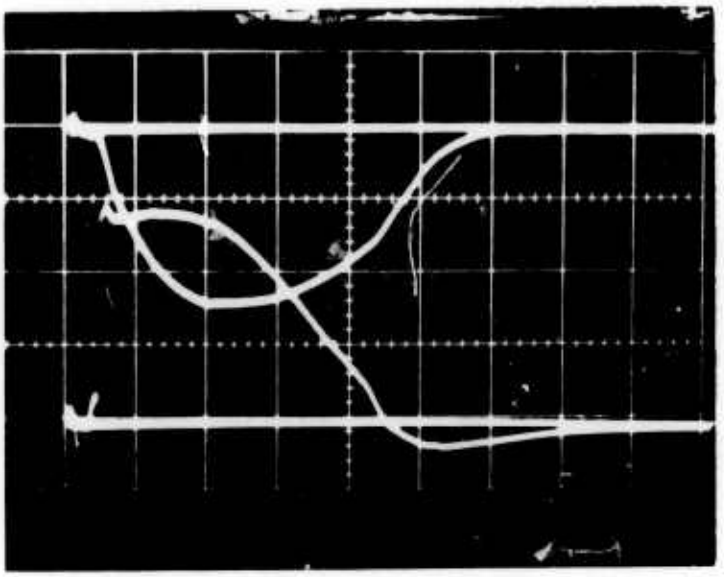

Upper Trace: West Channel Voltage, 975 Ω Load

Vertical Deflection 20 v/cm

Horizontal Deflection 50 μs/cm

Data Channel 21

Lower Trace: East Channel Voltage, 994 Ω Load

Vertical Deflection 20 v/cm

Horizontal Deflection 50 μs/cm

Data Channel 23

*Leak in channel-gas was probably helium-air mixture.

X-MHD-9 (Continued)

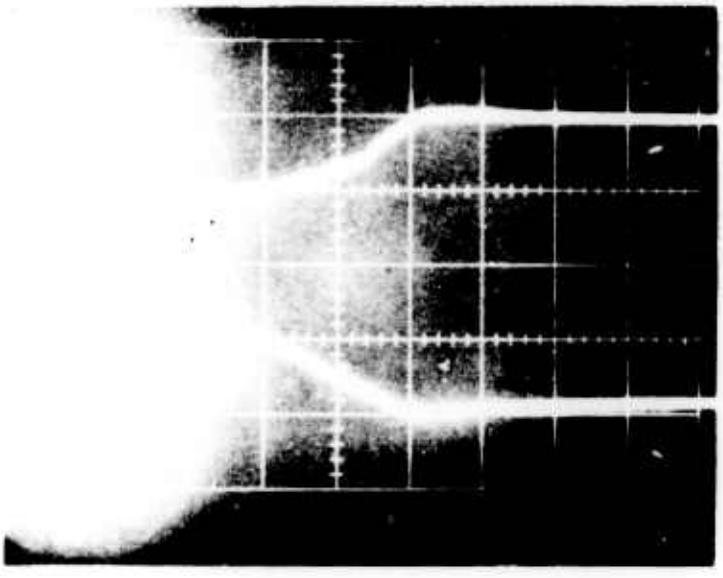

Upper Trace: West Channel Voltage, 975 Ω Load

Vertical Deflection 5 v/cm

Horizontal Deflection 50 μs/cm

Data Channel 21 with 10X attenuation

Lower Trace: East Channel Voltage, 994 Ω Load

Vertical Deflection 5 v/cm

Horizontal Deflection 50 μs/cm

Data Channel 23 with 10X attenuation

Notes:

On disassembly, "O" ring was found to be out of groove at combustion-channel interface. This may have caused air to leak into channel.

X-MHD-9 (Continued)

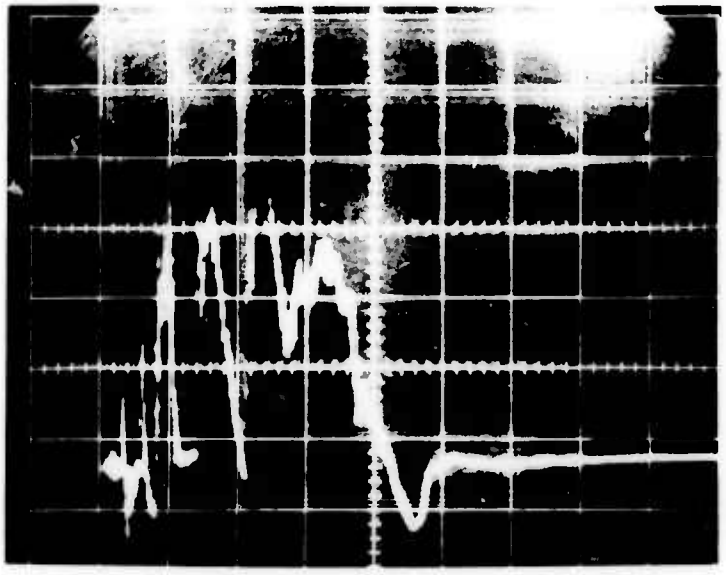

Upper Trace: West Channel Ionization Pins
975 Ω Load, * Pin Spacing
Vertical Deflection 20 v/cm
Horizontal Deflection 50 μs/cm
Data Channel 22

Lower Trace: _____ Channel Ionization Pins
_____ Load, _____ Pin Spacing
Vertical Deflection ____ v/cm
Horizontal Deflection ____ μs/cm
Data Channel _____

Notes:

*Refer to Test No. 5.

Firing No. X-MHD-10 Date June 27, 1974

Charge Specifications:

Composition C-4 Weight: 100 gm

Seed ($CsNO_3$) Weight: 2.7 gm/side

Standoff Material: 12.5 gm/side

Driver Location: West Channel

Fill Gas: Helium . Initial Pressure: 2 Torr.

Magnet Current: 11,000 amps.

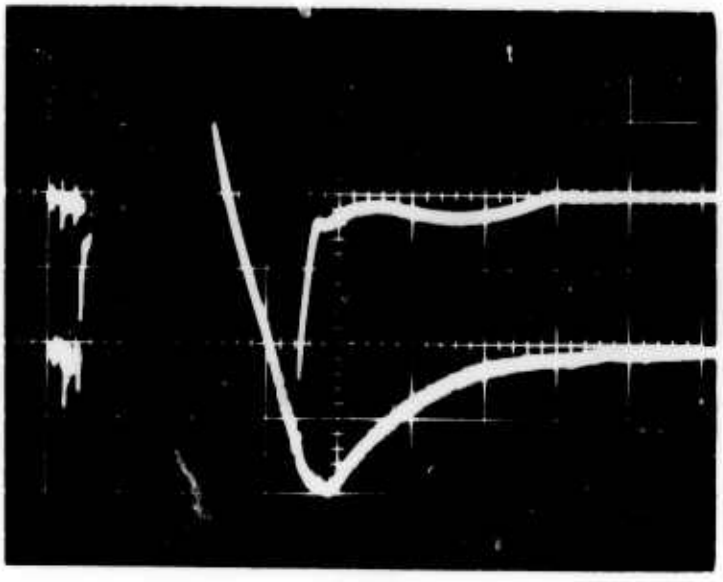

Upper Trace: West Channel Voltage, 975 Ω Load

Vertical Deflection 5 v/cm

Horizontal Deflection 50 μs/cm

Data Channel 21 with 10X attenuation

Lower Trace: East Channel Voltage, 994 Ω Load

Vertical Deflection 5 v/cm

Horizontal Deflection 50 μs/cm

Data Channel 23 with 10X attenuation

X-MHD-10 (Continued)

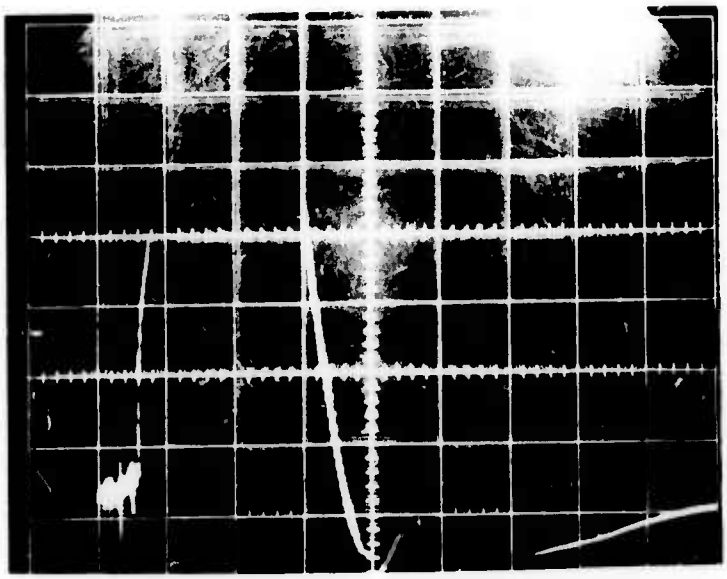

Upper Trace: West Channel Ionization Pins

975 Ω Load, * Pin Spacing

Vertical Deflection ____ v/cm

Horizontal Deflection ____ μs/cm

Data Channel 22

Lower Trace: _____ Channel Ionization Pins

_____ Load, _____ Pin Spacing

Vertical Deflection ____ v/cm

Horizontal Deflection ____ μs/cm

Data Channel _____

Notes:

Ionization pin lead wire apparently shorted to high potential electrode

*Refer to Test No. 5.

Firing No. X-MHD-11 Date June 28, 1974

Charge Specifications:

Composition C-4 Weight: 100 gm

Seed ($CsNO_3$) Weight: 2.5 gm/side (surface)

Standoff Material: 12.5 gm/side

Driver Location: East Channel

Fill Gas: Helium . Initial Pressure: 2 Torr.

Magnet Current: 11,000 amps.

Data lost when scopes failed to trigger properly.

Upper Trace: _____ Channel _____ Load

Vertical Deflection ____ v/cm

Horizontal Deflection ____ μs/cm

Data Channel ____

Lower Trace: _____ Channel _____ Load

Vertical Deflection ____ v/cm

Horizontal Deflection ____ μs/cm

Data Channel ____

Firing No. X-MHD-12 Date July 2, 1974

Charge Specifications:

Composition C-4 Weight: 100 gm

Seed ($CsNO_3$) Weight: 2.5 gm/side (surface)

Standoff Material: 12.5 gm/side

Driver Location: East Channel

Fill Gas: Helium . Initial Pressure: 2.5 Torr.

Magnet Current: 9,500 amps.

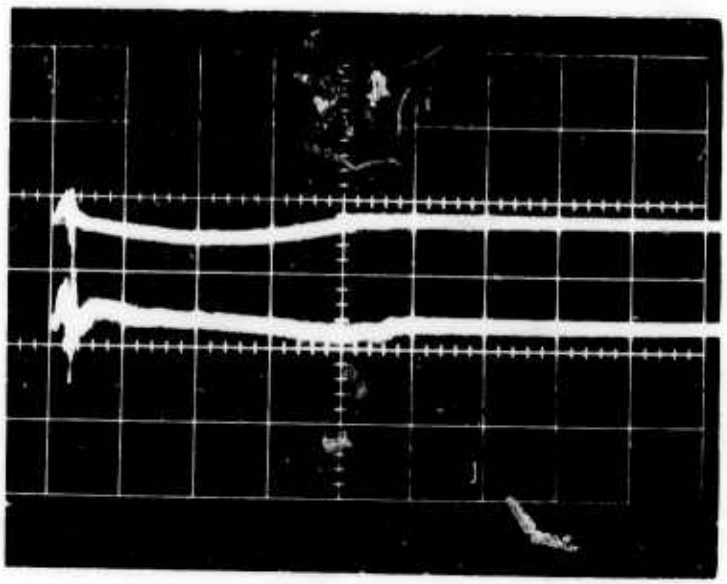

Upper Trace: East Channel Current, $4.89 \times 10^{-3}\Omega$ Load

Vertical Deflection 20 v/cm

Horizontal Deflection 50 μs/cm

Data Channel 25

Lower Trace: East Channel Voltage, $4.89 \times 10^{-3}\Omega$ Load

Vertical Deflection 10 v/cm

Horizontal Deflection 50 μs/cm

Data Channel 23 with 10X attenuation

Note: No data on west channel due to failure of scope to trigger properly.

Firing No. X-MHD-13 Date July 3, 1974

Charge Specifications:

Composition C-4 Weight: 100 gm

Seed ($CsNO_3$) Weight: 2.5 gm/side (surface)

Standoff Material: 12.5 gm/side

Driver Location: East Channel

Fill Gas: Helium . Initial Pressure: 2.5 Torr.

Magnet Current: 9,500 amps.

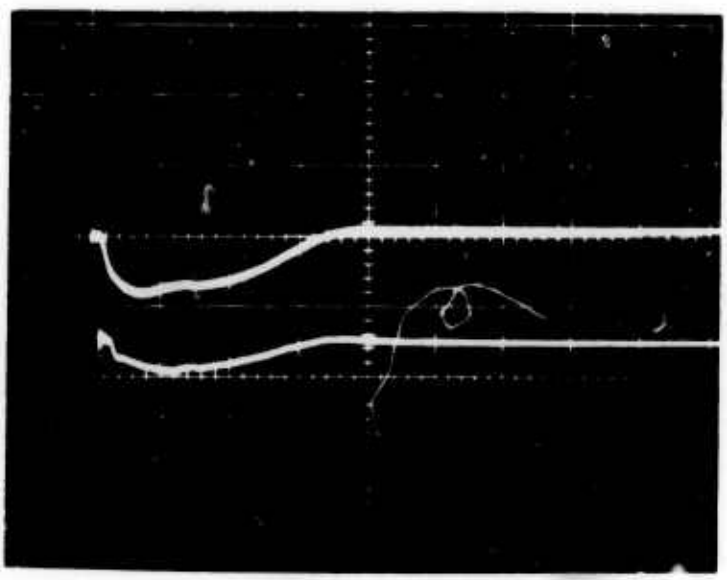

Upper Trace: West Channel Current, $8.42 \times 10^{-3}\ \Omega$ Load

Vertical Deflection 10 v/cm

Horizontal Deflection 50 μs/cm

Data Channel 24

Lower Trace: West Channel Voltage, $8.42 \times 10^{-3}\ \Omega$ Load

Vertical Deflection 5 v/cm

Horizontal Deflection 50 μs/cm

Data Channel 21 with 10X attenuation

X-MHD-13 (Continued)

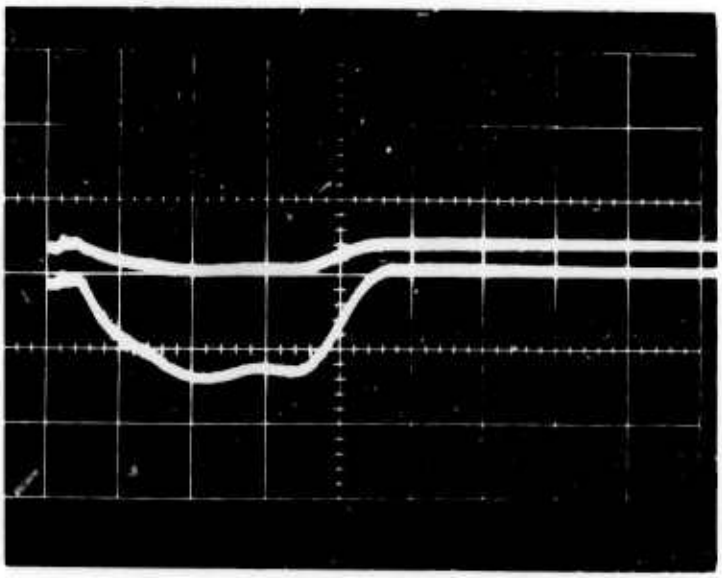

Upper Trace: East Channel Current, shorted Load

Vertical Deflection 20 v/cm

Horizontal Deflection 50 μs/cm

Data Channel 25

Lower Trace: East Channel Current, shorted Load

Vertical Deflection 5 v/cm

Horizontal Deflection 50 μs/cm

Data Channel 25

Notes:

Firing No. X-MHD-14 Date July 9, 1974

Charge Specifications:

Composition C-4 Weight: 100 gm

Seed ($CsNO_3$) Weight: 2.5 gm/side (surface)

Standoff Material: 12.5 gm/side

Driver Location: East Channel

Fill Gas: Helium . Initial Pressure: 3 Torr.

Magnet Current: 9,500 amps.

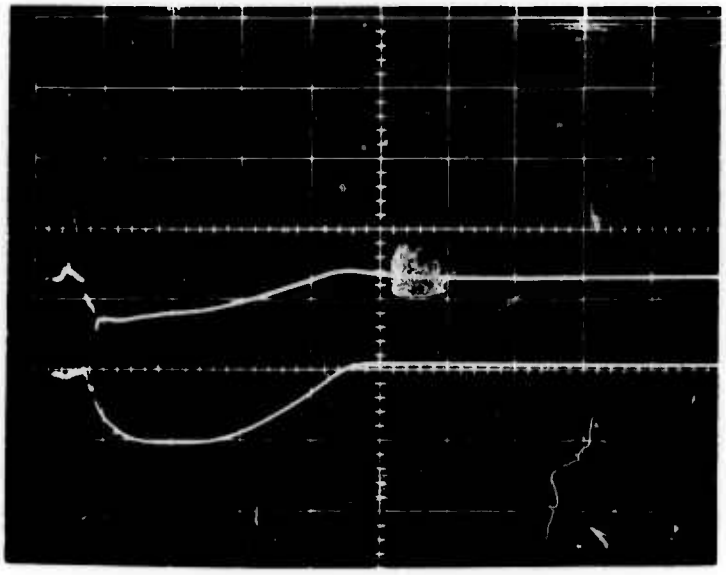

Upper Trace: West Channel Voltage, $8.42 \times 10^{-3}\ \Omega$ Load

Vertical Deflection 5 v/cm

Horizontal Deflection 50 μs/cm

Data Channel 21 with 10X attenuation

Lower Trace: West Channel Current, $8.42 \times 10^{-3}\ \Omega$ Load

Vertical Deflection 10 v/cm

Horizontal Deflection 50 μs/cm

Data Channel 24

X-MHD-14 (Continued)

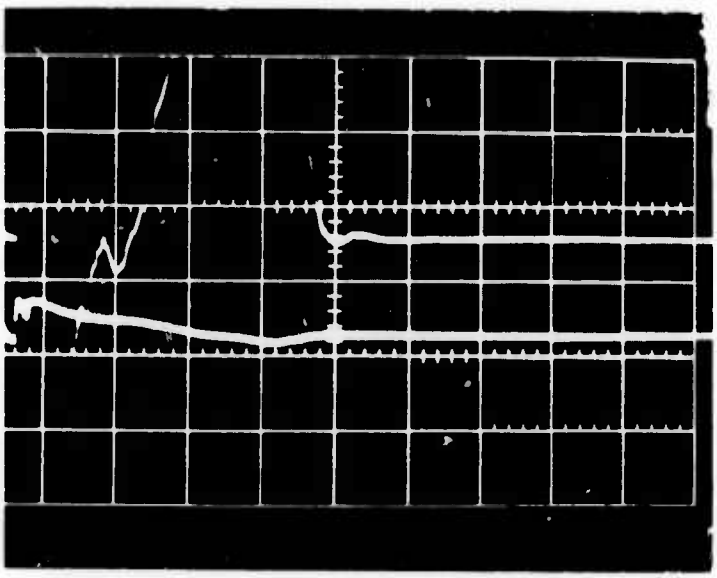

Upper Trace: West Channel $\frac{di}{dt}$, 8.42×10^{-3} Ω Load

Vertical Deflection 20 v/cm

Horizontal Deflection 50 μs/cm

Data Channel 24

Lower Trace: East Channel Voltage, 994 Ω Load

Vertical Deflection 20 v/cm

Horizontal Deflection 50 μs/cm

Data Channel 23 with 10X attenuation

Notes:

X-MHD-14 (Continued)

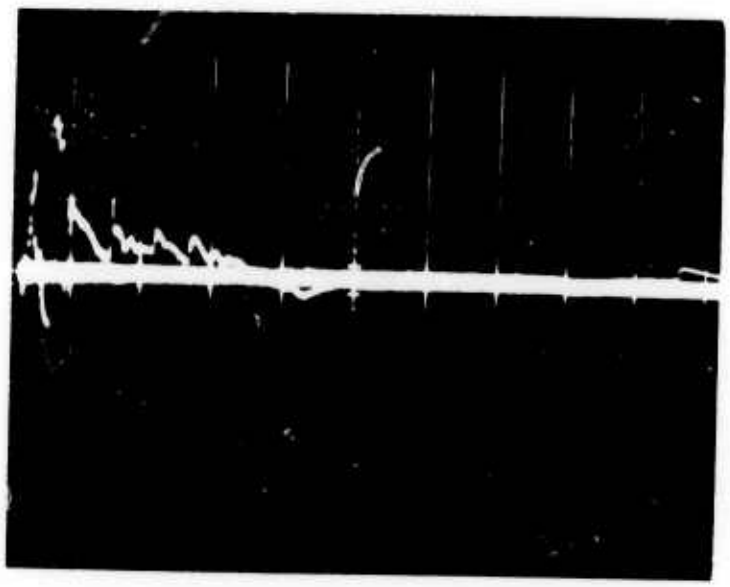

Upper Trace: West Channel Ionization Pins

8.42×10^{-3} Ω Load, * Pin Spacing

Vertical Deflection 20 v/cm

Horizontal Deflection 50 μs/cm

Data Channel 22

Lower Trace: _____ Channel Ionization Pins

_____ Load, _____ Pin Spacing

Vertical Deflection ____ v/cm

Horizontal Deflection ____ μs/cm

Data Channel _____

Notes:

Contact surfaces on load and channel were sanded before attaching load to channel.

*Refer to Test No. 5.

Firing No. XMHD-15 Date August 14, 1974

Charge Specifications:

Composition C-4 Weight: 100 gm.

Seed ($CsNO_3$) Weight: 2.5 gm/side (surface)

Standoff Material: 12.5 gm/side

Driver Location: East Channel

Fill Gas: Helium . Initial Pressure: 2.5 Torr.

Magnet Current: 10,500 amps.

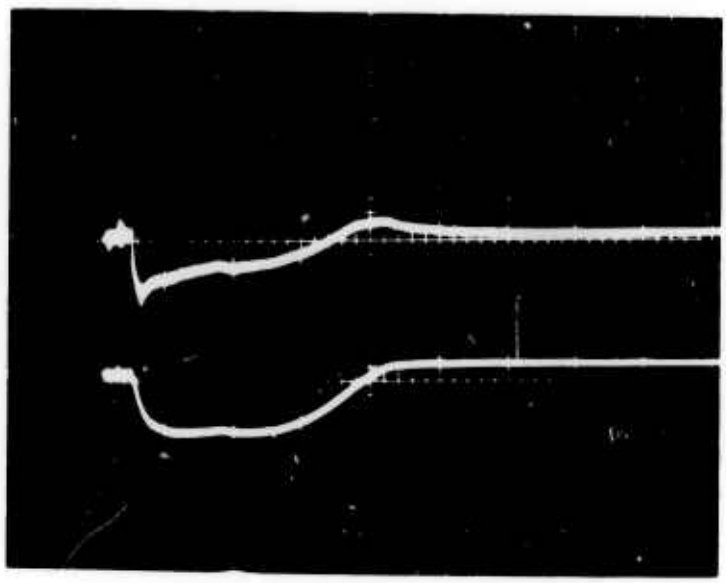

Upper Trace: West Channel Voltage, 8.22×10^{-3} Ω Load

Vertical Deflection 5 v/cm x 10

Horizontal Deflection 50 μs/cm

Data Channel 21

Lower Trace: West Channel Current, 8.22×10^{-3} Ω Load

Vertical Deflection 10 v/cm

Horizontal Deflection 50 μs/cm

Data Channel 24

XMHD-15 (Continued)

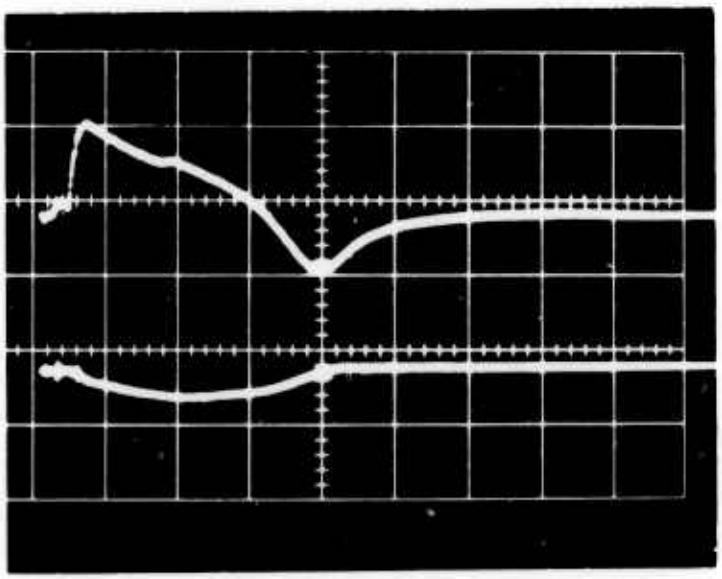

Upper Trace: East Channel Voltage, $8.42 \times 10^{-3}\Omega$ Load

Vertical Deflection 5 v/cm

Horizontal Deflection 50 μs/cm

Data Channel 23

Lower Trace: East Channel Current, $8.42 \times 10^{-3}\Omega$ Load

Vertical Deflection 10 v/cm

Horizontal Deflection 50 μs/cm

Data Channel 25

Notes:

XMHD-15 (Continued)

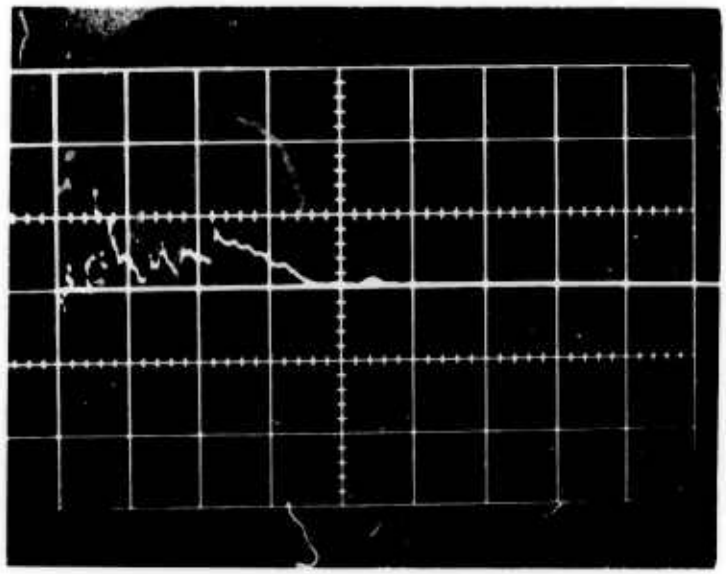

Upper Trace: West Channel Ionization Pins

$8.22 \times 10^{-3}\Omega$ Load, * Pin Spacing

Vertical Deflection 20 v/cm

Horizontal Deflection 50 μs/cm

Data Channel 8

Lower Trace: _____ Channel Ionization Pins

_____ Load, _____ Pin Spacing

Vertical Deflection _____ v/cm

Horizontal Deflection _____ μs/cm

Data Channel _____

Notes:

*Refer to Test No. 5.

Firing No. XMHD-16 Date August 15, 1974

Charge Specifications:

Composition C-4 Weight: 100 gm.

Seed ($CsNO_3$) Weight: 2 5g/side + 5 gm bulk

Standoff Material: 12.5 gm/side

Driver Location: East Channel

Fill Gas: He-Ar . Initial Pressure: 3.5 Torr.

Magnet Current: 10,500 amps.

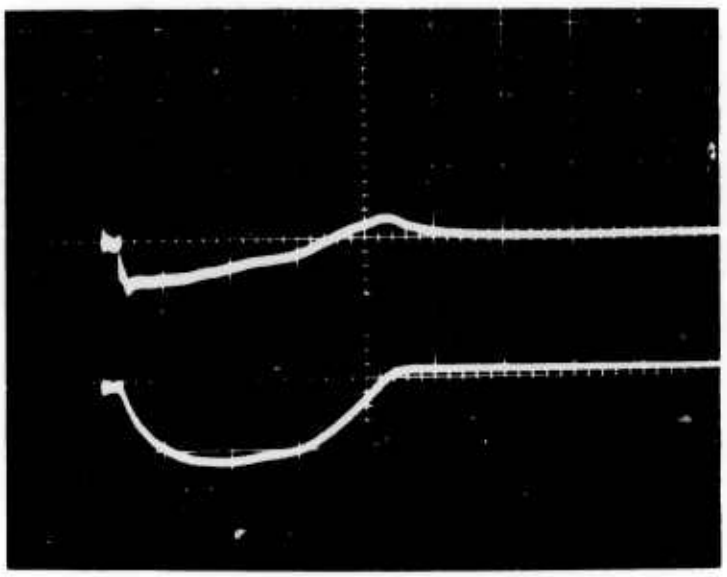

Upper Trace: West Channel Voltage, $4.89 \times 10^{-3}\Omega$ Load

Vertical Deflection 5 v/cm

Horizontal Deflection 50 μs/cm

Data Channel 21

Lower Trace: West Channel Current, $4.89 \times 10^{-3}\Omega$ Load

Vertical Deflection 10 v/cm

Horizontal Deflection 50 μs/cm

Data Channel 24

XMHD-16 (Continued)

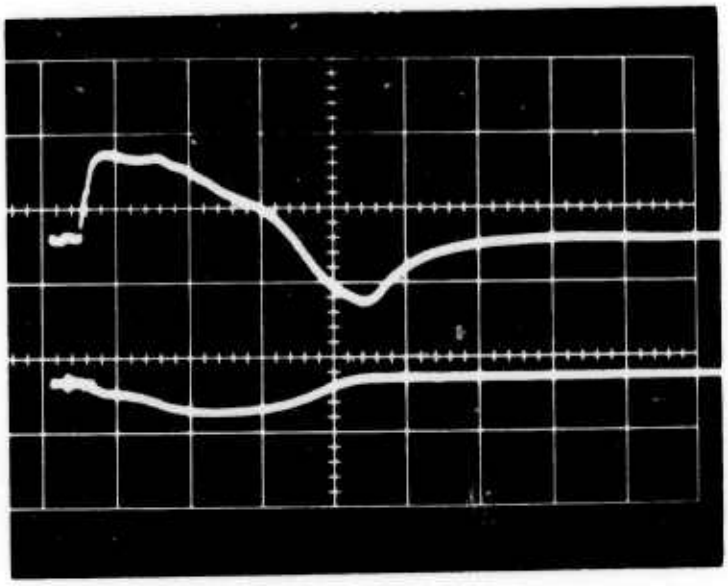

Upper Trace: East Channel Voltage, $8.42 \times 10^{-3}\ \Omega$ Load

Vertical Deflection 5 v/cm

Horizontal Deflection 50 μs/cm

Data Channel 23

Lower Trace: East Channel Current, $8.42 \times 10^{-3}\ \Omega$ Load

Vertical Deflection 10 v/cm

Horizontal Deflection 50 μs/cm

Data Channel 25

Notes:

XMHD-16 (Continued)

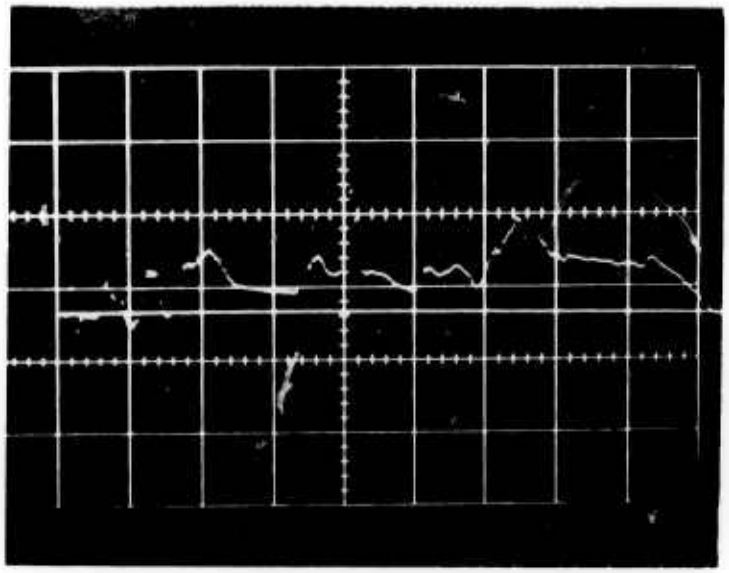

Upper Trace: West Channel Ionization Pins

$4.89 \times 10^{-3}\ \Omega$ Load, * Pin Spacing

Vertical Deflection 20 v/cm

Horizontal Deflection 20 μs/cm

Data Channel 8

Lower Trace: _____ Channel Ionization Pins

_____ Load, _____ Pin Spacing

Vertical Deflection ____ v/cm

Horizontal Deflection ____ μs/cm

Data Channel _____

Notes:

*Refer to Test No. 5.

Firing No. XMHD-17 Date August 16, 1974

Charge Specifications:

Composition C-4 Weight: 140 gm

Seed ($CsNO_3$) Weight: 5 gm/side (surface)

Standoff Material: None

Driver Location: East Channel

Fill Gas: He-Ar . Initial Pressure: 280 Torr.

Magnet Current: 10,500 amps.

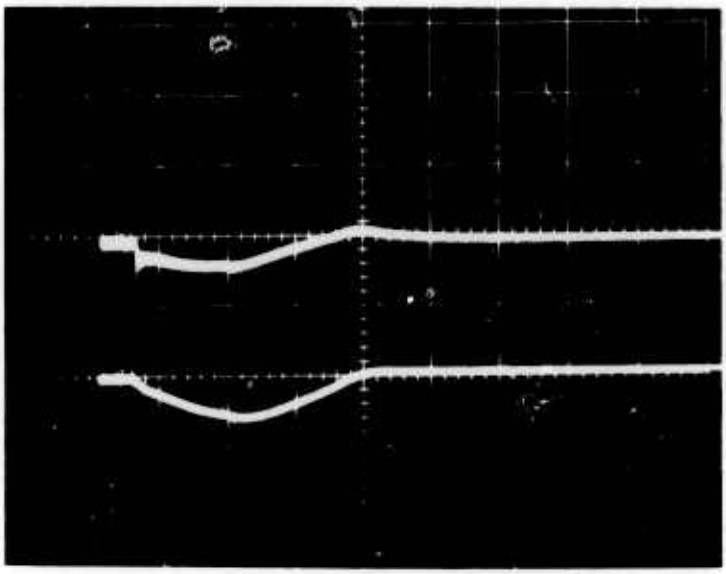

Upper Trace: West Channel Voltage, $8.22 \times 10^{-3}\Omega$ Load

Vertical Deflection 5 v/cm

Horizontal Deflection 50 μs/cm

Data Channel 21

Lower Trace: West Channel Current, $8.22 \times 10^{-3}\Omega$ Load

Vertical Deflection 10 v/cm

Horizontal Deflection 50 μs/cm

Data Channel 24

XMHD-17 (Continued)

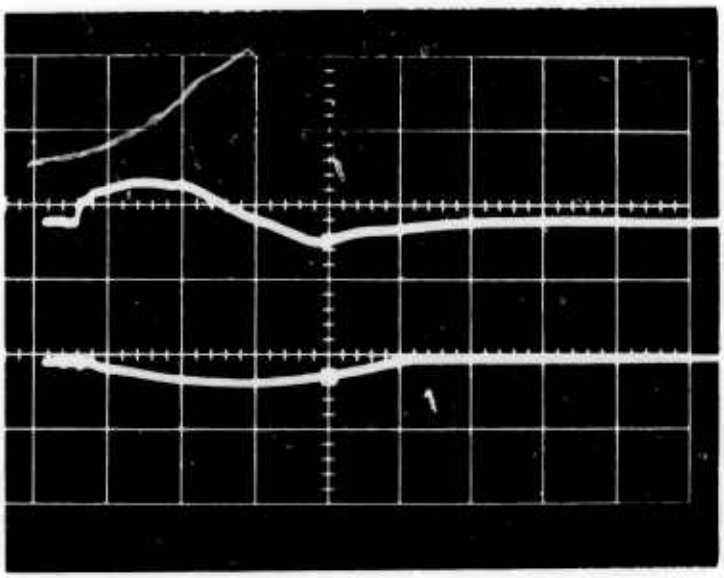

Upper Trace: East Channel Voltage, $8.42 \times 10^{-3} \Omega$ Load

Vertical Deflection 5 v/cm

Horizontal Deflection 50 μs/cm

Data Channel 23

Lower Trace: East Channel Current, $8.42 \times 10^{-3} \Omega$ Load

Vertical Deflection 5 v/cm

Horizontal Deflection 50 μs/cm

Data Channel 25

Notes:

XMHD-17 (Continued)

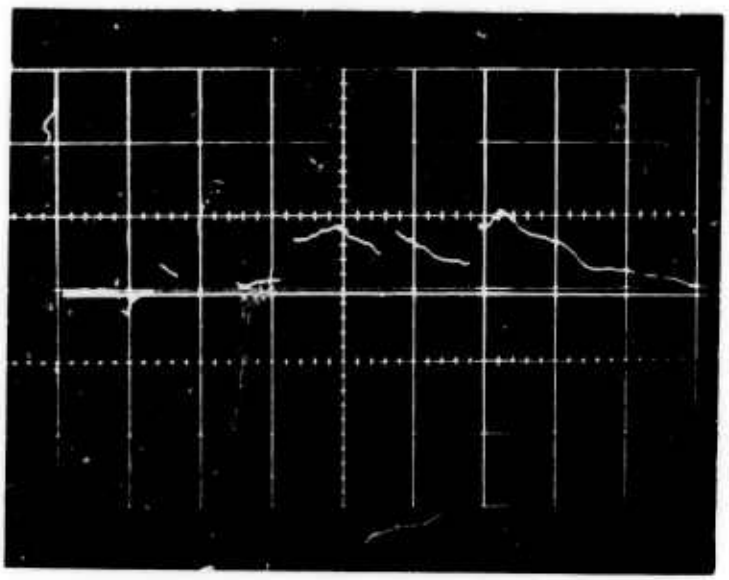

Upper Trace: West Channel Ionization Pins
8.22×10^{-3} Ω Load, * Pin Spacing
Vertical Deflection 20 v/cm
Horizontal Deflection 20 μs/cm
Data Channel 8

Lower Trace: _____ Channel Ionization Pins
_____ Load, _____ Pin Spacing
Vertical Deflection ____ v/cm
Horizontal Deflection ____ μs/cm
Data Channel _____

Notes:

*Refer to Test No. 5.

Firing No. XMHD-18 Date August 19, 1974

Charge Specifications:

Composition C-4 Weight: 140 gm.

Seed ($CsNO_3$) Weight: 5 gm/side (surface)

Standoff Material: None

Driver Location: West Channel

Fill Gas: He-Ar . Initial Pressure: 280 Torr.

Magnet Current: 10,500 amps.

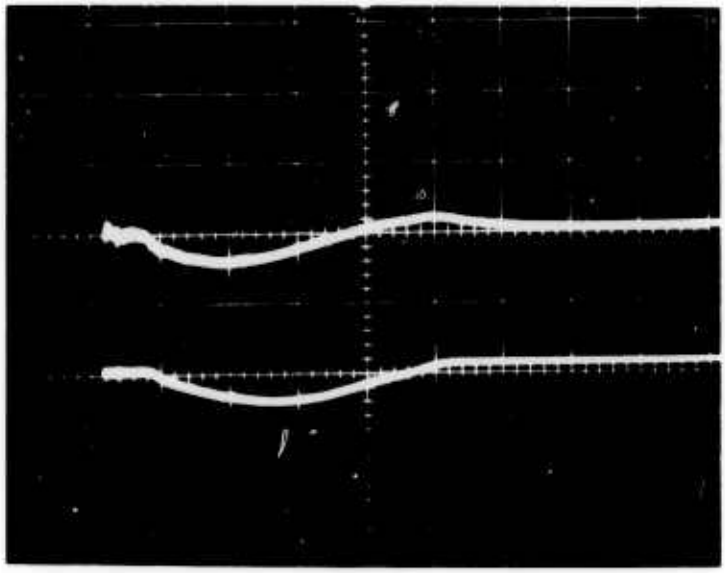

Upper Trace: West Channel Voltage, $8.22 \times 10^{-3}\Omega$ Load

Vertical Deflection 2 v/cm

Horizontal Deflection 50 μs/cm

Data Channel 21

Lower Trace: West Channel Current, $8.22 \times 10^{-3}\Omega$ Load

Vertical Deflection 5 v/cm

Horizontal Deflection 50 μs/cm

Data Channel 24

XMHD-18 (Continued)

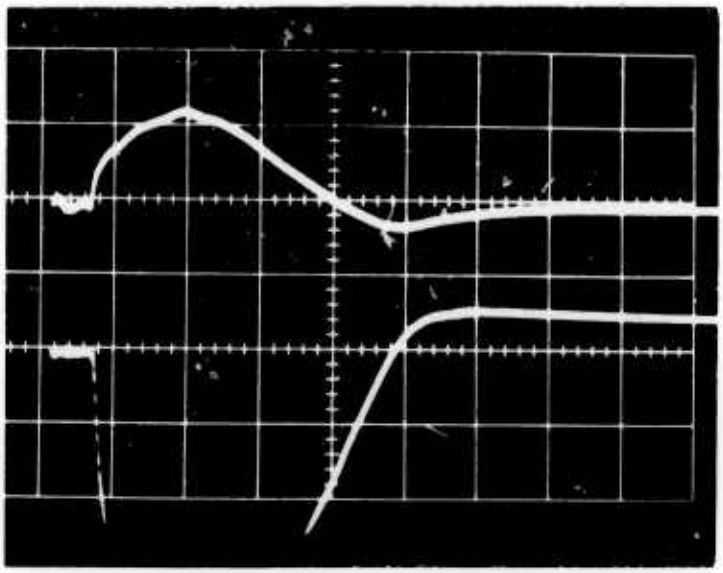

Upper Trace: East Channel Voltage, $8.42 \times 10^{-3}\ \Omega$ Load

Vertical Deflection 2 v/cm

Horizontal Deflection 50 μs/cm

Data Channel 23

Lower Trace: East Channel Current, $8.42 \times 10^{-3}\ \Omega$ Load

Vertical Deflection 2 v/cm

Horizontal Deflection 50 μs/cm

Data Channel 25

Notes:

Driver changed to west channel this test to determine if driver was causing lower power output in east channel.

XMHD-18 (Continued)

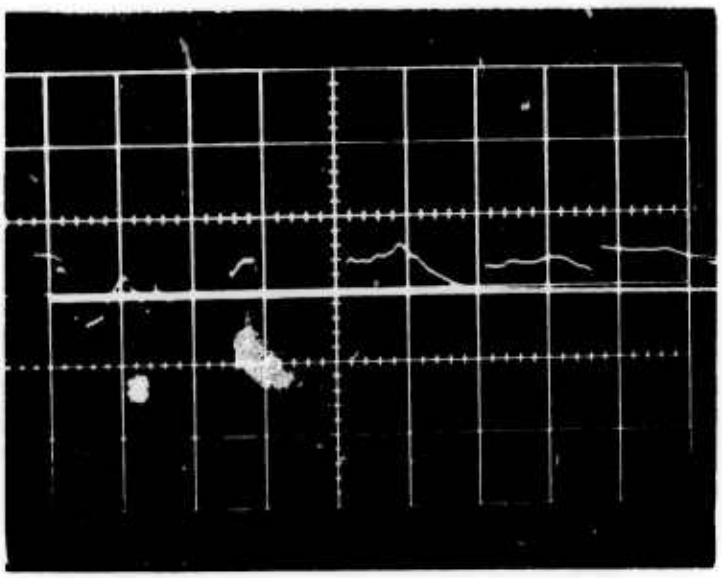

Upper Trace: West Channel Ionization Pins

$8.22 \times 10^{-3}\ \Omega$ Load, * Pin Spacing

Vertical Deflection 20 v/cm

Horizontal Deflection 20 μs/cm

Data Channel 8

Lower Trace: _____ Channel Ionization Pins

_____ Load, _____ Pin Spacing

Vertical Deflection _____ v/cm

Horizontal Deflection _____ μs/cm

Data Channel _____

Notes:

*Refer to Test No. 5.

Firing No. X-MHD-19 Date August 21, 1974

Charge Specifications:

Composition C-4 Weight: 100 gm.

Seed ($CsNO_3$) Weight: 5 gm/side

Standoff Material: None

Driver Location: * Channel

Fill Gas: He-Ar . Initial Pressure: 3 Torr.

Magnet Current: 10,500 amps.

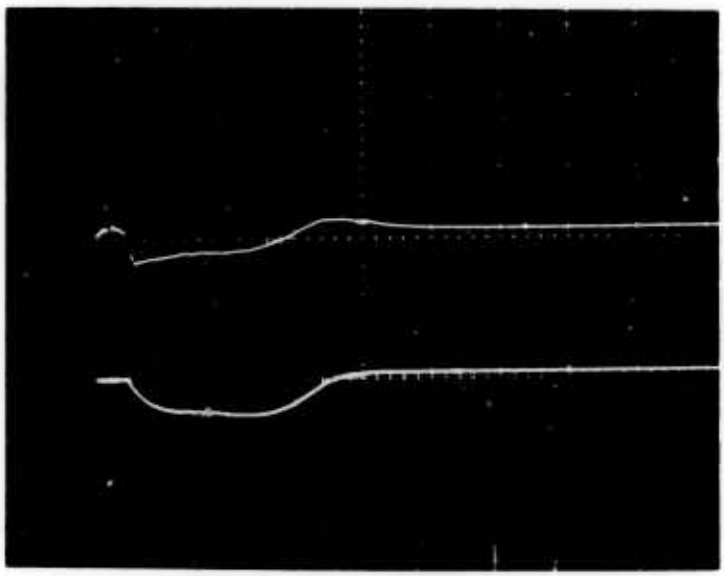

Upper Trace: West Channel Voltage, $8.22 \times 10^{-3}\Omega$ Load

Vertical Deflection 5 v/cm x 10

Horizontal Deflection 50 μs/cm

Data Channel 21

Lower Trace: West Channel Current, $8.22 \times 10^{-3}\Omega$ Load

Vertical Deflection 10 v/cm

Horizontal Deflection 50 μs/cm

Data Channel 24

*Cap placed perpendicular to channel axis at center of charge. One-fourth inch diameter x one-eighth inch thick deta sheet cemented to end of cap.

X-MHD-19 (Continued)

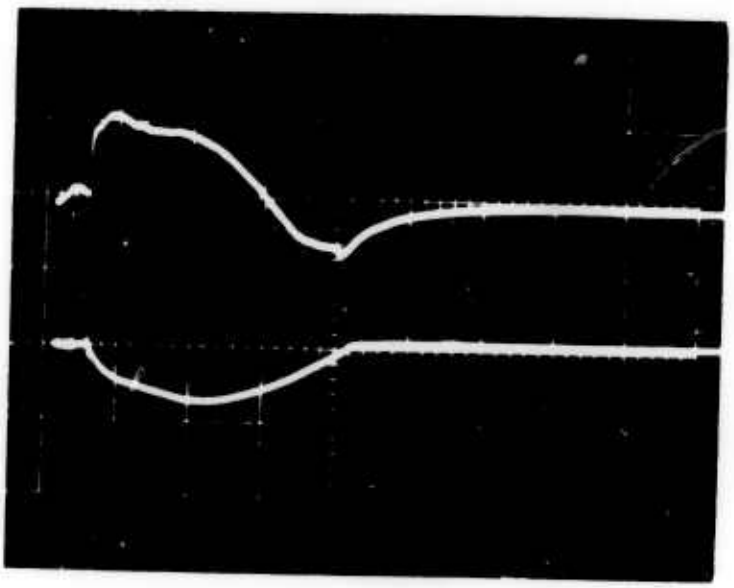

Upper Trace: East Channel Voltage, $8.42 \times 10^{-3}\Omega$ Load

Vertical Deflection 5 v/cm x 10

Horizontal Deflection 50 μs/cm

Data Channel 23

Lower Trace: East Channel Current, $8.42 \times 10^{-3}\Omega$ Load

Vertical Deflection 10 v/cm

Horizontal Deflection 50 μs/cm

Data Channel 25

Notes:

X-MHD-19 (Continued)

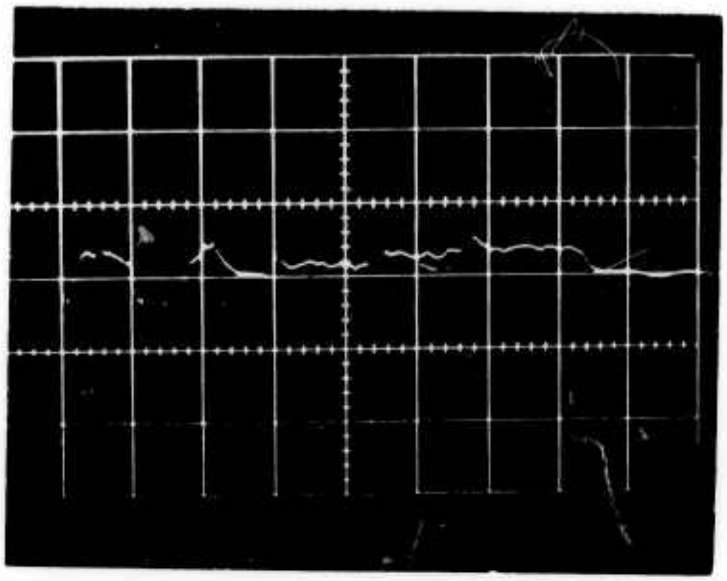

Upper Trace: West Channel Ionization Pins
$8.22 \times 10^{-3}\ \Omega$ Load, * Pin Spacing
Vertical Deflection 20 v/cm
Horizontal Deflection 20 μs/cm
Data Channel 8

Lower Trace: _____ Channel Ionization Pins
_____ Load, _____ Pin Spacing
Vertical Deflection ____ v/cm
Horizontal Deflection ____ μs/cm
Data Channel _____

Notes:

*See Test No. 5.

APPENDIX C

VOLTAGE, CURRENT AND ENERGY OUTPUT FOR SELECTED X-MHD TESTS

TIME (μs)	EAST CHANNEL				WEST CHANNEL			
	CURRENT		VOLTAGE		CURRENT		VOLTAGE	
	OUTPUT (V)	MEAS.* (kA)	OUTPUT (V)	MEAS.** (V)	OUTPUT (V)	MEAS.* (kA)	OUTPUT (V)	MEAS.** (V)
0	0	0	0	0	0	0		
10	0.2	2.1	0	0	2.3	24.4		
20	0.8	8.4	24	1080	3.8	40.5		
30	1.3	13.8	31	1400	4.5	48.4		
40	2.0	21.2	34	1530	5.0	54.1		
50	2.3	24.6	37	1670	5.3	57.8		
60	2.8	30.1	39	1760	5.6	61.6		
70	2.9	31.4	39	1760	6.0	66.4		
80	3.0	32.8	39	1760	6.3	70.2		
90	3.0	33.1	39.5	1780	7.0	78.3		
100	2.8	31.3	39.5	1780	7.3	82.2		
110	2.5	28.5	40	1800	7.7	87.2		
120	2.3	26.6	39	1760	7.8	89.1		
130	2.0	23.7	36	1620	7.3	84.6		
140	1.5	18.7	30	1350	7.0	82.2		
150	1.1	14.6	24	1080	6.3	75.5		
160	0.6	9.5	16	720	5.5	67.7		
170	0.2	5.3	10	450	4.4	56.6		
180	-0.2	1.2	5	225	3.6	48.6		
190	-0.	1.0	0	0	2.5	37.3		
200	-0.6	- 3.1	- 6	- 270	1.4	25.9		
210	-0.7	- 4.2	-12	- 540	0.2	13.3		
220	-0.7	- 4.3	-17	- 765	-0.6	4.9		
230	-0.5	- 2.3	-20	- 900	-0.8	2.7		
240	-0.4	- 1.3	-16	- 720	-0.9	1.5		
250	-0.3	- 0.3	-12	- 540	-0.9	1.4		
260	-0.3	- 0.3	-10	- 450	-0.9	1.3		

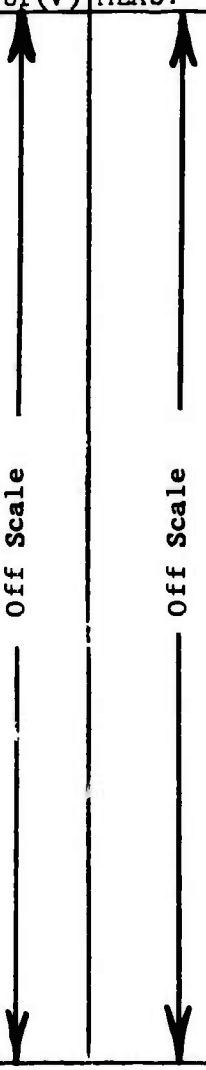

* $i = (10.4 \times 10^3 \text{ A/V})[v_o + (10^3/s)\int_o^t v_o dt]$

** $v = (45.0)\, v_m$

$\int vidt \cong 5.79$ kJ

$\int_o^T i^2 R dt \cong (9.18 \times 10^4 \text{ J}/\Omega)(25 \times 10^{-3}\ \Omega) = 2.3$ kJ

* $i = (10.5 \times 10^3 \text{ A/V})[v_o + (10^3/s)\int_o^t v_o dt]$

$\int i^2 R dt \cong (8.44 \times 10^5 \text{ J}/\Omega)(4.89 \times 10^{-3}\ \Omega) = 4.13$ kJ

TIME (μs)	EAST CHANNEL				WEST CHANNEL			
	CURRENT		VOLTAGE		CURRENT		VOLTAGE	
	OUTPUT (V)	MEAS.* (kA)	OUTPUT (V)	MEAS.** (V)	OUTPUT (V)	MEAS.* (kA)	OUTPUT (V)	MEAS.** (V)
0	0	0	0	0				
10	-3.5	-36.8	+3.0	+1350				
20	1.0	10.1	-1.0	- 450				
30	2.0	20.7	+2.0	+ 900				
40	2.5	26.2	1.8	810				
50	3.5	37.0	1.2	540				
60	4.0	42.6	0.9	405				
70	4.0	43.0	0.8	360				
80	4.5	48.7	0.7	315				
90	5.0	54.4	0.6	270				
100	5.0	54.9	0.5	225				
110	5.5	60.7	0.4	180				
120	5.5	61.3	0.3	135				
130	5.5	61.8	0.2	90				
140	5.0	57.1	0.0	0	NO DATA OBTAINED DUE TO FAILURE			
150	4.5	52.4	-0.1	- 45				
160	4.0	47.6	-0.2	- 90	OF SCOPE TO TRIGGER			
170	3.0	37.5	-0.5	- 225				
180	2.5	32.6	-0.8	- 360				
190	1.5	22.4	-1.0	- 450				
200	1.0	17.3	-1.0	- 450				
210	0.0	6.9	-0.8	- 360				
220	-0.5	1.6	-0.5	- 225				
230	-0.5	1.6	-0.5	- 225				
240	-0.5	1.5	- 0.2	- 90				
250	-0.5	1.5	0	0				

* $i = (10.4 \times 10^3 A/V)[v_o + (10^3/s)\int_o^t v_o dt]$

** $v = (450)\, v_m$

$\int vidt \cong 1.08$ kJ

$\int i^2 R dt \cong (3.75 \times 10^5 J/\Omega)(4.89 \times 10^{-3} \Omega) = 1.83$ kJ

TIME (μs)	EAST CHANNEL CURRENT OUTPUT (V)	EAST CHANNEL CURRENT MEAS.* (kA)	EAST CHANNEL VOLTAGE OUTPUT (V)	EAST CHANNEL VOLTAGE MEAS.** (V)	WEST CHANNEL CURRENT OUTPUT (V)	WEST CHANNEL CURRENT MEAS.* (kA)	WEST CHANNEL VOLTAGE OUTPUT (V)	WEST CHANNEL VOLTAGE MEAS.** (V)
0	0	0	Short Circuit		0	0	0	0
10	1.25	13.1			6.0	63.6	0	0
20	3.0	31.6			7.5	80.2	1.3	560
30	3.75	39.8			8.5	91.6	1.6	690
40	4.25	45.5			8.1	88.2	2.0	862
50	5.0	53.8			7.5	82.7	2.1	905
60	5.5	59.6			7.2	80.3	2.0	862
70	6.1	66.4			7.5	84.2	1.9	819
80	6.5	71.3			7.0	79.7	1.9	819
90	6.7	74.1			6.7	77.3	1.75	754
100	6.5	72.6			6.2	72.7	1.5	647
110	6.25	70.7			5.5	65.9	1.3	560
120	6.0	68.7			4.7	58.0	1.0	431
130	6.0	69.3			3.5	45.8	0.75	323
140	6.1	71.0			2.5	35.5	0.5	216
150	6.2	72.7	0	0	1.5	25.2	0.2	86
160	5.75	68.6			0.5	14.7	0.0	0
170	4.5	56.1			-0.2	7.4	-0.2	- 86
180	2.75	38.2			-0.7	2.1	-0.2	- 86
190	1.1	21.1			-0.8	0.9	-0.1	- 43
200	0.0	9.7			-0.8	0.8		
210	-0.5	4.4			-0.8	0.7		
220	-0.75	1.8			-0.8	0.7		
230	-0.75	1.7			-0.8	0.6		
240	-0.75	1.6			-0.8	0.5		
250	-0.75	1.5			-0.8	0.4		

* $i = (10.4\text{x}10^3 \text{A/V})[v_o + (10^3/\text{s})\int_o^t v_o dt]$

* $i = (10.5\text{x}10^3 \text{A/V})[v_o + (10^3/\text{s})\int_o^t v_o dt]$

** $v = (431)\, v_m$

$\int vidt \cong 6.52$ kJ

$\int i^2 Rdt \cong (7.66\text{x}10^5 \text{J}/\Omega)(8.42\text{x}10^{-3}\ \Omega) =$ 6.45 kJ

TIME (μs)	EAST CHANNEL CURRENT OUTPUT (V)	EAST CHANNEL CURRENT MEAS.* (kA)	EAST CHANNEL VOLTAGE OUTPUT (V)	EAST CHANNEL VOLTAGE MEAS.** (V)	WEST CHANNEL CURRENT OUTPUT (V)	WEST CHANNEL CURRENT MEAS.* (kA)	WEST CHANNEL VOLTAGE OUTPUT (V)	WEST CHANNEL VOLTAGE MEAS.** (V)
0			0	0	0	0	0	0.0
10			-3	-1350	0.5	5.3	0	0.0
20			8	3600	0.0	5.3	0	0.0
30			7.5	3380	1.5	16.0	2.0	862
40			6	2700	6.0	63.8	3.0	1290
50			5	2250	8.0	85.7	3.0	1290
60			4	1800	9.0	97.1	2.8	1210
70			3.5	1580	9.5	103	2.6	1120
80			3	1350	10.0	110	2.5	1080
90			3.0	1350	10.0	111	2.4	1030
100			2.5	1130	10.0	112	2.3	991
110			2	900	10.0	113	2.2	948
120			1.5	675	9.5	109	2.1	905
130			1	450	9.0	104	2.0	862
140			0	0	8.5	99.9	1.7	733
150			-0.5	- 225	7.5	90.2	1.4	603
160			-1.0	- 450	6.5	80.4	1.1	474
170			-1.5	- 675	5.5	70.5	0.8	345
180			-2.0	- 900	4.5	60.4	0.5	216
190			-2.0	- 900	3.0	45.0	0.0	0.0
200			-1.5	- 675	1.5	29.4	-0.4	- 172
210			-1.0	- 450	0.0	13.7	-0.6	- 259
220			-0.5	- 225	-1.0	3.1	-0.7	- 302
230			0	0	-1.5	0	-0.6	- 259
240			0	0	-1.5	0	-0.4	- 172
250			0	0	-1.5	0	-0.2	- 86
260			0	0	-1.5	0	-0	0.0

Open Circuit

Open Circuit

*

** $v = (450)\, v_m$

* $i = (10.5 \times 10^3 A/V)[v_o + (10^3/s)\int_o^t v_o dt]$

** $v = (431)\, v_m$

$\int vidt \cong 12.7$ kJ

$\int i^2 R dt \cong (1.40 \times 10^6 J/\Omega)(8.42 \times 10^{-3} \Omega) = 11.8$ kJ

TIME (μs)	EAST CHANNEL				WEST CHANNEL			
	CURRENT		VOLTAGE		CURRENT		VOLTAGE	
	OUTPUT (V)	MEAS.* (kA)	OUTPUT (V)	MEAS.** (V)	OUTPUT (V)	MEAS.* (kA)	OUTPUT (V)	MEAS.** (V)
0	0.0	0.0	0.0	0	0.0	0.0	0.0	0
10	0.0	0.0	0.75	338	0.0	0.0	0.0	0
20	0.5	5.25	5.3	2390	4.0	42.4	3.8	1640
30	1.5	15.8	6.0	2700	7.0	74.7	3.2	1380
40	2.0	21.2	5.5	2480	8.0	86.0	3.0	1290
50	2.5	26.7	4.8	2160	8.1	87.9	2.7	1160
60	2.8	30.1	4.4	1980	8.0	87.7	2.5	1080
70	3.0	32.5	4.0	1800	8.0	88.5	2.2	948
80	3.2	34.9	3.6	1620	7.8	87.2	2.1	905
90	3.5	38.4	3.6	1620	8.0	90.2	2.2	948
100	3.5	38.7	3.1	1400	8.2	93.1	2.2	948
110	3.2	36.0	2.8	1260	8.0	91.9	2.0	862
120	3.0	34.2	2.4	1080	7.8	90.6	1.9	819
130	2.9	33.4	1.9	855	7.2	85.1	1.5	647
140	2.7	31.6	1.2	540	6.8	81.6	1.3	560
150	2.3	27.7	0.3	135	5.5	68.5	0.8	345
160	2.1	25.9	-0.75	- 338	4.2	55.3	0.4	172
170	1.5	19.8	-2.0	- 900	3.0	43.0	-0.1	- 43
180	0.9	13.6	-3.2	-1440	1.3	25.3	-0.6	- 259
190	0.0	4.27	-3.3	-1490	0.2	13.8	-0.8	- 345
200	-0.2	2.17	-3.0	-1350	-1.0	1.06	-0.9	- 388
210	-0.2	2.15	-2.1	- 945	-1.2	- 1.17	-0.7	- 302
220					-1.3	- 2.35	-0.5	- 216

* $i = (10.4 \times 10^3 A/V)[v_o + (10^3/s)\int_o^t v_o dt]$

** $v = (450)\, v_m$

$\int vidt \cong 5.36$ kJ

$\int i^2 R dt \cong (1.42 \times 10^5 J/\Omega)(8.42 \times 10^{-3} \Omega) = 1.20$ kJ

* $i = (10.5 \times 10^3 A/V)[v_o + (10^3/s)\int_o^t v_o dt]$

** $v = (431)\, v_m$

$\int vidt \cong 10.9$ kJ

$\int i^2 R dt \cong (1.03 \times 10^6 J/\Omega)(8.22 \times 10^{-3} \Omega) = 8.50$ kJ

TIME (μs)	EAST CHANNEL				WEST CHANNEL			
	CURRENT		VOLTAGE		CURRENT		VOLTAGE	
	OUTPUT (V)	MEAS.* (kA)	OUTPUT (V)	MEAS.** (V)	OUTPUT (V)	MEAS.* (kA)	OUTPUT (V)	MEAS.** (V)
0	0.0	0.0	0.0	0	0.0	0.0	0.0	0
10	0.0	0.0	0.0	0	1.0	10.6	1.5	647
20	0.2	2.10	3.0	1350	4.8	51.0	2.8	1210
30	1.4	14.7	5.7	2570	7.0	74.8	2.8	1210
40	1.6	17.0	5.7	2570	9.0	96.8	2.7	1160
50	1.9	20.3	5.3	2390	10.0	108	2.7	1160
60	2.4	25.7	5.3	2390	10.5	115	2.5	1080
70	3.0	32.3	5.4	2430	10.8	119	2.3	991
80	3.5	37.9	5.0	2250	10.9	121	2.1	905
90	3.9	42.4	4.5	2030	10.9	122	1.9	819
100	4.0	43.9	4.0	1800	10.7	121	1.8	776
110	4.2	46.4	3.3	1490	10.3	118	1.5	647
120	4.0	44.7	3.3	1490	10.0	116	1.4	603
130	3.9	44.1	2.5	1130	9.5	112	1.	517
140	3.7	42.4	2.0	900	9.2	110		431
150	3.4	39.6	1.2	540	8.5	103		345
160	3.0	35.8	0.3	135	7.0	88.	0.	172
170	2.3	28.7	-0.8	- 36	5.5	73.	-0.1	- 43
180	1.5	20.6	-2.1	- 945	3.5	52.	-0.6	- 259
190	1.0	15.5	-3.3	-1490	2.0	36.9	-1.0	- 431
200	0.5	10.3	-3.8	-1710	0.3	19.0	-1.3	- 560
210	-0.1	4.09	-4.2	-1890	- 1.0	5.29	-1.3	- 560
220	-0.2	3.03	-4.0	-1800	- 1.5	- 0.12	-0.9	- 388
230	-0.3	1.96			- 1.8	- 3.45		
240	-0.3	1.92			- 1.8	- 3.64		

* $i = (10.4 \times 10^3 A/V)[v_o + (10^3/s)\int_o^t v_o dt]$

** $v = (450)\, v_m$

$\int vidt \cong 6.16$ kJ

$\int i^2 Rdt \cong (2.01 \times 10^5 J/\Omega)(8.42 \times 10^{-3} \Omega) = 1.69$ kJ

* $i = (10.5 \times 10^3 A/V)[v_o + (10^3/s)\int_o^t v_o dt]$

** $v = (431)\, v_m$

$\int vidt \cong 12.0$ kJ

$\int i^2 Rdt \cong (1.81 \times 10^6 J/\Omega)(4.89 \times 10^{-3} \Omega) = 8.86$ kJ

TIME (μs)	EAST CHANNEL				WEST CHANNEL			
	CURRENT		VOLTAGE		CURRENT		VOLTAGE	
	OUTPUT (V)	MEAS.* (kA)	OUTPUT (V)	MEAS.** (V)	OUTPUT (V)	MEAS.* (kA)	OUTPUT (V)	MEAS.** (V)
0	0.0	0.0	0.0	0	0.0	0.0	0.0	0
10	0.0	0.0	-0.1	- 45	0.0	0.0	0.0	0
20	0.0	0.0	1.1	495	0.2	2.12	0.0	0
30	0.1	1.05	1.8	810	1.8	19.1	1.0	431
40	0.3	3.16	2.1	945	2.1	22.5	1.2	517
50	0.5	5.29	2.4	1080	3.0	32.2	1.4	603
60	0.7	7.45	2.6	1170	3.9	42.1	1.6	690
70	0.9	9.62	2.7	1220	4.2	45.7	1.7	733
80	1.0	10.8	2.5	1130	4.9	53.6	1.7	733
90	1.1	11.9	2.4	1080	5.5	60.4	1.7	733
100	1.2	13.1	2.1	945	5.7	63.1	1.6	690
110	1.3	14.3	1.6	720	5.5	61.6	1.3	560
120	1.4	15.4	1.1	495	5.0	56.9	1.0	431
130	1.5	16.6	0.6	270	4.3	50.0	0.7	302
140	1.4	15.7	0.1	45	3.3	39.8	0.4	172
150	1.3	14.8	0.0	0	2.9	35.9	0.2	86
160	1.2	13.9	-0.5	- 225	2.0	26.7	0.0	0
170	1.1	13.0	-0.7	- 315	1.0	16.3	-0.3	- 129
180	1.0	12.1	-1.1	- 495	0.3	8.99	-0.5	- 216
190	0.9	11.1	-1.1	- 495	-0.2	3.72	-0.6	- 259
200	0.7	9.11	-0.5	- 225	-1.0	- 4.79	-0.5	- 216
210	0.5	7.08	-0.4	- 180	-1.0	- 4.89	-0.3	- 129
220	0.3	5.03	-0.3	- 135	-1.0	- 5.00	-0.1	- 43
230	0.1	2.96	-0.3	- 135				
240	0.0	1.92	-0.2	- 90				
250	-0.3	-1.23	-0.1	- 45				
260	-0.3	-1.26	0.0	0				
270	-0.3	-1.29	0.0	0				

* $i = (10.4\text{x}10^{3}\text{A/V})[v_o+(10^{3}/s)\int_o^t v_o dt]$

** $v = (450)\, v_m$

$\int vidt \cong 0.673$ kJ

$\int_T^T i^2Rdt \cong (2.60\text{x}10^{4}\text{J}/\Omega)(8.42\text{x}10^{-3}\Omega) = 0.219$ kJ

* $i = (10.5\text{x}10^{3}\text{A/V})[v_o+(10^{3}/s)\int_o^t v_o dt]$

** $v = (431)\, v_m$

$\int vidt \cong 3.09$ kJ

$\int i^2Rdt \cong (2.97\text{x}10^{5}\text{J}/\Omega)(8.22\text{x}10^{-3}\Omega) = 2.44$ kJ

TIME (μs)	EAST CHANNEL				WEST CHANNEL			
	CURRENT		VOLTAGE		CURRENT		VOLTAGE	
	OUTPUT (V)	MEAS.* (kA)	OUTPUT (V)	MEAS.** (V)	OUTPUT (V)	MEAS.* (kA)	OUTPUT (V)	MEAS.** (V)
0	Off Scale	Off Scale, Peak > 49 kA	0.0	0	0.0	0.0	0.0	0
10			0.0	0	0.0	0.0	0.2	86
20			0.0	0	0.0	0.0	0.1	43
30			1.1	495	0.0	0.0	0.1	45
40			1.6	720	0.7	7.42	0.5	216
50			1.7	765	0.9	9.62	0.6	259
60			1.9	855	1.4	15.0	0.8	345
70			2.1	945	1.5	16.2	0.8	345
80			2.2	990	1.7	18.5	0.9	388
90			2.4	1080	1.9	20.8	0.95	409
100			2.2	990	2.0	22.1	0.9	388
110			2.1	945	2.1	23.3	0.8	345
120			1.9	855	2.2	24.6	0.7	302
130			1.6	720	2.3	25.9	0.6	259
140			1.3	585	2.1	24.0	0.5	216
150			1.0	450	2.0	23.2	0.4	172
160			0.7	315	1.7	20.2	0.3	129
170			0.5	225	1.5	18.3	0.2	86
180			0.3	135	1.2	15.2	0.1	43
190			0.1	45	1.0	13.3	0.0	0
200			0.0	0	0.8	11.2	-0.1	- 43
210			-0.2	- 90	0.6	9.20	-0.15	- 65
220			-0.4	- 180	0.3	6.08	-0.2	- 86
230			-0.5	- 225	0.1	3.99	-0.3	- 129
240			-0.5	- 225	-0.2	0.82	-0.3	- 129
250			-0.4	- 180	-0.4	- 1.32		
260			-0.3	- 135	-0.4	- 1.37		

* $i = (10.4 \times 10^3 A/V)[v_o + (10^3/s)\int_o^t v_o dt]$

** $v = (450)\, v_m$

* $i = (10.5 \times 10^3 A/V)[v_o + (10^3/s)\int_o^t v_o dt]$

** $v = (431)\, v_m$

$\int vidt \cong 0.732$ kJ

$\int i^2 R dt \cong (6.25 \times 10^4 J/\Omega)(8.22 \times 10^{-3} \Omega) = 0.513$ kJ

TIME (μs)	EAST CHANNEL				WEST CHANNEL			
	CURRENT		VOLTAGE		CURRENT		VOLTAGE	
	OUTPUT (V)	MEAS.* (kA)	OUTPUT (V)	MEAS.** (V)	OUTPUT (V)	MEAS.* (kA)	OUTPUT (V)	MEAS.** (V)
0	0.0	0.0	0.0	0	0.0	0.0	0.0	0
10	0.0	0.0	1.5	675	0.0	0.0	0.0	0
20	0.0	0.0	1.0	450	0.0	0.0	1.5	647
30	3.0	31.5	5.3	2390	2.8	29.7	2.0	862
40	4.5	47.6	5.8	2610	3.9	41.7	1.8	776
50	5.0	53.3	5.1	2300	4.2	45.2	1.6	690
60	5.6	60.1	4.9	2210	4.3	46.7	1.5	647
70	6.0	64.9	4.8	2160	4.5	49.3	1.5	647
80	6.8	73.9	4.7	2120	4.6	50.9	1.6	690
90	7.0	76.7	4.5	2030	4.8	53.5	1.6	690
100	7.1	78.5	4.0	1800	4.9	55.0	1.5	647
110	7.0	78.2	3.5	1580	5.0	56.6	1.3	560
120	6.5	73.7	2.8	1260	4.5	51.8	1.1	474
130	6.0	69.1	1.8	810	4.0	47.0	0.7	302
140	5.5	64.5	0.6	270	3.2	38.9	0.3	129
150	4.5	54.5	-0.5	- 225	2.0	26.5	-0.2	- 86
160	3.8	47.7	-1.8	- 810	0.8	14.0	-0.8	- 345
170	3.0	39.7	- 2.5	-1130	0.0	5.62	-0.7	- 302
180	2.0	29.5	-2.7	-1220	-0.8	- 2.87	-0.6	- 259
190	1.0	19.2	-2.8	-1260	-0.9	- 4.01	-0.5	- 216
200	-0.5	3.52	-2.5	-1130	-1.0	- 5.17	-0.4	- 172
210	-0.8	0.31	-1.5	- 675				
220	-0.8	0.23	-1.0	- 450				

* $i = (10.4\times10^{3}\,A/V)[v_o+(10^{3}/s)\int_o^t v_o dt]$

** $v = (450)\,v_m$

$\int_o^T vidt \cong (10^{-5}s)\Sigma(vi) = 12.6$ kJ

$\int_o^T i^2Rdt \cong (5.99\times10^{5}\,J/\Omega)(8.42\times10^{-3}\,\Omega) = 5.05$ kJ

* $i = (10.5\times10^{3}\,A/V)[v_o+(10^{3}/s)\int_o^t v_o dt]$

** $v = (431)\,v_m$

$\int_o^T vidt \cong (10^{-5}s)\Sigma(vi) = 3.26$ kJ

$\int_o^T i^2Rdt \cong (2.83\times10^{5}\,J/\Omega)(8.22\times10^{-3}\,\Omega) = 2.33$ kJ

APPENDIX D

CURRENT AND INDUCTANCE IN THE X-MHD GENERATOR

Faraday's Law, applied to a circuit with moving boundaries, is

$$\oint_{C(t)} \vec{E}' \cdot d\vec{l} = -\frac{d}{dt} \iint_{A(t)} \vec{B} \cdot \hat{n} ds \qquad (1)$$

where $\vec{E}'$ is the electric field measured in a frame of reference attached to the moving element of path length $d\vec{l}$ and $\vec{B}$ is the magnetic flux density. The unit vector $\hat{n}$ is normal to the surface bounded by the closed path $C(t)$. The path of interest for the explosive MHD generator is in the x-y plane*

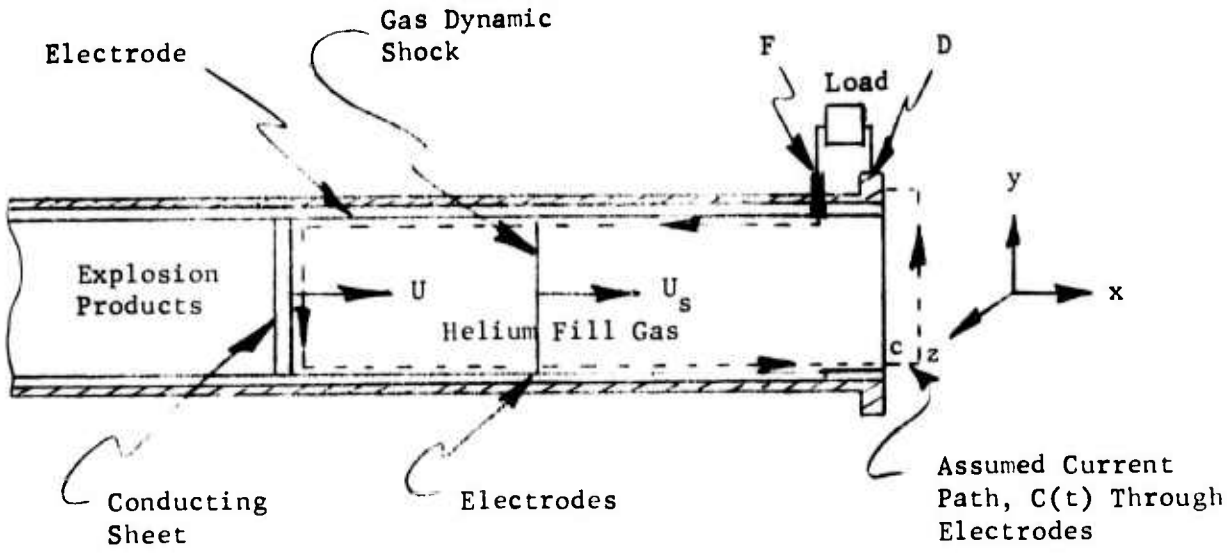

Figure 1.

as shown in Figure 1. The unit normal, $\hat{n}$, is parallel to the z-axis so Equation (1) becomes

$$\int_A^B E_y' dy + \int_B^C E_x' dx + \int_C^D \vec{E}' \cdot d\vec{l} + \int_D^E \vec{E}' \cdot d\vec{l}$$

$$+ \int_F^A E_x' dx = -\frac{d}{dt} \iint_{A(t)} B_z \, dxdy \qquad (2)$$

*Note that we are assuming a single current path between C and D, whereas the real current flow is through the duct walls and flange on both sides of the channel.

The integral

$$\int_A^B E'_y dy$$

can be written in terms of current density by using

$$\vec{E}' = \frac{\vec{J} + \beta_e \vec{J} \wedge (\vec{B}/B)}{\sigma}$$

$$= (\vec{J}/\sigma) + (1/n_e e)\vec{J} \wedge \vec{B} \tag{3}$$

where

$\vec{J}$ = current density,

σ = plasma conductivity,

n_e = electron density in the plasma,

e = magnitude of the charge on the electron.

If we assume that

$$J_x \cong J_z \cong 0$$

in the plasma, then

$$(\vec{J} \wedge \vec{B})_y = 0$$

and

$$E'_y \cong J_y/\sigma. \tag{3a}$$

With this substitution,

$$\int_A^B E'_y dy \cong \int_A^B (J_y/\sigma) dy. \tag{4}$$

We will also take

$$J_y \cong - i(t)\, w(y)(\Delta x)_c \tag{5}$$

where

$i(t)$ = (counterclockwise) current flowing through the load,

$w(y)$ = width of the duct at height y,

$(\Delta x)_c$ = thickness of the conducting sheet at height y.

Then

$$\int_A^B E'_y dy \cong - i(t) \int_A^B \frac{dy}{\sigma w(y)(\Delta x)_c}$$

$$\cong i(t) \int_B^A \frac{dy}{\sigma w(y)(\Delta x)_c}$$

$$\cong i(t)\, R_c \qquad (6)$$

where R_c is the resistance of the conductor defined by

$$R_c \equiv \int_B^A \frac{dy}{\sigma w(y)(\Delta x)_c} \quad .$$

A similar treatment of the current paths B-C, C-D and F-A using the conductivities of the electrodes and the flange give

$$\int_B^C E'_x dx = i(t)\, R_{LE}(t) \quad , \qquad (7a)$$

$$\int_F^A E'_x dx = i(t)\, R_{UE}(t) \quad , \qquad (7b)$$

$$\int_C^D \vec{E} \cdot d\vec{l} = i(t)\, R_F \quad . \qquad (7c)$$

The upper and lower electrode resistances, R_{UE} and R_{LE}, are functions of time because their working length grows shorter as the conducting sheet moves down the channel. Because of the high conductivity of these parts, however, these resistances will be neglected as will the flange resistance, R_F, for the same reason.

The integral over the current path D-F gives the voltage drop across the load,

$$\int_D^F \vec{E}' \cdot d\vec{l} = iR_L + L_L \frac{di}{dt} \tag{8}$$

with

R_L = load resistance,

L_L = load inductance.

Both of these parameters will be assumed to be constants.

Substitution of (6), (7a) through (7c), and (8) into (2) yields the approximate equation

$$i(R_c + R_L) + L_L \frac{di}{dt} \cong - \frac{d}{dt} \iint_{A(t)} B_z dxdy \tag{9}$$

which governs current flow in the explosive MHD generator.

The magnetic flux, $\iint B_z \, dxdy$, can also be written in terms of i by using Ampere's Law as follows:

$$\vec{B}(\vec{r}) = B_o \hat{z} + \frac{\mu_o}{4\pi} \iiint \frac{\vec{J}(\vec{r}') \times \hat{R}}{R^2} dx'dy'dz'$$

with

$\vec{r}$ = position of observation point with components x, y, z,

B_o = magnitude of applied magnetic flux density,

$\hat{z}$ = unit vector along the z-axis,

μ_o = permeability of vacuum,

$\vec{r}'$ = position at which current density is evaluated, with components x', y', z',

$\hat{R}$ = unit vector pointing from $\vec{r}'$ to $\vec{r}$,

$R^2 = (x-x')^2 + (y-y')^2 + (z-z)^2$ (square of the distance from $\vec{r}'$ to $\vec{r}$).

This expression can be transformed into a slightly more useful form:

$$\vec{B}(\vec{r}) = B_o \hat{z} + \frac{\mu_o}{4\pi} \nabla \times \iiint \frac{\vec{J}(\vec{r}')}{R} dx'dy'dz'$$

where the operator ∇ only applies to unprimed coordinates. With this expression,

$$\iint_{A(t)} B_z dxdy = \iint \vec{B}\cdot\hat{z}\, ds$$

$$= \iint B_o dxdy + \frac{\mu_o}{4\pi} \iint \left[\nabla \wedge \iiint \frac{\vec{J}(\vec{r}')}{R}\, dx'dy'dz' \right] \cdot \hat{z} ds$$

$$= D' \int_{x_c}^{x_F} B_o(x)dx + \frac{\mu_o}{4\pi} \oint_{C(t)} \left[\iiint \frac{\vec{J}(\vec{r}')}{R}\, dx'dy'dz' \right] \cdot d\vec{l}$$

where

D' = diameter of the duct + 2/3 of electrode thickness,*

x_c = x position of path through the conducting sheet,

x_F = x position of path through flange.

If we assume the current is uniformly distributed across each conductor cross-section, $A_\perp$, then

$$\vec{J}(\vec{r}') = \frac{i(t)}{A(\vec{r}')}\, \hat{\alpha}$$

where $\hat{\alpha}$ is a unit vector along the direction of the current density. With this expression,

$$\iint_{A(t)} B_z dxdy = D' \int_{x_c}^{L} B_o(x)dx + \frac{\mu_o i(t)}{4\pi} \oint_{C(t)} \left[\iiint \frac{\hat{\alpha}}{RA_\perp}\, dx'dy'dz' \right] \cdot d\vec{l} \qquad (10)$$

The inductance, L, of the generator is just the coefficient of i in the second term on the right:

$$L \equiv \frac{\mu_o}{4\pi} \oint_{C(t)} \left[\iiint \frac{\hat{\alpha}}{RA_\perp}\, dx'dy'dz' \right] \cdot d\vec{l} \qquad (11)$$

*The integration path was assumed to include only 1/3 of the thickness of an electrode on each side instead of 1/2 as a rough compensation for the curvature of the electrodes.

Using this definition, $\iint B_z dxdy$ can be written

$$\iint_{A(t)} B_z dxdy = D' \int_{x_c}^{x_F} B_o(x)dx + Li \tag{12}$$

The use of Equation (12) in (9) allows us to write

$$i(R_c + R_L) + L_L \frac{di}{dt} \cong D'UB_o(x_c) - \frac{d}{dt}(Li)$$

with the conducting sheet velocity, U, defined by

$$U = \frac{dx_c}{dt} .$$

Reorganizing and noting that L_L is constant,

$$\frac{d}{dt}[(L + L_L)i] + (R_c + R_L)i \cong D'UB_o(x_c) \tag{13}$$

Equation (13) can be integrated to give

$$i \cong \left(\frac{D'}{L + L_L}\right)\left[\exp\left(-\int_{x_e}^{x_c}\left(\frac{R_c + R_L}{L + L_L}\right)\frac{dx}{U}\right)\right].$$

$$\left[\int_{x_e}^{x_c} B_o(x)\exp\left(\int_{x_e}^{x}\left(\frac{R_c + R_L}{L + L_L}\right)\frac{dx'}{U}\right)dx\right] \tag{14}$$

where x_e is the position at which the electrodes start (i.e., the position at which current can start to flow).

The inductance, L, can be calculated by the techniques outlined in Reference 1. This results in an inductance of the form

$$L = (0.004\ \mu h/cm)\left\{D'\ell n\left[\frac{D' + \sqrt{(D')^2 + [(0.2237)(w + x)]^2}}{0.2237(w + s)}\right]\right.$$

$$\left. - \sqrt{D'^2 + [(0.2237)(w + s)]^2} + 0.2237\ (w + s)\right.$$

$$+ (x_F - x_c) \ln \left[\frac{(x_F - x_c) + \sqrt{(x_F - x_c)^2 + [(0.2237)(w + s)]^2}}{0.2237\ (w + s)} \right]$$

$$- \sqrt{(x_F - x_c)^2 + [(0.2237)(w + s)]^2} + 0.2237\ (w + s) \Bigg\}$$

$$- 0.004\ \mu h/cm \left\{ D' \ln \left[\frac{D' + \sqrt{(D')^2 + R_1^2}}{R_1} \right] \right.$$

$$- \sqrt{(D')^2 + R_1^2} + R_1$$

$$+ (x_F - x_c) \ln \left[\frac{(x_F - x_c) + \sqrt{(x_F - x_c)^2 + [1.022\ D']^2}}{1.022\ D'} \right]$$

$$\left. - \sqrt{(x_F - x_c)^2 + (1.022\ D')^2} + 1.022\ D' \right\} \qquad (15)$$

where

$D' = 16.30$ cm,

w = width of electrodes = 8.731 cm,

s = thickness of electrodes = 1.588 cm,

$R_1 = [k - 0.2644(w/x_F - x_c)]\ (x_F - x_c) + 0.2237\ (w + s)$,

k = parameter from Table II of Reference 1.

Note that in arriving at (15), the currents through both the conducting sheet and the flange have been assumed to have the same width and thickness as the electrodes. The departure from this ideal will be assumed constant and lumped in with L_L.

REFERENCES

1. F. W. Grover, Inductance Calculations, Working Formulas and Tables, (Dover Publ., New York, 1962).